https://dspace.org/

A study of flotation froth phase behaviour

Bhondayi, Clayton

2015-05-07
http://hdl.handle.net/10539/17676

Downloaded from a DSpace repository. https://dspace.org/

A STUDY OF FLOTATION FROTH PHASE BEHAVIOUR

Clayton Bhondayi

MSc Eng (Wits)

A thesis submitted to the Faculty of Engineering and the Built Environment, University of the Witwatersrand, Johannesburg, in fulfilment of the requirements for the degree of Doctor of Philosophy in Engineering

Johannesburg, November 2014

Declaration

I declare that this thesis is my own, unaided work. It is being submitted for the Degree of Doctor of Philosophy to the University of the Witwatersrand, Johannesburg. It has not been submitted before for any degree or examination in any other University.

Clayton Bhondayi

…… day of …… year ……..

Abstract

The performance of the froth phase, usually evaluated as froth recovery determines overall flotation performance. In most flotation operations, recovery across the froth is rate controlling; consequently understanding the froth phase is very critical. Although much research effort to understand the physics of the froth has been expended, not many techniques to optimise froth recovery have been implemented industrially. This is partly due to the complexity of the froth, brought about by the large number of variables involved and the lack of measurement techniques that can provide data to validate our current understanding of this phase. The work covered in this thesis both addresses the lack of measurement techniques and explores possible non-conventional ways in which froth phase sub-processes can be altered with the sole intention of optimising froth performance.

In response to the known lack of techniques to quantify froth phase sub-processes, an electro-resistivity technique was developed and tested to estimate froth phase bubble sizes in non-transparent flotation cells as a function of height above the pulp froth interface. Comparison of the froth bubble size estimates obtained from this new technique with the Sauter-mean diameter obtained using the photographic method established a linear correlation. The effect of pulp chemistry and solids content on the applicability of the estimation technique was also tested and it was concluded that a signal amenable to froth bubble size estimation can be obtained irrespective of the pulp chemistry. The applicability of the technique was further tested by investigating the effect of froth depth and gas rate on froth phase bubbles sizes. Results indicated that as superficial gas velocity was increased, bubble size estimates decreased. Increasing froth height at fixed gas rate resulted in an increase in froth phase bubble size estimates especially close to the froth surface.

In a quest to develop novel ways of optimising recovery across the froth phase, a cell was designed that enabled the study of the effects of different air distribution profiles across the pulp-froth interface on flotation performance. Three distinct gas fluxes viz. high gas flux at the back of the flotation cell (impeller at the back), uniform gas distribution (impeller at the centre) and high gas flux close to the concentrate weir (impeller in front) were investigated using an artificial ore comprised of 80% silica as gangue and 20 % limestone as floatable component. Results indicated that high gas flux at the back of the flotation cell resulted in higher recovery of limestone when

compared to the other two gas flux distributions while producing grade values similar to those obtained when high gas flux was supplied close to the concentrate weir. The effect of gas flux distribution profile on limestone grade was found to dwindle as froth height was increased. Froth surface velocities were then used to explain the flotation performance changes as a result of gas flux distribution changes but were found to be inadequate. This led to the use of numerical models to aid understanding. The 2D stream function equation was chosen as the primary model since it has been previously found to adequately describe the flow of froth by a number of workers e.g. Moys (1979), Murphy et al. (1996). A semi-analytical method called the method of false transients was used to obtain a solution to the stream function equation subject to boundary conditions defined according to the gas distribution fluxes obtained experimentally. Results from the endeavour confirmed changes in bubble and particle residence time distribution which were suspected to be partly responsible for the observed flotation performance changes.

In another endeavour to develop ways of manipulating froth phase sub-processes, the use of a froth baffle previously suggested by Moys (1979) was tested in a laboratory mechanical flotation cell. Results indicated that a froth baffle has a profound effect on both recovery and grade. The presence of a froth baffle resulted in increased grade at the expense of recovery when compared to an un-baffled froth. The stream function equation was also solved subject to boundary conditions that represent the presence of baffles. A solution was developed using finite difference methods on a rectangular map obtained by using Schwarz-Christoffel (SC) mapping. Results from the simulations indicated a change in particle residence time distribution in a manner that reduces spread. The change in residence time distribution helped in developing an explanation of the experimental data.

Thus results in this thesis clearly show that froth bubble sizes can be estimated in a non-transparent flotation cell and also that gas flux profiling in a single flotation cell changes flotation performance. The use of froth baffles as originally coined by Moys (1979) has also been shown to impact on flotation performance.

.

Dedications

To my family members

Publications

Paper published by the author on the contents of this thesis are as follows:

C Bhondayi and M Moys. (2014). Measurement of a proxy for froth phase bubble sizes as a function of froth depth in flotation machines Part 1. Theoretical development and testing of a new technique. International Journal of Mineral Processing 130 (2014) 8–19

Paper accepted for publication as a conference paper (IMPC 2014) on the contents of this thesis:

C Bhondayi and M Moys. Quantifying the effects of froth depth and gas rate on an estimate of flotation froth phase bubble sizes. IMPC 2014- reviewed and accepted for publication

Papers submitted for publication on the contents of this thesis:

C Bhondayi and M Moys. Effects of gas distribution profile on flotation cell performance: an experimental investigation. (*provisionally accepted by (IJMP) with corrections*)

C Bhondayi and M Moys. (2014). Measurement of a proxy for froth phase bubble sizes as a function of froth depth in flotation machines Part II. Investigating the effects of pulp chemistry and froth solids content.

Other papers

C Bhondayi and M Moys. (2011). Determination of sampling pipe (riser) diameter for a flotation bubble load measuring device. Minerals Engineering 24 (2011) 1664–1676

Acknowledgements

I would like to register my gratitude to the following, who in one way or another, made the completion of this work possible.

My supervisor, Prof. Michael, H. Moys for his guidance, and support throughout the execution of this work. I want to acknowledge the effort he put in reading through every Chapter in this thesis and correcting and sometimes rereading them more than I can remember.

Workshop staff, Mr. Theo Prassinos, Mr. Rhod McRae-Samuel and Phathu Sikhwari for their patience and vital ideas during the construction of the flotation cell. It wasn't easy. I am grateful.

Dr. Ian Baker for stimulating discussions and helpful suggestions during the development of the circuit to measure froth phase bubble sizer

Dr Frank Kienhofer for providing the SCXI 1520 data acquisition device used during bubble size measurements.

Mr. Dario Fanucchi from wits school of Applied and Computational mathematics for his assistants in coding

Lonmin platinum and Dr. Victor Ross for providing financial support. Dr. Victor Ross as a flotation expert is further acknowledged for many suggestions he made during experimentation and write-up. This work would not be what it is without his suggestions.

I am also indebted to my family (Father, mother, brothers and sisters) for standing by me through all the hard times; thank you guys.

Stella and Anashe for their unconditional love. I kept going because of you guys.

Lastly to God, for all things are possible with his grace.

Table of contents

Declaration i
Abstract ii
Dedications iv
Publications v
Acknowledgements vi
Table of contents vii
List of Figures xvi
List of Tables xxiv
Chapter 1 1
1.1 Background and motivation 1
1.1 Thesis objectives 2
1.2 Thesis layout 3
Chapter 2 5
2.1 Introduction 5
2.2 Review of the flotation process 5
2.2.1 Slurry preparation 6
2.2.1.1 Effect of particle size 6
2.2.1.2 Effect of chemical conditioning 7
2.2.2 Operating conditions 7
2.2.2.1 Effect of gas dispersion properties 8
2.2.2.2 The degree of solid suspension 10
2.2.3 Particle transport 11
2.2.3.1 True flotation 11
2.2.3.2 Entrainment 12
2.3 Basics of flotation froths 12
2.3.1 Froth formation 12
2.3.2 Bubble coalescence and particle detachment 13

2.3.3 Particle reattachment and selectivity 14
2.3.4 Liquid drainage 14
2.3.5 Froth stability 15

2.4 Flotation modelling 16
2.4.1 Single rate kinetic models 17
2.4.2 Distributed rate kinetic models 18

2.4.2.1 Distributed rate models based on size 18
2.4.2.2 Distributed rate models based on particle sizes 19

2.4.3 Double distributed parameter models 20
2.4.5 Entrainment modelling 21
2.4.6 Water recovery modelling 24

2.4.6.1 Water recovery as function of solids recovery 24
2.4.6.2 Water recovery as a function of froth residence time 25
2.4.6.3 First order water recovery models 26
2.4.6.4 Drainage model for water recovery 27
2.4.6.5 Fundamental approach to water recovery modelling 28

2.5 Froth Recovery as a froth performance measure 29
2.5.1 Methods of froth recovery measurement 31

2.5.1.1 Froth drop-back measurement techniques 32
2.5.1.2 Mass balance techniques 33
2.5.1.3 Changing froth depth 33

2.6 Froth phase modelling 35
2.6.1 Review of froth transport models 36

2.6.1.1 Moys, 1984 36
2.6.1.2 Zheng et al. (2004) 39
2.6.1.3 Discussion of froth phase modelling 41

2.7 Summary and conclusions 41
Chapter 3 43
3.1 Introduction 43

3.2 Flotation cell 43
3.2.1 Flotation cell description 43

3.2.1.1 Flotation cell base plate design 46
3.2.1.2 Flotation cell agitation mechanism 47
3.2.1.3 Flotation cell level control 49

3.3 Experimental programs 50
3.3.1 Laboratory set up for continuous experiments 50
3.3.2 Ore preparation 51
3.3.3 Slurry preparation 52

3.4 Sampling and data collection 52
3.4.1 Stream sampling and video recording of the froth phase 52
3.4.2 Froth phase video recording 53
3.4.3 Superficial gas velocity measurement 54
3.4.4 Sampling error comment 54

3.5 Flotation cell commissioning 54
3.5.1 Flotation cell hydrodynamic testing 55

3.5.1.1 Agitator calibration 55
3.5.1.2: Determination of impeller critical speed for just off-bottom suspension 56
3.5.1.3: Discussion-solids suspension 58

3.5.2 Gas dispersion characteristics testing 59

3.5.2.1: Bubble size measurement 59
3.5.2.2: Superficial gas velocity (J_g) 59
3.5.2.3: Gas hold-up and bubble surface area flux calculations 60
3.5.2.4 Discussion-solids suspension 61

3.6: Difficulties encountered 61
Chapter 4 63
4.1 Introduction 63
4.2 Development of the method and testing in two phase foam 65
4.2.1 Use of electrical conductivity to estimate bubble sizes 65

4.2.2 New technique measuring principle. 66
4.2.3 Froth bubble-sizer description..... 67

4.3 Experimental testing of the technique..... 69
4.3.1 Air-water (Bubble air-bubble lamella simulation) experiments..... 69
4.3.2 Froth bubble size measurement in mini-flotation column 70

4.4 Results..... 71
4.4.1 Air-water (Bubble-air bubble-lamella simulation) experiments..... 71

4.4.1.1 Discussion: Air-water (Bubble air-bubble lamella simulation) experiment..... 74

4.4.1.1.1 Discharge of polarisation capacitance set between an electrolyte and electrode 74
4.4.1.1.2 Viscous effects of the water which result in a thin film/sheath of water following the probe as it moves out of water. 75

4.4.2 Mini-flotation column results 77

4.4.2.1 Bubble sizer results obtained using 0.0075M CuSO4 (aq) as the pulp phase 77
4.4.2.2 Photographic results of actual froth bubble sizes 81
4.4.2.3 Comparison of IIDs to actual froth bubble sizes 85
4.4.2.4 Discussion of froth bubble size measurement..... 86

4.4.2.4.1 Probe velocity overestimation 87
4.4.2.4.2 Conductivity probe passing though vertical Plateau borders. 88

4.5 Summary 92
4.5.1 Further remarks on froth bubble size measurement..... 93

4.6 Effect of pulp chemistry and froth solids content on the measurement of a proxy for froth phase bubble sizes 93
4.6.1 Introduction..... 93
4.6.2 Froth bubble size measurement results obtained using water..... 94

4.6.2.1 Comparison of average IID to Sauter-mean diameters for water..... 97
4.6.3 Froth bubble size measurement results obtained using for 0.0075M NaOH (aq) solution..... 98

4.6.3.1 Comparison of average IID to actual froth bubble sizes for NaOH solution 100

4.6.4 Bubble size measurement results obtained using 2%w/w limestone as the pulp phase 102

4.6.4.1 Comparison of IIDs to actual froth bubble sizes for 2% limestone pulp phase 104

4.7 Concluding remarks 105

Chapter 5 107

5.1 Introduction 107

5.2 Brief experimental description 108

5.2.1 Flotation tests set-up 108

5.2.2 IID measurement set-up 108

5.3 Results 109

5.3.2 Illustration of the estimation of IID 109

5.3.2.1 Variation of IID with height 113

5.3.3 Effect of froth depth 114

5.3.4 Effect of gas rate on IID 116

5.4: Conclusions 117

Chapter 6 119

6.1 Introduction 119

6.2 Brief experimental description 120

6.2.1 Slurry preparation 121

6.3 Results 121

6.3.1 Variation of superficial gas velocity with impeller position 121

6.3.2 Effect of impeller position on limestone recovery 124

6.3.3: Effect of impeller position on limestone grade (concentrate) 127

6.3.4: Effect of impeller position on silica recovery, water recovery and entrainment. 130

6.3.4.1 Effect of impeller position on entrainment 132

6.3.4.1 Effect of impeller position on water recovery 133

6.3.5: Summary of the effects impeller position, gas rate and froth height on flotation performance 135

6.3.5.1 Conclusions 137

6.4: Using froth surface velocities to explain flotation performance changes. 138

6.4.1. Froth surface trajectories and velocities profiles for the three gas flux distribution at froth height of 6.3cm and gas flux of 0.90cm/s 139

6.4.1.1 Surface velocity profiles when impeller was at the back 140

6.4.1.2 Surface velocity profiles when impeller was at the centre of the flotation cell 141

6.4.1.3 Surface velocity profiles when impeller was near the concentrate weir. 142

6.4.2. Recovery and grade- froth surface velocities link 143

6.4.2. Froth surface trajectories and froth surface velocities profiles for the three gas flux distribution at froth height of 10.1cm and 0.90cm/s gas flux 145

6.4.3. Effect of froth depth on surface velocity. 147

6.5 Summary and conclusions on surface velocity link 148

Chapter 7 150

7.1 Introduction 150

7.2. Model 151

7.2.1 Boundary conditions 152

7.2.1 Solid walls (2), (3) and (6) 153

7.2.1.1 Boundary (2) Flotation back plate (0≤y≤h1) 153

7.2.1.2 Boundary (3) Flotation crowder (0≤x≤Hf-h1) and (h1≤y≤Hf) 153

7.2.1.3 Boundary (6) concentrate weir wall (0≤y≤hf) 154

7.2.2 Permeable walls (1), (4) and (5) 154

7.2.2.1 Pulp-froth interface boundary (1) $(0 \le x \le L, y = 0)$ 154

7.2.2.2 Froth surface boundary (4) (Hf-h1≤x≤L) 155

7.2.2.3 Concentrate weir boundary (5) 156

7.2 Numerical solution development 157
7.2.1 Method of Lines (MOL**)** 157

7.2.1.1 Treatment of boundary conditions 158

7.3 Discussion of results 158
7.3.1 Permeable boundary specification 159

7.3.1.1 Pulp-froth interface flux 159
7.3.1.2 Bubble breakage flux 160

7.3.2 Effect of gas distribution on air recovery 162
7.3.3 Effect of gas distribution on froth residence time 165

7.3.3.1 Bubble residence time 165

7.3.1.1: Comparison of simulation data with experimental data 168

7.3.3.2 Effect of gas distribution on particle residence time 169

Chapter 8 173

8.1 Introduction 173
8.2 Review of froth transport models 175
8.2 Brief experimental description 176
8.4 Results 177
8.4.1 Limestone recovery 178
8.4.2 Concentrate grade 182
8.4.3 Silica recovery 185
8.4.4 Water recovery 186

8.5 Results summary 188
8.6. Conclusion 188
8.7 Further remarks 189
8.7.1 Drainage patterns 190
8.7.2 Bubble coalescence 190
8.7.3 Bubble coalescence 190

Chapter 9 192

9.1 Introduction..... 192
9.2. Boundary conditions..... 193
9.2.1 Baffle position BP 1 ($L - x_b; 0 \leq y \leq hf$) 193
9.2.2 Angled baffle positions..... 194
9.2.2.1 Baffle position BP 3 196
9.2.2.2 Baffle position BP 2 197
9.2.3 Boundaries (1) to (6) shown in Figure 9. 2 197
9.3 Numerical solution development 198
9.3.1 Schwarz-Christoffel (SC) mapping..... 198
9.4 Discussion of results 201
9.4.1 Effect of froth baffles on bubble streamlines 201
9.4.2 Effect of froth baffles on velocity distribution 202
9.4.3 Effect of froth baffles on particle residence time distribution..... 205
9.4.4 Effect of distance x_b on residence time distribution 207
9.5 Conclusions..... 210
Chapter 10 211
10.1 introduction..... 211
10.2 Conclusions from froth phase bubble-sizer development and testing..... 211
10.3 Conclusions from techniques to optimize froth phase performance through altering froth residence times..... 213
10.3.1 Conclusions on the effect of gas flux distribution across the pulp-froth interface. 213
10.3.2 Conclusions on the froth baffles..... 215
10.4 Overall conclusions and recommendations 215
Appendix A.....217
Pump Calibration data 217
A1: Pump calibration..... 217
A1.1: Testing pump delivery consistence..... 218

A2: Air rotameter calibration 219

Appendix B.....220

Appendix C.....226

C.1 Matlab function file to find local minima and maxima 226

C.2.0 Matlab script file to calculate the derivative of a signal 227

C.3 Matlab function file to solve Stream function equation using the method of lines (MOL 229

C.4 Matlab script file to solve Stream function equation using the method of lines (MOL) 231

C.5 Mathematica code to plot bubble streamline 232

C.6 Matlab function file to implement Schwarz-Christoffel Mapping in the presence of a froth baffle 235

C.7 Matlab function file to solve stream function equation on the rectangular map and transforming it back to the physical domain 237

C.8 Matlab function file to visualize the solution in Matlab 238

C.9 Matlab script file that calls functions C.6 to C.9 to solve flows when there is baffle in the froth 239

C.10 Matlab script file that calls functions C.6 to C.9 to solve flows when there is no baffle in the froth 240

C.11 Mathematica code to plot bubble streamline, velocity vector and density plots and calculate froth residence times..... 241

References 253

List of Figures

Figure 2.1: Recovery as a function of particle sizes, (after Trahar, 1981) 6

Figure 2.2: Classification function for solids suspension in the Outokumpu 150 m^3 tank cell at the Newcrest Cadia copper concentrator (after Zheng et al., 2005) 11

Figure 2.3: Interaction between zones in a flotation cell (Vera et al., 2002) 30

Figure 2.5: Boundary conditions for solution of the two-dimensional froth flow behaviour (after Moys 1984) 37

Figure 2.6: Two-stage tractable model (after Moys 1984) 38

Figure 2.7: Effect of flow modifiers on bubble streamlines in the froth phase (after Moys 1984) 39

Figure 3.1: Variable-depth variable-rotor position flotation cell used for both batch and continuous experiments 44

Figure 3.2: Side view of the flotation cell showing the table, flotation cell, motor and impeller shaft arrangement 45

Figure 3.3: Picture of flotation cell, showing stand and VSD drive and stator. 46

Figure 3.4: Picture showing (a) flotation cell base, relative to the fixed agitation mechanism (b) side view with the agitation mechanism at the centre (c) side view with agitation mechanism at the back close to the concentrate launder (d) side view with agitation mechanism in front of the flotation cell. 47

Figure 3.5: Design details of the flotation cell agitation mechanism 48

Figure 3.6: Pictures of the rotor (a,b,c) and rotor size compared to stator (d) 49

Figure 3.7: Schematic of the pseudo-steady state experimental rig. 50

Figure 3.8: Particle size distribution (PSD) for limestone and silica used in all experiments 51

Figure 3.9: Agitator speed in rpm as function of VSD frequency. 56

Figure 3.10a: Picture showing settled silica sand when the agitator is stationery..... 57

Figure 3.9b: Picture showing silica sand rising as agitator speed is increased to 700rpm. 57

Figure 3.10c: Picture showing almost all sand particles suspended in the water agitator speed at 1500 rpm. 58

Figure 3.10d: Picture showing all sand particles suspended in the water agitator speed at 2000 rpm..... 58

Figure 3.11: Bubble size distribution at 1200 rpm and 20 mg/l Dowfroth 250..... 59

Figure 3.12: Typical gas superficial velocity distribution profile when agitator is at the centre. 60

Figure 4.1: Theoretical illustration of the output voltage signal that is obtained when a conducting thin wire cuts through froth phase..... 67

Figure 4.3: Schematic of the conductivity probe, showing the insulated copper wire, Mild steel rod and the PVC stopper with dimensions included 69

Figure 4.4: Schematic of the experimental set-up to measure bubble size in the mini-flotation column 71

Figure 4.5: Conductivity probe response as it is moved in and out of water at regular intervals (a) probe connected to the negative terminal (b) probe connected to the negative terminal. 73

Figure 4.8: Typical bubble-sizer signal (a) and its derivative (b) when bubble size measurements are taken in 0.0075M copper sulphate solution. 78

Figure 4.9: Average IID (individual drops) as a function of height above the pulp-froth interface 80

Figure 4.10: Average IID (nine drops) as a function of height above the pulp-froth interface for 0.0075M CuSO4 solution..... 80

Figure 4.11: IID distribution for the two froth segments..... 81

Figure 4.12: Cumulative IID distribution for the two froth segments 81

Figure 4.13: Illustration of manual bubble size measurement using ImageJ with lines indicating measured diameters 83

Figure 4.14: Sauter-Mean bubble diameter obtained using the photographic method as a function of froth depth. 84

Figure 4.15: Comparison of bubble size distribution (BSD) in froth segments 85

Figure 4.16: Comparison of the bubble-sizer IID and the Sauter-mean diameter 86

Figure 4.17: Comparison of probe velocity inside the froth when (a) free fall conditions are assumed and (b) when froth resistance is taken into account 88

Figure 4.18: Illustration of the simulation of the new bubble size measuring technique with emphasis of the different kinds of IIDs 90

Figure 4.19: Variation of average IIDs with froth height resulting from bubble-sizer simulation experiments 91

Figure 4.20: Comparison of the average IIDs obtained with (i) the simulation experiments and (ii) the actual bubble size measurement with (iii) the Sauter-mean diameter obtained using the photographic method. 91

Figure 4.22: Typical signal (a) and its derivative (b) obtained when bubble-sizer probe cuts through froth generated from water dosed with frother. 96

Figure 4.23: Average IIDs for individual probe drops as a function of height above the pulp-froth interface for water dosed with frother. 97

Figure 4.24: Variation of IID with froth height for all the six drops for water. 97

Figure 4.25: Comparison of the bubble-sizer average IID to the Sauter-mean diameter obtained using the photographic method as a function of height above the pulp-froth interface for water dosed with frother. 98

Figure 4.26: Typical bubble-sizer signal (a) and its derivative (b) when bubble size measurements are taken in 0.0075M NaOH (aq) solution. 99

Figure 4.27: Average IIDs for individual probe drops as a function of height above the pulp-froth interface for 0.0075M sodium hydroxide solution 100

Figure 4.28: Variation of IID with froth height for all the six drops for the 0.0075M Sodium hydroxide solution..... 100

Figure 4.29: Variation of Sauter mean diameter (d32) with height above pulp-froth interface for NaOH (aq) solution. 101

Figure 4.30: Comparison of the bubble-sizer average IID to the Sauter-mean diameter for NaOH solution. 101

Figure 4.31: Typical signal (a) and its derivative (b) obtained when bubble-sizer probe cuts through frother (2% limestone solids content). 103

Figure 4.32: Average IIDs for individual probe drops as a function of height above the pulp-froth interface for 2% limestone pulp phase 104

Figure 4.33: Variation of IID with froth height for all the eight drops for 2%limestone pulp 104

Figure 4.34: Comparison of the bubble-sizer average IID to the Sauter-mean diameter as obtained by photographic method for 2% Limestone..... 105

Figure 5.1: Schematic of the experimental set-up to measure IID..... 109

Figure 5.2: Typical bubble-sizer signal (a) and its derivative (b) IID measurements were taken 0.57cm/s gas flux and froth depth of 11cm 111

Figure 5.3a: Illustration of IID determination showing average IIDs for each of the nine drops 112

Figure 5.3b: Average IID for the nine drops shown in figure 5.3a, error bars based on standard deviations. 112

Figure 5.4: Picture showing variation in bubble sizes above the pulp-froth interface. 114

Figure 5.5: Graph illustrating effects of froth depth at a fixed superficial gas velocity of 0.97cm/s..... 115

Figure 5.6: Graph illustrating effects of froth depth at a fixed superficial gas velocity of 0.57cm/s..... 116

Figure 5.7: Effect of gas rate on IID when froth depth was fixed at 6.3cm..... 117

Figure 5.8: Effect of gas rate on IID when froth depth was fixed at 11cm..... 117

Figure 6.1: The plan view of the flotation cell showing points at which superficial gas velocity was measured. 121

Figure 6.2: Variation of superficial gas velocity with agitator position (a) representing gas flux profile when the agitator is at the back of the flotation cell (b) agitator at the centre (c) agitator close to the concentrate weir 123

Figure 6.3: Variation of limestone recovery with impeller position and gas rate at two froth depth (a, b) and with impeller position and froth height (c, d) at different air flowrates. 126

Figure 6.4: Variation of limestone grade with impeller position and gas rate at two froth depths (a, b) and with impeller position and froth height at two superficial gas velocities (c, d) 129

Figure 6.5: Variation of silica recovery with impeller position and gas rate at two froth depths (a &b) and variation of silica recovery with froth height at two fixed gas rates (c &d)..... 132

Figure 6.6: Typical silica PSDs for the concentrate and feed when impeller was at the centre. 133

Figure 6.8: Variation of water recovery with impeller position and gas rate at (a) froth height of 6.3cm and (b) froth height of 10.1cm..... 134

Figure 6.9: Plot of silica recovery as a function of water recovery for the three impeller positions at froth height of 6.3cm and three different gas rates (0.57, 0.90 and 1.24cm/s)..... 135

Figure 6.10: A picture illustrating how froth surface velocities and streamline position was determined using Tracker..... 139

Figure 6.10: Surface trajectories (a) and velocity profiles (b) when impeller was at the back of the flotation cell for a gas flux of 0.90cm/s and froth depth 6.3cm 141

Figure 6.11: Surface trajectories (a) and velocity profiles (b) when impeller was at the centre of the flotation cell for a gas flux of 0.90cm/s and froth depth 6.3cm 142

Figure 6.12: Surface trajectories (a) and velocity profiles (b) when impeller was close to the concentrate weir for a gas of flux 0.90cm/s and froth depth 6.3cm..... 143

Figure 6.13: Comparison of average surface velocity at a froth height of 6.3cm for the three impeller positions at a superficial gas velocity of 0.90cm/s 144

Figure 6.14: Surface trajectories and velocity profiles for the three impeller positions for gas rate 0.90cm/s and froth depth 10.1cm..... 146

Figure 6.15: Comparison of average surface velocities for froth height of 10.1cm for the three impeller positions at a superficial gas velocity of 0.90cm/s 147

Figure 6.16: Comparison of average surface velocities for froth height of 10.1cm and 6.3cm for the three impeller positions at a superficial gas velocity of 0.90cm/s..... 148

Figure 7.1: Two-dimensional flow domain showing the boundaries that need to be defined. 153

Figure 7.2: Gas flux distribution at the pulp-froth for (a) high gas rate close to the concentrate weir (b) high gas rate the centre (c) high gas rate at the back of the flotation cell 159

Figure 7.3: Froth surface velocity as a function of distance from the back of the flotation (a,b,c) and fluxes across the surface of the froth (d,e,f) obtained for the three gas fluxes 161

Figure 7.4: Bubble streamline plot for (a) high gas flux is supplied close to the concentrate weir (G-front) (b) high gas flux at the centre (Ge-centre) (c) high gas flux at the back of the flotation cell (G-back) and air recovery values for the three fluxes 163

Figure 7.5: Summary of flotation performance obtained when froth depth and average gas rate was set at 0.9cm/s 164

Figure 7.6: Simulated velocity distributions in the froth phase for each of the gas distribution profiles..... 164

Figure 7.7: Variation of bubble residence times as a function of distance from the back of the flotation cell. 167

Figure 7.8: Cumulative bubble residence time distribution for the three gas flux distribution profiles..... 167

Figure 7.9: variation particle residence times as a function of distance from the back of the flotation cell..... 170

Figure 7.10: Cumulative bubble residence time distribution for the three gas flux distribution profiles..... 171

Figure 8.1: effect of flow modifiers on bubble streamlines in the froth phase (after Moys 1984) 176

Figure 8.2: schematic representation of froth baffle positions investigated (a) baffle at 45^{o} to the horizontal, (b) baffle at 67^{o} to the horizontal and (c) baffle at 90^{0} to the horizontal..... 177

Figure 8.4: illustration of the most important regions and cross sectional areas when a froth baffle is inserted into the froth..... 182

Figure 8.5: Grade-recovery plot of the three baffle positions..... 185

Figure 8.6: Variation of water recovery with baffle position and angle..... 187

Figure 9.2: Illustration of the development of boundary conditions for angled froth baffle 195

Figure 9.3: Bubble streamlines when there was (a) No baffle in the froth (b) 90^{0} baffle in the froth (c) 45^{0} in the baffle and (d) 67^{0} baffle in froth, with (x_b) set at 5cm. 203

Figure 9.4: Velocity distribution when there was (a) No baffle in the froth (b) 90^{0} baffle in the froth (c) 45^{0} in the baffle and (d) 67^{0} baffle in froth with x_b set at 5cm..... 204

Figure 9.5: Variation of bubble residence times as a function of distance from the back of the flotation cell. 206

Figure 9.6: Cumulative particle residence time distributions for the four baffle positions when L_B was 5cm 207

Figure 9.7: Variation of particle residence time distribution with distance between baffle and concentrate weir wall (x_b) for (a) 90^0 baffle (b) 67^0 baffle and (c) 45^0 baffle 209

List of Tables

Table 3.1: Mixing tank specifications 52

Table 3.2: Summary of gas dispersion properties 61

Table 6.1: Statistical analysis for limestone recovery 125

Table 6.4: Post-Hoc Test for limestone based on Tukey's honestly significant difference (HSD) 128

Table 7.1: Residence time distribution for 50% of bubbles with longest residence time 166

Table 8.1a: One-Way Anova for limestone recovery- results summary 180

Table 8.1b: Tukey HSD test results summary 180

Table 8.2a: One-Way Anova for limestone grade- results summary 184

Table 8.2b: Tukey HSD test results summary 184

Table 8.3a: One-way ANOVA for Silica recovery results summary 186

Table 8.3b: Tukey HSD test results for silica recovery. 186

Table 8.4a: One-way ANOVA for water recovery results summary 187

Table 8.4b: Tukey HSD test results for water recovery 187

Chapter 1

Introduction

1.1 Background and motivation

Froth flotation as a unit operation has found extensive use in the mineral processing industry especially in beneficiating low grade ores. It consists of two phases, viz. the pulp-phase and the froth phase. In the pulp-phase rising air bubbles preferentially collect hydrophobic particles and rise with them to the top of the pulp phase where froth is created. In the froth phase, the loaded bubbles coalesce and break-up; particles detach and re-attach to the available bubble surface area; interstitial and bubble film water drains back into in the pulp phase. The overall effect of all these sub-processes is the transport and recovery of valuable minerals.

Of the two distinct flotation phases, the pulp phase seems to be fairly well understood and flotation cell designs and circuits that maximise the governing sub-processes have and are being designed. This cannot be said of the froth phase. The inherent complexities of the froth and the lack of robust techniques to measure and quantify important froth phase sub-processes such as bubble coalescence has limited our insight and made progress towards optimal operation difficult. For instance the Platinum industry in South Africa, beneficiate the PGMs via the flotation process; surprisingly recoveries across the froth phase have been reported to be in the order of 5-10 percent (Ross, 2012). Vera et al. (2002) had also previously reported froth recoveries as low as 10 percent. This clearly shows the importance of the froth phase and its impact when neglected.

Control of froth phase sub-processes (bubble coalescence, drainage, particle detachment and reattachment) for given feed and chemical conditions is typically achieved through manipulating froth residence time by changing froth depth or/and gas rate. For a given pulp chemical conditioning, froth residence time influences froth drainage, froth stability and mobility. While froth stability governs the degree of bubble coalescence; froth drainage and mobility influences the recovery of both the detached particles and entrained particles. Changing froth depth and gas rate does

not only impact froth phase sub-processes but also the pulp phase sub-processes, consequently these variables can only be changed within a limited range. This imposes an operational constraint on the quest to optimise froth performance. One way in which this can be addressed is designing flotation chambers with additional manipulated variables that can alter froth residence time at a given froth depth and gas rate. Such designs have been suggested in literature e.g. the froth flow modifier suggested by Moys (1979). Another way of addressing this constraint is by looking at the way gas is distributed across the pulp-froth interface. It is envisaged that there exists an optimum gas flux profile distribution that optimises particle residence time distribution in the froth phase.

Froth residence time also affects bubble coalescence which in turn influences particle detachment. The rate of bubble coalescence is a measure of the stability of the froth and thus bubble coalescence is a key froth phase sub-process. Despite this importance, no method exists so far that can provide a measure of how froth phase bubble sizes change above the pulp-froth interface especially in non-transparent flotation cells. Development of methods or techniques to measure rate of change of bubbles size in the froth is a huge step in trying to integrate bubble coalescence and its impact on recovery across the froth phase into flotation froth phase models.

Consequently, froth phase studies described in this thesis focuses on development of techniques to measure froth phase bubbles sizes and ways of manipulating froth residence times to optimise recovery across the froth phase. Froth residence time manipulation techniques studied herein include manipulating gas flux distribution across the pulp-froth interface and using froth baffle/froth flow modifiers as previously describe by Moys (1979).

1.1 Thesis objectives

The main thrust of this thesis is to contribute to the on-going attempts to understand the froth phase. Further, it seeks to understand how the froth phase can be manipulated to improve flotation performance. It is divided into two sections. The first section’s objective is solely to develop and test a method of measuring froth phase bubble sizes in froth systems where the photographic method cannot be applied. Froth phase bubbles are important in that they provide information on the rate of coalescence within the froth. Successful development of a method to infer bubble sizes within froths is a huge step in understanding the froth phase as no other

method exists yet. The second section's aim is to develop ways of manipulating froth phase performance through manipulating froth residence time, water drainage patterns and bubble flow patterns. It is our belief that by designing froth chambers, that allows the optimisation of froth residence time distribution within the froth, flotation performance can be increased. Two non-conventional experimental approaches that involve manipulating gas flux across the pulp-froth interface and manipulating bubble streamlines with froth baffles are studied.

1.2 Thesis layout

This thesis is organised into 10 Chapters, the current Chapter provides the motivation for carrying out the current research; it sets out the objectives of the research and the scope of work.

Chapter 2 reviews literature related to flotation froths, it begins with a brief background on froth flotation, highlighting the important variables and how they affect the flotation process. The Chapter goes on to describe flotation performance measures with emphasis on methods to measure froth performance, a discussion of the froth transport models is also covered.

Chapter 3 offers a description of the experimental techniques, equipment, ores and analysis methods developed to achieve the set objectives.

Chapter 4 presents a description of the development of a novel technique to measure froth phase bubble sizes. In this Chapter, the developed technique is tested and results obtained are compared to bubble sizes obtained using the photographic technique. The effect of slurry chemical conditioning is also reported in this Chapter.

Chapter 5 is a step further in the development of the froth bubble-sizer. Results of measurement of bubble sizes from industrial slurry are presented and effect on froth depth and gas rate on froth phase bubble sizes investigated.

Chapter 6 is dedicated to the quest of optimising froth performance through manipulation of froth residence time. The approach taken in this Chapter is to study the effects of gas flux distribution across the pulp-froth interface. Three positions of the impeller to change gas flux across the pulp-froth interface are studied and flotation performance measured. Froth surface velocities are used to explain the observed flotation performance.

Chapter 7 is a consequence of Chapter 6 as it is dedicated to using mathematical models to explain the effects of gas flux distribution across the pulp-froth interface. The stream function equation which has been found to adequately describe the flow of bubbles in froths is applied to our flow chamber subject to the three gas flux distribution profiles described in Chapter 6. Results of that quest are presented in this Chapter.

Chapter 8 presents further work on optimisation of froth performance, it specifically describes effects of froth baffles on flotation performance. Froth flow froth baffles alter froth residence time distributions at given froth depth and gas rate. Results from this exercise are discussed in this Chapter.

Chapter 9 uses Schwarz-Christoffel mapping technique in conjunction with finite difference methods to solve the Stream function equation as a way of explaining the results obtained in Chapter 8. Results of how the froth baffles alters froth residence time distribution are reported in this Chapter.

Chapter 10 provides the main conclusions from the work covered in this thesis highlighting areas that needs further research.

Chapter 2

Literature review

2.1 Introduction

The importance of froth phase to flotation cell design, flotation modelling and optimisation and flotation scale-up has been highlighted by early flotation workers (Arbiter and Harris, 1962; Watson and Grainger-Allen, 1973; Moys, 1979; Cutting et al., 1986; Ross, 1991). Consequently significant research effort has been directed towards understanding and modelling of the froth phase. This Chapter presents a brief discussion on the progress that has been made to date on froth phase studies. The literature survey will start with a general review of the flotation process, discussing flotation variables and the sub-processes that have a bearing on recovery and grade. It will go on to discuss froth phase basics such as froth formation, froth stability and mobility and froth stability measurement. A general discussion of flotation modelling follows but emphasis will be placed on workers who included the effects of froth phase in their models. Available froth transport models will also be included as they are vital to understanding the various experiments carried out in this thesis.

2.2 Review of the flotation process.

According to Arbiter and Harris (1962) the flotation process is affected by more than 100 variables making it very difficult to understanding. The challenges brought about by the complex nature of the process have thus far made reliable flotation scale-up elusive and optimisation of the froth phase empirical. Broadly, the flotation process will be discussed under three categories viz. feed preparation, operating conditions and particle transport.

2.2.1 Slurry preparation

2.2.1.1 Effect of particle size

Mineral extraction process begins with the grinding circuit, where the ore is first crushed, and then milled to obtain a particle size distribution that is typically between 10-100*μm* (Wills, 1992). The particle size distribution of the flotation feed is very crucial and a lot of research effort has been directed to the subject (Gaudin et al., 1931; Mehrotra and Kapur 1974; Collins and Jameson, 1976; Trahar et al., 1976; Trahar, 1981). Trahar, (1981) classified particles in flotation systems as fine (5 to 10μm) intermediate (10 to 70μm) and coarse (larger the 70μm). The recovery of course particles depends on their hydrophobicity as they are too heavy to be recovered by entrainment and they also show a lower tendency to be transported by bubbles due to their weight. The fine particles are less dependent on surface properties (Sutherland, 1948) and have lower probability of colliding with a bubble. They also have a high probability of being entrained. Thus it is accepted that it is in the intermediate size that the rate of flotation reaches maximum. A typical graph showing recovery as a function of particle size from Trahar (1981) is shown in Figure 2.1

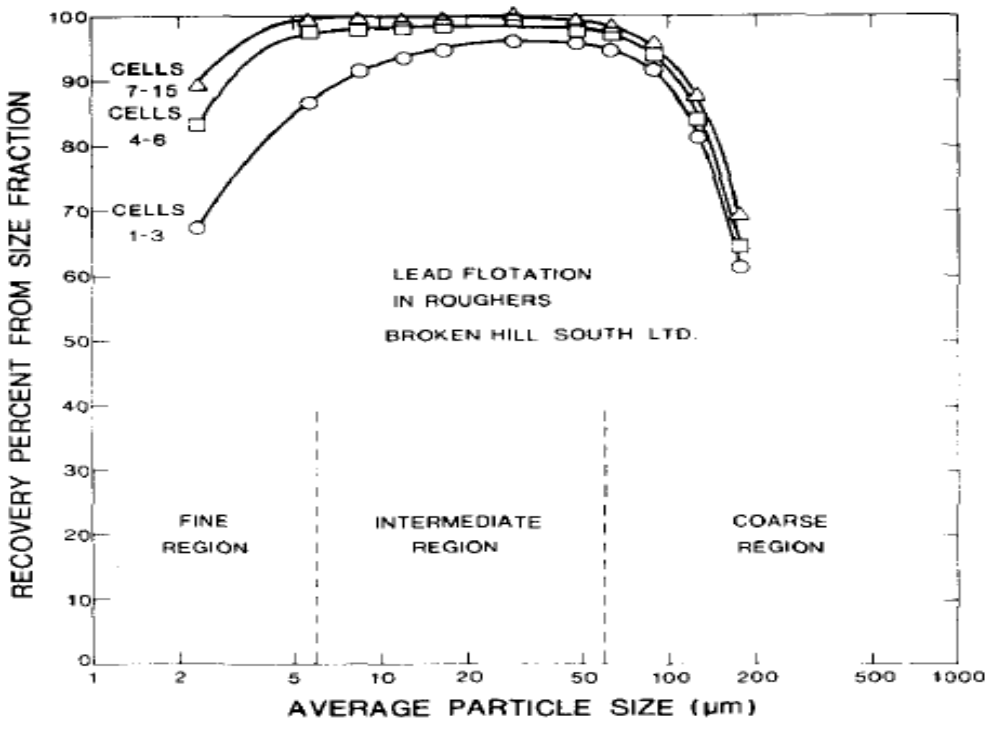

Figure 2.1: Recovery as a function of particle sizes, (after Trahar, 1981)

2.2.1.2 Effect of chemical conditioning

The chemical state of the pulp in the flotation cell is of utmost importance to ensure that optimal performance is achieved. For a particle to attach to a rising bubble, it must be water repellent i.e. hydrophobic. There is a certain degree of hydrophobicity that a desired mineral should have to effectively separate it from the gangue minerals. To achieve this, various reagents (Collectors, Frothers, and Regulators) are added to the pulp.

1) Collectors

These are chemicals which when adsorbed onto the surface of minerals renders them hydrophobic and so enable bubble-particle bonding. It is important for flotation collectors to be selective to avoid recovery of undesired minerals.

2) Frothers

These are surface active reagents that interact with the water content of the slurry, reducing its surface tension. This allows for the formation of thin liquid films that make up the froth layer. A good frother produces a froth which is just stable enough to facilitate the transfer of floated mineral from the cell surface to the collecting launder (Wills, 1992)

3) Regulators

These are chemicals that are added to modify the action of collectors. They are classed as activators, depressants, or pH modifiers. *Activators* are added to modify the surface of minerals so that it becomes hydrophobic by the action of collectors. *Depressants* render certain minerals hydrophilic when adsorbed to the mineral surface. The action of depressants increases the selectivity of the flotation process as it allows the collector to act on the desired mineral. Pulp alkalinity is also a very important control variable in flotation, It regulates the function of collectors which adsorb on to the surfaces of minerals at certain pH values. Chemicals used to control alkalinity are called *pH modifiers*

2.2.2 Operating conditions

To optimize the flotation process, an environment that maximizes the governing sub-processes such as particle-bubble interactions and drainage of entrained particles must be created. These interactions require the creation of bubbles of a specific size

in the flotation cell. Bubbles that are very large have less surface area to which particles can attach (Gaudin et al., 1931). Bubbles that are too small may not provide enough buoyancy to lift particles out of the pulp. The degree of mixing in the pulp phase also needs to be at an optimum. Enough energy must be expended to keep the particles in suspension and constant contact with bubbles. The suspended particles should have enough momentum to pass through the liquid lamella around the bubbles. The mixing should not be too intense, as this may cause particle detachment from bubbles and can destabilize the froth zone. The residence time of floatable particles in the froth should also be optimised to allow for the drainage of entrained particles but at the same time it should not be too long for attached particles to be lost in the froth.

2.2.2.1 Effect of gas dispersion properties

Gas dispersion properties (bubble size, velocity gas hold up and bubble surface area flux) have significant impact on flotation performance. Ahmed and Jameson (1985) found that the flotation rate was very strongly affected by the bubble size, they reported an increase of up to one hundred-fold when the bubble size was reduced from 655 um to 75um. The probability of contact between particles and bubbles in flotation varies as the inverse of the bubble size raised to a power of between 1 and 2 (Yoon and Luttrell, 1989). Gorain et al. (1996) found that neither of the three gas dispersion factors (bubble size, gas holdup and superficial gas velocity) could be related to flotation rate individually; but when lumped to together into a bubble surface area flux in the cell they related to flotation rate extremely well. Their work showed a linear correlation between the collection rate constant (k_c) and the bubble surface area flux (S_b) as shown in equation [2.1]. Bubble surface area flux is directly proportional to the superficial gas velocity (J_g) and inversely proportional to the Sauter-mean bubble diameter (d_b) as shown in equation [2.2]. They went on to conclude that it can be used as a single, scaleable parameter to characterize the physical contribution of the flotation cell to the rate of mineral recovery. Finch et al. (2000) proposed to replace bubble surface area flux with gas hold up (ε_g), but their further work indicated that gas hold up (ε_g) and bubble are surface flux were related by $S_b = 5.5\varepsilon_g$.

$$k_c = P.S_b \qquad [2.1]$$

where P is floatability which depends on operational and chemical factors.

$$S_b = 6\frac{J_g}{d_b} \qquad [2.2]$$

When they investigated the effects of froth depth on the $k - S_b$ relationship, Gorain et al. (1997) realized that the floatability (P) decreased as froth height was increased; this was contrary to the definition of (P) the inherent floatability of a mineral. Consequently an additional parameter to account for the effects of the froth phase on the overall rate constant was added to the initial relationship. Equation [2.3] shows the new relationship. It is important to note that this equation is only valid for maximum recovery in the collection zone.

$$k_{o.i} = R_f.P_i.S_b \qquad [2.3]$$

P_i floatability of component (i)

R_f froth recovery parameter

$k_{o;i}$ Overal flotation rate constant associated with component (i)

The research on gas dispersion properties discussed in flotation literature and summarised above assumes an average superficial gas velocity which is then taken to be uniform across the flotation cell. It does not take into account the effects of air distribution across the pulp-froth interface. In simulating his two dimensional model for the froth phase Moys (1979) recognised the influence of air flux distribution across the pulp froth interface. He suggested that the air flux distribution in a flotation cell could be described by $g(x) = g_o \sin(\pi x / L)$ wihere $g(x)$ representing a superficial gas velocity a distance (x) from the back plate of a cell of length (L) and g_o represents air flux at the centre of the cell. Ross and van Deventer (1987) made measurements in industrial flotation cells which supported this proposal. Moys *op cit*. simulations revealed that the sinusoidal form gas distribution profile which is normally found in mechanically agitated vessels with impeller at the centre of the cell results in negative velocity profiles at the back of the cell which results in reduction of the effective froth volume. Thus though the importance of air distribution profile to froth performance has been recognised by early froth phase practitioners, work to

characterise the best air distribution profiles in a flotation cell seems scant in the flotation literature.

In view of the above, a section in this thesis is focused on answering whether or not profiling gas flux in a single flotation cell can optimise cell performance.

2.2.2.2 The degree of solid suspension

Flotation takes place in a highly turbulent environment (impeller $\mathrm{Re} = 1x10^{6} - 1x10^{7}$) (Schubert and Bischofberger, 1978). True flotation depends upon successful bubble particle interaction. These interactions include bubble-particle collision, attachment and possible detachment. The probability of collision is very important for successful collection of floatable particles from the pulp phase and is a function of the degree of solid suspension. Entrainment another important particle transport process in flotation is influenced by the hydrodynamic environment existing in a flotation cell. The effect of solids suspension to the flotation process has been extensively researched by many workers (Cliek and Yilmazer, 2003; Zheng et al., 2005). By defining classification for solids suspension with equation [2.4], Zheng et al. (2005) found that for a 150 m^3 flotation cell the classification function varied with particle sizes as given in Figure 2.

$$CF_i = \frac{\omega_i^p}{\omega_i^t} \qquad [2.4]$$

CF_i classification function for solids in size class i

ω_i^p mass of solids in i th size class per unit mass of water in the pulp

ω_i^t mass of solids in i th size class per unit mass of water in the tailings

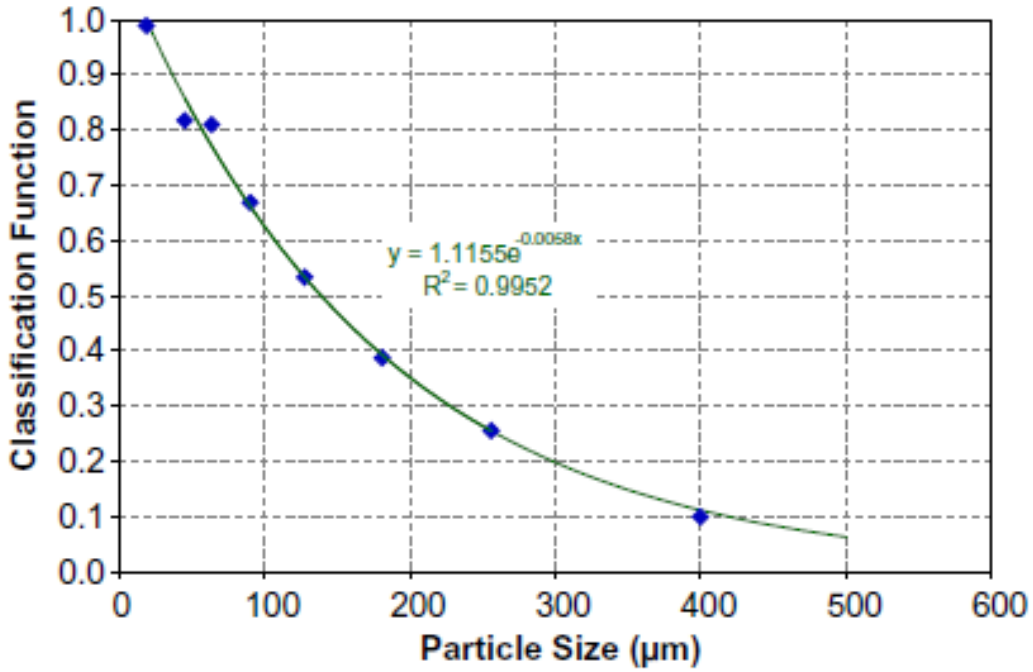

Figure 2.2: Classification function for solids suspension in the Outokumpu 150 m^3 tank cell at the Newcrest Cadia copper concentrator (after Zheng et al., 2005)

2.2.3 Particle transport

Transportation of particles from the pulp phase to the froth phase is achieved by two main mechanisms viz. attachment to bubbles/true flotation and entrainment. Discussion of each of these mechanisms is given below.

2.2.3.1 True flotation

True flotation is the process by which particles are transported from the pulp phase to the froth phase by attachment to rising air bubbles. This happens after a successful particle-bubble interactions coupled to enough buoyancy from the bubble to rise to the froth phase. The bubble particle attachment should be strong enough to resist detachment forces that may exist in the flotation environment. When the bubble-particle aggregate reaches the pulp froth interface, there is a sudden change in momentum and drainage of water from the bubble lamella which may lead to particle detachment. True flotation is achieved by those particles which successfully overcomes these detachment mechanism and reports to the concentrate. The recovery of valuable minerals is mainly by true flotation, thus it is the objective of the flotation process to optimize true flotation.

2.2.3.2 Entrainment

Parallel to true flotation is a non-selective and possible deleterious process called entrainment. Entrainment is the process by which particles enter the base of flotation froth and are transferred up and out of the flotation cell suspended in the water between bubbles (Smith and Warren, 1989). Two mechanisms are used to explain entrainment, viz. unattached particles carried upwards in bubble lamellae (Moys, 1979) and particles being carried in the wake of ascending air bubbles (Yianatos et al., 1986). Smith and Warren (1989), using the bubble swarm theory suggested that water in the pulp phase is mechanically pushed into the froth phase by a rising swarm of bubbles. Entrainment always occurs in parallel with true flotation and is responsible for most gangue recovery especially fines. Entrainment recovery has a significant effect on concentrate grade. Several models have been developed to estimate entrainment recovery in flotation. A number of researchers have shown consistently that there is a strong correlation between the water recovery and gangue recoveries (Zheng et al., 2005; Savassi et al., 1998; Neethling and Cilliers, 2002)

The recovery of particles by entrainment of ith size class $R_{ent,i}$ is related to water recovery (R_w) through the degree of entrainment (ENT_i) as shown by equation [2.5] which was proposed by Zheng et al, (2005) and is stated as follows

$$R_{ent,i} = ENT_i \times R_w \qquad [2.5]$$

where the degree of entrainment is expressed as a classification function as follows:

$$ENT_i = \frac{mass\,of\ free\ gangue\ particles\ of\ the\ i^{th}\ size\,class\ per\ unit\,of\ water\ in\,the\ concentrate}{mass\,of\ free\ gangue\,of\ the\ i^{th}\ size\,class\ per\ unit\,of\ water\ in\,the\ pulp}$$

2.3 Basics of flotation froths

2.3.1 Froth formation

Bubbles (typically 0.5-3mm) that are generated by the shearing action of the rotor on air in the case of mechanical cells and by specially designed spargers in flotation columns picks up hydrophobic particles as they rise through the pulp phase. Upon arrival on top of the pulp phase they tend to crowd forming foam and eventually froth (King, 2001). The bubbles which are mostly spherical in shape carry with them a

liquid film. As more bubbles arrive at pulp-froth interface, the layer of froth increases in height and the bubbles move close together. Meanwhile their liquid skins drain becoming thinner and thinner until coalescence begins. Consequently the bubbles become larger and polyhedral in shape (King, 2001). At the edges of the polyhedral bubbles, tubular conduits in which drained water and detached particles flow are formed. These conduits are called Plateau borders. Detached particles may reattach to available surfaces or drain back into the pulp phase as drop-back (Moys, 1979, Yianatos et al., 1988). These sub-processes i.e. bubble coalescence, liquid drainage, particle detachment and reattachment dictates froth performance. Given below is a discussion on some of these sub-processes.

2.3.2 Bubble coalescence and particle detachment

Detachment of particles from bubbles is caused by a number of factors; Klassen and Mokrousov (1963) identified a number of ways which can provide enough energy to cause particle detachment. Among the identified ways, the only mechanism which can cause detachment in the froth phase is impact on a stationery object and bubble coalescence in the bulk of the froth; in the froth phase case, the stationary object is the pulp-froth interface (Seaman et al., 2006).

In the bulk of the froth, particle detachment is mainly as a result of bubble coalescence. Bubbles coalesce in froth phase as their lamellae raptures (Ata, 2012). Its result is detachment of particles. Detachment as a result of bubble coalescence is most likely non-selective towards particle type as coalescence is instantaneous and all particles previously attached falls to the base of the newly formed bubble (Seaman et al., 2006). Detached particles will drain back to the pulp phase or reattach to available surfaces. If the detached particles preferentially reattach to bubble surfaces further upgrading is achieved (Moys,1979) but a high degree of detachment and reattachment in the froth phase has disadvantages in that it can reduce flotation cell throughput due to froth overloading and flow between the pulp and the froth phase(Ata *op cit*). Research on the detachment of particles in froth flotation has been done by many workers (Cutting, 1989; Falutsu and Dobby, 1992; Ross, 1990; Van Deventer et al., 2004). Mostly bubble coalescence, hence particle rejection happens just above the pulp froth interface where bubbles begin to crowd (Yianatos et al., 1988). Ata et al. (2003) measured bubble coalescence as change in bubble size above the pulp-froth interface phase showed that coalescence is a strong function of attached particle size and hydrophobicity. Understanding coalescence in

the froth is thus very important in understanding and optimizing the froth phase. Modelling of the bubble coalescence exist in flotation literature e.g. Neethling and Cilliers (2003) but techniques to measure the changes in bubble sizes above the pulp-froth interface in non-transparent flotation cells are making training of the available models difficult. A part of this thesis shall be dedicated to addressing the lack of methods to measure bubbles sizes above the interface by developing a technique that can be used to measure froth phase bubble sizes as a function of height above the pulp-froth interface.

2.3.3 Particle reattachment and selectivity

Particles that detach may reattach to available surfaces in the froth phase. Froth selectivity happens when froth preferentially rejects previous attached particles based on some particle property such as particle size, density or hydrophobicity (Seaman et al., 2006). This selective reattachment or rejection of previously attached particles in the froth phase results in additional upgrading of the concentrate (Moys, 1979; Cutting et al., 1981). Although a number of researchers have reported this kind of froth selectivity (Young, 1982; Ata, 2002; Seaman et al., 2004; Seaman et al., 2006) others found only apparent selectivity with respect to particle size (Alexander et al., 2003; Savassi et al., 1997; Vera et al., 1999a).

2.3.4 Liquid drainage

As rupture of bubble skins occurs, some liquid is released, this liquid drains back to the pulp phase (Ata, 2012). This process of froth drainage removes particles that are weakly attached to bubbles and those that detach as a result of bubble coalescence or break up (Moys, 1979). Froth drainage has an impact on froth performance. Drainage of weakly attached gangue material or entrained particles is desirable as it enriches the concentrate grade (Subrahmanyam and Forssberg, 1988). Moys (1979) recognised particle drainage as selective and he proposed that the drainage of these particles is proportional to the concentration in each size class. The importance of froth drainage has also been recognised by Klassen and Mokrousov (1963) who then suggested that spraying the froth column with water could improve both grade and recovery. Cutting et al. (1986) identified two drainage modes viz. film drainage and column drainage. Film drainage happens around the bubbles as both water and particles slowly drain from the bubbles. It happens everywhere in the froth column and does so at a very slow rate. Column drainage on the other hand is rapid and

happens at single vertical location in the froth. Column drainage starts at any vertical position where local concentrations of solids invert the hydrostatic gradient (Cutting *op-cit*). Cutting et al. (1981) suggested that in an equilibrium cell, drainage can adequately be characterised by equation [2.6a] and for a flowing froth by equation [6b].

$$-\frac{dC}{dh} = \beta C_i + \gamma C_i^{\,2} \qquad [2.6a]$$

$$\frac{dC}{dh} = \beta C_i + \gamma C_i^{\,2} + \Omega \qquad [2.6b]$$

where

C_i material concentration of species i in the froth phase

β film drainage parameter

γ column drainage parameter

Ω parameter which relates to material flow through the froth to the removal point

2.3.5 Froth stability

Froth stability defined as the ability of bubbles in froths to resist coalescence and bursting is an important parameter in flotation systems as it plays a significant role in determining mineral grade and recovery (Farrokhpay, 2011). Mineral froths should be stable enough to enable recovery of the valuable minerals while allowing drainage of gangue materials. It should be easy to handle i.e. the froth should break down quickly to allow recovery of the solids. A froth that is too stable will result in high froth recoveries, high water recovery and high entrainment of fine particles. Froth stability depends on a number of factors such as frother type and concentration, particle size and hydrophobicity (Johansson et al., 1992; Ata, 2012). Properties such as quality of process water and gas dispersion characteristics and particle contact angle also influence froth stability (Farrokhpay, *op cit*). A number of parameters have been used to asses froth stability in froths, these include froth half-life time (Iglesias et al., 1995), froth maximum height at equilibrium (Barbian et al. 2003; Barbian et al., 2006), bubble growth across the froth phase (Ata et al.,2003), air recovery and solids

loading on bubbles on top of the froth surface (Moys, 1984; Barbian et al. 2006; Hadler et al., 2010) and froth lateral and vertical velocity (Barbian et al., 2005; Zanin et al. 2009; Ventura-Medina et al.,2002). Froth retention time (FRT), defined as the ratio of the froth volume to the concentrate volumetric flow rate has also been used as an indicator of froth stability (Laplante et al., 1983; Malysa et al., 1987). Gorain et al. (1998) then related froth retention time to froth recovery (R_f) as shown by equation [2.7]

$$R_f = e^{-\beta.FRT} \qquad [2.7]$$

where

β is a dimensionless parameter related to the physical and chemical properties of the froth

Zanin et al. (2008) then modified equation [2.7] to include froth half-life time ($t_{\frac{1}{2}}$) defined as the time needed for the froth to collapse to 50% of its initial equilibrium height as shown in equation [2.8]

$$R_f = e^{-\beta\left(\frac{FRT}{t_{\frac{1}{2}}}\right)} \qquad [2.8]$$

Although equation [2.7] and [2.8] shows a relationship between froth recovery and indicators of stability, it should be noted that explicitly factors affecting froth stability such as frother type and concentration and nature of suspended particles are not included (Farrokhpay, 2011). In this work froth stability shall be inferred by assessing the way bubble sizes vary above the pulp-froth interface.

2.4 Flotation modelling

The importance of flotation modelling has been realized by a number of workers (Schumann, 1942; Arbiter and Harris, 1962; Jowett and Ghosh, 1965). Models make it possible to assess and predict flotation performance (Fichera and Chudacek, 1992). Depending on their outcome models can be classified as deterministic or stochastic. While deterministic models ignore random variations and predict the same outcome from a given starting point, stochastic models are more statistical and

predict the distribution of possible outcomes. Within these broad categories models can be classed as mechanistic, empirical and semi-empirical. Mechanistic models attempt to describe mathematically the actual phenomenon of the process, this type of model may not be suitable to model highly complex processes such as flotation; they are limited to studying processes under highly controlled conditions. Empirical models are generated by fitting observed data from operating plants to a preconceived equation or model. They are not based on the understanding of the actual mechanisms taking place in a system. Empirical models are mainly used for plant optimization and are process specific; this means a new model would have to be generated for every new process. Semi-empirical models are by and large a combination of empirical and mechanistic models. They include empirical parameters with physical significance. This approach is suitable for complex processes such as flotation.

Some of these modelling approaches have been applied to flotation modelling with semi-empirical models being predominant. The following section gives an overview of the flotation models as found in literature, a discussion of batch kinetic models will be based on a review by Fichera and Chudacek, (1992) and froth phase models/ two phase models by a review paper by Mathe et al. (2000)

2.4.1 Single rate kinetic models

The first attempt to relate flotation rate with a first order model was done by Zuniga (1935), he found that the rate of flotation was proportional to the amount of mineral in the cell. Many other workers (Schumann, 1942; Morris, 1952; Kelsall, 1961) were also in agreement with first order kinetic. Thus the rate of flotation was modelled as given by equation [2.9]

$$\frac{dC}{dt} = -kC \qquad [2.9]$$

Studies done by other workers (Arbiter, 1952; Hukki, 1953, Bennet et al., 1960) seemed to suggest a deviation from first order kinetics, higher order kinetics were suggested first, but were eventually rejected based on the work done by Tomlinson and Fleming (1965) who suggested that even at high pulp densities where collisions are expected to be high, the specific rate of flotation or the rate constant would still vary between 1 and 0. To explain the observed deviations from first order kinetics, Jowett and Safvi (1960) suggested that the flotation rate constant is a function of all

possible flotation variables, including such variables which cannot be maintained constant such as particle sizes, shape and mineralogical compositions. Thus it was agreed that because of the heterogeneous nature of the flotation feed, deviations from first order kinetics are expected and any accurate flotation model should recognize that particle properties were not constant.

2.4.2 Distributed rate kinetic models

The realization that the particle properties have to be represented by a distribution function of the given parameter led to the attempt to model flotation as a more complex function incorporating the heterogeneous nature of the feed.

2.4.2.1 Distributed rate models based on size

Gaudin et al. (1942) performed continuous flotation test on galena which they had subdivided into sizes classes. Using the known amount in each size class in the feed, recovery per size class was calculated. The rate of flotation was found to be adequately represented by equation [2.10]. Tomlinson and Fleming (1965) tested the model in a batch test. By using equation [2.10] they were able to predict recoveries from a known flotation feed mass. When they compared model results to experimental results they found excellent agreement.

$$\frac{dC}{dt} = -\sum_{i=1}^{m} k_i C_i \qquad [2.10]$$

where

C_i concentration of particles in size class i

k_i flotation rate constant of size class i

m number of size classes

t Cumulative flotation time

Volkova, (1946) described the distribution of particles sizes as a continuous distribution instead of the discrete form described above. Sutherland (1948) described the size distribution as a density function as given by equation [2.11] and the rate of flotation was thus given by equation [2.12]. However, particle sizes are

easily determined in a discrete form and not in a continuous form as such equation [2.9] was found to be more useful when calculating flotation rates

$$\int_0^{\infty} F(r)dr = 1 \qquad [2.11]$$

$$\frac{dCr}{dr} = \int_0^{\infty} k(C_{\infty} - C_r).F(r)dr \qquad [2.12]$$

2.4.2.2 Distributed rate models based on particle sizes

The inherent floatability of a particle is a function of such factors as particle size and mineralogical composition, degree of liberation and reagent coverage. Thus floatability is expected to vary in a given flotation feed. This variation would result in different flotation responses, with a spectrum of specific flotation rate constant. With the advent of distributed first order rate constants models, models that recognize the inherent distribution of floatabilities were proposed. Gaudin (1957) recognized that the flotation rate constant would vary over the flotation period with the more floatable particles floating first. Imaizumi and Inoue (1965) then used a graphical approach to interpret deviations from first order kinetics as actually representing first order rate with deviations representing particles with different floatabilities. This discrete floatability model was represented in form of equation [2.13]. The authors also suggested a continuously distributed floatability represented by a density function $G(k)$. The recovery after a given time was represented by equation [2.14]

$$M = \sum_{h=1}^{n} M_{0,h}(1 - e^{-k_h t} dk) \qquad [2.13]$$

$$M = M_0(1 - \int_0^{\infty} G(k)e^{-kt} dk) \qquad [2.14]$$

where

$G(k)$ floatability density function

M amount of mineral floated

M_0 initial amount of mineral in the ore

h denotes a particular floatable component of the feed with rate constant k_h

Woodburn and Loveday (1965) proposed a parametric rather than a graphical solution to describe the floatability density function. They assumed that the distribution of floatabilities has the form of a gamma function as given by equation [2.15]

$$G(k) = \frac{b^{a+1} + k^a e^{-bk}}{\Gamma(a+1)} \qquad [2.15]$$

Although this gamma function method gives better fit to experimental data (Harris and Chakravarti, 1970), it reduces to a curve fitting procedure thus highlighting its empiricism. (Fichera and Chudacek, 1992). Woodburn et al. (1984) criticized the distributed floatability models, pointing out that it does not differentiate between or determine the effects of influencing parameters such as particle size or mineralogical composition on flotation. In contrast the first order distributed models based on particle size will at least give an account of the effect of particle size to flotation response.

2.4.3 Double distributed parameter models

There are some particles that are in the flotation feed that can never be recovered (Zuniga 1935, Bushell, 1962; Morris 1952) thus the rate of flotation is proportional to the amount of floatable particles in the cell. Morris (1952) accounted for this non floatable component per size class and generated a recovery equation as represented by equation [2.16]. Equations of this form are referred to as distributed double parameter models as they take into account the particle size distribution and the distribution of flotabilities within a size class.

$$M = \sum_{1=1}^{m} (M_{o,i} - X_i)(1 - e^{-k_i t}) \qquad [2.16]$$

where

X_i fraction of non-floatable particles in size class i initially in the cell

Jowett and Safvi, (1960) expressed doubt on whether X_i actually represents the non-floatable fraction. After carrying out successive re-floatation tests, they found that not all minerals were recovered. The authors hence suggested that the factor X_i was related to pulp density. To circumvent this non-floatable particle notion, Kelsall, (1961) suggested that particles can be described as either fast floating or slow floating instead of being floatable or non-floatable. While analysing their experimental data Kelsall *op cit* found that, the apparent non-first order kinetics they observed was actually two first order equations superimposed on each other. The line with the greater slope represent the fast floating material $M_{A,i}$ in size class i, with a rate constant $k_{A,i}$ while $M_{B,i}$ represented the slow floating fraction with rate constant $k_{B,i}$. Frew and Trahar. (1981) later represented the total recovery of mineral from a feed with m size classes with equation [2.17]

$$M = \sum_{1}^{m} \left[M_{0,A,i}\left(1-e^{-k_{A,i}\,t}\right) + \left(M_{0,i} - M_{0,A,i}\right)\left(1-e^{-k_{Bi}\,t}\right) \right] \qquad 2.17$$

Fichera and Chudacek, (1992) suggested equation [2.18] as the best form of double distributed rate parameter models. They suggested that if equation [2.13] is modified to represent the distribution of floatabilities within a size class and if there are m number of classes and n is the maximum number of rate constants within a size class, then total recovery is as given by.

$$M = \sum_{i=1}^{m}\sum_{h=1}^{n} M_{0,i,h}\left(1-e^{-k_{i,h}\,t}\right) \qquad [2.18]$$

2.4.5 Entrainment modelling

Entrainment recovery is directly proportional to water recovery with proportionality constant referred to as the degree of entrainment. Thus modelling of entrainment is transformed into the task of modelling the degree of entrainment if the water recovery is known (Zheng et al, 2006).Since water recovery can be measured directly; correlations/models to estimate the degree of entrainment are needed and some of

the models to estimate the degree of entrainment developed and mentioned in literature are discussed below.

Ross and Van Deventer (1988) proposed equation [2.19] after conducting laboratory batch tests.

$$X_i = 1 - 0.429 \log(d_i - 1).(\rho_s - 1) \qquad [2.19]$$

where: $X_i = \frac{E_i.C_w}{W_i C_m}$ =degree of entrainment

$E_i =$ cumulative mass of entrained solids recovered (g)

W_i = cumulative mass of water recovered (g)

C_w = concentration of water in the pulp (g/l)

C_m =concentration of solids in pulp (g/l)

$d_i =$ particle size

ρ_s =solids density

Maachar and Dobby (1992) as reported by Savassi et al. (1998) conducted tests in a laboratory column presented equation [2.20]

$$\frac{E_s}{R_{FW}} = \exp(-0.0325 * -\Delta\rho).\exp(-0.0063.d_i) \qquad [2.20]$$

where: $E_s =$ recovery of entrained solids

$\Delta\rho$ = difference in specific gravity of the mineral and that of the water

R_{FW} = recovery of water which is calculated from:

$$R_{FW} = 2.58 \frac{\exp(-13.1.J_b)}{J_f}$$

J_b = water bias in the froth

J_f = superficial feed rate (volumetric flowrate/cell area)

d_i = particle size

Kirjavainen (1996) conducted flotation tests in laboratory and suggested that

$$P = \frac{W^{0.7}}{W^{0.7} + b.s.v^{-0.5}.m^{0.5s^{0.4}}} \qquad [2.21]$$

where: P = entrainment factor = ratio of the recoveries of gangue and water.

W = water recovery rate (kg/m^2/s)

m = particle recovery (pg)

v = slurry viscosity (mPa s)

s =dynamic shape factor

b = constant = 0.00694

All these empirical models were developed from laboratory experiments where conditions were highly controlled. Savassi et al. (1998) presented an empirical partition curve that describes the degree of entrainment within a conventional flotation cell as:

$$ENT_i = \frac{2}{\exp\left(2.292\left(\frac{d_i}{\xi}\right)^{adj}\right) + \exp\left(-2.292\left(\frac{d_i}{\xi}\right)^{adj}\right)} \qquad [2.22]$$

$$adj = 1 - \frac{\ln(1/\delta)}{\exp\left(d_i/\xi\right)}$$

where: d_i = particle size

ξ = entrainment parameter, or the particle size for which the degree of entrainment is 20%.

δ = drainage parameter, related to the preferential drainage of coarse particles.

2.4.6 Water recovery modelling

Modelling of water recovery is very important as it determines circulating flows and residence times in individual process units. Additionally important parameters such as froth recovery and entrainment are also strongly influenced by water recovery. According to Xheng et al. (2006) water recovery can be defined as the fraction of the water entering the flotation cell that is recovered in the concentrate. Alternatively for a batch system it can be defined as the fraction of total water in the cell that is recovered to the concentrate. A brief summary of water recovery models found in literature will be given in this section; the review is based on a paper by Xheng et al. (2006). They divided water recovery models into five categories viz.

1) Those that relate water recovery to certain aspects of the cell performance usually solids recovery (King, 1973; Alford, 1990)

2) Those that relate water recovery as a function of froth residence times

3) First order recovery models (Harris, 2000)

4) Drainage models for water recovery (Moys, 1979)

5) Those that takes a fundamental approach to water recovery modelling (Neethling et al., 2003)

2.4.6.1 Water recovery as function of solids recovery

The volumetric flowrate of water in the concentrate can be determined by equation [2.23] (King, 1973); this model was developed based on the conservation of volume and solids in a given stream. The model does not require any information about the cell operating conditions. And also implicit in this model is the assumption that percentage of solids in the concentrate remains constant which is not valid in practice.

$$Q_W = \frac{1-X}{X} \cdot \frac{1}{SG_W} \cdot F_S \qquad [2.23]$$

where

Q_W volumetric flowrate of water

F_S mass flowrate of solids

X mass fraction of solids in the stream

SG_W specific gravity of water

Alford, (1990) in JKSimFloat postulated water recovery as a power function of concentrate solids equation [2.24]. This model fits most plant data very well (Xheng et al.,2006), however it is specific to a flotation cell, it also does not take operating conditions into account, thus it is not appropriate for simulating alternative plant configurations.

$$Q_W = a.F_S^b \qquad [2.24]$$

where a and b are empirically fitted parameters.

2.4.6.2 Water recovery as a function of froth residence time

Froth residence time is one of the factors that affect water recovery, in fact the recovery of water in a flotation cell happens in two stages, the first step is the transport of water from the pulp phase to the froth phase and the second step is the transfer of water from the froth phase to the concentrate launder. Savassi et al. (1998) identified the froth residence time as the key factor controlling water recovery. He proposed an empirical water recovery model as a power function of froth residence time equation [2.25].

$$R_W = c.\tau_f^d \qquad [2.25]$$

where c and d are empirically fitted parameters and froth residence time is defined as given below:

$$\tau_f = \frac{H_f}{J_g} \qquad [2.26]$$

where H_f and J_g are froth height and superficial gas velocity respectively.

Gorain et al. (1998) also defined froth recovery factor as an exponential factor of froth residence time equation [2.27]. Overall water recovery if the back flow of water from the froth phase is treated as additional water to flotation cell pulp is then given by equation [2.28]

$$R_f = e^{-\beta.\tau_f} \qquad [2.27]$$

where β is an empirically fitted parameter

$$R_W = R_{CW}.\exp(-\beta.\tau_f) \qquad [2.28]$$

where R_{CW} is the recovery of water from the pulp phase to the froth phase.

Although water recovery models based on froth residence times fit experimental data well, they still have a limitation in that they use a single parameter to characterize the entire froth transport in the cell. This does not distinguish the effect of air rate and froth height. According to Xheng et al. (2006), a single parameter cannot be used to determine froth transport properties such as its water content.

2.4.6.3 First order water recovery models

Analogous to floatable particle recovery in flotation cells, Harris (2000) proposed that the recovery of water from the pulp phase follows first order kinetics. The froth recovery of water was modelled as an exponential function of froth residence. The overall water recovery models was obtained by combining the pulp phase and froth phase water recovery and is given by equation [2.29]

$$R_W = 1 - \frac{1}{1 + P_W.S_b.\tau.\Omega.\exp\ (\delta.V_f - \chi.\tau_f)} \qquad [2.29]$$

where

δ , Ω , χ are constants

τ mean residence of the pulp slurry

S_b bubble surface area flux

P_W is a constant for given flotation system

V_f effective volume of the froth zone

2.4.6.4 Drainage model for water recovery

Moys (1979) developed a water recovery model, based on a two-step process as well. He suggested that the water enters the froth phase in the film of the air bubbles. This water needs to survive the drainage process and bubble bursting on the surface of the froth before it can reach the concentrate launder. By assuming that the bubble film thickness is constant for a given flotation system, the initial amount of water entering the froth phase was calculated using equation [2.30]

$$Q_W(0) = A.S_b.\delta \qquad [2.30]$$

where

A is the cross sectional area of the pulp-froth interface

δ is the volume of water per surface area of air bubble

If the rate at which water drains back to the pulp phase is assumed to be proportional to the concentration of water at that particular froth level and if the cross sectional area of the froth phase is assumed to be constant through the entire froth phase. If the amount of water that drains back into the pulp phase as a result of bubbles bursting at the top of the froth is taken into account; the froth recovery of water was given by

$$R_{fw} = \alpha.\exp(-k_{wd}.\tau_f) \qquad [2.31]$$

where

k_{wd} is the drainage rate constant of water

α is the fraction of froth that eventually reports to the concentrate

Concentrate water flow is calculated by combining equation [2.30] and [2.31] as shown by equation [2.32]

$$Q_W = A.S_b.\delta.\alpha.\exp(-k_{wd}.\tau_f) \quad [2.32]$$

2.4.6.5 Fundamental approach to water recovery modelling

Neethling et al. (2003) developed a water recovery model as given by equation [2.33]; this equation was developed based on the fundamental structure of the froth. They stated that most of the water in froth is held in plateau borders, which exist as a network of interconnected channels. The model was developed by calculating the length and cross sectional areas of the plateau borders. The model ignores the water in the lamellae, and according to Xheng et al. (2004) variation of froth properties across the horizontal direction is also ignored.

$$Q_W = \alpha.\, Q_a.\left(\frac{1}{1-\frac{255.6}{r^2}\cdot J_g\cdot(1-\alpha)\cdot\frac{\eta}{\rho\cdot g}} - 1\right) \quad [2.33]$$

where

η is the viscosity of water in the froth

α is the fraction of froth that eventually reports to the concentrate

r bubble radius

Q_a rate of air passing through the froth zone

ρ water density

g gravitational constant

2.5 Froth Recovery as a froth performance measure

The function of the froth phase is to act as a separator, allowing the recovery of hydrophobic particles while rejecting gangue minerals recovered by entrainment. As discussed above the froth phase sub-processes have an influence on froth separation performance. A performance measurement criterion is necessary to enable optimisation of the froth performance. Froth zone recovery (R_f) is typically used as the metallurgical performance measure for the froth phase and Rahman et al. (2012) acknowledges that froth recovery is the only parameter that reflects the collective effect of all the froth zone sub-processes. Finch and Dobby (1990) defined froth recovery as the fraction of particles attached to air bubbles entering the froth phase that reports to the concentrate. Savassi et al. (1997) also defined froth recovery as shown by the equation below:

$$R_f = \frac{\text{Flowrate of particles to the concentrate via the particle - bubble attachment process}}{\text{Flowrate of particles attached to bubbles entering the froth phase}}$$

Figure 2.3 is a schematic depiction of the interaction of the pulp and froth zone showing collection zone recovery (R_c), froth recovery (R_f) and drop-back which is defined as the fraction of particles entering the froth phase that returns to the pulp phase and is calculated from the expression ($R_c.(1-R_f)$) as shown in Figure 2.3. The overall flotation recovery (R) is then mathematically defined as shown by equation [2.34].

$$R = \frac{R_c R_f}{R_c R_f + (1 - R_f)} \qquad [2.34]$$

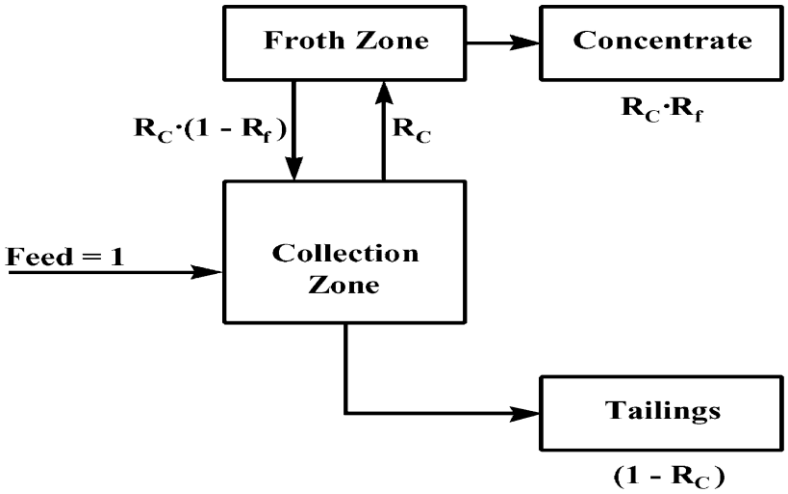

Figure 2.3: Interaction between zones in a flotation cell (Vera et al., 2002)

Froth recovery parameter can also be calculated as the ratio of the total rate of transfer from the pulp to concentrate $(k_{overall}.CV)$ to the rate of transfer from the pulp to the froth $(k_{pulp}.CV)$ as shown in equation [2.35] (Savassi et a., 1997). The total rate constant is calculated from equation [2.36] after considering the system as a perfect mixer with mean residence time (τ) and overall recovery (R). Note that equation [2.35] is valid for maximum recovery in the collection zone.

$$R_f = \frac{k_{overall}}{k_{pulp}} \qquad [2.35]$$

$$k_{overall} = \frac{R}{\tau(1-R)} \qquad [2.36]$$

Several empirical models to evaluate froth recovery have also been developed. Yianatos et al. (1998) developed a semi-empirical model based on operating variables given by equation [2.37] to estimate froth recovery in an industrial flotation column. A good agreement between this model and experimentally estimated data of froth recovery was observed.

$$R_f = 95\exp(-1.44*10^{-2}\frac{H_f(1+3J_w)}{J_g^{\,3}} \qquad [2.37]$$

where

H_f froth depth

J_g superficial gas velocity

J_w superficial water rate

Vera et al. (2002) also developed an empirical model to predict froth zone recovery, using the exponential relationship between froth retention time (FRT) and froth recovery as described by Gorain et al. (1998). The model, equation [2.38] was successfully used to predict froth recovery of a laboratory batch cell, however the authors acknowledge that froth retention time which was defined as the ratio of froth volume to concentrate flowrate cannot be easily predicted using available water recovery models.

$$R_{f(i)} = \exp(-\beta FRT) + [1 - \exp(-\beta FRT)]\left[\frac{1}{1+\omega_i FRT}\right] \qquad [2.38]$$

where

ω_i parameter representing fraction of detached particle of size class i in froth

β parameter related to the rate at which bubbles are coalescing and breaking up

2.5.1 Methods of froth recovery measurement

Several methods to measure froth recovery have been generated during the last few years. Moys et al. (2010) summarised them as follows.

1) The use of specially designed laboratory apparatus which effectively separates the collection zone from the froth zone and allows the collection of particles dropping out from the froth zone (Falutsu and Dobby, 1989; Rahman et al., 2012).

2) Measurement of a wide range of variables and development of a model based on certain assumptions leading to the ability to solve for flowrates into the froth phase. Van Deventer et al. (2001) fitted a comprehensive model for column hydrodynamics

to experimental data involving measurements of gas holdup and pulp concentrations in the column in addition to the usual measurements required to establish the overall mass balance.

3) Measurement of the effect of froth depth h_f on overall flotation recovery; the assumption that R_f tends to 1 as h_f tends to 0 allows the estimation of froth zone recovery (Vera et al., 1999).

4) Direct measurement of loading on bubbles:

Falutsu and Dobby (1992) measured loading on bubbles using a pipe passing downwards to below the froth phase with counter-current addition of water to ensure slurry does not get sampled. Dyer (1995) and Seaman et al. (2004), developed methods to measure bubble loading for calculating froth recovery parameter. Yianatos et al. (2008) and Bhondayi (2010) also developed bubble load measuring techniques for estimation of froth recovery. Runge et al. (2010) grouped froth recovery methods into three categories viz. changing froth depth, direct measurement of bubble load and mass balance estimation of bubble load. They went on to provide a comprehensive review of these techniques. A summary critique of each of the techniques is given below.

2.5.1.1 Froth drop-back measurement techniques

Falutsu and Dobby (1989) developed apparatus which effectively separates the collection zone from the froth zone and allows the collection of particles dropping off from the froth zone. They were able to evaluate both the recovery across the froth and the collection zone in this laboratory column. The limitation of this technique is that it has only been used in laboratory environment. Rahman et al. (2012) developed a device to measure froth drop back in industrial flotation froths. The device consists of two concentric tubes. The inner tube known as the drop-back collector collects the particles that drop off from the froth. Despite the reported good reproducibility, the authors acknowledge that the flotation conditions inside and outside of the designed device maybe different i.e. froth properties in the device maybe significantly different from those in the cell, which acts as an isolated reaction chamber inside the flotation

2.5.1.2 Mass balance techniques

Mass balancing techniques to estimate froth recovery have been developed by several authors. Savassi at al. (1997) proposed a methodology where samples were taken from the pulp phase by vacuum pumping. A funnel was used to preferentially collect bubbles when the funnel was in a vertical position and slurry when the funnel was in a horizontal position. A third sample containing no bubbles was taken from the pulp phase using a specially designed device. Using these three samples a mass balance to determine the amount of attached particles bubbles per litre of air was performed. The authors commented that this technique can only be used when there is a significant difference between the grade of attached particles and suspended particles. Consequently this technique is only applicable in rougher cells and usually not scavengers or cleaner cells (Seaman et al., 2004)

2.5.1.3 Changing froth depth

This method was initially introduced by Feteris et al. (1987) and Vera et al. (1999a, b) further developed it. It is based on the relationship given by equation [2.35]. By performing experiments at different froth depths and constant pulp levels, flotation rate constant at each froth depth is determined. Plotting the overall flotation rate constant against froth depth produces a straight line with a negative gradient see Figure 2.4. By extrapolating this line to zero froth depth the collection zone rate constant is found. Vera et al. (2002) further developed the method to enable calculation of froth recovery at any depth by manipulating equation [2.35] and equation [2.39] to get the expression given by equation [2.40]. Note that equation [2.39] expresses the linear relationship between froth depth and flotation rate constant as noted many authors (Feteris et al., 1987; Hanumanth and Williams, 1990)

$$k = a - b(FD) \qquad [2.39]$$

where

$a = k_c$, when froth depth is equal to zero

$b = \frac{k_c}{(FD)_{k=0}}$ which is the gradient of the line, $(FD)_{k=0}$ is the intercept of the straight line with the $x-$axis, i.e. when $k = 0$, which is equivalent to a very deep froth so that no material is transferred from the froth to the concentrate.

$$R_f = 1 - \frac{(FD)}{(FD)_{k=0}} \qquad [2.40]$$

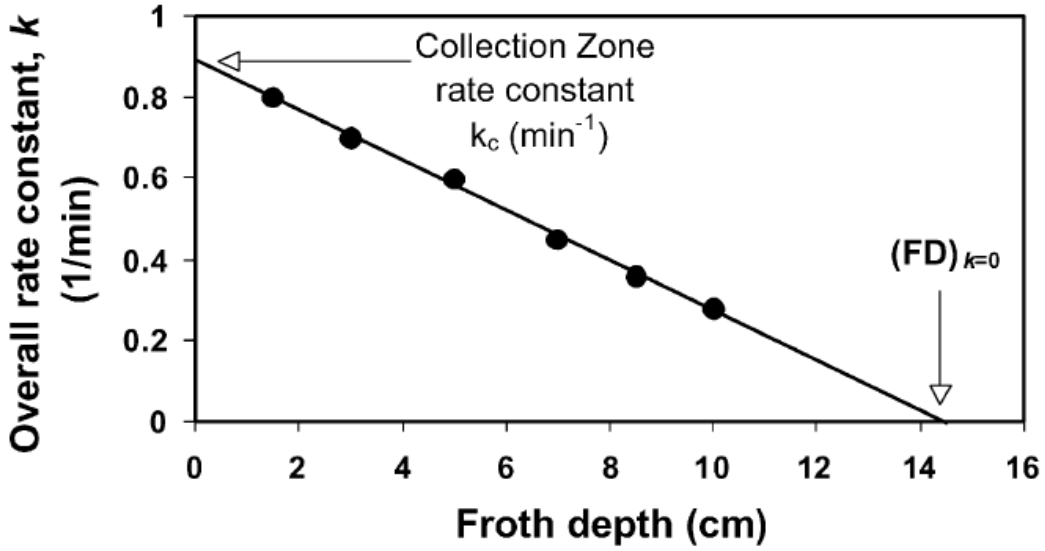

Figure 2.4: flotation rate constant as a function of froth depth (Vera et al., 2002)

Limitations of this method according to Runge et al. (2010) include: - the methodology often cannot be applied successfully in industry as it is time consuming and it takes hours for the cell to reach equilibrium. Furthermore the success of the method is hinged upon feed conditions remaining constant over the period of the test. Seaman et al. (2006) have shown that the method gives higher froth recoveries than bubble load because it only accounts for losses that happen within the froth and not losses at the pulp-froth interface. Runge *op cit* also pointed out that collection zone recovery may change as froth depth is increases due to increased drop-back of fast floating material which then acts as new feed resulting in higher collection zone rate and a decrease in the slope of overall rate constant versus froth depth.

2.6 Froth phase modelling

Mathe et al. (2000b) provide a comprehensive review of froth modelling, they divided froth models into two categories viz. Steady state models- those derived from froths whose properties do not change with time i.e. froths in continuous systems and equilibrium cells and non-steady state models typically derived from froths whose properties change with time e.g. batch cells. Arbiter and Harris (1962) were the first to partition the contents of a flotation cell into pulp and froth phases in recognition of the fact of flotation process that the contents exists as a pulp phase and froth phase. In developing models for each phase they assumed perfect mixing but the assumption of perfect mixing in froth phase is not to true (Moys, 1979). Ross (1991) states that this model in its present state does not scale-up well because it does not take into account water flows between the two phases and airflow. Regardless of these limitations Ross *op cit* recognises that this model was largely the cause of stimulating research into the froth phase. Variations of the two phase model have also been proposed, Hanumanth and Williams (1992) proposed a three phase model consisting of the pulp and two distinct froth phases. The primary froth was defined as that close to the pulp phase; its gas volume is low with a higher liquid and solid content which prevents coalescence. The remaining part of the froth was termed the secondary froth, it is characterise by high air volume and low liquid and solid s content. The authors also assumed that these two distinct froth phases are well mixed. Harris (1978) then went on to prove that at steady state multiphase models can be reduced into two phase (pulp-froth) systems.

Moys (1979) developed a froth model based on the assumption of plug flow in the froth. Flow of particles within the froth was represented by equation [2.41]. Mass fraction of mineral $g_i(z)$ at height h was calculated from equation [2.42]. In formulating this model a number of postulations were made, among them include: - the rate of detachment of particles of size class i is proportional to their concentration at the point of interest; both entrained and attached particles rise at a velocity equal to the rise velocity of bubble films ($v(z)$); the net upward flow of water remains constant and is equal to the concentrate flowrate; solids which diffuse from the upward flowing stream enter the downward flowing stream at a velocity $u(z)$ and rate $m_{ri}(z)$

$$\frac{dm_i(h)}{dz} = \frac{m_{fi}(z) + m_{ei}(z)}{v(z)} + \frac{m_{ri}(z)}{u(z)} \quad [2.41]$$

$$g_i(z) = \frac{dm_i(z)}{\sum_j dm_j(z)} \quad [2.42]$$

where

$m_{ei}(z)$ entrained mass flowrate

$m_f i(z)$ flowrate of species i attached to bubbles

Using the plug flow approach of Moys (1979), Ross (1991) developed model showing that the total mass flowrate of species $m_{t,i}$ ascending to level z above the pulp-froth interface is given by equation [2.43]

$$m_{t,i} = m_{fi}(z) + m_{ei}(0)\exp(-\int \frac{kd_{ei}(z)}{v(z)} dz) \quad [2.43]$$

where

kd_{ei} is the drainage rate constant of species i

2.6.1 Review of froth transport models

2.6.1.1 Moys, 1984

Moys *op cit* reported two comprehensive models to describe froth transport. The first model termed the two-dimensional streamline behaviour of the flotation froths can easily be derived from the Navier stokes equations if inviscid flow, in rectangular duct is assumed. This would result in a flow governed by the diffusive transport term, with the rate term, the advective transport term and the source/sink term being zero. The resulting Laplace equation for two-dimensional froth transport was given by equation [2.44].

$$\frac{\partial^2 \phi}{\partial x^2} + \frac{\partial^2 \phi}{\partial z^2} = 0 \quad [2.44]$$

where ϕ is the velocity potential, x distance from the back of the cell and z is the height above the pulp-froth interface. To solve this equation, boundary conditions given in Figure 1 in addition to the no-penetration condition on all walls were assumed and an analytical solution was obtained. Different froth fluxes $g_f(x)$ across the pulp-froth interface and the flux across the surface of the froth as a result of bubble break up $g_b(x)$ were considered. From the solution froth residence times and froth velocity profiles were evaluated.

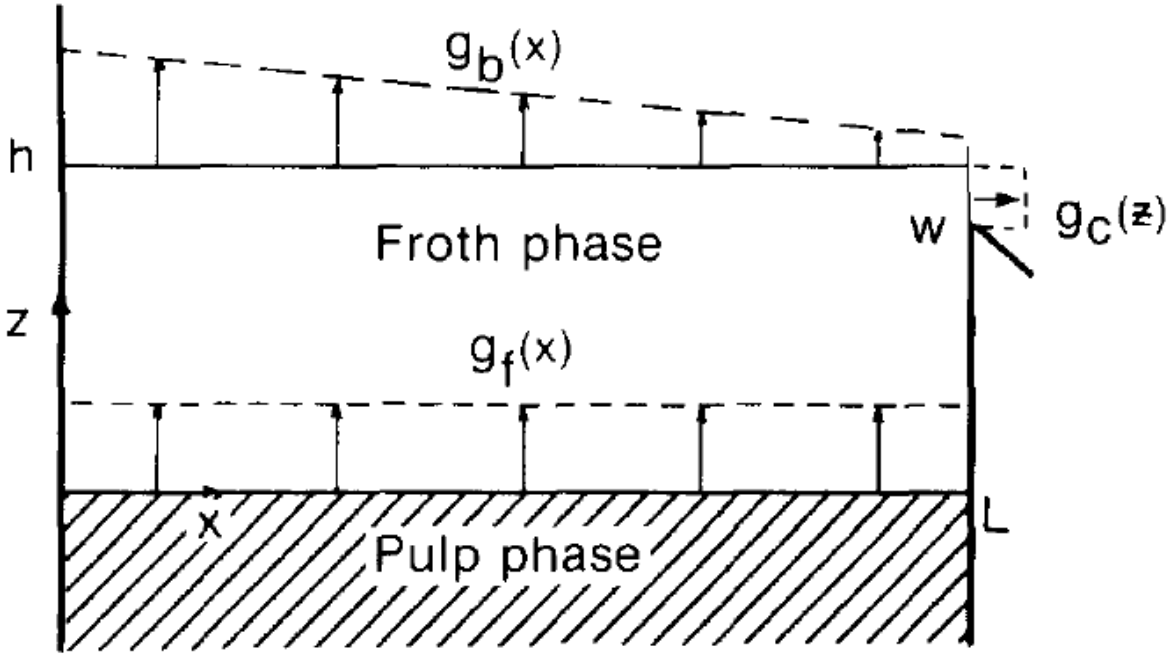

Figure 2.5: Boundary conditions for solution of the two-dimensional froth flow behaviour (after Moys 1984)

Besides being a highly theoretical depiction of the froth, the author, acknowledges that a number of conflicting assumptions had to be made to enable computation of an analytical solution. Some of the assumptions made could be avoided by pursuing a numerical solution with software such as CFD. Having realized that the complexity involved in coming up with the solution to the Laplace equation governing two-dimensional froth flow, Moys, (1984*)* suggested a simple model that could be incorporated into existing flotation models as shown in Figure 2.6, with α representing froth stability. This model was termed the two-stage tractable model.

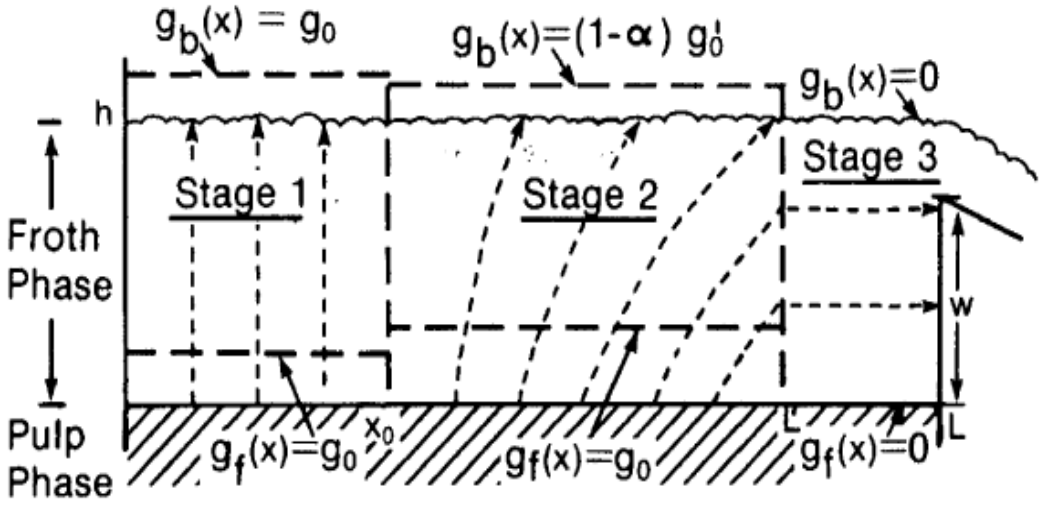

Figure 2.6: Two-stage tractable model (after Moys 1984)

In this model the froth was divided into three compartments or stages as shown in Figure 2.6. In stage 1 all the bubbles break-up upon reaching the surface while in stage 2 only a fraction of the bubbles entering this stage breaks on the surface with the reminder reporting to the concentrate. Bubbles that enter the froth in stage 3 reports to the concentrate. Moys (1984) managed to show that for a perfectly floatable particle that enters the froth phase in stage 2 and leaves with the concentrate, its total residence time is given equation [2.45].

$$\tau(x) = \tau_{\min} + \bar{\tau} \ln \frac{L' - x_0}{x - x_0} \qquad [2.45]$$

where $\bar{\tau} = \tau_{avg}(1 - \alpha\delta)$ and $\delta = \frac{\tau_{\min}}{\tau_{plug}}$; the average residence time is: $\tau_{avg} = \frac{h}{\alpha g_0}$

$\tau_{\min}$ and τ_{plug} the minimum residence times for particles in the froth and the residence time of particles rising in the froth as plug flow.

As a consequence of these froth residence time studies, Moys, *op cit.* suggested and tested several froth chamber design options. Of concern to this work is the froth flow modifier or the froth baffle (Figure 2.7). The duty of the flow modifier was to alter the path followed by bubbles streamlines as they rise from the pulp-froth interface. All bubbles are forced by the flow modifier to rise near the back of the cell. Simulations

of the plug flow model for froth residence times had shown an increase in average residence times when a flow modifier was included.

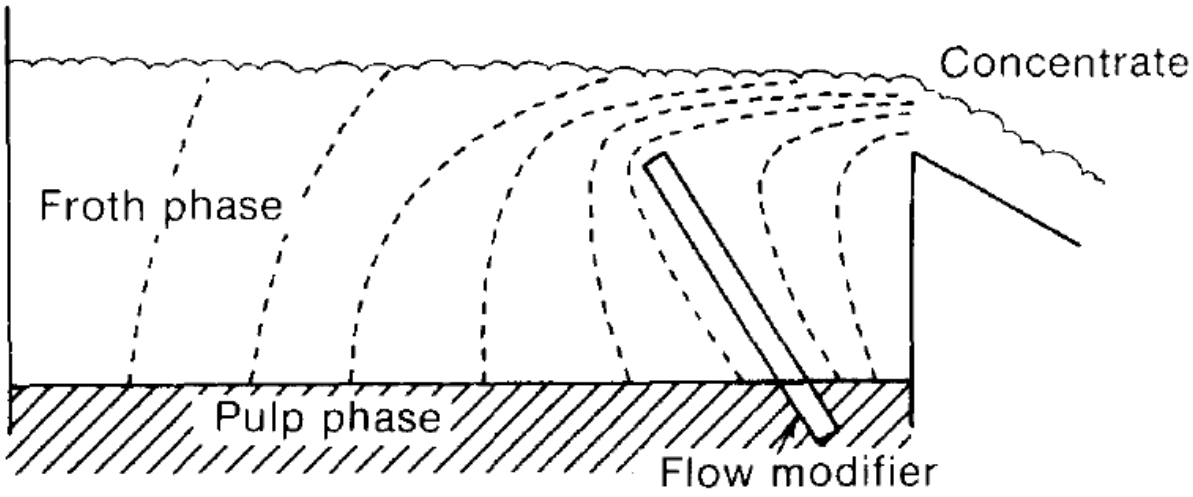

Figure 2.7: Effect of flow modifiers on bubble streamlines in the froth phase (after Moys 1984)

2.6.1.2 Zheng et al. (2004)

Zheng et al. (2004) following in the footsteps of Moys (1984), Ross (1990) and Neethling (1999) adopted the fundamental approach of froth transport modelling. Their model is based on Moys (1984) two-stage tractable model. In this model, the froth was described as composed of three stages as shown in Figure 2.8. Bubbles that enter the froth phase in stage 1 will break up on the surface and none would report to the concentrate, a fraction of bubbles that enter the froth in stage 2 would burst on the surface and the remainder reports to the concentrate while all bubbles that enter the froth on stage 3 would report to the concentrate. Zheng et al. (2004) modelling approach involved determining velocity distribution on the surface of the froth and estimation of froth residence time distributions. An air balance coupled with cell dimensions and operating conditions such as froth height were used to generate equations that describe bubble residence times. It was emphasized by the authors that equations [2.46] to equation [2.50] only describe the motion of bubbles and the attached particles. The transport of entrained particles and water was not accounted for. The vertical rise velocity (v_{fv}) of bubbles in region of vertical froth transport for a given air hold-up (ε_f) and constant froth superficial gas velocity (J_g) was determined by equation [2.47]. The horizontal velocity distribution was determined through froth flow balances in addition to height of froth above concentrate launder lip

(h_f), radius (r) and the volume of froth burst per unit time per unit surface area (δ). The horizontal velocity of the surface of froth ($v_{fh}(r)$) was then modelled by equation [2.47]. Equation [2.48] describes the horizontal froth transportation time while equation [2.49] gives the total froth transportation time including both horizontal and vertical components. The mean froth residence time with froth bursting on the surface was given by equation [2.50].

$$v_{fv} = \frac{J_g}{\varepsilon_f} \qquad [2.46]$$

$$v_{fh}(r) = \frac{J_g - \delta}{2.h_f.\varepsilon_f}.r \qquad [2.47]$$

$$t_{fh}(r) = \frac{2.h_f.\varepsilon_f}{J_g - \delta}.\ln\left(\frac{R}{r}\right) \qquad [2.48]$$

where (R) is the radius of the flotation cell.

$$t_f(r) = \frac{H_f.\varepsilon_f}{J_g} + \frac{2.h_f.\varepsilon_f}{J_g - \delta}.\ln\left(\frac{R}{r}\right) \qquad [2.49]$$

$$\tau_f = \frac{H_f.\varepsilon_f}{J_g} + \frac{h_f.\varepsilon_f}{J_g - \delta} \qquad [2.50]$$

where H_f is height of froth to concentrate launder lip

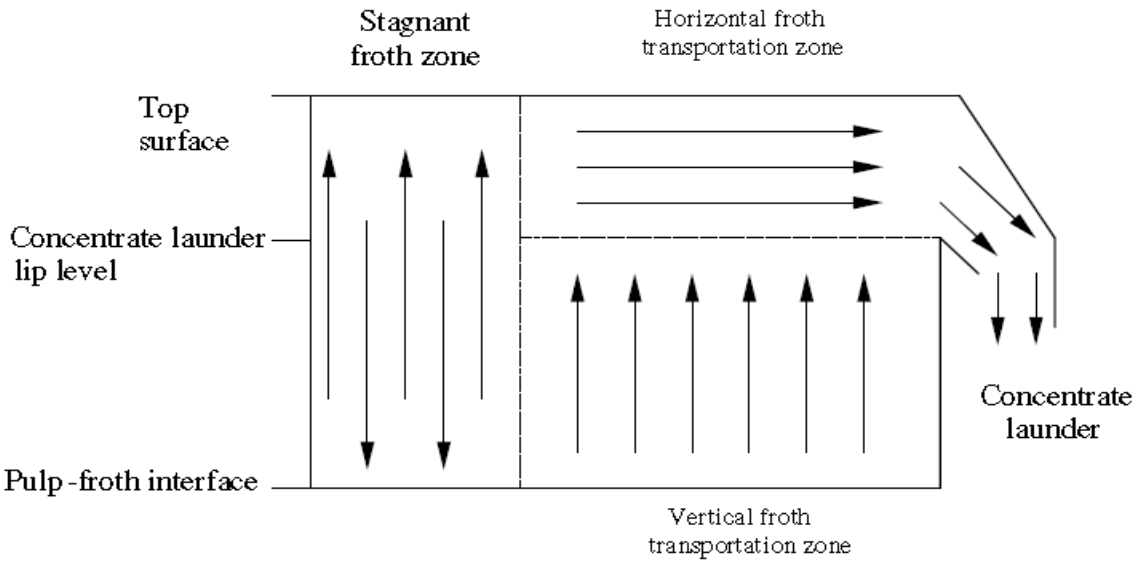

Figure 2.8: Froth model for a cylindrical industrial flotation cell (after Zheng et al., 2004)

In their follow up paper, Zheng et al., 2004 further developed the above equations to include the effect of froth crowders in 50m^3 Outokumpu flotation cell. Detailed development of the equations and the associated assumptions can be found in their paper. The inclusion of froth crowder in the models is important to this work as experiments were performed in flotation cell with a crowder.

2.6.1.3 Discussion of froth phase modelling

Modelling of the froth phase is a complex task and often a number of untenable assumptions have to be made, these assumptions are necessary as measurement techniques to characterise all parameters may not be available. The froth phase modelling approach taken by Moys (1979) and Zheng et al., (2004) which relates the operating variables such as air rate and froth depth and flotation cell dimensions to the overall recovery are explored in this work. This approach is more suitable for our operations as froth rise velocity and horizontal velocity can be estimated by video analysis.

2.7 Summary and conclusions

A background on the flotation process has been given; the important process parameters mentioned and their impact on the whole process discussed. The froth phase in particular was thoroughly analysed through analysis of the main sub-processes that influences the performance of the froth. The sub-processes of

importance are bubble coalescence and particle detachment and froth drainage. To fully understand these sub-processes important parameters such as froth residence time, froth stability and mobility need to be clearly understood. In discussing these parameters several areas that seem to be lacking in flotation literature which became the basis of this thesis were identified. These include (1) lack of accurate measurement techniques to assess the how bubble sizes change above the pulp-froth interface as a result of bubble coalescence. Measuring the bubble sizes above the interface is important as it can help to provide industrial data to test bubble coalescence models. Secondly the rate of how the sizes of bubbles change above the interface can also be used as a way of measuring froth stability. The second aspect identified for investigation is gas dispersion. The distribution of gas or the variation of gas flow across the entire flotation cell has not received much attention although it can influence parameters such as drainage, froth stability and residence times. Experiments were designed to examine the influence of gas flux distribution across the pulp-froth interface. The third stems from the influence of froth residence time on flotation performance. It is well captured in literature (equation [2.27 and 2.28]) that froth residence time affects flotation performance (both grade and recovery) through its influence on water recovery and froth recovery factor. Regardless of this importance the only way it has and still is being manipulated is through variation of gas velocity and froth depth. Moys (1979) suggested the use of a baffle to alter the mobility of bubbles inside a froth. Reanalysing this method forms the third major investigation objective of this thesis.

In summary work in this thesis shall cover (1) development and testing of techniques to measure the rate of change of bubble sizes as function of height above the pulp-froth interface. (2) Investigate the effect of gas flux distribution across the pulp-froth interface as an additional gas dispersion parameter. (3) Assess the effect of froth flow modifiers on froth performance.

Chapter 3

Equipment and experimental description

3.1 Introduction

The equipment, equipment set-up and experimental procedures are presented in this Chapter. The first section describes the design of the variable-depth variable rotor position flotation cell followed by equipment set up description used to study the froth phase. Description of the slurry and set-up used to investigate the effect of air distribution profile and the effect of a froth baffle to flotation performance is also included. A section that discusses, difficulties and challenges that were encountered during the course of this work is included.

3.2 Flotation cell

3.2.1 Flotation cell description

The flotation experiment work was carried out in variable-depth variable rotor position flotation cell. The flotation cell was designed with a bottom entry agitator to avoid the disturbance of the froth by the impeller shaft. The flotation cell (Figure 3.1) was designed in such a way that its volume can vary from 8 litres to 20 litres by changing the height of the cell front panel. This design enabled studies of the effect of froth height at fixed pulp volumes. The flotation cell was also designed in such a way that the position of the agitation mechanism could be changed relative to the centre of the flotation cell. This required the flotation cell base to be designed with a false bottom that can also be sealed when the agitator has been moved to a new position. Figure 3.2 is a side view of the flotation cell showing the bottom entry agitator, flotation cell and the table upon which the cell is sitting. The flotation cell is made from transparent Perspex 6mm thick, with sides and back 500mm tall and 200mm wide. The fixed front panel is 200mm high and 200mm wide, this configuration provides an initial 8 litre volume. On top of this front panel, additional panels can be added to increase

the total volume of cell to 20litres. The cell is equipped with an inlet and outlet port which allows continuous operation. A batch operation drain valve is also included. An adjustable deflector block is provided at the back of the cell to facilitate free flow of froth without scraping. The cell is mounted on a 500 x 500 x 400mm stand made from 25x 25mm mild steel square tubing reinforced with 25 X 25mm angle iron. On top, the stand is covered by 600 x 600 x 10mm transparent Perspex sheet. Figure 3.3 is a picture of the assembled flotation cell.

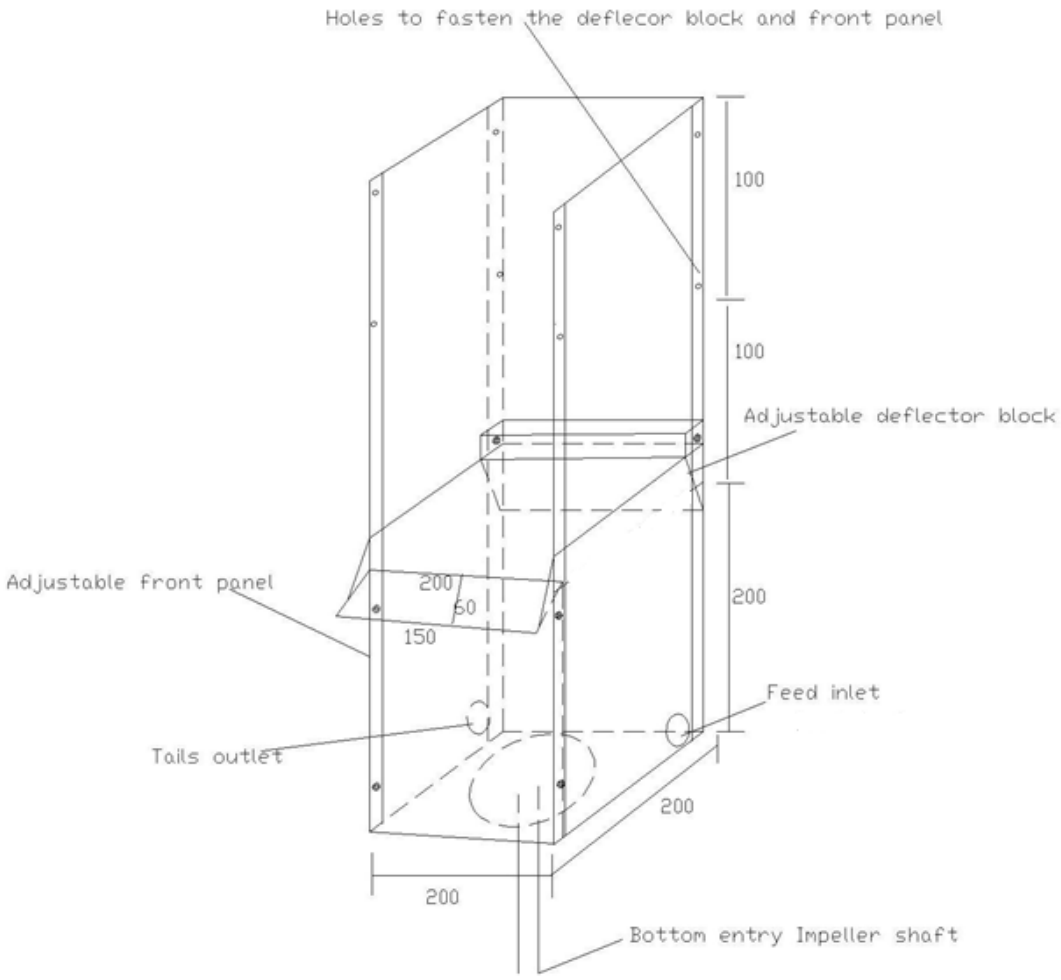

Figure 3.1: Variable-depth variable-rotor position flotation cell used for both batch and continuous experiments

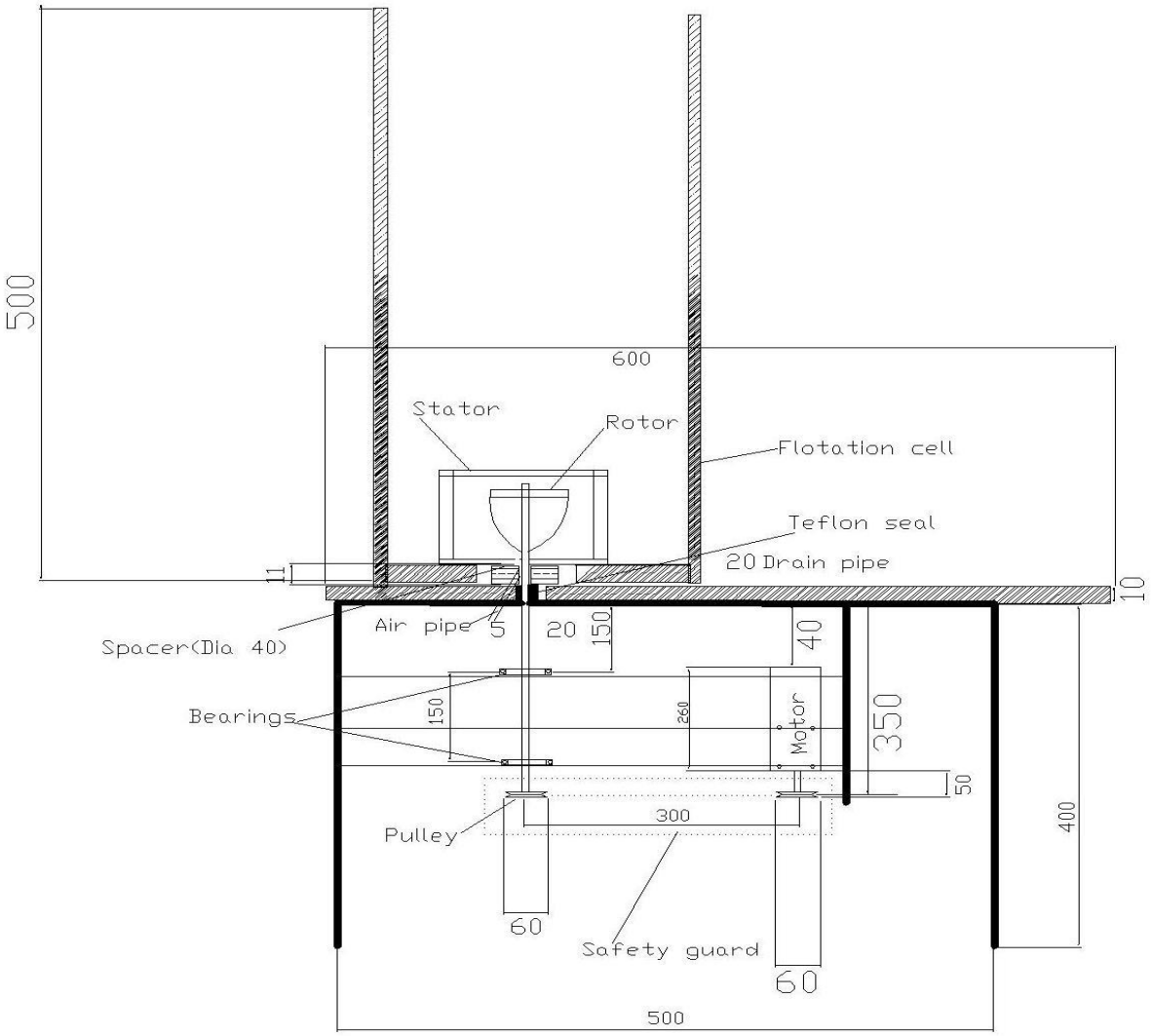

Figure 3.2: Side view of the flotation cell showing the table, flotation cell, motor and impeller shaft arrangement

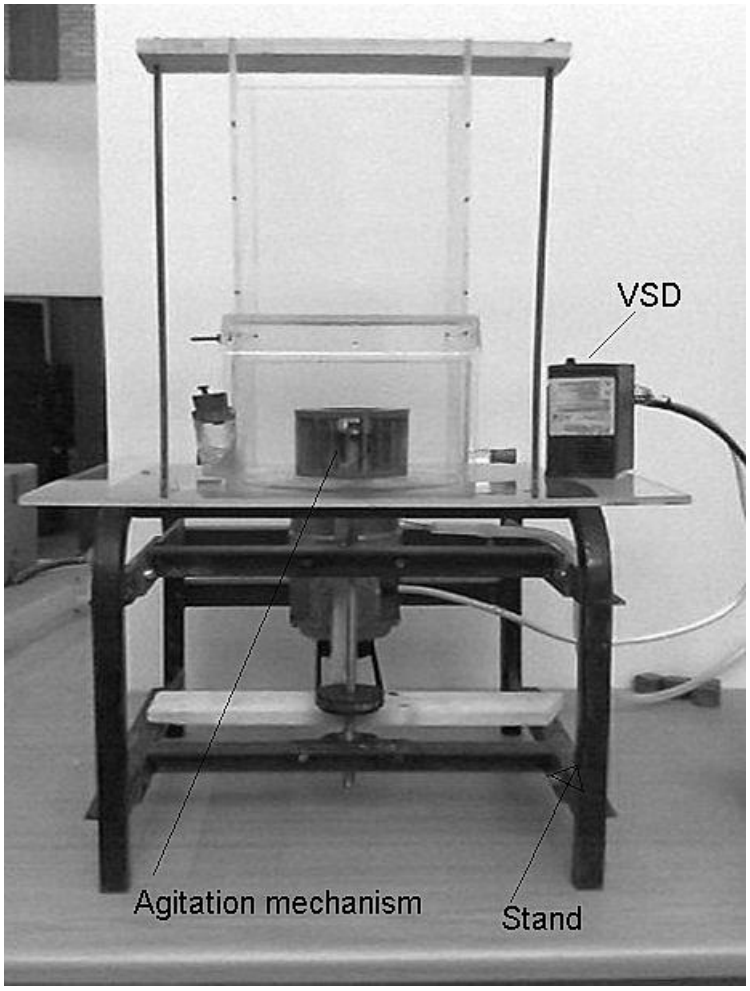

Figure 3.3: Picture of flotation cell, showing stand and VSD drive and stator.

3.2.1.1 Flotation cell base plate design

The base of the flotation cell has a rectangular hole measuring 110 mm X 120 mm; its purpose is to facilitate movement of the flotation cell relative to a fixed agitation mechanism. The agitator mechanism is fixed to the flotation table in such a way that the flotation cell can be removed or pushed back and forth or sideways. An O-ring is mounted in a groove on the bottom side of the false flotation cell bottom, to act as a seal when the flotation cell is pressed down by specially designed clamps. Figure 3.4a is a picture of the flotation cell bottom, showing the O-ring and rectangular hole and how it fits on the agitation mechanism that is fixed on the flotation cell table. Figure 3.4b to 3.4d are side view pictures of the flotation cell showing the position of agitation mechanism as the flotation cell is moved back and forth. It is noteworthy that the remaining space on the square whole is covered by perfectly fitting and specially designed Perspex strips to avoid accumulation of solids in the space between the table and the flotation cell bottom.

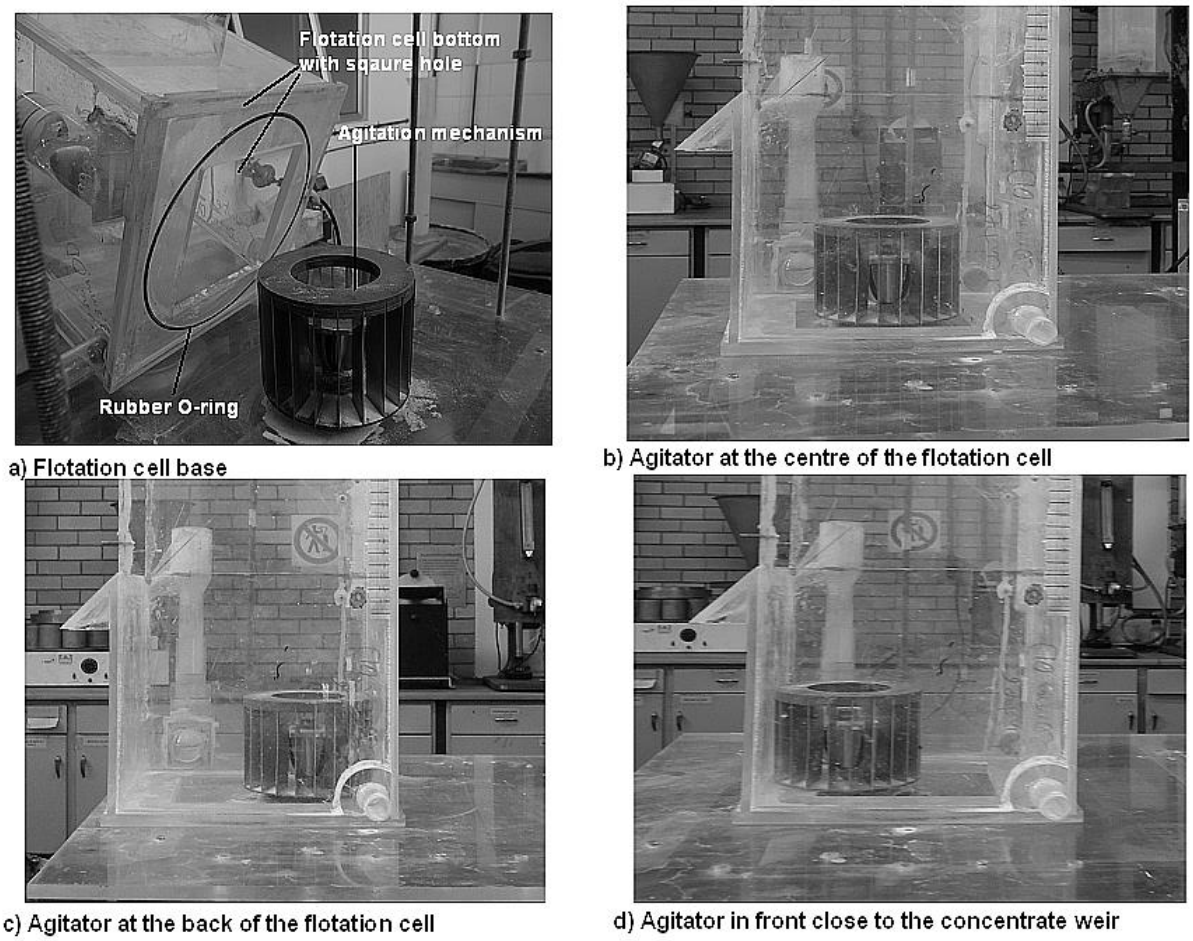

Figure 3.4: Picture showing (a) flotation cell base, relative to the fixed agitation mechanism (b) side view with the agitation mechanism at the centre (c) side view with agitation mechanism at the back close to the concentrate launder (d) side view with agitation mechanism in front of the flotation cell.

3.2.1.2 Flotation cell agitation mechanism

The agitator is a scaled down Outotec agitator with rotor and stator dimensions shown in Figure 3.5. The rotor is made of stainless steel while the stator base and top are made from gray PVC; the vanes are made from 1 mm thick mild steel. To avoid leaking at the point where the agitator shaft enters the flotation cell, two seals are provided; a standard 12mm ID seal as provided by Bearing Group Man (BMG) and a 'locked' bearing seal which is appended above the standard seal. The design of the sealing system allows for changes of the seals if need arises. Two pillow block bearings mounted below the cell are used to hold the agitator shaft to a fixed position. The agitator is driven by a 0.37 kW motor with a maximum speed of 2760rpm. Motor pulley to agitator shaft pulley ratio is 1. Speed control is achieved by means of a variable speed drive (VSD) with a frequency up to 100Hz. Figure 3.6b shows pictures of the rotor (a, b and c) and rotor size relative to stator (c).

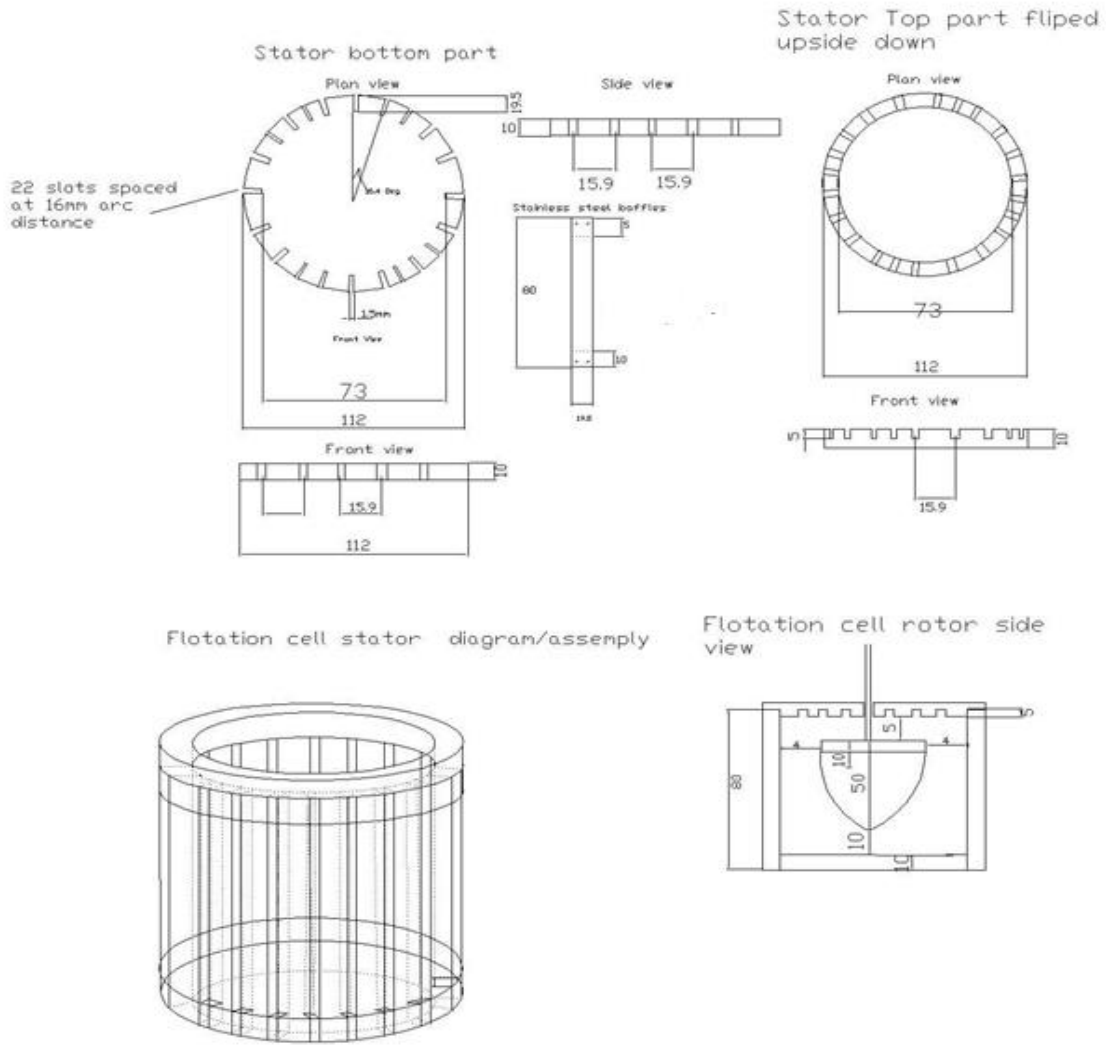

Figure 3.5: Design details of the flotation cell agitation mechanism

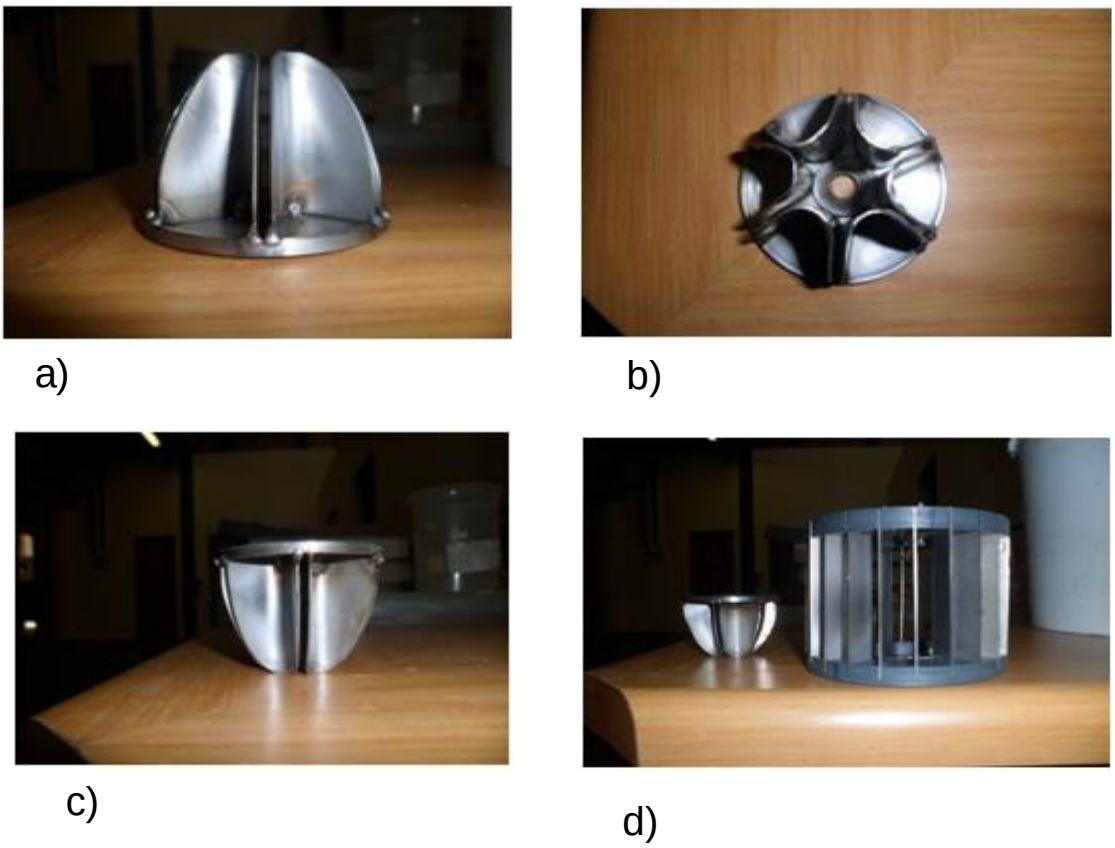

Figure 3.6: Pictures of the rotor (a,b,c) and rotor size compared to stator (d)

3.2.1.3 Flotation cell level control

The cell was designed with a level control strategy for each experimental mode i.e. batch and continuous. The batch mode level control strategy uses an inverted 3 litre Perspex container connected to the flotation cell via a variable speed peristaltic pump. This control strategy works on supplying constant amount of water (containing frother) to the flotation cell. Continuous mode flotation cell level control was achieved by an overflow method. In this method, the position of the tailings flow pipe is raised to a level such that tailings flow from the flotation cell will only commence if the set level overshoots. It ensures that the tailings flowrate is a function of both feed and concentrate flowrate.

3.3 Experimental programs

3.3.1 Laboratory set up for continuous experiments

The flotation cell was operated in a continuous manner by connecting it to an 85 litre mixing tank with tails and concentrate from the flotation cell flowing back into the mixing tank as shown in Figure 3.7. Slurry was metered from the mixing tank into the flotation cell at pre-determined flowrate using a Watson Marlow 604U peristaltic pump (calibration curve shown in Appendix A). Air flow into the flotation cell was controlled by a pressure regulator and an air rotameter. The calibration curve for the air rotameter is shown in Appendix A. The air was forced into the impeller region from the bottom of the flotation cell.

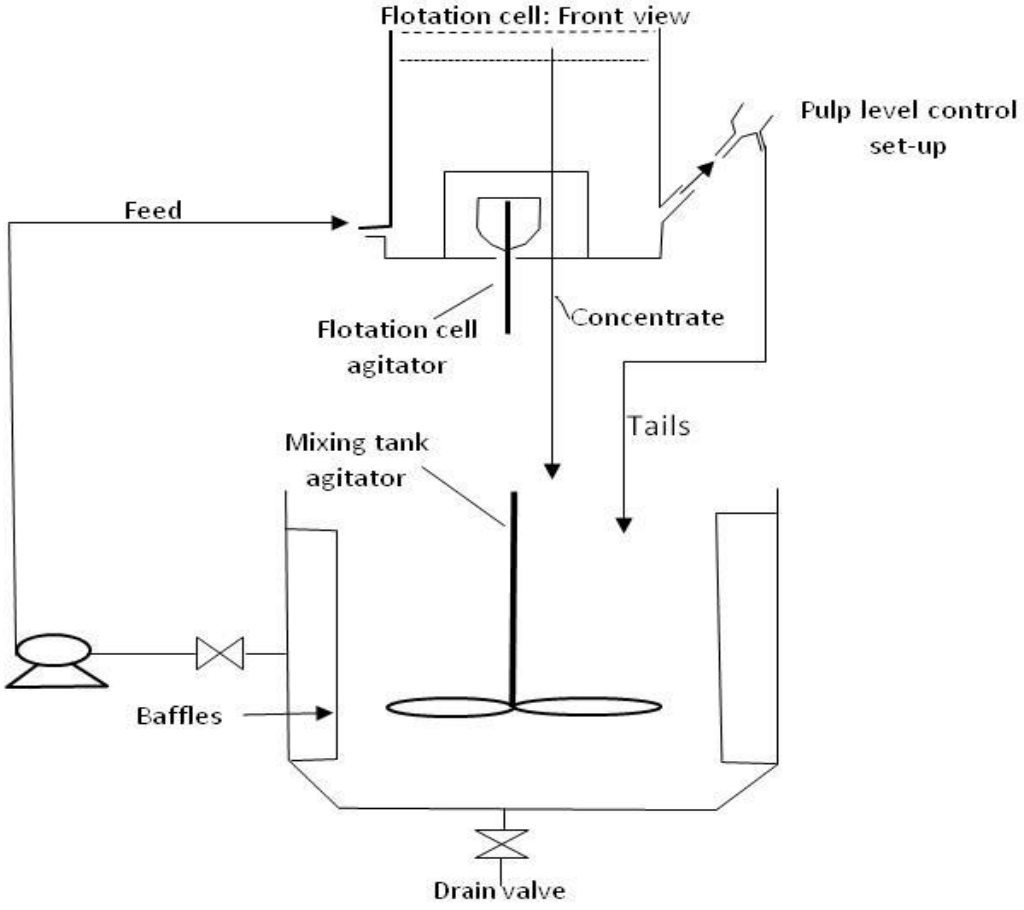

Figure 3.7: Schematic of the pseudo-steady state experimental rig.

3.3.2 Ore preparation

An artificial ore comprised of 80% silica and 20% limestone was chosen for all the experiments in this work, it was chosen mainly because of its availability in suitable size ranges and also the fact that it can be used in a closed circuit without problems of surface oxidation (of sulphide ores). Furthermore, analysis of samples (concentrate and tailings) is relatively easy, since dilute hydrochloric acid can easily be used to digest the limestone.

A 600 kg sample of ultrafine silica (>99% SiO_2) with particle size distribution (PSD) shown in Figure 3.8 was received from Silica Quartz a South African company. Bulk splitting of the sample into approximately 60kg samples was done using the cone and quartering method. A rotary splitter was used to further break the 60kg samples into 10.67kg samples which were required for the steady state experiments. Limestone with $CaCO_3$ content of approximately 93% and a PSD shown in Figure 3.8 was received in 50kg bags from SA Lime & Gypsum. Using a combination of rifflers and rotary splitters, the limestone was broken down into 2.67kg samples. Samples for particle size distribution using Malvern Mastersizer and $CaCO_3$ content determination using an acid digestion method were also prepared.

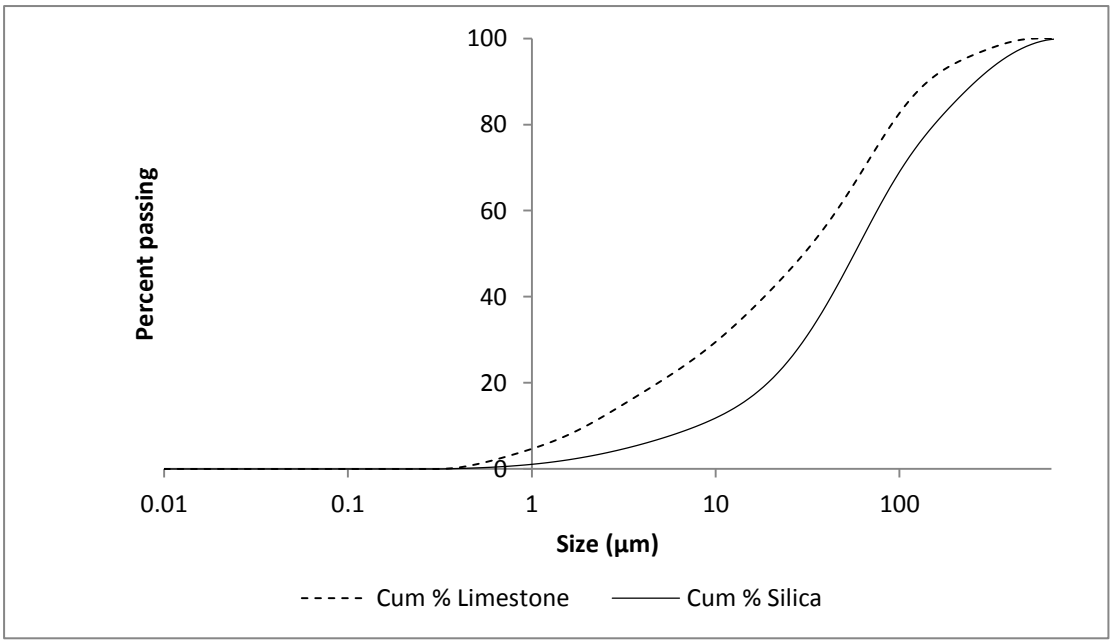

Figure 3.8: Particle size distribution (PSD) for limestone and silica used in all experiments

3.3.3 Slurry preparation

Dowfroth 250 and oleic acid were used as the frother and collector respectively. Dowfroth 250 was supplied by Betachem (Pty) Ltd and oleic acid (88%) by Merck chemicals in South Africa. Dowfroth was added at a rate of 30mg per litre of water while oleic acid dosage was 30g/ton of limestone. Since limestone is naturally floatable, slurry conditioning times were set at 2 minutes for oleic acid and 1 minute for Dowfroth. Solids concentration was maintained at 15%w/w in all experiments. Impeller speed was set at 1200 rpm. Conditioning of slurry was done in an 85 litre stainless steel mixing tank shown in Figure 3.8 with specifications shown in Table 3.1. Experiments to assess the mixing efficiency of this tank were carried out and it was found out that it was capable of suspending particles of all sizes efficiently.

Table 3.1: Mixing tank specifications

Parameter	**Specification**
Tank diameter (L)	50.2 cm
Pitched six blade turbine (D)	16.0 cm
Shaft diameter (d)	2.50cm
Shaft extension (L)	49.0cm
Shaft speed (N)	500rpm
Off the bottom clearance (C)	5.00cm
Number of baffles	4.0
Baffle width	6.00cm
Baffle Length	50.0cm

3.4 Sampling and data collection

3.4.1 Stream sampling and video recording of the froth phase

The plant was allowed to reach steady state before sampling commenced. At steady state, simultaneous cuts of tailings and concentrate streams were taken, each cut of the whole stream lasted 20 seconds. Three repeat samples were taken at 5 minutes intervals. These samples were weighed and dried for further analysis. Wet and dry samples were obtained for both tailings and concentrate. Dry samples were split using rotary splitters and a part was send for size analysis using the Malvern Mastersizer. The remaining portions of the samples were then analysed for limestone

by reacting it with 37%w/w Hydrochloric acid according to the chemical equation [3.1].

$$CaCO_3 + 2HCl \rightarrow CaCl_2 + CO_2 + H_2O \quad [3.1]$$

The products of the reaction were filtered and washed until all Calcium chloride was removed. The remaining solids were dried and weighed to determine the amount of silica. The difference in dry solids mass between the initial mass per size class (M_{Ci}) reacted with HCl and the dry filter retentate represents the mass of digestable $CaCO_3$ per size class $(M_{CaCO_3 i})$. The limestone used in these experiments had on average about 93% acid digestible $CaCO_3$ and 7% insolubles (M_{INSi}). This mass of the insoluble per size class (M_{INSi}) was subtracted from the mass of the filter retentate to get the mass of entrained silica per size class (M_{SCi}). The mass balance equations used to perform these calculations are shown below.

$$M_{Ci} = M_{SCi} + M_{LCi} \quad [3.2]$$

$$M_{LCi} = M_{CaCO_3} + M_{INSi} \quad [3.3]$$

$$M_{SCi} = M_{Ci} - M_{CaCO_3 i} - M_{INSi} \quad [3.4]$$

3.4.2 Froth phase video recording

Concurrent to sampling of the plant streams, videos of the froth phase were also recorded. The recordings were made of both the surface of the froth and from the side of the flotation cell. A Samsung ES90 camera operating at 30fps was used for this purpose. Videos of the surface of the froth were taken after sprinkling small polystyrene beads on to the froth surface. These beads enabled easier estimation of froth surface velocities as they made tracking simpler. Open-source softwares such as Tracker (http://www.cabrillo.edu/~dbrown/tracker) were used to identify bubble streamlines as well as velocity profiles while bubble size estimation was done using ImageJ (http://imagej.nih.gov/ij/, 1997-2012).

3.4.3 Superficial gas velocity measurement

Measurement of superficial gas velocity (J_g) across the flotation cell was done using a specially designed probe similar in concept to the one described by Burgess. (1997). The device consisted of a 50 cm transparent Perspex tube 3 cm in diameter with valve at the bottom and a mechanism to bleed air out of the tube at the top. Measurements were taken just below the pulp-froth interface by following these steps (1) filling the 50 cm pipe with water and closing the valve at its bottom (2) carefully placing the device at the required position and required depth below the pulp-froth interface. (3) Opening the bottom valve to allow air into the pipe and starting the stop watch. After sufficient amount of water has been displaced by the rising air, the valve at the bottom was closed and time recorded. The air bleeding valve at the top was opened before calculating the volume of water displaced, which is approximately equal to the volume of air collected. Since the diameter of pipe is known and the volumetric flow rate can be estimated from the volume of displaced air and time, superficial gas velocity can be estimated easily.

3.4.4 Sampling error comment

It is known that sampling errors and their treatment are an important aspect in mineral processing industry. It is important that these errors are minimised during experimentation. Two stages were identified as possibly having high errors viz. the actual sample collection stage and the sample weighing stage. At the sample collection stage, timing the duration of the cuts, introduces reaction time errors. For instance an error of +/-0.5 seconds on a 20 second long sample introduces a relative error of 2.5%. Although repeat samples were taken to minimize the impact of errors in measurements, it is important to note that the measurements reported herein are subject to a +/-0.25 second error corresponding to the average human reaction time to a visual stimuli. Weighing of the samples can also introduce errors. It was established that the relative error is lower on wet sample weighing than dry sample weighing because of their larger mass. An electronic scale that can measure to within +/-0.01g was used for weighing samples

3.5 Flotation cell commissioning

Prior to use in detailed froth phase investigations, the flotation cell needed to be tested to ascertain whether it can produce optimum flotation conditions. To optimize

the flotation process, an environment that maximizes the governing sub-processes such as particle-bubble interactions must be created. These interactions require the creation of bubbles of a specific size in the flotation cell typically between 0.5 and 3mm. Bubbles that are very large have less surface area per bubble volume to which particles can attach (Gaudin et al., 1931). Smaller bubbles (less than 0.5mm) may not provide enough buoyancy to lift particles out of the pulp. The degree of mixing also needs to be optimum. Enough energy is required to keep the particles in suspension and in the same vicinity as the bubbles. The suspended particles should have enough force to overcome the liquid lamella surrounding the bubbles. The mixing should not be too intense, as this may cause particle detachment from bubbles and can destabilize the froth zone. In respect of this, the following characteristics were tested during flotation cell commissioning.

(1) Hydrodynamic testing: - tested as the ability to suspend coarser size particles i.e. particles in the range +212- 425

(2) Gas dispersion characteristic: - ability to produce acceptable bubble size distribution i.e. bubbles sizes in the range 0.5 to 3mm per given operating conditions and superficial gas velocity distribution across the surface of the froth.

3.5.1 Flotation cell hydrodynamic testing

3.5.1.1 Agitator calibration

The variable speed drive (VSD) provided by BMG changed the agitator speed by varying frequency. In order to know the speed in revolutions per minute that the agitator is running at, calibration was necessary. Speed measurements were done using a contact digital tachometer. Figure 3.9 shows the agitator speed in rpm as a function of the VSD frequency. Typically, laboratory flotation machines are operated with a speed range of 700-1500rpm depending on type of machine, and operating conditions.

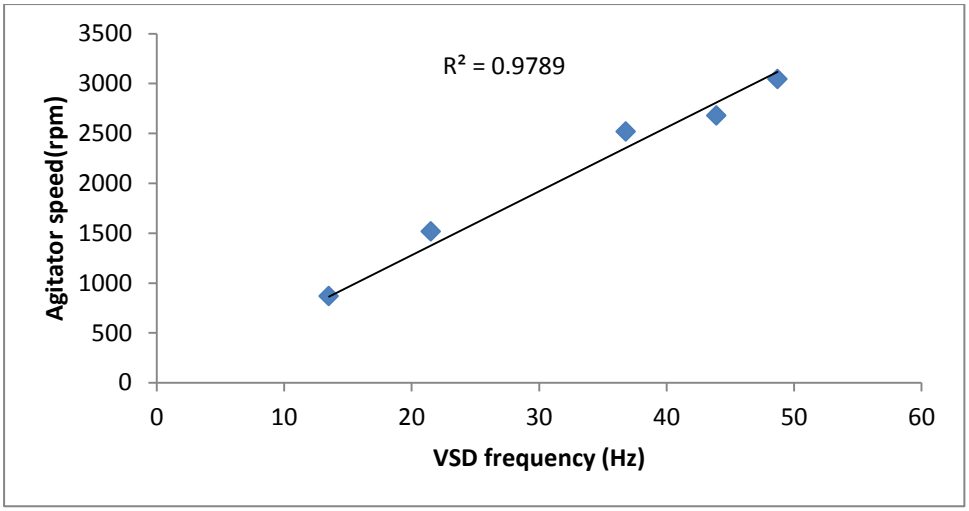

Figure 3.9: Agitator speed in rpm as function of VSD frequency.

3.5.1.2: Determination of impeller critical speed for just off-bottom suspension

In agitated vessel solids tend to settle because of their superior density when compared to the fluid. To keep solids suspended, a force is required. Usually, an impeller supplies energy to the fluid particles which then picks up the solid particles from the bottom of the vessel using its drag and lift forces. Turbulent eddies generated in the fluid by the rotating impeller also help to lift particles (Jafari et al., 2012). The minimum impeller speed that is required to lift solid particles from the bottom of vessel and suspend them in the fluid allowing short time contact with the bottom of the vessel is called the critical speed required for just off-bottom solid suspension (N_{js}). According to Jafari *op cit,* this condition is required for most solid-liquid operations including the flotation process. Thus determination of N_{js} becomes vital for us to be able to determine the range of frequencies on the VSD in which this flotation cell should be operated.

The visual technique as first used by Zwietering (1958) was used to estimate of N_{js} for the flotation cell. For this experiment, 0.167kg silica sand of size range +212 - 425µm was added to 6 litres of water. A video camera was used to record particle behaviour at the bottom of the flotation cell as function of impeller speed. Experiments to determine the value of N_{js} were done with the impeller at the central position of the flotation cell and also without air. We take note that introduction air increases N_{js} value because it reduces the pumping capacity of the impeller and all parameters responsible for solid suspension (Jafari et al., 2012).

Figure 3.10a to 3.10d are pictures of the bottom of the flotation cell as agitator speed was increased from zero to 2000 rpm. A bed of settled silica particles is clearly visible at the bottom of the flotation cell when the agitator speed was zero, see Figure 3.10a. When speed of the agitator was increased to 700 rpm; particles started to move from the bottom of the cell and getting suspended in water, regions where all silica particles have been swept off the bottom of the cell are clearly visible. Obscuration also increased as shown in Figure 3.10b. Increasing the agitator speed further, resulted in almost all particles moving of the bottom of the cell although some particles were occasionally coming into contact with the bottom of the cell for short periods and rising up again. If the definition of Njs as proposed by Zwitering (1958) is applied, it can be inferred in this work that at the speed of 1500 rpm, the critical impeller speed for just off-bottom suspension was reached. This stage is illustrated by Figure 3.10c. Figure 3.10d shows appearance in the flotation cell when speed was increased to 2000 rpm.

Figure 3.10a: Picture showing settled silica sand when the agitator is stationery

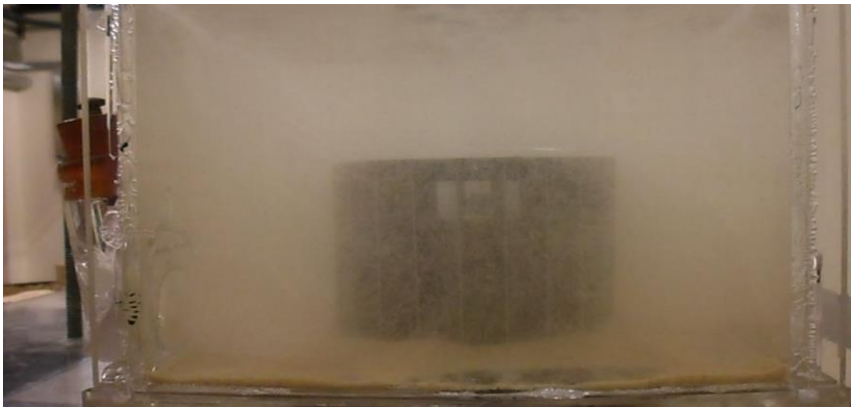

Figure 3.9b: Picture showing silica sand rising as agitator speed is increased to 700rpm.

Figure 3.10c: Picture showing almost all sand particles suspended in the water agitator speed at 1500 rpm.

Figure 3.10d: Picture showing all sand particles suspended in the water agitator speed at 2000 rpm.

3.5.1.3: Discussion-solids suspension

It is evident that the flotation cell is capable of maintain the coarser sizes classes in suspension albeit at higher speeds than the laboratory Denver D12 flotation machine (700-1200 rpm). The need for higher speed to suspend all particles in this flotation machine was attributed to the stator and rotor design. The base of the stator stands 10mm from the base of the flotation cell creating corners on which particles accumulated; increasing the speed result in these particles rising up. Substantial reduction in impeller speed was achieved by removing the 90^0 angle between flotation cell base and stator base. The angle was reduced to 20^0 to the horizontal and N_{js} was reduced to 1200 rpm.

3.5.2 Gas dispersion characteristics testing

3.5.2.1: Bubble size measurement

Bubble sizes were estimated from pictures taken from the sides of a specially designed bubble-sizer similar in concept to that developed by Grau and Laskowski (2006). These measurements were taken at an impeller speed of 1200 rpm and a superficial gas velocity of 1.7 cm/s with frother addition maintained at of 20 mg/l of water. To enable clear observation and videoing of bubbles experiments were carried out without solids. Bubbles sizes were estimated manually from the pictures with the aid of open-source software ImageJ (http://imagej.nih.gov/ij/, 1997-2012), at least 200 bubbles were measured and results are shown in Figure 3.11.

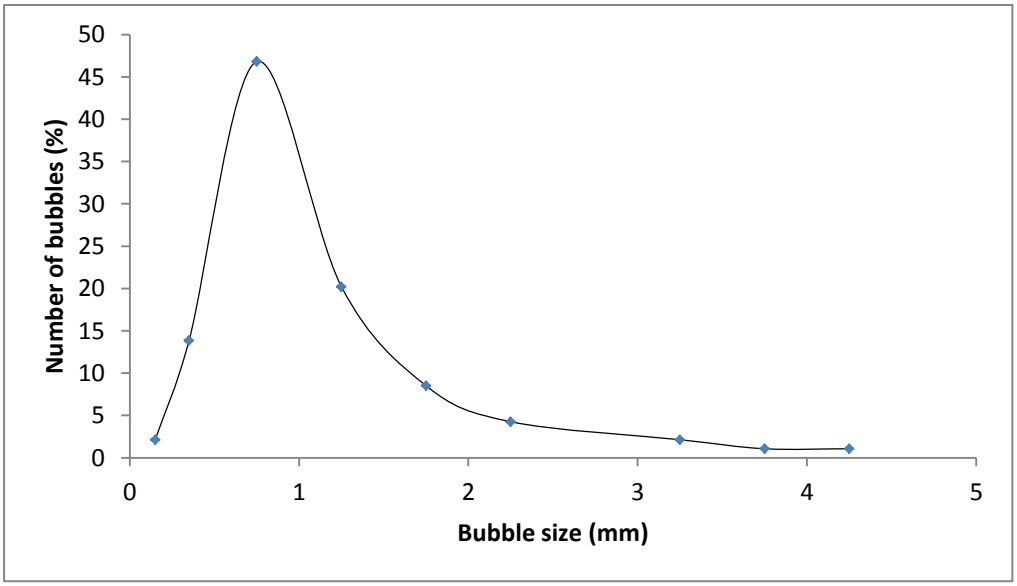

Figure 3.11: Bubble size distribution at 1200 rpm and 20 mg/l Dowfroth 250

3.5.2.2: Superficial gas velocity (J_g)

Superficial gas velocity is also used as a way of characterising gas properties in flotation machines as it measures the aeration ability of the flotation cell. In this thesis, two methods were used to evaluate Jg. The first method used involved calculating it from air flowrate which was set at 27 l/min, cross-sectional area of the cell, impeller cross-sectional area and stator annulus area using equation [3.6]. The effective cross-sectional area was calculated by subtracting impeller cross-sectional area from flotation cell cross-sectional area. The value of J_g obtained from this method constitutes an average value for the cell. The second method involved measurement of superficial gas velocity at several positions across the surface of the

flotation cell. Measurements were taken just below the pulp-froth interface using a superficial gas velocity probe described in section 3.4.3. Results of gas distribution profile as measured just below the pulp-froth interface when rotor is at the middle of the flotation cell and set at 1200 rpm are shown in Figure 3.12. This method provided a distribution of superficial gas velocity across the flotation cell.

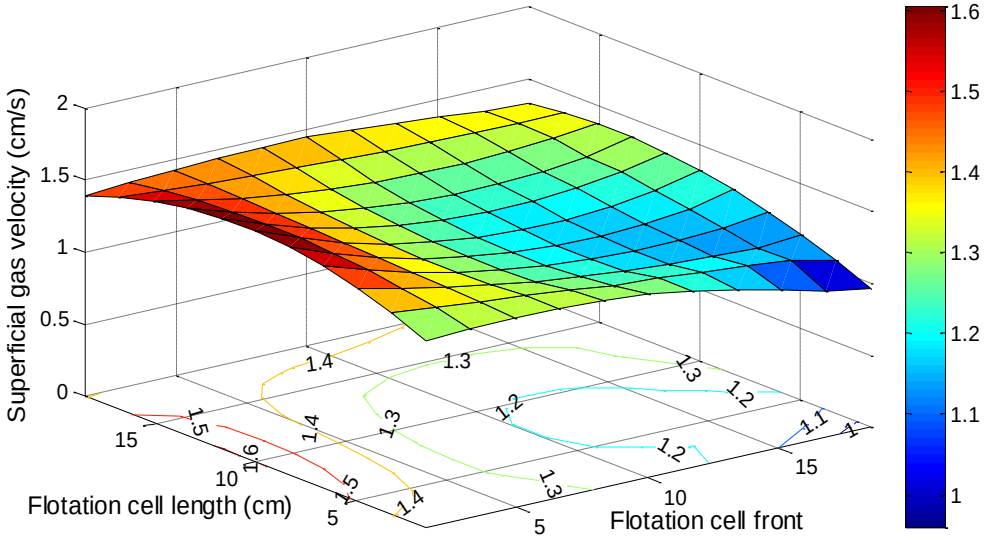

Figure 3.12: Typical gas superficial velocity distribution profile when agitator is at the centre.

3.5.2.3: Gas hold-up and bubble surface area flux calculations

Gas holdup (ε_g) was estimated from its relationship with bubble surface area flux (Sb) as developed by Finch et al. (2000). This relationship which was developed in for flotation column is given by equation [3.7]. The bubble surface area flux (Sb) was first calculated from the measured Sauter-mean bubble size and superficial gas velocity using equation [3.8]. The Sauter-mean bubble diameter (d_{32}) was calculated from the bubble size distribution data. It is defined as the volume to surface mean diameter and is calculated using equation [3.5]. A summary of these gas dispersion properties is given in Table 3.2.

$$d_{32} = \frac{\sum n_i d_i^3}{\sum n_i d_i^2} \qquad [3.5]$$

$$Superficial\ gas\ velocity = \frac{Gas\ \ flowrate}{Effective\ \ cross\ \text{sectional}\ \ area\ \ of\ \ cell} \quad [3.6]$$

$$S_b = 5.5\varepsilon_g \quad [3.7]$$

$$S_b = 6\frac{J_g}{d_{32}} \quad [3.8]$$

Table 3.2: Summary of gas dispersion properties

Gas property	**Value**
Sauter-mean bubble diameter(mm)	1.40
Superficial gas velocity (cm/s)	1.30
Bubble surface area flux (cm/s.cm)	55.70
Gas holdup (%)	10.13

3.5.2.4 Discussion-solids suspension

The gas dispersion properties obtained from the cell commissioning experiments indicate that the flotation cell can produce acceptable aeration conditions. Typical superficial gas velocity ranges between 0.5 and 2.5 cm/s; a superficial gas velocity value of 1.3cm/s was obtained at a gas rate of 27l/min. Values obtained above can easily be changed by varying operating conditions of the flotation cell.

3.6: Difficulties encountered

Several challenges were encountered during the design and experimental set-up of the flotation cell system. The main problem was to make the flotation cell leak proof. Since the flotation cell had a false bottom to ensure its movement relative to a stationery rotor-stator system, a considerable amount of time was spend designing a system that eliminate leaking from the false bottom. Use of a rubber O-ring engraved into the flotation cell bottom and pressed against the flotation cell table top proved to be the most efficient method to eliminate the leaking. Although this set-up was effective, it required that the flotation cell table top to be flat and to remain flat as the flotation cell volume was increased. This meant that the table structure had to be reinforced with angle iron bars. As with all bottom entry impeller reactors, the main challenge that the designer faced was to make it ‘leak proof’. The use of standard

seals seemed to be the most obvious route to take; it proved to be the wrong solution in this design and set-up. Using a standard seal worked only for an hour in each run after which leaking of the slurry would start and tests had to be stopped. Inspection of the seal would reveal that it was still intact, but the impeller shaft was eroded from a diameter of 12 mm to 10.5 mm. Fine silica which was used as the gangue material formed a grinding paste that was ingressing between the shaft and the seal, grinding away the shaft and resulting in slurry leakage. Replacing the seal with a ‘locked’ bearing appended below the flotation cell table surface and removing the seal eliminated leakage and shaft erosion. The bearing was locked to the impeller shaft and its Perspex housing glued to the base of the flotation cell table, friction forces were drastically reduced as rotation was taking place within the bearing.

Chapter 4

Development of a measuring technique to estimate froth phase bubble sizes as a function of height above the pulp-froth interface

Work in this Chapter was presented at flotation 13 conference in Cape town South Africa. It was subsequently divided into two papers part I and part II which were submitted for publication with the International Journal of Mineral Processing (IJMP). While part 1 of these papers has already been published part II is still under review. A patent on the work covered in this Chapter has been lodged.

4.1 Introduction

Froth phase sub-processes such as bubble coalescence result in an increase in bubble sizes above the pulp-froth interface and particle detachment from the bubbles (Yianatos et al., 1988, King, 2001). If the detached particles reattach to the available bubble surface area based on a property such as floatability then further cleaning action takes place (Moys, 1979). Generally the initial separating action of the froth phase starts at the pulp-froth interface as alluded to by a number of workers e.g. (Falutsu and Dobby, 1989, Yianatos et al., 1986a, 1986b, 1988; Finch and Dobby, 1990). Further cleaning action may take place in the bulk of the froth phase as particles detach due to coalescence (Seaman et al., 2006). Consequently the rate at which bubbles coalesce within the froth is important for assessing and optimising recovery across the froth phase. Unfortunately methods/ techniques that can be used to measure change of bubble sizes with height above the pulp-froth interface in flotation froths produced in non-transparent flotation cells are not available yet.

Bubble coalescence results in a general increase of froth bubble sizes from the pulp-froth interface to the top/surface of the froth resulting in drastic reduction in available bubble surface area. For example Cilliers (2006) reported a loss of surface area of up to 97% for a 0.5 mm bubble that enters a 100 mm thick froth at a superficial gas velocity of 2 cm/s. The rate of bubble coalescence is affected by such factors as froth stability, gas rate and froth depth (Ata et al., 2003). At a given gas rate and froth depth, froth stability determines the rate of bubble coalescence (Farrokhpay, 2011) and therefore rate of change of bubble sizes. By knowing the rate of change of bubble size, properties such as froth stability and rate of bubble coalescence can be inferred. The size of bubbles at the top of the froth have been correlated with concentrate grade (Forbes, 2007) but according to Murphy et al. (1998) information obtained from observing the surface of the froth is not enough. The use of top of the froth bubble sizes has been partly necessitated by lack of a reliable and industrially applicable method to measure bubble sizes within the froth. A measure of bubble size in the froth and an understanding of the rate at which bubble sizes change within the froth phase can provide quantitative information which will assist understanding of froth phase sub-processes especially bubble coalescence.

Work in this Chapter focuses on developing a method to measure a proxy for froth phase bubble sizes in flotation machines as a function of height above the pulp-froth interface. An electro-resistivity method is proposed as a basis of measuring this proxy. It is envisaged that the distribution of the proxies obtained with this new method is related to froth bubble sizes distribution per given height above the interface. Measurements of the proxy obtained with the new technique are compared to the Sauter-mean bubble diameter obtained by a photographic method. The photographic technique is the most commonly used method to obtain froth bubble size distributions in laboratory flotation froths (Ata et al. 2003). Its use in industrial flotation machines is limited as it requires the flotation cell walls to be transparent to enable clear videoing. The equipment used in this work will enable estimation of froth bubble size distribution in industrial flotation froths via the measurement of electrical conductivity thus the flotation cell walls need not be transparent. The work is divided into two sections viz.

(1) Development of the method and testing it in two phase foam generated from water containing Cu^{2+} ions.

(2) Testing the effects of chemical conditioning of the water/slurry from which the froth is generated on bubble size estimation using the developed technique.

Although the technique developed in this Chapter does not provide actual bubble sizes, it is important to emphasise that data obtained can provide an insight into the dynamics of coalescence in froths. Consequently in the absence of any other method to measure bubble sizes in froths, this work constitute a bold step forward in the endeavour to understand flotation froths.

4.2 Development of the method and testing in two phase foam

4.2.1 Use of electrical conductivity to estimate bubble sizes

The use of foam electrical conductivity as a way of estimating bubble sizes has been used by some researchers e.g. Xie et al. (2004) developed a method to estimate bubbles sizes in bubble columns that uses electrical conductivity of foams as its basis. Liquid flowrate in the foam (q_1), electrical conductivity when the column was filled with water only (Vi) and electrical conductivity when the column had froth inside (V) were used to calculate an average bubble size. Using these values, the average bubble size (d_b) was calculated using equation [4.1]. While parameter (v_g) in equation [4.1] represents superficial gas velocity, the constants $k_1 \; and \; k_2$ are chosen depending on the assumed geometry of the bubble. Bubble sizes comparable to the photographic method were reported, a relative error of less than 4.2% was observed. Although this method is relatively simple and has a potential to be used in industrial froth, the determination of the values of the empirical constants $k_1 Vi$ and $k_2 Vi$ introduces errors as these may need to be determined in a separate transparent flotation cell operating at similar conditions. Equation [4.1] was developed based on dry foam theory and as mentioned by the authors, it is applicable to foams with water content up to 5% by volume.

$$d_b = \sqrt{\frac{\left(\frac{k_1 V_i}{V} - \frac{q_1}{v_g}\right) V^2 v_g}{k_2 V_i^2}} \qquad [4.1]$$

Pancho and Davies (2003) also developed an electrical capacitance based method to study foam structure. Froth bubble sizes were estimated from this method. Zhou et al. (2012) developed a probe to study two-phase flow systems; data from their probe was also used to estimate sizes of slugs in bubbly flow.

4.2.2 New technique measuring principle.

Unlike the method by Xie et al. (2004) this new froth bubble size measurement technique uses the actual difference in electrical conductivity between water forming bubble films and air contained within a bubble. Water is generally a good conductor of electricity while air is a poor conductor. It is expected that the electrical conductivity would jump from a low value to high value when a conductivity probe moves from air into water. This difference in electrical conductivity can be exploited for bubble size determination purposes. Using this principle the output signal can be used to trace the moments when the probe makes contact with a bubble film/bubble lamella and when the probe was inside a bubble as illustrated in Figure 4.1. Figure 4.1 is a qualitative representation of the expected output signal from a conductivity probe that is connected to a resistive voltage divider circuit when a small probe traverses the froth along the line AB. The output signal is represented as a voltage in Figure 4.1 not as conductivity. The open circuit (probe in air) voltage was plotted as rising up to the air voltage while the probe tip passes through the air inside the bubble. When the probe contacts a bubble surface the voltage drops to the water voltage. This in practice may not be true as the air contained within the bubbles might have a lower resistance than atmospheric air since it may have a higher humidity as it would have been sparged through water. Change in air resistance as a result of differences in air humidity and relative amounts of dissolved ions in the evaporated liquid has been reported by some researchers e.g. Simpson (1909), Blanchard (1961), Carlon (1980). The closed circuit voltage (probe in contact with liquid) is a function of the relative amounts of water and air at a given position within the froth. Intuitively a decrease towards the water/pulp voltage is expected as the probe moves towards the pulp-froth interface because the water content of the froth is increasing. Of interest also in Figure 4.1 are the points of sharp change in voltage. These points take place when the conducting probe comes into contact with water .i.e. the probe has to be moving from air into water. They are signified by a very rapid drop in voltage and are herein defined as points of significant impact. The distance between successive points of significant impact defines the intra-bubble impact distance (IID). For a conducting probe cutting through the froth phase at a given velocity, the time

taken between successive points of significant impact and the speed at which the probe is cutting through the bubbles are used to calculate the IID. If the conductivity probe is dropped into the froth phase several times, the average IID obtained is the proxy that is related to the actual bubble sizes.

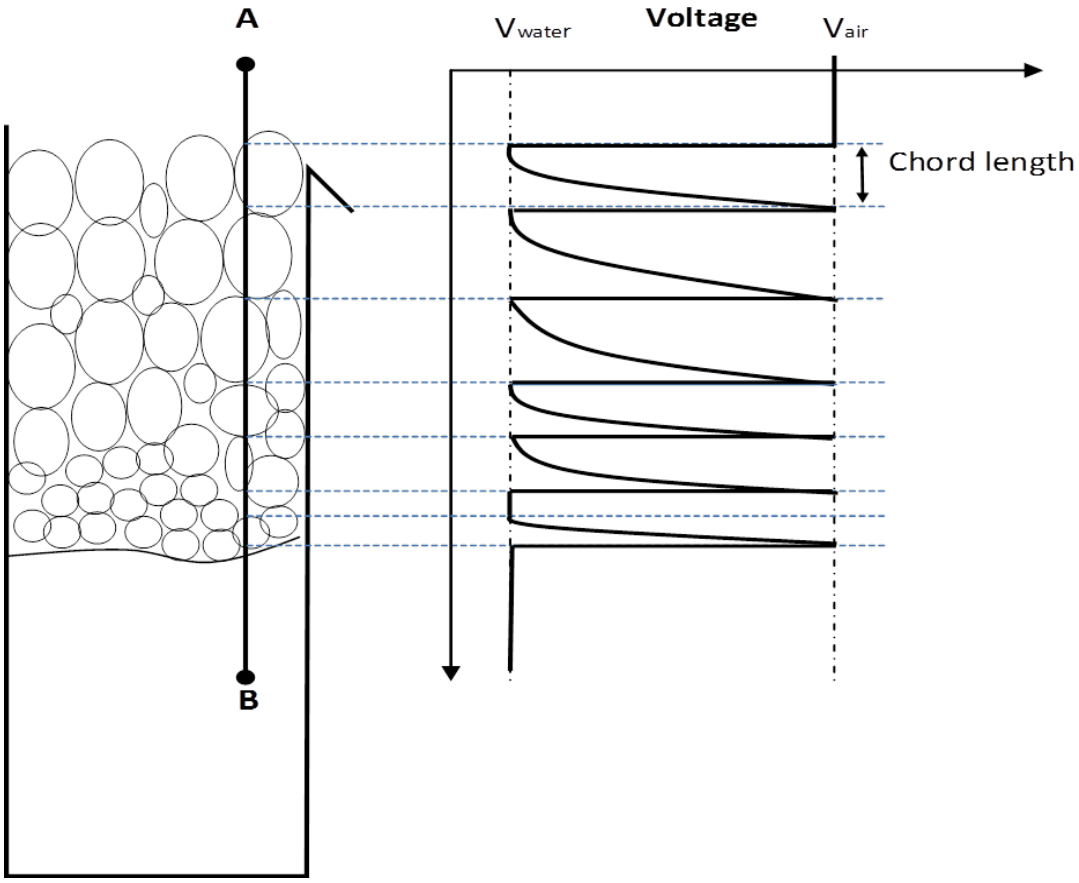

Figure 4.1: Theoretical illustration of the output voltage signal that is obtained when a conducting thin wire cuts through froth phase

4.2.3 Froth bubble-sizer description

The bubble-sizer consists of a DC signal generator that is connected to a conductivity probe through a 1MΩ resistor to form a resistive voltage divider circuit as shown in Figure 4.2. The conductivity probe is a made out of 0.3mm diameter insulated copper transformer wire with the tip exposed to conduct electricity. The conducting wire is wrapped onto a 4mm diameter and 40cm long mild steel rod. Attached at the back of this rod is a rectangular PVC strip to stop the probe from falling into the flotation cell as shown in Figure 4.3 giving the probe assembly a total mass of 90 grams. The tip of the insulated copper conducting wires was exposed by cutting it with a pair of scissors; it was also chosen to be thin to enable measurement of small bubbles

(above 0.5 mm) and to avoid popping the bubbles. The signal from the bubble-sizer circuit is routed to a PC through a data logger. It can easily be deduced from Figure 4.2 that the output voltage (V_{out}) depends on the resistance between the ground and the probe (R_f), the fixed resistance (R_1) and the input voltage (V_{in}) and it is calculated using equation [4.2].

$$V_{out} = \frac{R_f}{R_f + R_1} V_{in} \qquad [4.2]$$

The resistance between the probe and the ground i.e. froth resistance (R_f) can be viewed as a variable resistor that can assume a value that ranges widely as the probe tip moves from bubble lamella into a bubble.

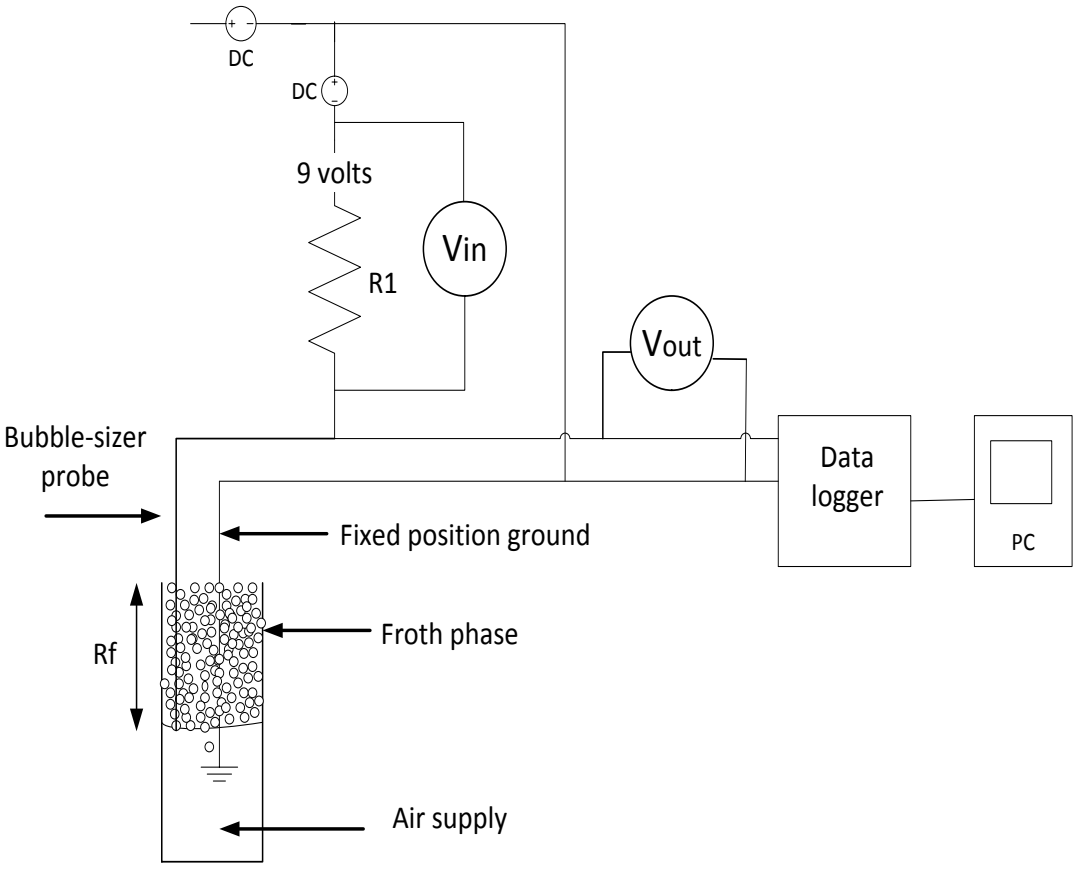

Figure 4.2: Bubble-sizer circuit and bubble size measurement set-up

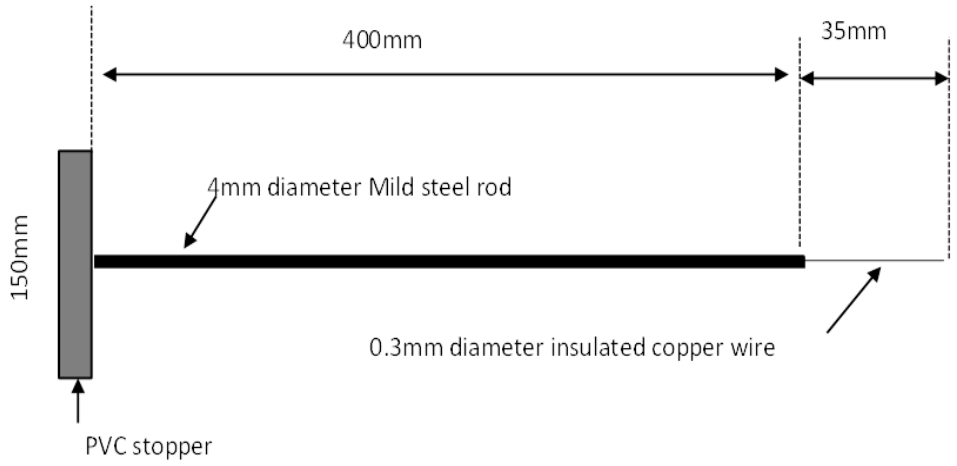

Figure 4.3: Schematic of the conductivity probe, showing the insulated copper wire, Mild steel rod and the PVC stopper with dimensions included

4.3 Experimental testing of the technique

To enable development, testing and validation of the new froth bubble measuring technique, two different types of experiments were performed. The first set of experiments was done to analyse the signal produced when an electrical conducting wire is moved in and out of water at regular intervals. These experiments simulated bubble lamella and bubble air conditions and results would show how the probe signal behaves when coming into contact with water and when it is moving out of water. The second experiments basically tested bubble size estimation on a two phase system in a mini-flotation column and comparing the obtained results to the photographic method. Thus concurrent to these experiments, videos of the froth were also taken.

4.3.1 Air-water (Bubble air-bubble lamella simulation) experiments

Initial experiments to simulate the response of the bubble-sizer circuit when its probe cuts through froth were done by repeatedly dipping the conductivity probe in an out of water at regular intervals. In these experiments the instances when the probe was in contact with water would simulate a probe in contact with bubble lamella in actual froth while the times it was in air represent moments when probe was in contact with air contained within a bubble. These experiments would provide a general indication of how voltage signal would change as the probe cuts through bubbles within the froth phase. The response rate can also be assessed from obtained data. Experiments were carried out in a 250ml measuring cylinder with frother (Dowfroth

250) dosed at 20 mg per litre of water; 9 volt batteries connected in series were used as the power source. Results were recorded on both an oscilloscope and a computer.

4.3.2 Froth bubble size measurement in mini-flotation column

The second set of experiments involved generating continuous foam using a mini-flotation column and dropping the conductivity probe into the froth from a fixed height above the surface of the froth as shown in Figure 4.4. The (13cm x 14cm x 50cm) flotation column was made out of transparent Perspex to enable photographing. Air flowrate into the column was controlled by an air rotameter and bubbles were generated by a sparger. The drop height position was controlled and marked by an adjustable pointer attached to a laboratory stand. A circular guide ensured that the probe fell along a fixed and controlled locus. Dropping the probe vertically downwards from a known height (Hd) above the froth surface enabled the calculation of the initial speed at which the probe touches the froth surface using Newton's equations of motion. The probe velocity profile inside the froth phase was obtained from the froth height (Hf) and time taken to cut across the froth as obtained from the signal. Concurrently pictures of the froth were taken with a Samsung ES90 camera for bubble size estimation. A graduated ruler was glued to the sides of the flotation cell to enable calibration during bubble size estimation. The arrangement of the camera relative to the flotation cell is shown in Figure 4.4. The output voltage response was recorded on a PC thorough a data logger SCX1-1520 supplied by National Instruments. This card has sampling rate of up to 100 kilosamples/s (kS/s) although all measurements reported herein were done at 40kS/s.

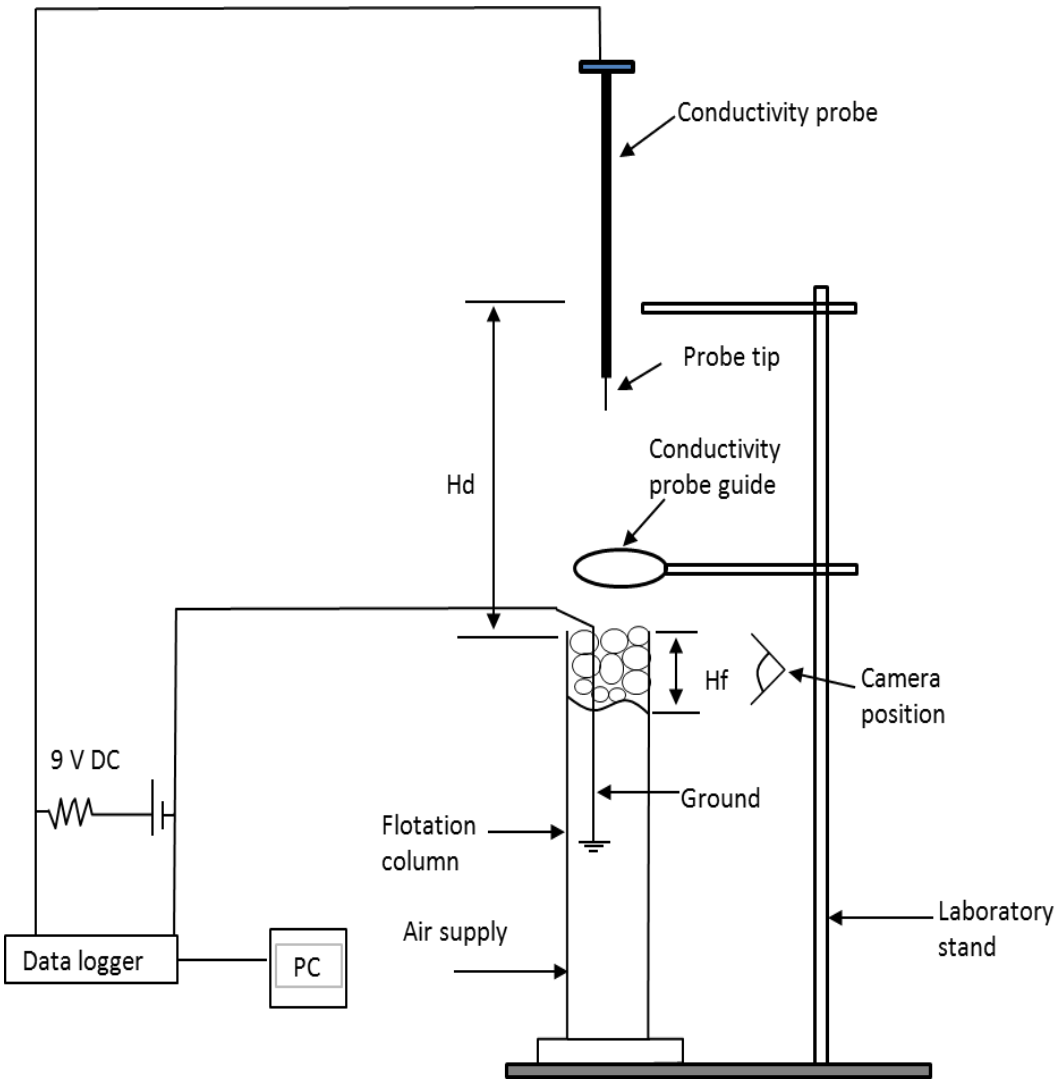

Figure 4.4: Schematic of the experimental set-up to measure bubble size in the mini-flotation column

4.4 Results

4.4.1 Air-water (Bubble-air bubble-lamella simulation) experiments

A summary of the results obtained from dipping the probe in and out of the water at regular intervals is shown in Figure 4.5. When the conductivity probe was in air i.e. open circuit, a DC signal of about 4 volts was recorded, when it came in contact with water, a sharp decrease in voltage from 4 to 0.4 volts was observed. The decrease took 0.1milliseconds as shown on the expanded subplot (a) of Figure 4.5a. Moving the probe out of water was characterised by a slow increase in voltage from 0.4 volts to 4 volts which took 2milliseconds to reach the open circuit voltage (Figure 4.5a subplot (b)). Reversing the polarity and connecting the probe to the negative terminal of the battery and repeating the experiment also produced step changes which upon

expansion revealed a similar pattern as was observed with the conductivity probe connected to the positive terminal of the battery i.e. a rapid response when making contact with water and sluggish response when moving out of water into air (Figure 4.5b). The calculated response times were also 0.1 milliseconds and 2 milliseconds respectively.

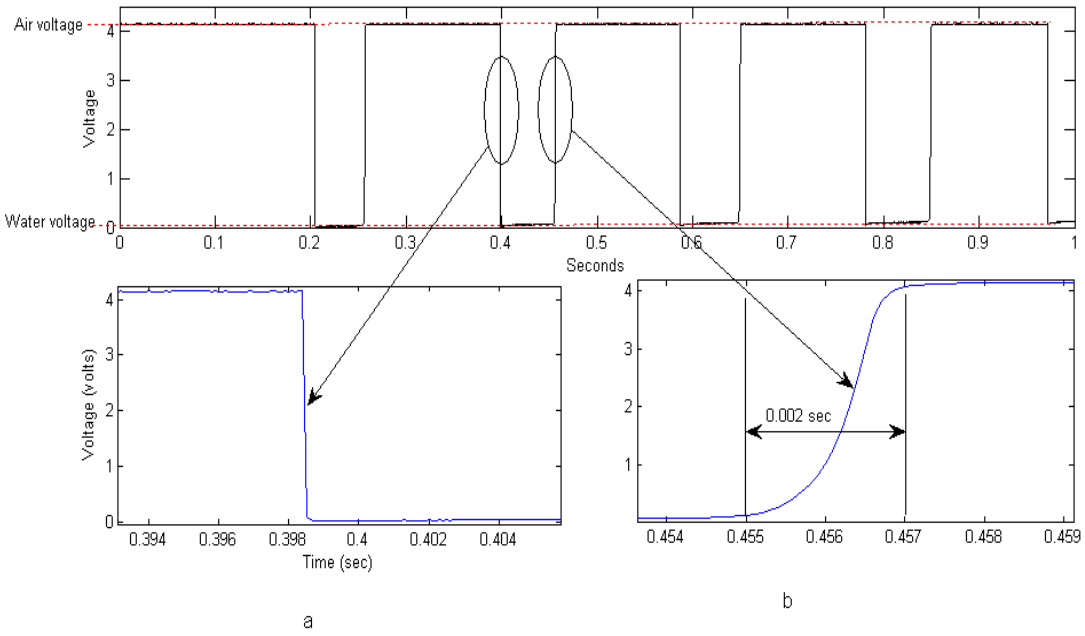

(a) probe connected to the positive terminal

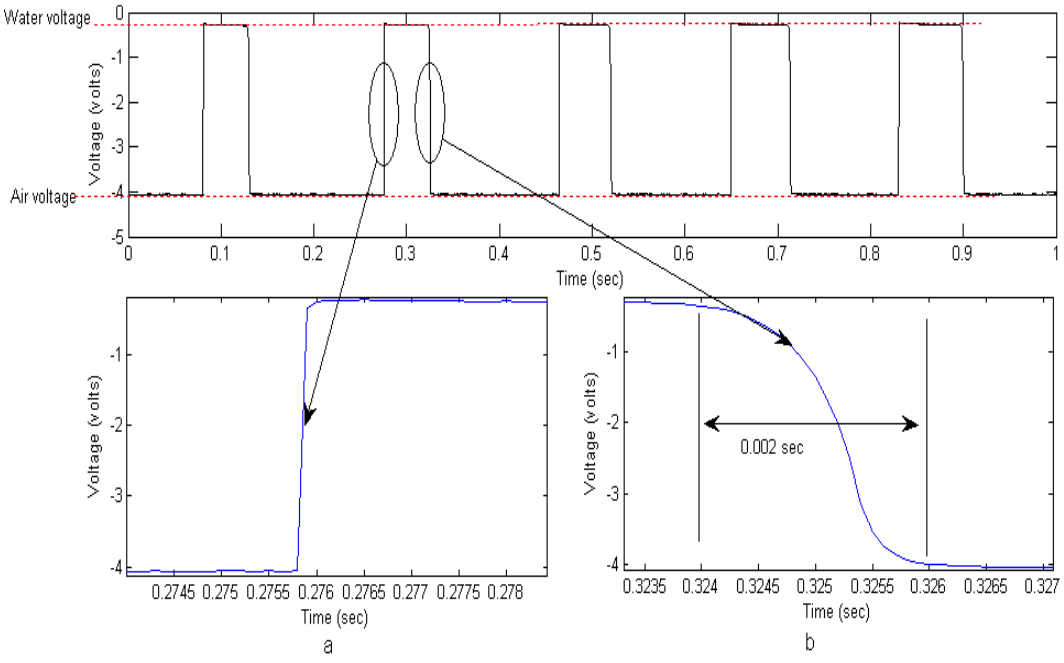

(b) probe connected to the negative terminal

Figure 4.5: Conductivity probe response as it is moved in and out of water at regular intervals (a) probe connected to the negative terminal (b) probe connected to the negative terminal.

4.4.1.1 Discussion: Air-water (Bubble air-bubble lamella simulation) experiment

The behaviour of the signal as the probe was moved out of water was unexpected. A sharp response similar to the one observed when the probe comes in contact with water was expected. A number of postulations were made to explain this observation viz. (i) Effects of polarisation and the slow discharge of a capacitor that is set between an electrolyte and electrode. (ii) Viscous effects of the water which results in formation of a water bridge that rapidly thins and breaks as the probe is removed from the water

4.4.1.1.1 Discharge of polarisation capacitance set between an electrolyte and electrode

When an electrode is immersed in an electrolyte, a potential is set up between the two phases. The spatial arrangement of the charge round each electrode commonly known as an electrical double layer is formed because of a number of reasons among them includes charge transfer between the liquid-solid interface. The interface can be viewed as consisting of voltage source (E), which emanates from the half-cell electrode potential which is in series with polarisation capacitance (C) as a result of the double layer and a polarisation resistance (R), (Khandpur, 2003). This depiction of the interface was first formulated into a circuit model by Warburg (1899). It was later modified to include a Faradic leakage resistance (Rf) as shown in Figure 4.6.

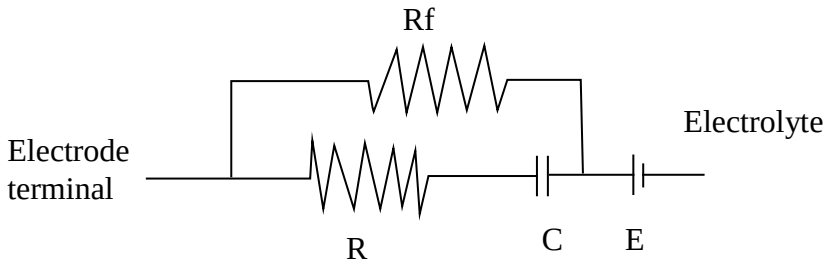

Figure 4.6: Modified Warburg model for an electrode/electrolyte interface after Khandpur (2003)

The time constant RC (Figure 4.6) that is formed at the interface governs the discharge rate of the formed capacitor and therefore determines the response time of the signal as the probe is moved out of the water. The discharge of a capacitor follows an exponential decay curve. This is a possible reason why there is a sluggish

response as the probe moves out of water. It is important to note that the sharp response observed when the probe comes into contact with water is not affected by this time constant (RC) as the double layer is formed when the probe is already in contact with the electrolyte.

4.4.1.1.2 Viscous effects of the water which result in a thin film/sheath of water following the probe as it moves out of water.

It is possible that when the probe is moving out of water a thin film of water will remain attached to the probe and it thins out as the distance between the probe and the surface of the water increases until it eventually breaks this is referred to as the drag-out problem (Wilson, 1982). As this sheath of water thins out its resistance increases, thus a gradual increase in voltage may be observed. This concept was tested by cutting the conducting wire, instead of pulling it out of water. Cutting the wire while the conducting part was still in water precludes the formation of the water bridge while creating open circuit condition. Results from these experiments are shown in Figure 4.7. By cutting the probe, the response time was reduced by 50% when compared to pulling it out i.e. reduction from 2milliseconds to 1millisecond. This value is still larger than the 0.1milliseconds that the circuit takes to respond when the probe is coming in contact with water. From these results it obvious that the water bridge formed around the probe contributes significantly to the response time, although it does not totally account for sluggish response that is observed. It is thus suggested that the response is a combination of viscous effects of water as well as the discharge of the polarisation capacitance that is set between the conducting wire and the electrolyte.

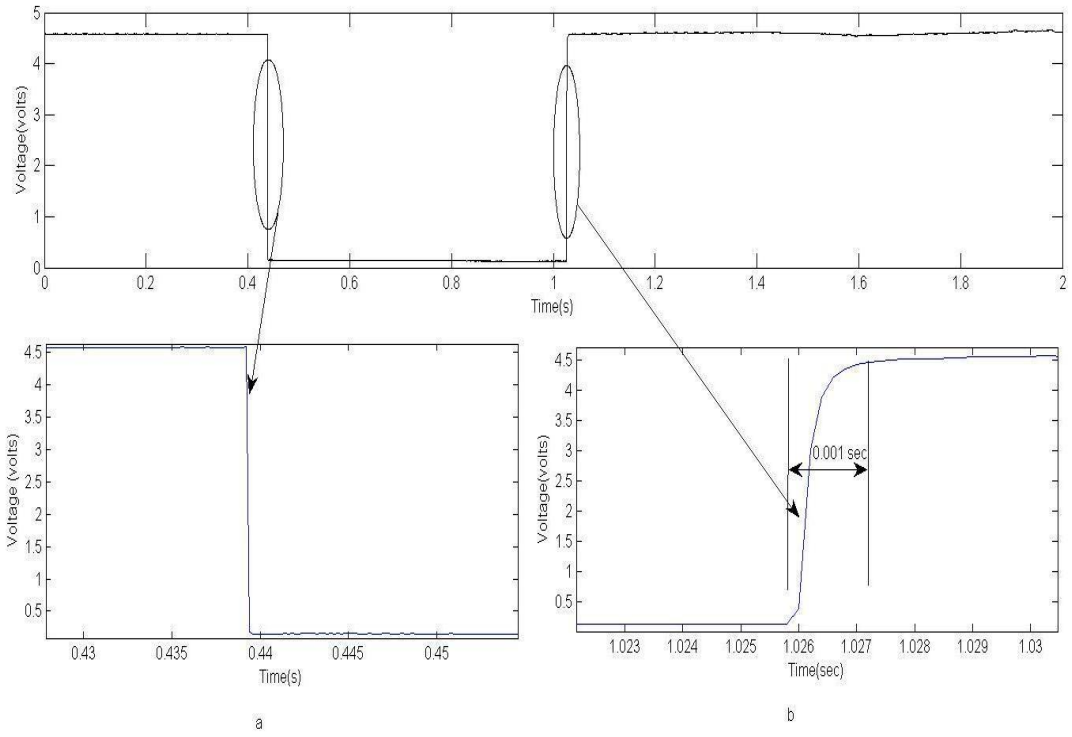

Figure 4.7: Bubble-sizer response when the conducting wire is moved out of water by cutting it.

Although the slow response may interfere with vital information that can be used in characterising bubbles, results shown in Figure 4.5 are of great importance to the quest of using electrical conductivity to estimate froth bubble sizes. A rapid change in the output voltage signal as it comes in contact with water and sluggish response as it comes out of water/comes in contact with air, can act as a signature that can be used to trace times when the probe was in contact with a bubble lamella and when it was not. Two successive sharp changes in a signal would represent two consecutive entries into bubble lamellas. This information is vital in the estimation of froth bubble sizes as the length between two successive bubble lamellas is related to the bubble size. Consequently analysis of the signal from the bubble sizer then involves identification of these sharp drops previously defined as points of significant impact and calculating time between successive impacts. These times together with the velocity of the probe would then be used to calculate the intra-bubble impact distance (IID).

4.4.2 Mini-flotation column results

4.4.2.1 Bubble sizer results obtained using 0.0075M CuSO4 (aq) as the pulp phase

For the bubble-sizer circuit to be able to follow the rapid changes in electrical conductivity that take place as the conductivity probe cuts across the froth phase, the water/slurry should contain a significant amount of ions to increase its electrical conductivity. Consequently these tests involved addition of copper (II) sulphate to 8 litres of water in the flotation column to make 0.0075 mol/litre solution. Since the probe is made out of copper metal, Cu^{2+} ions were chosen to be in solution to create Cu/Cu^{2+} electrode which has a well-known electrode potential and is also very common reference electrode. Air flowrate to the flotation column was maintained at 8.5 l/min resulting in a froth height of 11.7 cm. The conductivity probe was dropped 10 times into the flotation column from a height of 22 cm above the surface of the froth. Concurrently, still pictures of the froth were taken at shutter speed of 1/60 using a Samsung ES90 digital camera. Figure 4.8a shows the typical signal that was obtained after each drop when the sampling rate was set at 40kS/second while Figure 4.8b is the derivative of the signal plotted as a function of the time. Triggering of the signal started when the probe touched the surface of the froth, therefore it can also be used to calculate velocity changes within the froth. Noticeable in Figure 4.8a are the sharp consecutive drops marking the points of significant impact. The length between two successive points defines intra-bubble impact distances (IID). A closed circuit voltage (when probe was in contact with water) of 0.145volts was recorded; because of the high ion content, bubble lamella voltages were also dropping to the closed circuit voltage. Calculating the derivative of the signal and plotting it as a function of time as shown in Figure 4.8b enhances the points of significant impact and enables their identification. Superimposed on Figure 4.8b are asterisks marking the points of significant impact on the signal derivative. The differences in time between successive points of significant impact were taken as the time to travel from one bubble lamella to next bubble lamella. It was used to calculate IIDs. A cutoff threshold value of 500V/second was used as a basis to determine the points of significant impact. This value means that a change in voltage of 0.0125volts in two consecutive samples can be identified as having been caused by impact with a bubble surface. This threshold value is dependent upon the conductivity of the pulp/water and the sampling frequency set on the card and the susceptibility of the signal to noise. A matlab script shown in appendix C was used to perform the above

calculations. Identification of the points of significant impact was done by a matlab function file which is a slight modification of the open source version peakdet (http://www.billauer.co.il/peakdet.).

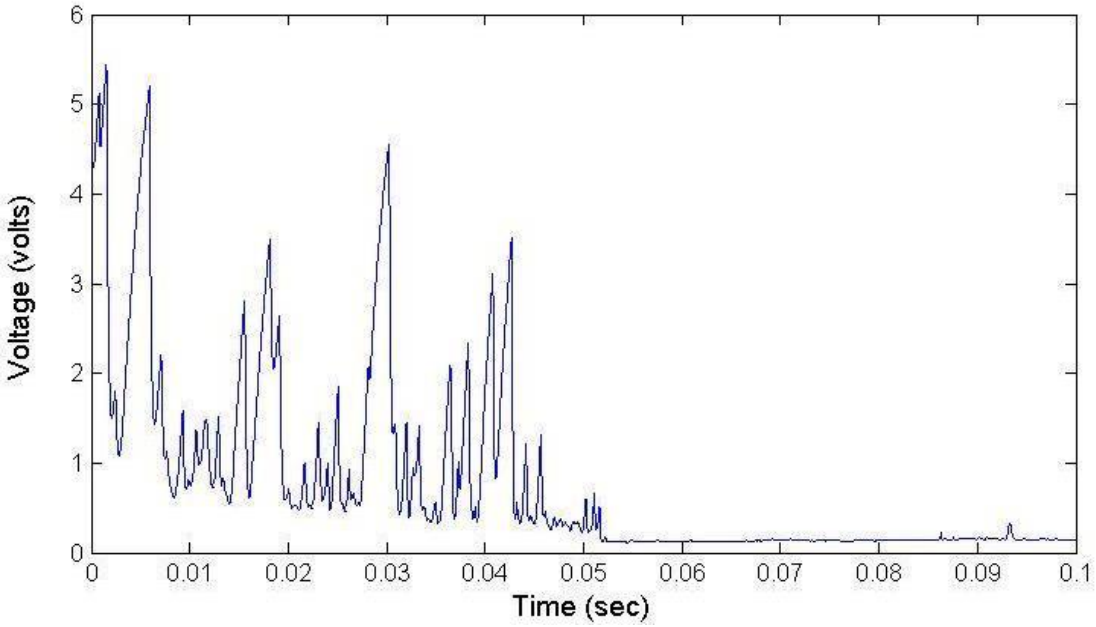

a) Signal

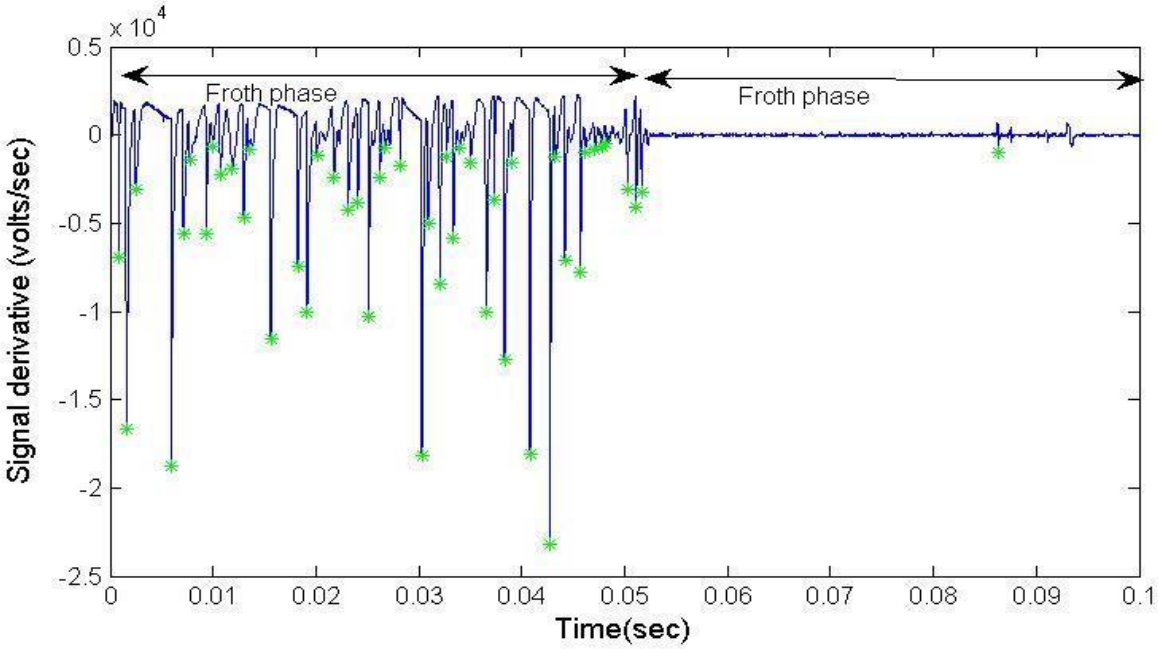

b) signal derivative

Figure 4.8: Typical bubble-sizer signal (a) and its derivative (b) when bubble size measurements are taken in 0.0075M copper sulphate solution.

Estimation of froth bubble sizes using the current froth bubble-sizer is based on the assumption that there is a relationship between the IIDs obtained using the bubble-sizer and the actual froth bubble sizes. The relationship is such that, if the bubble-sizer probe is dropped several times into the froth phase and it is cutting through consecutive bubbles, the average IID per given depth below surface of the froth shall always be less than or equal to the Sauter-mean bubble diameter provided that the probe does not pass through vertical Plateau borders. Vertical Plateau borders are defined as those Plateau borders that are parallel to the direction of motion of the probe. If the probe passes through these Plateau borders, the estimated IIDs will be greater than or equal to actual bubble sizes. The assumption can also be interpreted as stating that for a given froth, with fixed depth, fixed aeration and chemical conditions and at steady state, the average IID will reflect the average size of bubbles at a certain height above the pulp-froth interface regardless of whether the probe passed through vertical Plateau borders. To assess the variation in bubble sizes as a function of froth depth, the 11.7cm deep froth was divided into 5 segments. In each segment, an average IID was calculated for each drop and results are shown in Figure 4.9. By averaging the IID per segment for the drops a global average per segment was then calculated and Figure 4.10 shows the results obtained. From Figure 4.10, an increase in IID from the pulp-froth interface to the surface of the froth that follows a linear trend is observed. This general increase in the average IID as a function of height above the pulp-froth interface was expected as bubble coalescence results in an increase in froth bubble sizes as a function of height above the pulp-froth interface. Although the average of many drops show this trend (Figure 4.10), analysis of the averages of individual drops indicated that the trend is not always linear; the average IID of a segment lower can be higher than the one above it as shown in Figure 4.9, but the cumulative effect of several drops will reveal the trend shown in Figure 4.10. The gradient of Figure 4.10 can also provide vital information on bubble coalescence. Its gradient shows that on average bubbles sizes are changing at a rate 0.136mm for every 1cm change in froth depth, thus it can be used as well for assessing rate of bubble coalescence.

In addition to providing a global average for a segment, IID distributions (IIDD) can also be obtained from the bubble-sizer data. As an illustration, the froth was divided into two sections each 5cm deep i.e. the first segment was 5cm from above the pulp-froth interface and the second segment represented the remainder of the froth up to the surface. IIDs were then obtained for each segment and compared. Figure 4.11 shows the IIDD while Figure 4.12 is cumulative IID curve. Both graphs reveal that the

5-10cm segment has a coarser IID with an IID80 (intra-bubble distance at which 80% of all IIDs are less than or equal to) of 2.75mm when compared to 1.75mm IID80 for the 0-5cm segment. This agrees with prior knowledge (Ata et al., 2003) of flotation froths i.e. bubble size distribution (BSD) near the top of the froth exhibits a coarser P80 when compared to P80 of the bubbles near the pulp-froth interface. Thus this illustration reinforces the baseline assumption that a relationship exists between IIDs and actual froth bubbles sizes

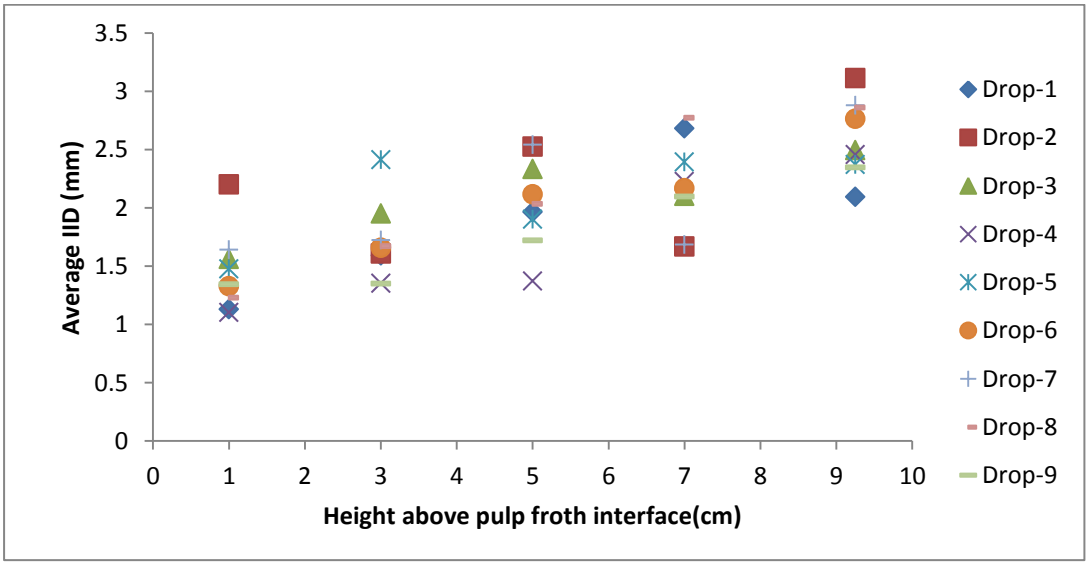

Figure 4.9: Average IID (individual drops) as a function of height above the pulp-froth interface

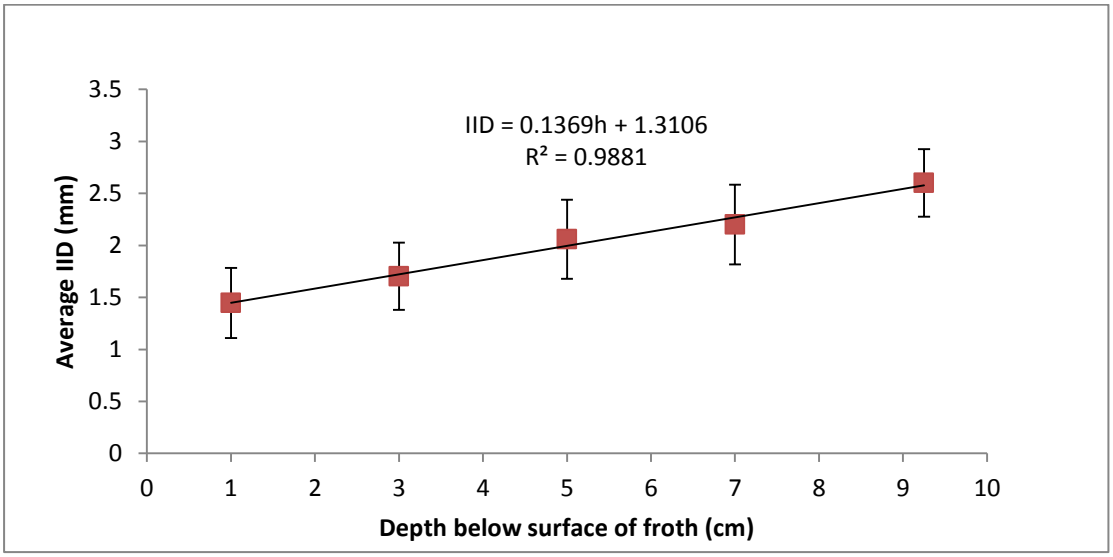

Figure 4.10: Average IID (nine drops) as a function of height above the pulp-froth interface for 0.0075M CuSO4 solution

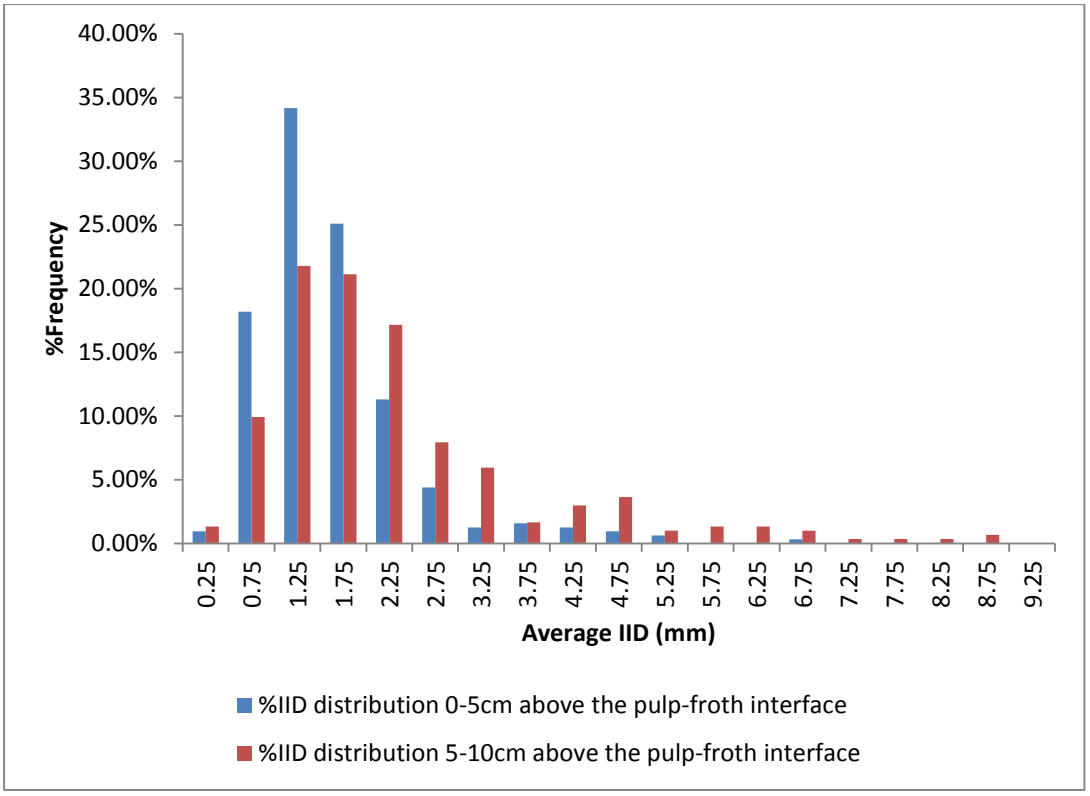

Figure 4.11: IID distribution for the two froth segments

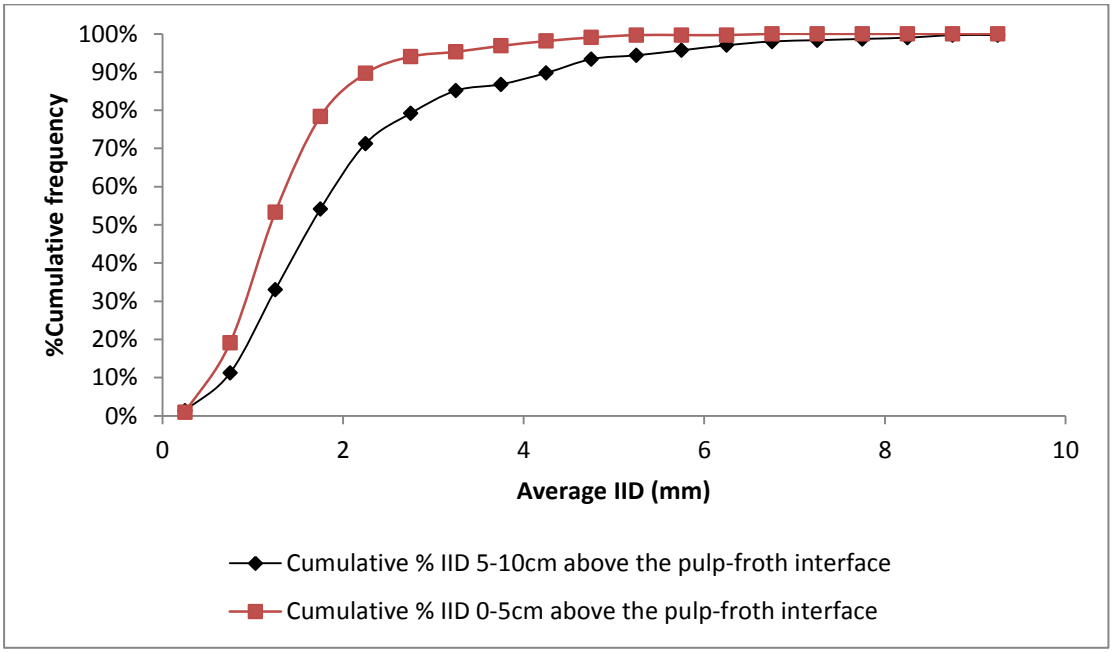

Figure 4.12: Cumulative IID distribution for the two froth segments

4.4.2.2 Photographic results of actual froth bubble sizes

To enable comparison of the two methods, photographs of the froth that were taken concurrently with the measurement of froth bubble sizes using the new technique

were analysed. An open source image analysis software ImageJ (http://imagej.nih.gov/ij/, 1997-2012) was used to analyse photos that were taken using a digital camera. Measurement of bubble sizes was done manually, and the number of bubbles measured per each photograph ranged between 150 and 350 depending on the number of bubbles contained in each picture. The number of bubbles contained in each picture depended on the size distribution of the bubbles; froth pictures closer to the pulp-froth interface containing more bubbles than pictures of the froth closer to the froth surface because the former are smaller. Results presented in this section compare froth bubbles sizes as a function of height above the pulp-froth interface. Figure 4.13 is an illustration of how bubble sizes were determined for a given segment of the froth.

It is important to note that the froth was divided into five segments, and a Sauter-mean bubble diameter (d_{32}) was calculated from the bubble size distribution data in each segment and results are shown in Figure 4.14. The Sauter-mean bubble diameter (d_{32}) was defined as a volume to surface mean diameter and was calculated from equation [4.2]. It is important to note that there is a sampling bias which would tend to exaggerate the relative number of large bubbles estimated from an image made at a surface of observation; however the size of the bubbles did not vary over a wide range so this problem was ignored.

$$d_{32} = \frac{\sum n_i d_i^3}{\sum n_i d_i^2} \qquad [4.2]$$

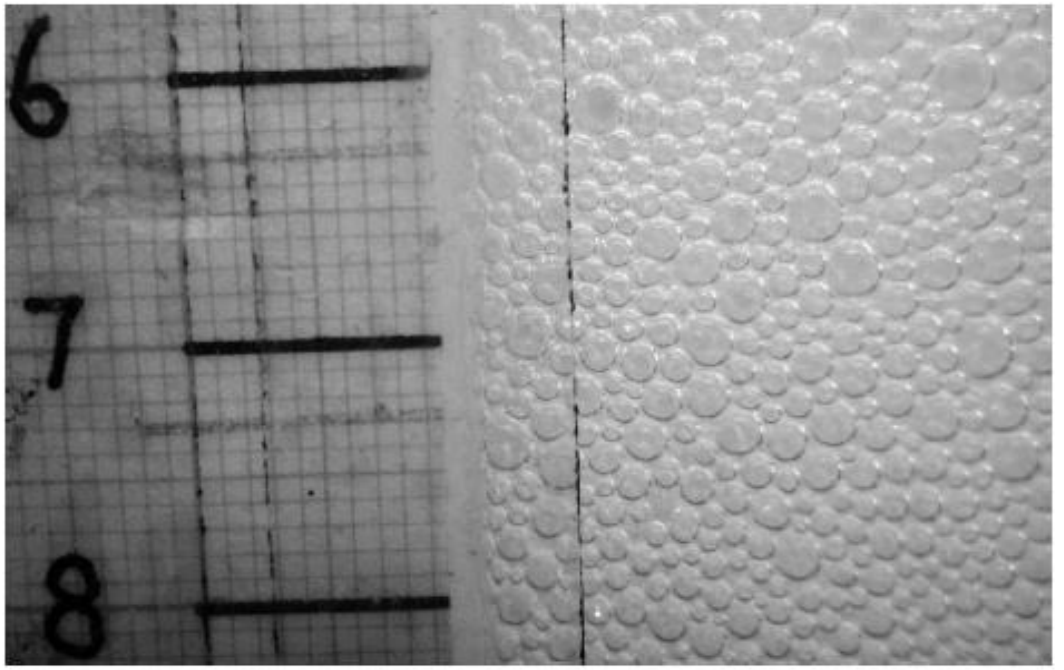

a

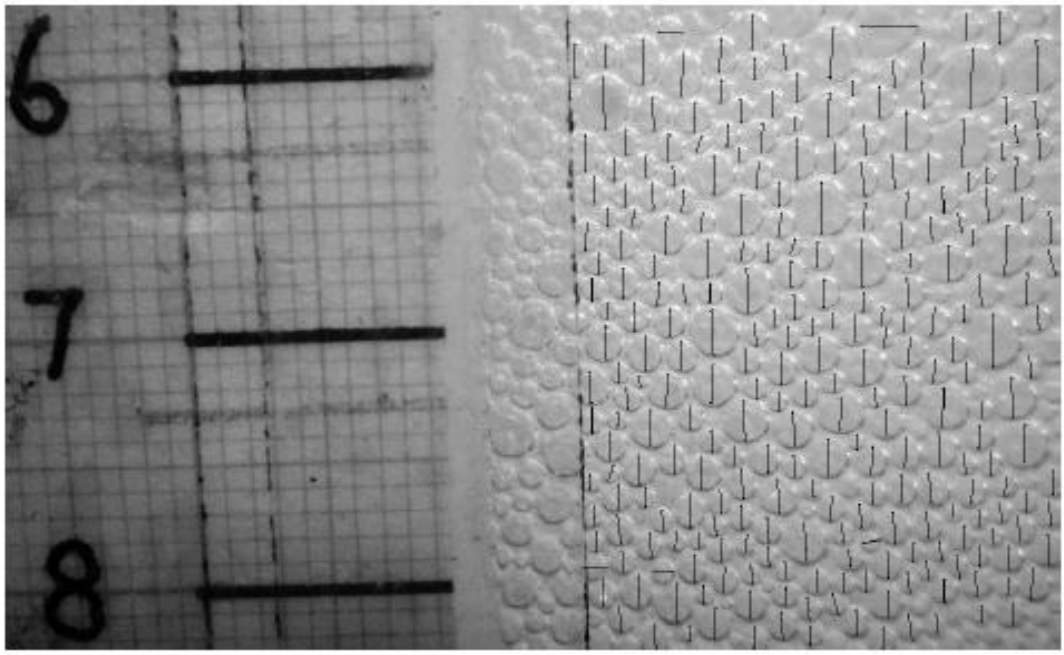

b

Figure 4.13: Illustration of manual bubble size measurement using ImageJ with lines indicating measured diameters

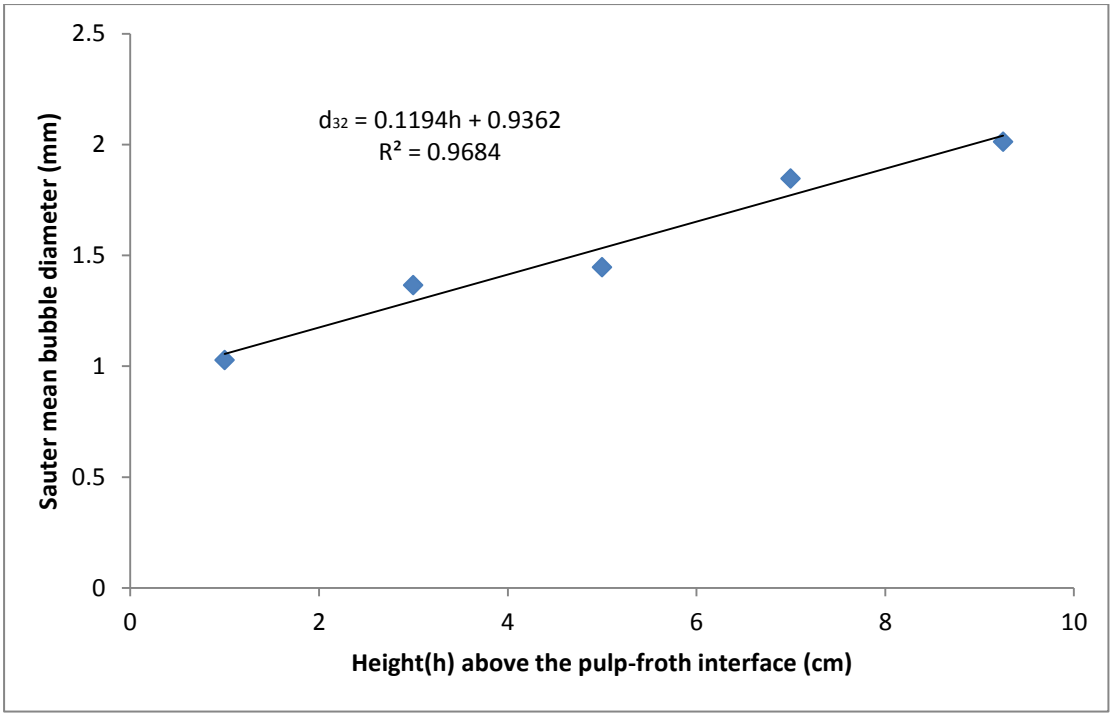

Figure 4.14: Sauter-Mean bubble diameter obtained using the photographic method as a function of froth depth.

As was expected, the Sauter-mean bubble diameter obtained shows an increase in bubble size as the height from the pulp-froth interface increases (Figure 4.14). The increase also follows a linear trend with a correlation coefficient of 0.98 with a rate of bubble size change with respect to height above pulp-froth interface of 0.119 mm/cm. The BSD obtained in each segment was plotted and results are shown in Figure 4.15, this graph also supports the existence of a coarser bubble size distribution in segments closer to the surface of the froth.

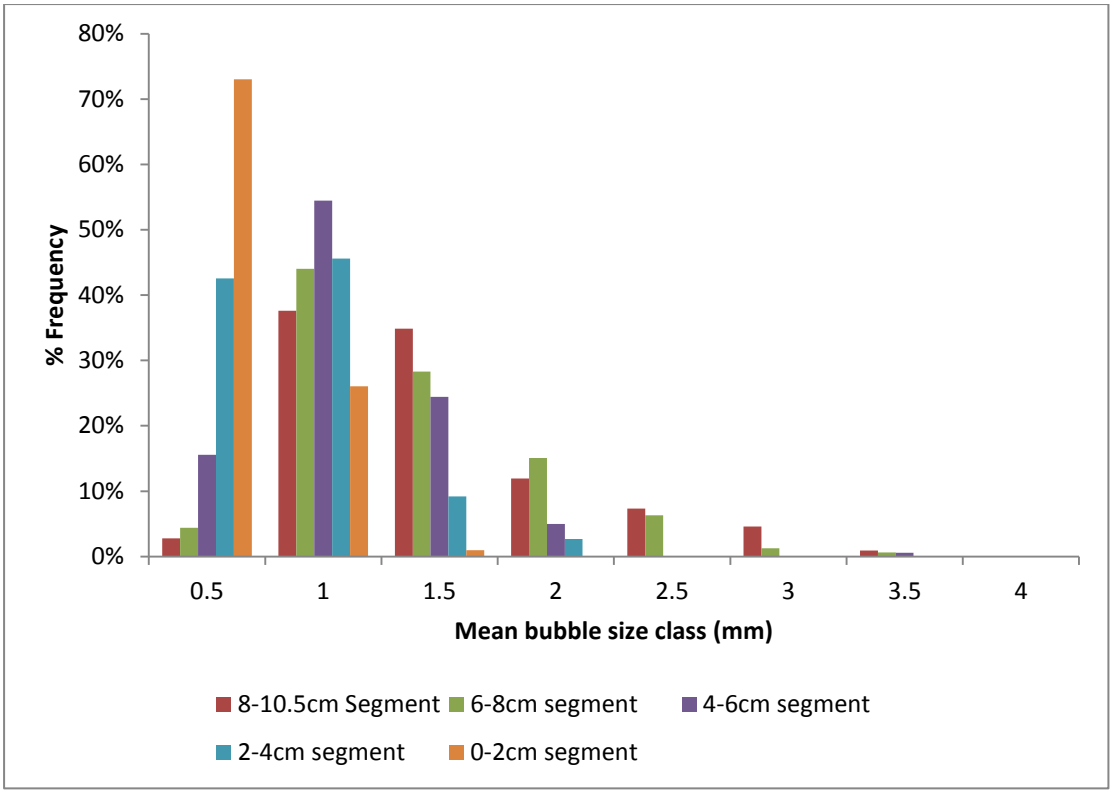

Figure 4.15: Comparison of bubble size distribution (BSD) in froth segments

4.4.2.3 Comparison of IIDs to actual froth bubble sizes

Analysis of results done in the above section has shown that the froth bubble-sizer is able to measure the changes in bubble sizes that take place in the froth phase. This section compares the IIDs obtained from the bubble-sizer to actual bubble sizes obtained from image analysis. Figure 4.16 is a plot of average bubble size obtained by each method as a function of height above the pulp-froth interface. As can be seen, the average IID is higher than the Sauter-mean bubble diameter for all froth segments. This result indicates that the conductivity probe maybe passing through vertical Plateau borders resulting in increase in the distance between points of significant impact. Further investigation of this possibility is done in section 4.4.2.4. Despite the overestimation of bubble sizes by the froth bubble sizer, a strong relationship exists between the IID and Sauter-mean bubble size. This relationship suggests that as the average IID increases the Sauter-mean bubble diameter also increases. Comparison of the rate of change of IID with respect to height above the pulp-froth interface and the rate of change of the Sauter-mean diameter with respect to height above the pulp-froth interface shows a 15% difference.

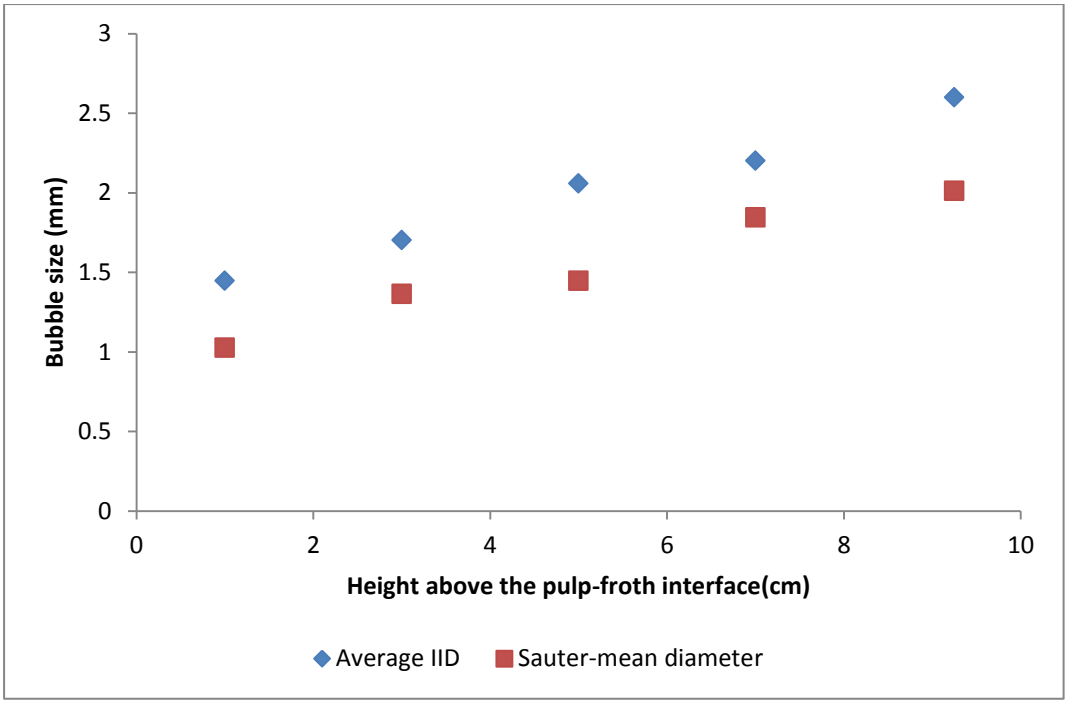

Figure 4.16: Comparison of the bubble-sizer IID and the Sauter-mean diameter

4.4.2.4 Discussion of froth bubble size measurement

The two methods used to estimate froth bubble sizes were able to show the general increase of froth bubble sizes as a function of height from the pulp-froth interface. The BSD and cumulative IID indicated a coarser distribution in the segments that are closer to the surface of the froth. In general results from the froth bubble size measurement campaign have confirmed that froth bubble sizes can be determined using the new technique. Both methods were successful in capturing the changes in bubble sizes above the pulp-froth interface albeit the new technique showing higher values than the photographic method. In this section an attempt to explain this is made. Two propositions that may have resulted in larger IIDs when compared to the Sauter-mean bubble diameter are advanced viz. (i) slowing down of the probe inside the froth phase, which results in it taking a longer to cut across the known froth height (Hf) than predicted by the equations of motion. If the probe slow down the result is an overestimation of probe velocity when equations of motion are used to calculated probe velocity. (ii) It is also possible that the probe may pass through vertical Plateau borders as it cut across the froth. This length of the Plateau border is considered as part of the IID.

4.4.2.4.1 Probe velocity overestimation

Work by Le Goff et al. (2008) has shown that the velocity of small spheres slows down when they are dropped into foam films. Their initial experiments on a single film indicated that the slowing down of velocity is insignificant. However, when the spheres where dropped into several parallel films (bamboo foams) slowing down and eventual stopping of the spheres was observed. Factors such as mass of the sphere and initial velocity played a critical role in determining the number of foam films that should be crossed before the sphere can be stopped. The maximum sphere mass they was used in their work was about 17mg which is approximately 4780 times lighter than the mass of the probe used in bubble size estimation. If we assume that the probe is slowing down within the froth then the acceleration part on the equations of motion should be less the gravitational acceleration in the froth. Measured values of drop height (Hd), froth height (Hf) and time from the output voltage signal were used to calculate acceleration inside the froth. The value of this acceleration was found to be 3.2% lower than the acceleration due to gravity indicating that indeed the probe was slowing down. Velocity profiles were recalculated using this new acceleration and compared to the velocity assuming no froth resistance, results obtained are summarised in Figure 4.17. As can be seen, the differences in velocities are minute; calculations showed that values predicated when froth resistance was considered were between 0 and 0.7% lower than values predicted assuming no froth resistance. Thus the error introduced by neglecting froth resistance effects is negligible and cannot be solely responsible for the overestimation of IIDs.

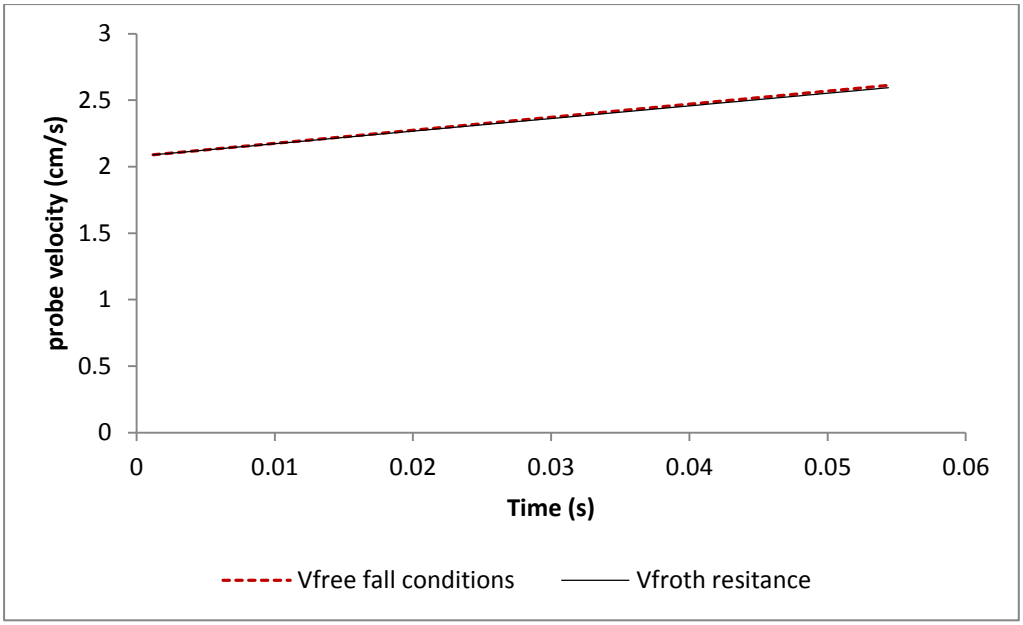

Figure 4.17: Comparison of probe velocity inside the froth when (a) free fall conditions are assumed and (b) when froth resistance is taken into account.

4.4.2.4.2 Conductivity probe passing though vertical Plateau borders.

According Fuerstenau et al. (2007), the width of Plateau borders is in the order of millimetres thus it is possible that the probe may pass through a vertical Plateau border. This will result in the length of the Plateau border being taken as part of the IID resulting in higher values when compared to Sauter-mean diameter. To test this theory, a digital bubble size measurement that simulates the operation of the bubble-sizer was performed. This involved drawing random vertical lines that cuts through a given section in the photographs and manually identifying points of significant impact. The vertical lines that are drawn through the picture represent possible trajectories that the conductivity probe would take when dropped into the froth. On each of these lines, points of significant impact are identified manually and the distance between them is taken as the IID. Figure 4.18(i) illustrates the simulation done on pictures that were taken. By closely looking at Figure 4.18(i), the marked points of significant impact provide two kinds of IIDs. Points that are labelled (b) on Figure 4.18(i) represent chords i.e. those defined as a line that crosses the circumference of a circle on two different points. IIDs labelled with a letter (a) have an additional length provided by the vertical Plateau borders in which the probe has traversed as shown in Figure 4.18(ii). This additional length results in higher average IID and thus average IIDs may also be higher than the measured Sauter-mean diameter. It is important to note that, an infinite number of lines can be drawn per each segment

and these lines determine the values of the average IID. Thus it was important that those trajectories that were drawn on each picture are random. The number of IIDs averaged per segment ranged from 56 to 120 depending on bubble sizes in each segment. Variation of IID with froth height results from the simulation experiments are shown in Figure 4.19 while comparison of the photographic method, the actual bubble-sizer technique results and the bubble-sizer simulation results are shown in Figure 4.20. The rate of change of IID is 0.126mm/cm which is comparable to 0.119mm/cm obtained with the actual bubble-sizer. From Figure 4.20, it can be observed that the Sauter-mean diameter is less than the bubble-sizer simulation average IIDs for all froth segments. The simulation average IIDs are slightly lower than the bubble-sizer results possibly because the manual determination of points of significant impact is not as accurate as the bubble-sizer.

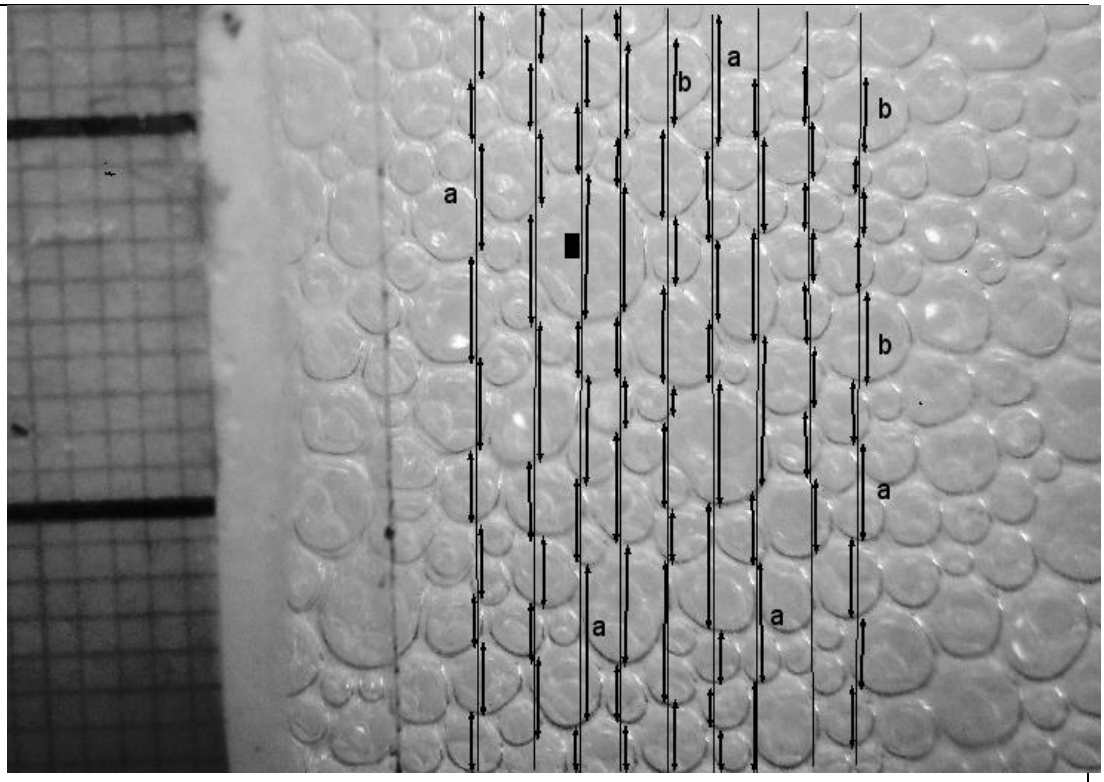

(i) Illustration of the simulation of froth bubble-sizer bubble measuring procedure, with continuous vertical lines representing bubble-sizer trajectory for each drop and double arrow lines representing IIDs.

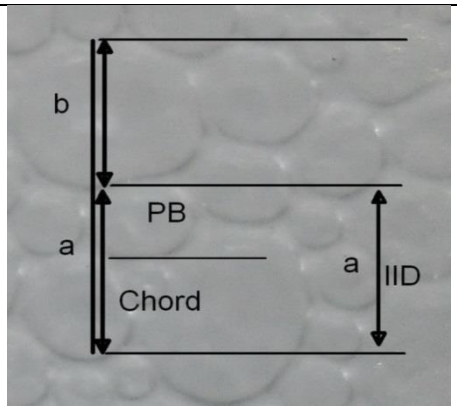

(ii) Pictures showing that IIDs of type (a) in (i) above is a sum of vertical plateau border (PB) travelled by the probe and the chord length of the next bubble it cuts across.

Figure 4.18: Illustration of the simulation of the new bubble size measuring technique with emphasis of the different kinds of IIDs

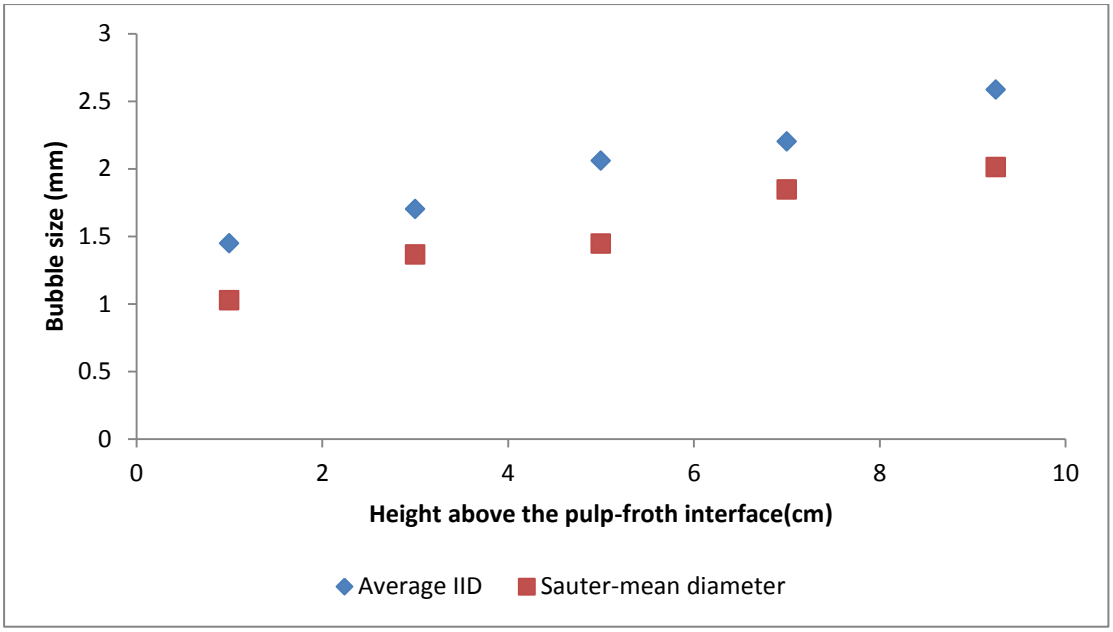

Figure 4.19: Variation of average IIDs with froth height resulting from bubble-sizer simulation experiments

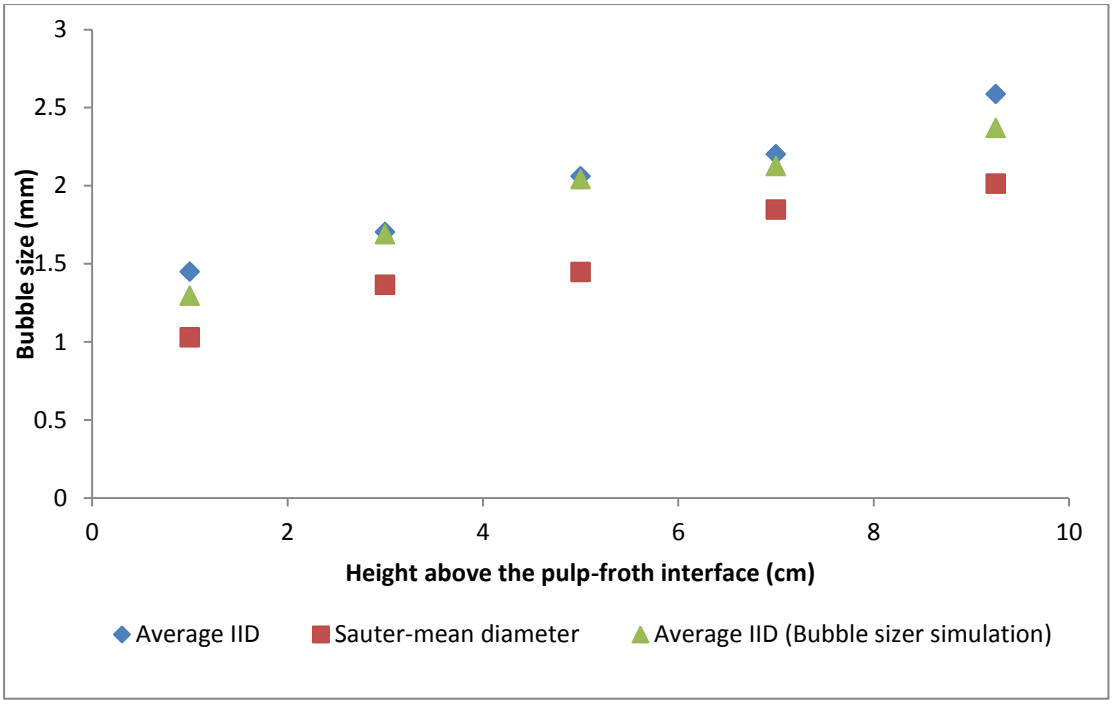

Figure 4.20: Comparison of the average IIDs obtained with (i) the simulation experiments and (ii) the actual bubble size measurement with (iii) the Sauter-mean diameter obtained using the photographic method.

Although the notion of the conductivity probe travelling in vertical Plateau borders is a plausible explanation of the over estimation of bubble size by IIDs, it is crucial to point out that other additional factors may also be responsible for this observation. For example, after presenting this work at the flotation 2013 conference, Dr Neethling

of imperial college, London suggested that the values of the Sauter-mean diameter calculated from photographic are an under estimation of the actual bubble sizes. His argument is that what we consider as bubble diameters for bubbles close to the wall in a froth are in fact cords and not diameters if we consider spherical bubbles. Plateau borders between consecutive bubbles are excluded and the wall of the flotation cell is left out when manually measuring bubble sizes. Consider Figure 4.21 for example; it is easy to see that the distance represented by D represent the actual diameter of the bubble while dB exclude the Plateau border formed between adjacent bubbles and the wall, and is smaller than the actual bubble size. The Length dB is what was measured when determining Sauter-mean diameter.

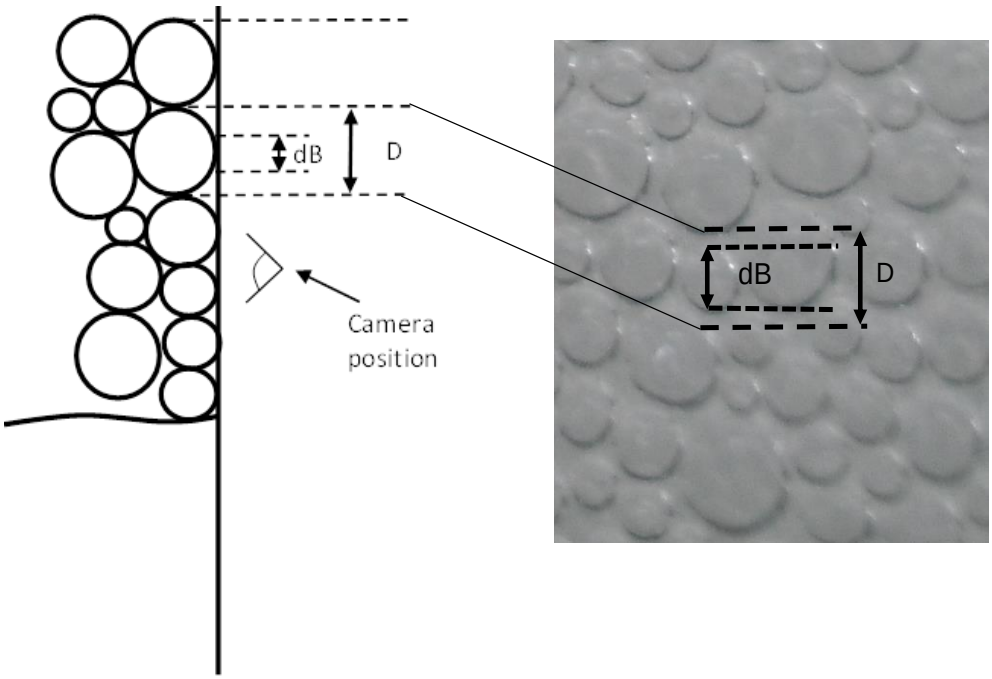

Figure 4.21: illustration of how Sauter-mean diameter estimated from photographs under-estimates the actual bubble sizes.

4.5 Summary

A new method to infer froth bubble sizes using the difference in electrical conductivities of air and slurry/liquid phase has been developed. Comparison of the new technique to the photographic method revealed that the new technique over-estimates the Sauter-mean diameter by up to 31%. An explanation for the overestimation was advanced and tested. Although the new technique was able to

capture the general increase in froth bubble sizes as a function of froth depth, it underestimated the bubble size growth rate as a function of height above the pulp-froth interface by about 15%. Despite the fact that the new technique does not give actual values of bubble sizes, its ability to provide trends that are related to bubble size and coalescence in the froth can play a vital role in froth phase sub-process understanding and optimisation. The information obtained using the froth bubble-sizer may be vital in assessing elusive froth properties such as froth stability, possibly by comparing the average IID just above the interface to the average IID just below the froth surface.

4.5.1 Further remarks on froth bubble size measurement

The froth bubble-sizer's operating principle requires that the water that constitutes the bubble films should have a higher electrical conductivity than the air contained within the bubble. The conductivity of water varies with the amount of dissolved ions, thus this technique can be sensitive to the chemical composition of the water in the froth so it is important that this technique be evaluated under different water chemical compositions. The effect of the presence of solids on the bubble lamellae needs to be assessed, thus results in section 4.6 of this Chapter focus on such assessments.

4.6 Effect of pulp chemistry and froth solids content on the measurement of a proxy for froth phase bubble sizes

4.6.1 Introduction

Testing of this electro-resistive technique reported in this Chapter so far was carried out on a two phase system (air and water) with the froth being generated from water containing copper sulphate. Results reported established that IIDs are related to froth bubble sizes. IID was defined as the distance between points of significant impact. Points of significant impact were defined as those points in the output signal where there is a sharp drop in voltage i.e. where the probe has made contact with a liquid film. All measurements of froth bubble sizes were done in a solution containing significant amounts of dissolved copper ions, which increased the electrical conductivity of the liquid films. The high ion content may have enabled the bubble-sizer circuit to follow the minute changes in voltage as the probe cuts across the froth.

The bubble-sizer is intended to work in an environment that may not contain Cu^{2+} ions, but other dissolved metallic ions. To establish whether the new technique works on froths with various chemical compositions and still produces reliable results i.e. an output signal amenable to bubble size estimation, the bubble-sizer needs to be tested in pulps/water of different chemical composition. The minimum ion content that can guarantee observable changes in electrical conductivity in froth bubble size measurements will occur in froths formed by distilled water, but obviously minimum froth content will be required to stabilise the froth. If results obtained are comparable to the photographic method, then it can safely be concluded that the new technique would work in an industrial froth of any chemical composition.

Results presented in this section were obtained from measurements using tap water and Sodium hydroxide (NaOH) solutions and were evaluated against results obtained using copper sulphate as reported in section 4.4. Further experiments to test whether the presence of solids on bubble lamellas would affect the results were done using slurry containing 2%w/w CaCO3; solids content was kept low to avoid solids interference with froth photographs. Further tests on the effect of solids were carried out in a mechanical flotation cell with 20 %w/w pulp solids content resulting in froth with on average 9%w/w solids content.

4.6.2 Froth bubble size measurement results obtained using water

Water dosed with Cu^{2+} ions produced average IIDs that were comparable to Sauter-mean bubble sizes obtained using the photographic method. Addition of $CuSO_4$ played an important role in that it increased the conductivity of water and reduced polarisation through the reversible reaction of the $Cu(s)/Cu^{2+}$ at the electrode. This may have enabled the circuit to follow the minute changes in voltage as the probe passes through the froth.

In this section the experiments with tap water with mean electrical conductivity of 23.85±4.64mS/m dosed with Dowfroth at a rate of 20mg/l of water are presented. Figure 4.22a shows the typical signal that was obtained after each drop when the sampling rate was set at 40kS/second. Figure 4.22b is its derivative plotted as a function of the time. Noticeable in Figure 4.22a are the sharp consecutive drops marking the points of significant impact similar to those found when measurements were done on froth generated from copper sulphate solution. A closed circuit voltage of 0.995volts was obtained; it is higher than the 0.145volts reported for 0.0075M for

copper sulphate solution. Another notable difference between signal obtained with 0.0075M copper sulphate solution (Figure 4.8a) and Figure 4.22(a) is that the closed circuit voltage is reached only when the conductivity probe is already in the pulp whereas in the copper sulphate solution case, some point of significant impacts in the froth also recorded the closed circuit voltage. These differences merely reinforce the fact that the electrical resistance of water is higher than the copper sulphate solution resistance. From the derivative of the signal, points of significant impact were identified and IIDs calculated. The 11.7cm deep froth was also divided into 5 segments each 2.3cm deep and average IID was calculated for each drop on each segment and results are shown in Figure 4.23. A global average was then calculated for the six drops and results showing an increase in average IID with froth height are shown in Figure 4.24. A linear fit to the experimental data revealed that the rate of change of bubble sizes under these conditions was 0.10mm/cm.

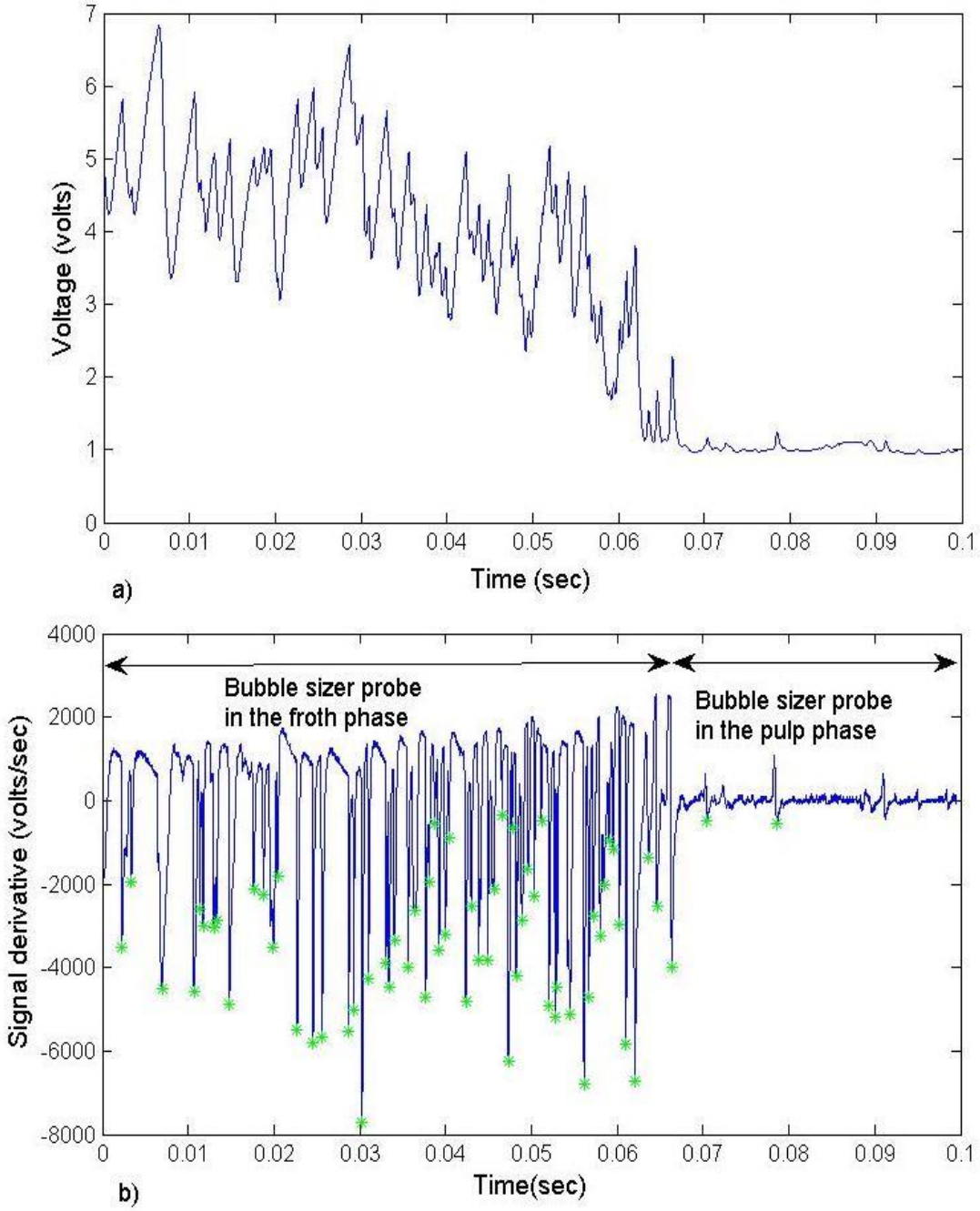

Figure 4.22: Typical signal (a) and its derivative (b) obtained when bubble-sizer probe cuts through froth generated from water dosed with frother.

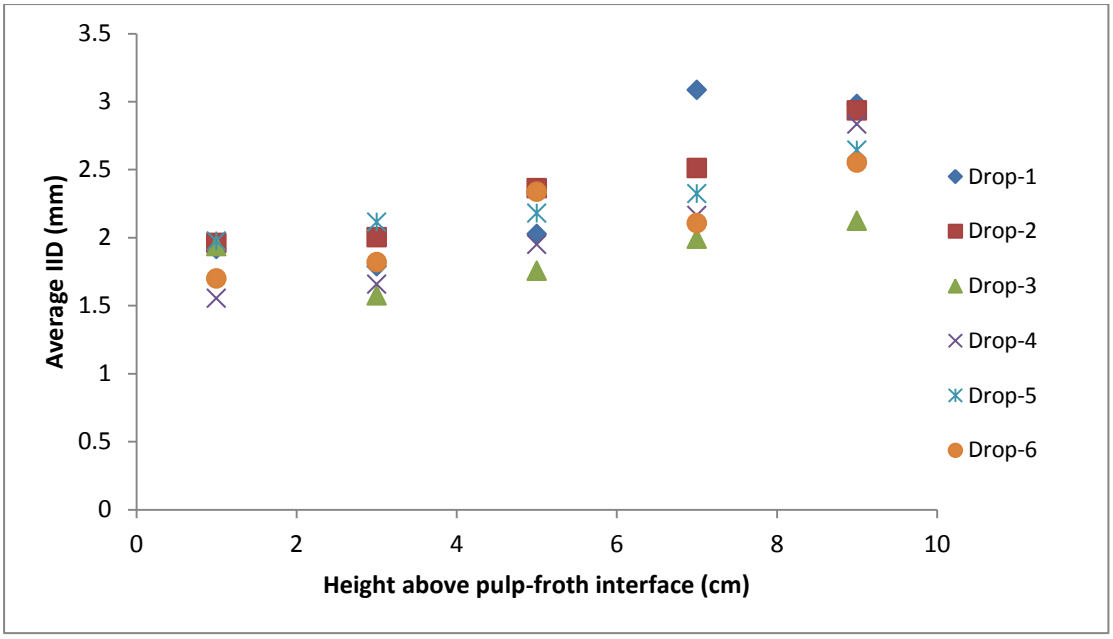

Figure 4.23: Average IIDs for individual probe drops as a function of height above the pulp-froth interface for water dosed with frother.

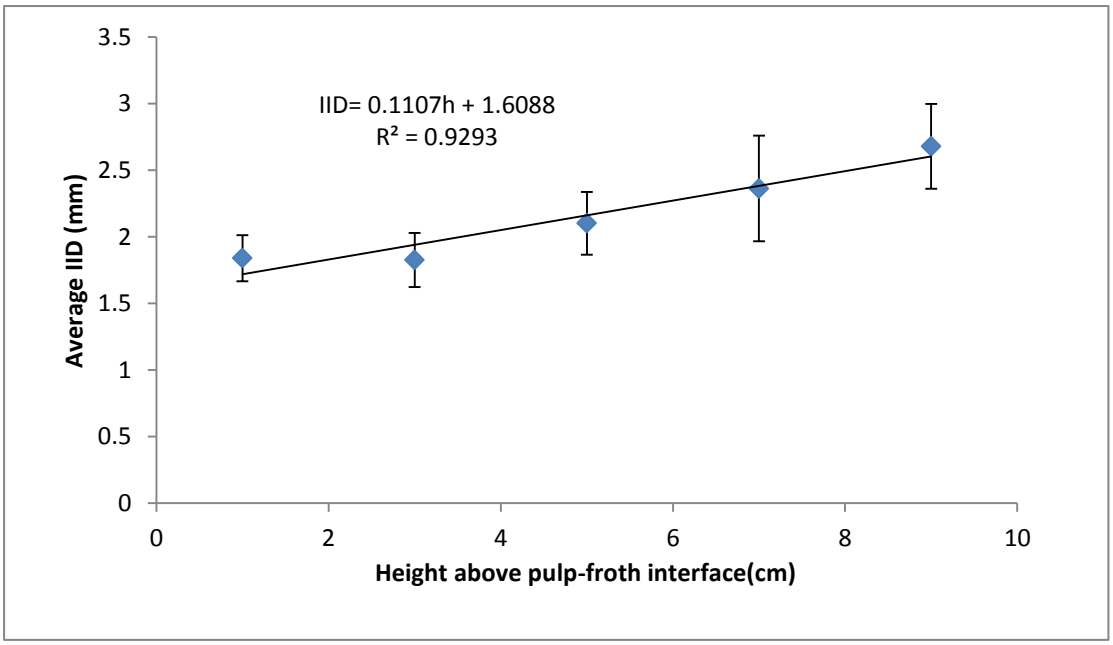

Figure 4.24: Variation of IID with froth height for all the six drops for water.

4.6.2.1 Comparison of average IID to Sauter-mean diameters for water

Actual bubble sizes for water only were manually estimated from pictures using ImageJ an open source software for image analysis according to the procedure described in section 4.4.2.2. A summary of the results are shown in Figure 4.25. As expected, an increase in Sauter-mean bubble diameter as a function of height above

the interface is observed. When estimates of bubble sizes from the photographic method were compared to the average IID by plotting them on the same axis (Figure 4.25), it was observed that the froth bubble-sizer produces average IIDs that are higher than the actual bubble size obtained from the photographic method. The difference (IID and Sauter-mean diameter) per given height above the interface ranging from as low as 5% to 13percent. This observation is consistent with the results obtained when experiments were done with froth generated from 0.0075M CuSO4 solution. The new technique shows the same rate of change in bubble sizes per unit change in froth height i.e. 0.11mm/cm as compared to 0.109mm/cm.

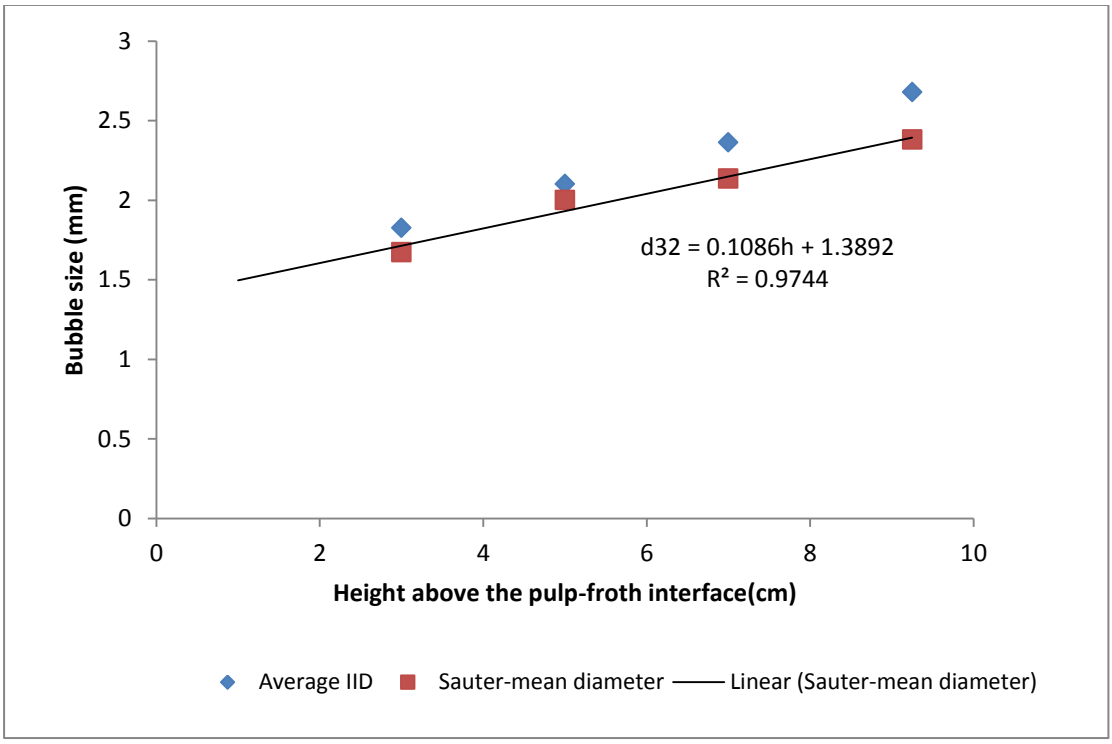

Figure 4.25: Comparison of the bubble-sizer average IID to the Sauter-mean diameter obtained using the photographic method as a function of height above the pulp-froth interface for water dosed with frother.

4.6.3 Froth bubble size measurement results obtained using for 0.0075M NaOH (aq) solution

Froth bubble size measurements were repeated with Sodium hydroxide dosed into the mini-flotation column to form 0.0075M NaOH (aq) solution. Seven drops were made from a fixed height of 24cm and froth height was maintained at 11.7cm above the pulp-froth interface. Signals similar to the one shown in Figure 4.26a were obtained for each drop with a typical derivative shown in Figure 4.26b. Segmentation of the froth into 2.3cm high segments and calculating average IID for each segment

for each drop produced results shown in Figure 4.27. Figure 4.28 is a plot of the global average of the seven drops per each segment above the pulp froth interface. As shown in Figure 4.28, the average IID per each 2.3cm froth segment above the pulp-froth interface shows a general increase in average IID as a function of height above the pulp-froth interface. A rate of change of bubble size of 0.11mm/cm is measured with a degree fitness value of 0.93 and errors bars shown are based on standard deviation.

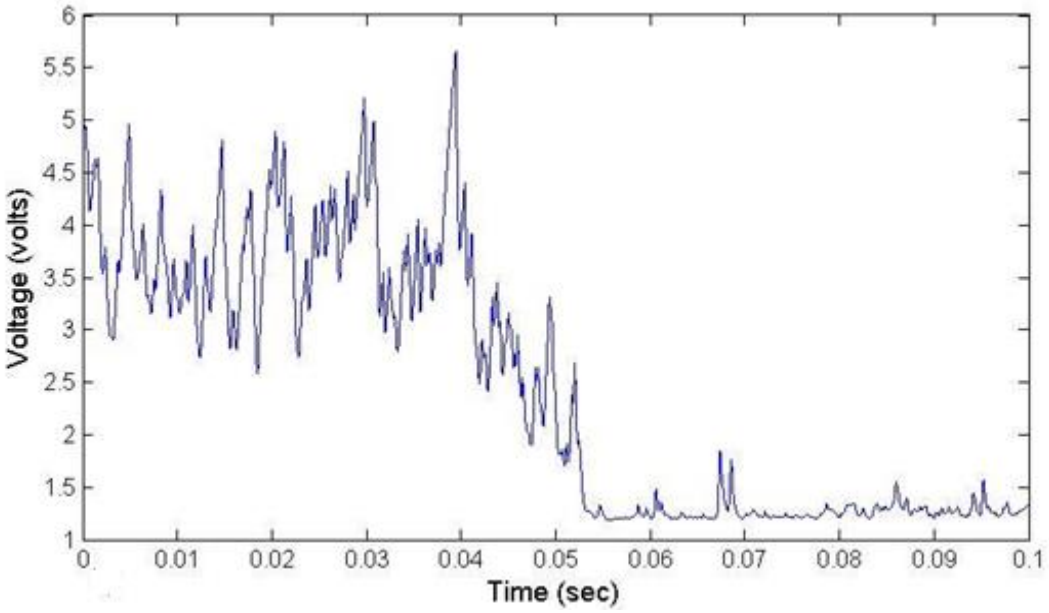

a) signal

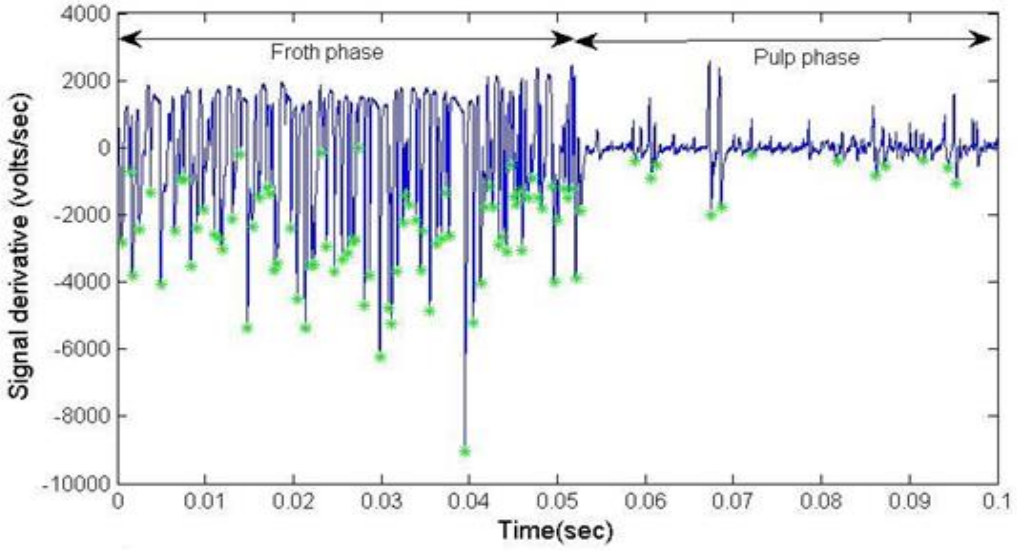

b) Signal derivative

Figure 4.26: Typical bubble-sizer signal (a) and its derivative (b) when bubble size measurements are taken in 0.0075M NaOH (aq) solution.

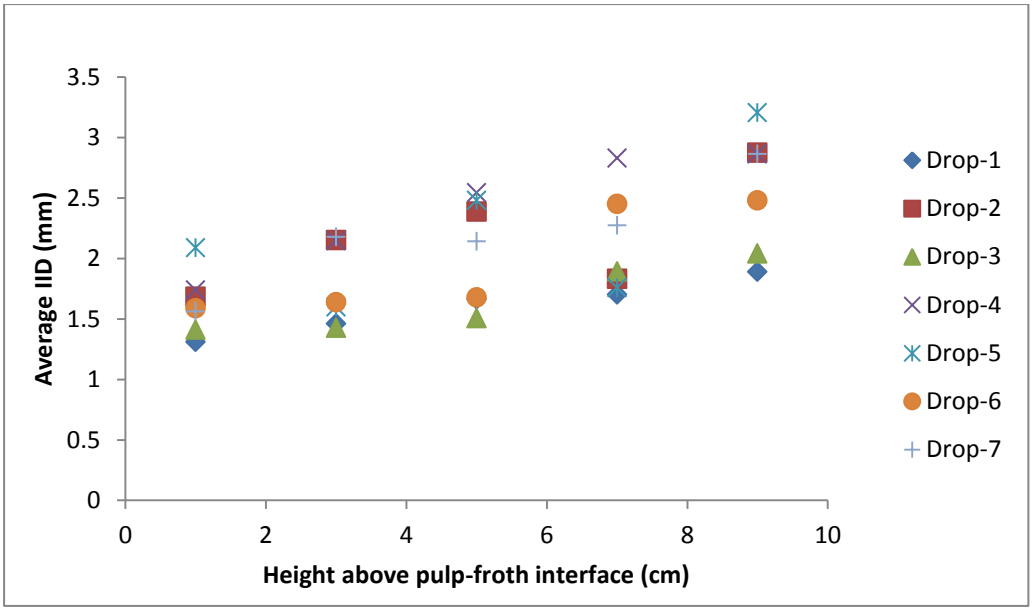

Figure 4.27: Average IIDs for individual probe drops as a function of height above the pulp-froth interface for 0.0075M sodium hydroxide solution.

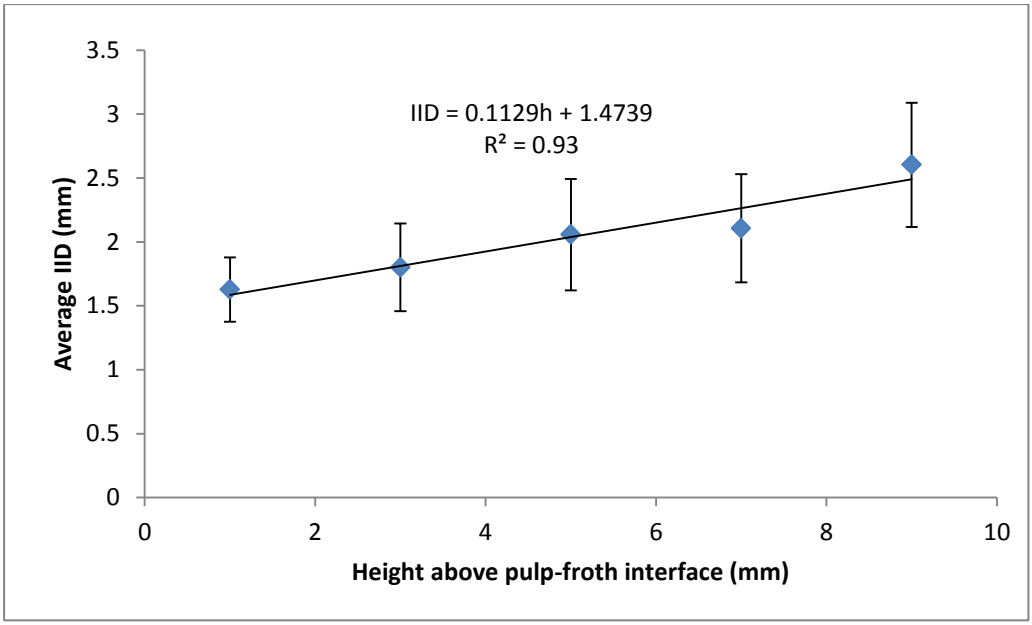

Figure 4.28: Variation of IID with froth height for all the six drops for the 0.0075M Sodium hydroxide solution

4.6.3.1 Comparison of average IID to actual froth bubble sizes for NaOH solution

Sauter-mean bubble diameters for NaOH solution were estimated from photographs and Figure 4.29 shows how Sauter-mean diameter varies with height above the pulp-froth interface. A linear correlation with a correlation coefficient of 0.99 and a rate of

change of bubble sizes of 0.12mm/cm is observed. When estimates of bubble sizes from the two techniques were compared by plotting them on the same axis (Figure 4.30) it is again observed that the froth bubble-sizer produces average IIDs that are higher than the actual bubble size obtained from the photographic method. The percentage difference per each point above the pulp-froth interface ranging from as low as 2% to as high as 19 percent.

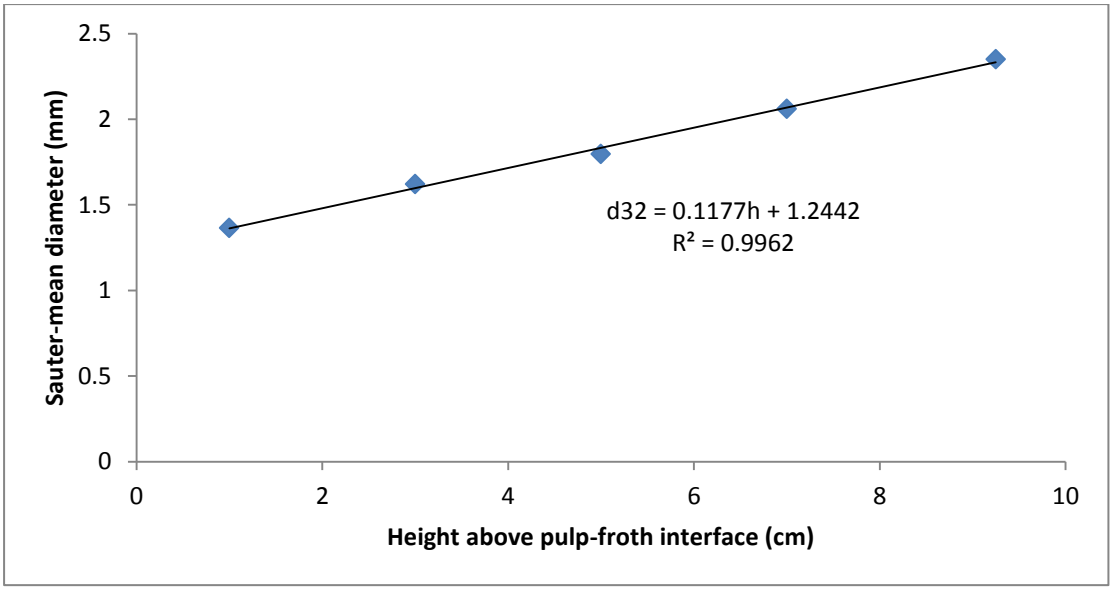

Figure 4.29: Variation of Sauter mean diameter (d32) with height above pulp-froth interface for NaOH (aq) solution.

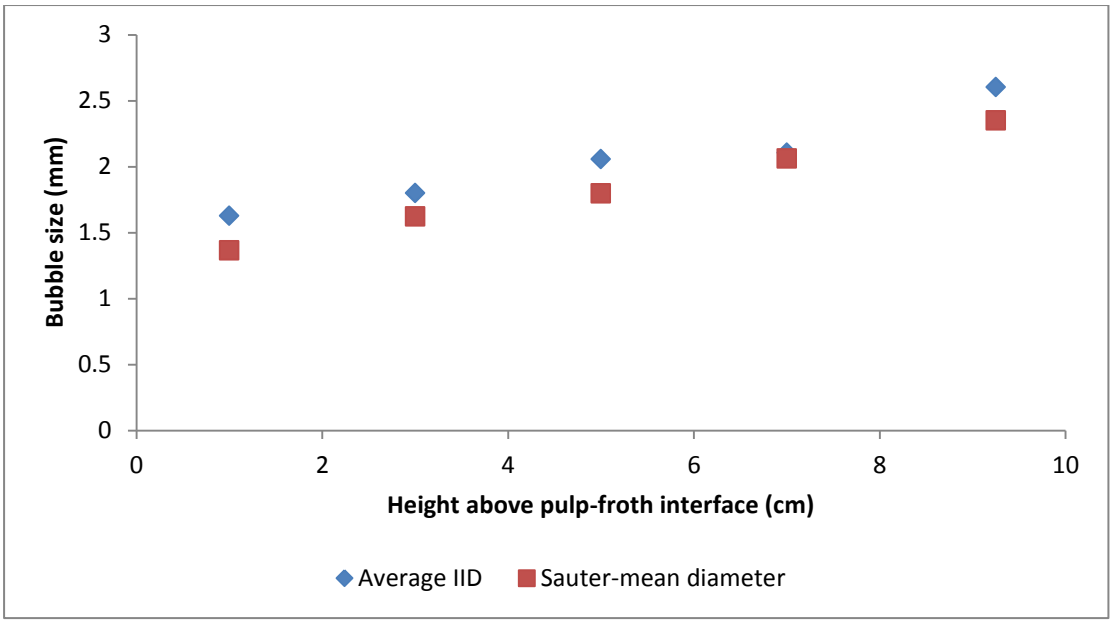

Figure 4.30: Comparison of the bubble-sizer average IID to the Sauter-mean diameter for NaOH solution.

4.6.4 Bubble size measurement results obtained using 2%w/w limestone as the pulp phase

Limestone was added to 8 litres of water dosed with frother in the test column to form a 2% solids content pulp phase. Low solids content was chosen in order to obtain pictures with clearly defined bubbles. Nine drops were made; each with a typical bubble-sizer signal as shown in Figure 4.31(a) while Figure 4.31(b) is the derivative of the signal showing the turning points/impact points. Plots of average IID per each 2.1 cm segment above the pulp-froth interface for each probe drop are shown in Figure 4.32. Figure 4.33 is a plot of the average for all the nine drops per each segment as a function of froth height. Both graphs show a general increase in average IID as height is increased above the pulp-froth interface, which is consistent with the froth bubble coalescence theory and results obtained with copper sulphate and water. The rate of change of bubble sizes with height of 0.08mm/cm was observed. This low rate of change of IID when compared to water that observed for water (0.11) and sodium hydroxide (0.11) points to the possible froth stabilising effect of limestone particles resulting in low bubble coalescence.

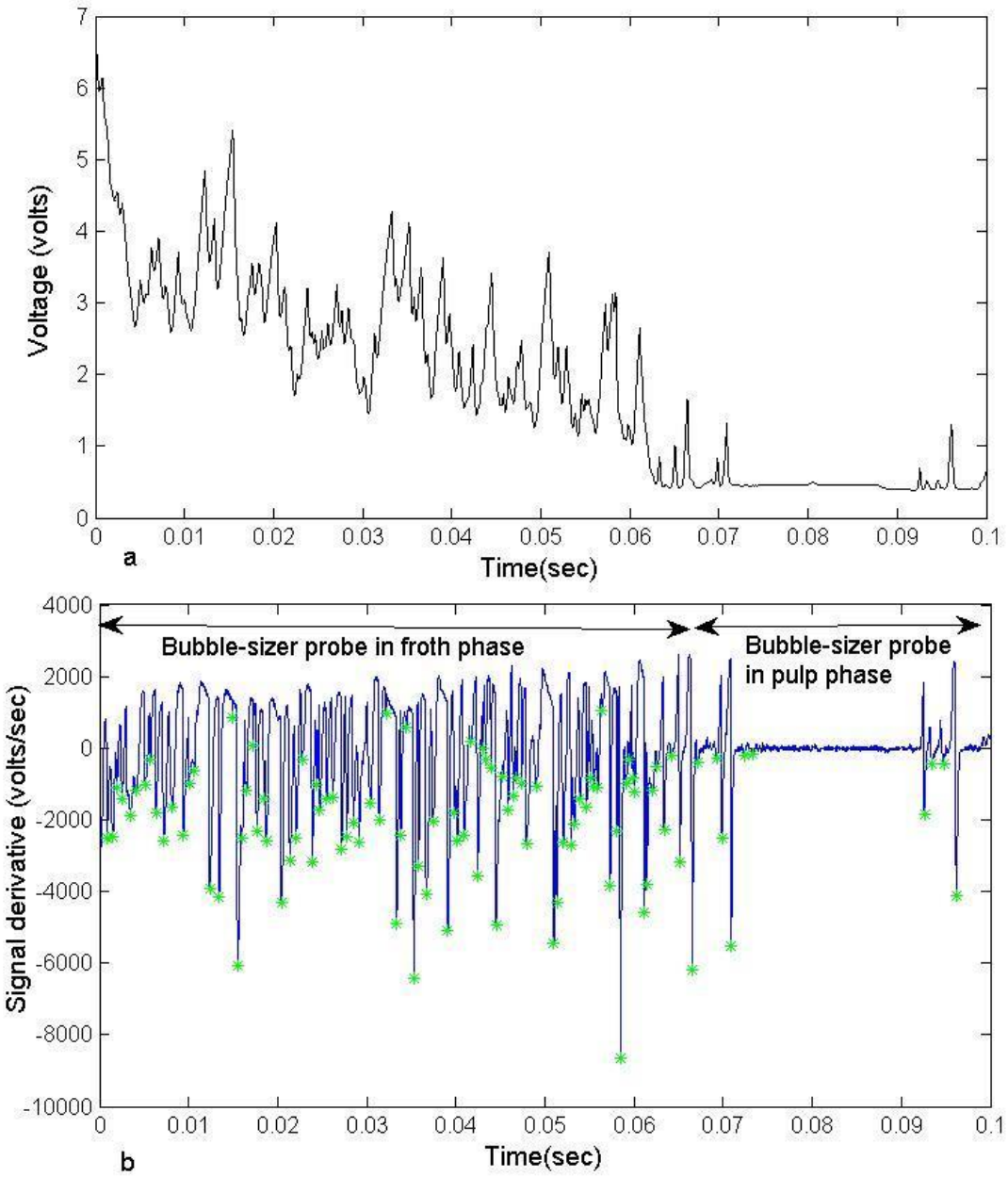

Figure 4.31: Typical signal (a) and its derivative (b) obtained when bubble-sizer probe cuts through frother (2% limestone solids content).

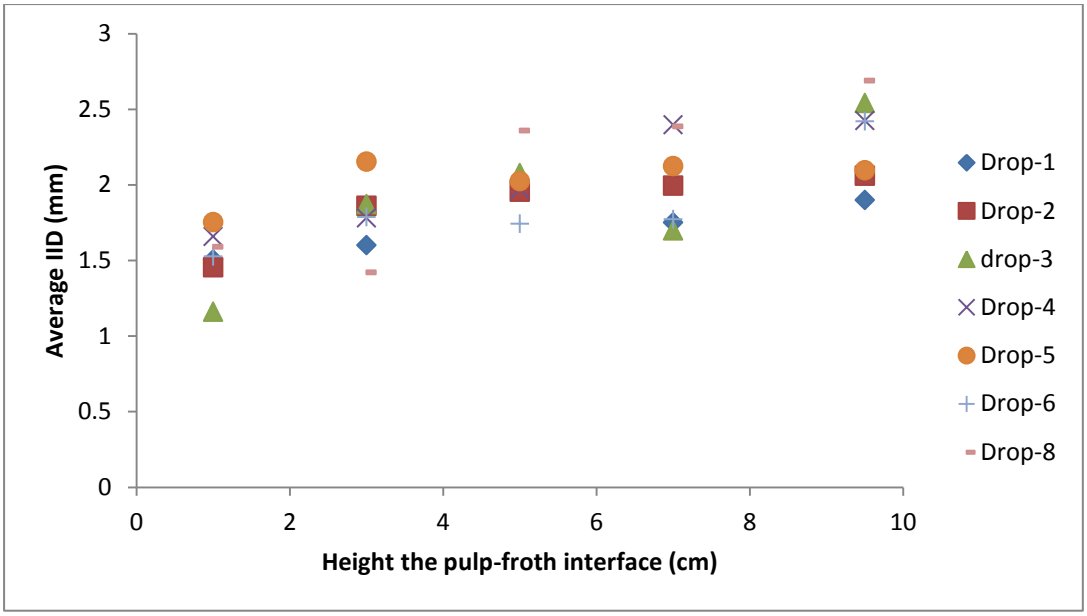

Figure 4.32: Average IIDs for individual probe drops as a function of height above the pulp-froth interface for 2% limestone pulp phase

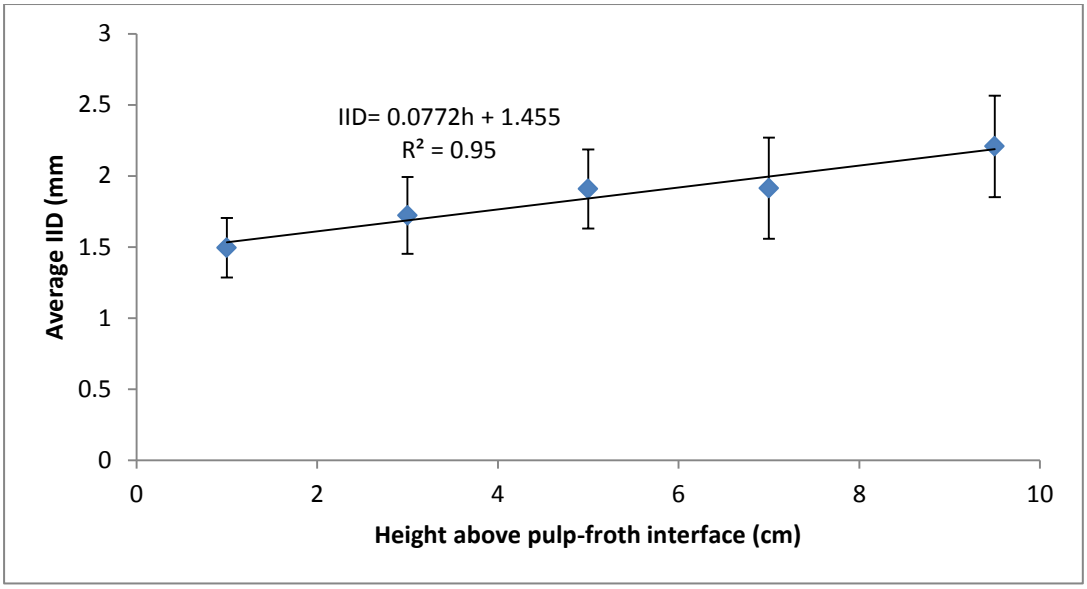

Figure 4.33: Variation of IID with froth height for all the eight drops for 2%limestone pulp

4.6.4.1 Comparison of IIDs to actual froth bubble sizes for 2% limestone pulp phase

A summary of bubble sizes as obtained from the photographic method under the above conditions is given by Figure 4.34; which then compares the Sauter mean diameter to the IIDs in each froth segment. Comparison of the Sauter-mean bubble diameter to the average IID confirms that the average IID per segment is higher than

the actual bubble size as obtained by the photographic method with the deference per segment ranging from 15% to 30percent. The rate of change of bubble sizes with height for the photographic method is 0.077mm/cm which is higher than that obtained by using the new froth bubble-sizer. A plot of Sauter-mean diameter as a function of average IID is shown in appendix B.

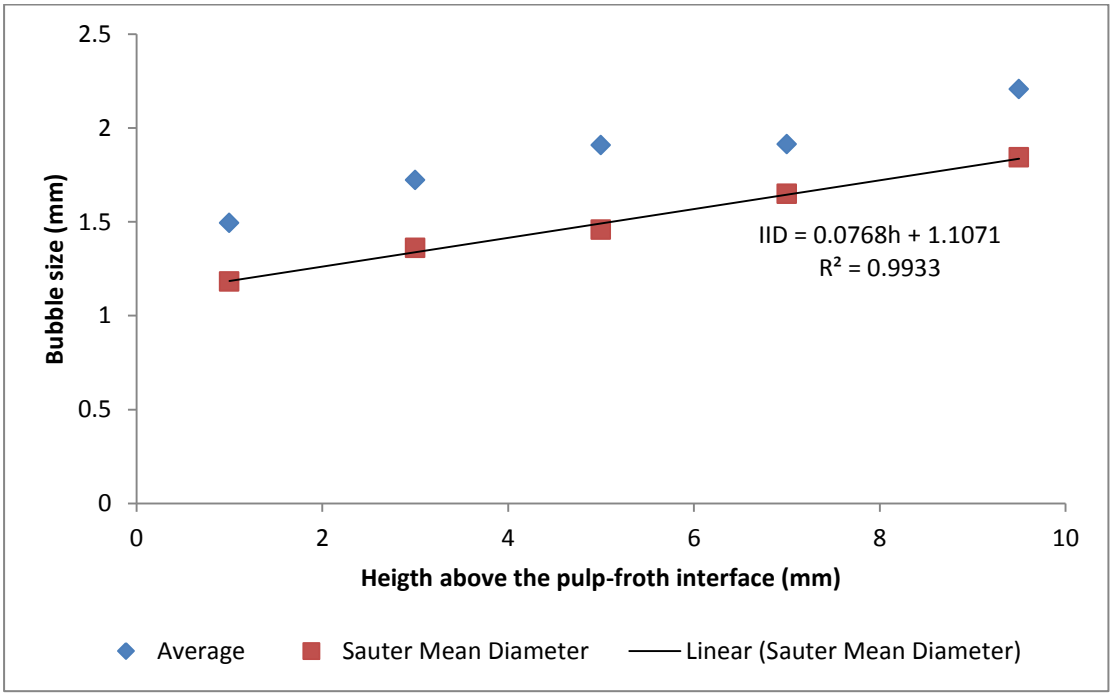

Figure 4.34: Comparison of the bubble-sizer average IID to the Sauter-mean diameter as obtained by photographic method for 2% Limestone

4.7 Concluding remarks

In this Chapter a new technique to measure a proxy for froth phase bubble sizes has been developed and tested under various slurry chemical conditions. Results from the first section which is dedicated to the development of the concept, indicate that a method to estimate froth phase bubble sizes that is comparable to the photographic method was developed. The second section of the Chapter is dedicated to testing the concept under different slurry chemical conditions and results indicate that the signals obtained are amenable to bubble size proxy estimation. A baseline condition of water dosed with frother only also produced a signal from which bubble size estimates were calculated. Addition of solids did not affect the bubble size signal although the % solids content was maintained low to avoid solid interference with bubble during videoing. The addition of limestone stabilised the froth resulting in a

low rate of change of bubble sizes resulting in a linear change in bubble size with height.

Now that a technique to estimate the changes in froth bubble sizes has been developed and tested in a laboratory mini-flotation column. It remains critical to find out how this technique would fair in a mechanical flotation cell with higher percentage solids pulp. Furthermore, can the new technique be used to assess the effects of say froth depth and gas rate on froth bubble sizes? Answers to such questions are provided in Chapter 5.

Chapter 5

Quantifying the effects of froth depth and gas rate on the proxy for froth phase bubble sizes.

Work in this Chapter was presented at the International Mineral Processing Congress 2014 (IMPC 2014) in Chile.

5.1 Introduction

In the previous Chapter, a novel technique to estimate a proxy for froth phase bubbles sizes (IIDs) was developed and tested under various slurry chemical conditions. The results from that exercise strongly suggested that a method to estimate bubbles sizes that does not depend on slurry chemical conditioning and compares well with photographic technique was developed. Central to froth phase performance is froth residence time, typically adjusted through changing froth depth and gas rate. Adjusting residence time influences froth phase bubbles sizes especially close to the froth surface. This Chapter is dedicated to investigating the effect of gas rate and froth depth on froth phase bubble sizes using the technique developed in Chapter 4.

Froth depth and gas rates are critical operating variables that are used to control the flotation process. By altering froth depth and air rate, flotation rate constant changes. It has been shown by Tomlinson and Fleming (1965) that the flotation rate constant is related to the probability that a particle survives the cleaning action of the froth phase. This probability depends on critical sub-processes in the froth phase such as bubble coalescence (froth stability), froth residence time and liquid drainage. Altering froth and gas rate has a direct impact on these froth processes. The effect of both gas rate and froth depth on froth residence time has been established by a number of workers e.g. Gorain *et al*. (1998) as the ratio of froth height to superficial gas velocity. Froth depth and gas rate also influence froth stability. Moys, (1979) has shown that

by increasing gas rate, froth stability is also increased and consequently water recovery increases. Feteris *et al.* (1987) proved that froth stability depends on froth height, with froth eventually collapsing as the froth height is increased. If froth stability is defined according to Farrokhpay (2011) definition i.e. the ability of bubbles in froth to resist coalescence and bursting, then a measure of how bubbles size changes from the pulp-froth interface to the surface of the froth can be used as a tool to asses froth stability.

5.2 Brief experimental description

5.2.1 Flotation tests set-up

An 80 litre sample of 35% w/w solids primary rougher tails slurry with a P75 of 53µm was received from Lonmin platinum's K3 concentrator. Upon reception, additional frother (MIBC) was dosed at rate of 20g/ton into the mixing tank before flotation commenced. Flotation tests were carried out in a mechanical cell with a capacity that varies from 8-20litres. The cell was operated in pseudo-steady state mode as described in section 3.3.1 and schematically represented by Figure 3.7. Slurry flowrate into the flotation cell was metered to maintain an average residence time of 3.0minutes. Froth depth (measured from the pulp froth interface to the concentrate launder) was set at 6.3cm and 11.0cm while average superficial gas velocity was changed between two values viz. 0.57cm/s and 0.97cm/s. The agitation rate was maintained at 1200 rpm in all experiments.

5.2.2 IID measurement set-up

The measurement of IID was done by dropping the conductivity probe several times into the froth phase from a known height (Hd) as depicted in the experimental set-up in Figure 5.1. Care was taken to ensure that the probe was falling vertically into the froth phase and within a fixed locus on the surface of the froth. The Electrical signals were routed to a PC through an SCXI 1520 data logger set at 40kilosamples per second. The measured value of the froth depth (Hf) and the time it takes the probe to cut across the froth (obtained from the output signal) were used to quantify the effect of froth resistance on probe velocity. Concurrent to these measurements, pictures of the froth were also taken for qualitative comparison with the obtained IIDs.

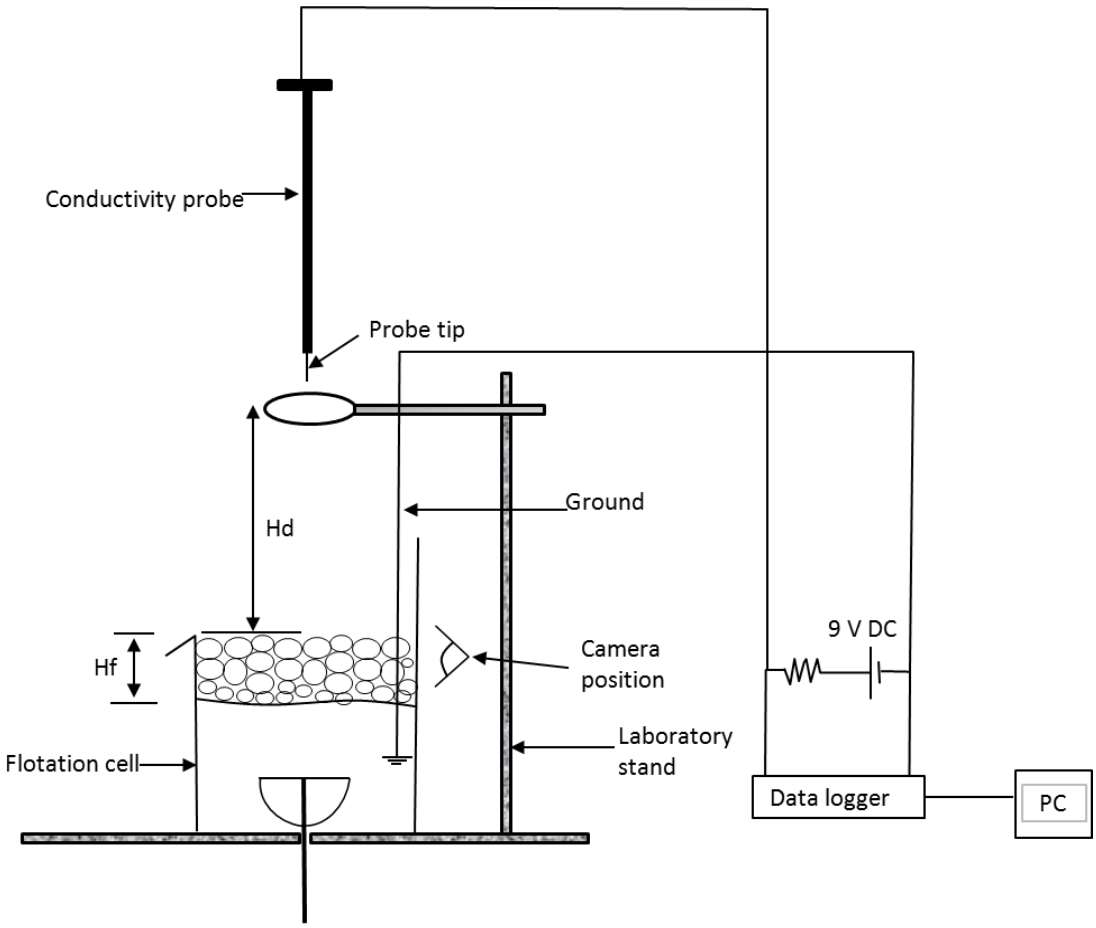

Figure 5.1: Schematic of the experimental set-up to measure IID

5.3 Results

5.3.2 Illustration of the estimation of IID

Figure 5.2 represents a typical signal and its derivative that were obtained when the conductivity probe was dropped into the froth phase. On this figure, the points of significant impact are enhanced by the asterisks. It is visible from this figure that as the probe moves closer to the pulp-froth interface, time between successive points of significant impact becomes shorter; which is the expected observation. Using a combination of the velocity (adjusted to account for the effect of froth resistance) at which the probe cuts across the froth and the time between successive sharp points on the signal derivative, values of IID were calculated. IIDs are not actual bubble sizes but are related to bubble sizes at given points above the pulp-froth interface. A value of IID that statistically represent bubble sizes a certain height above the interface, the conductivity probe need to be dropped several times into the froth

phase and an average of all the drops can be deemed representative of bubbles sizes.

To represent how the values of IID changes with height above the pulp-froth interface, the froth phase was segmented into approximately 3cm segments above the froth the pulp-froth interface. Figure 5.2 is an example of how the average IID values were obtained for superficial gas velocity of 0.57cm/s and froth depth of 11cm (measured to the concentrate weir lip). The average IIDs obtained for each drop are represented in Figure 5.3a while Figure 5.3b is the average of the nine drops done at these particular conditions. The relative standard deviation values ranged from 14 to 30percent. These values are too high and they are possibly due to a number of reasons, among them include that each 3cm segment contains a distribution of bubble sizes from the smallest un-coalesced bubble to the largest bubble resulting from successive coalescence, thus the standard deviation is expected to be high. In spite of this high variation in IID values, it is clear from Figure 5.3b that regions close to the surface of the froth contain larger bubble sizes and also high rates of bubble coalescence. The rate of change of IIDs can be calculated from the gradient of Figure 5.3b. It shows slower rates of change of IIDs close to the pulp-froth interface and high rate of change close to the surface of the froth. High and constant rates of bubble coalescence are expected close to the pulp-froth interface as a result of crowding of bubbles as they rise from the pulp phase. Results presented in Figure 5.3b show slower rates of change of IIDs close to the pulp-froth interface. This contrast to expectation can be as a result of the probe showing a sampling bias towards the larger bubble sizes in the regions close to the interface Or high bubble coalescence in the first 3cm above the pulp-froth that results in a bias toward the large bubbles when the average IID within this segment is calculated such that the IID value in this region represents more of the products of coalesced bubbles than the original bubbles generated in the pulp phase.

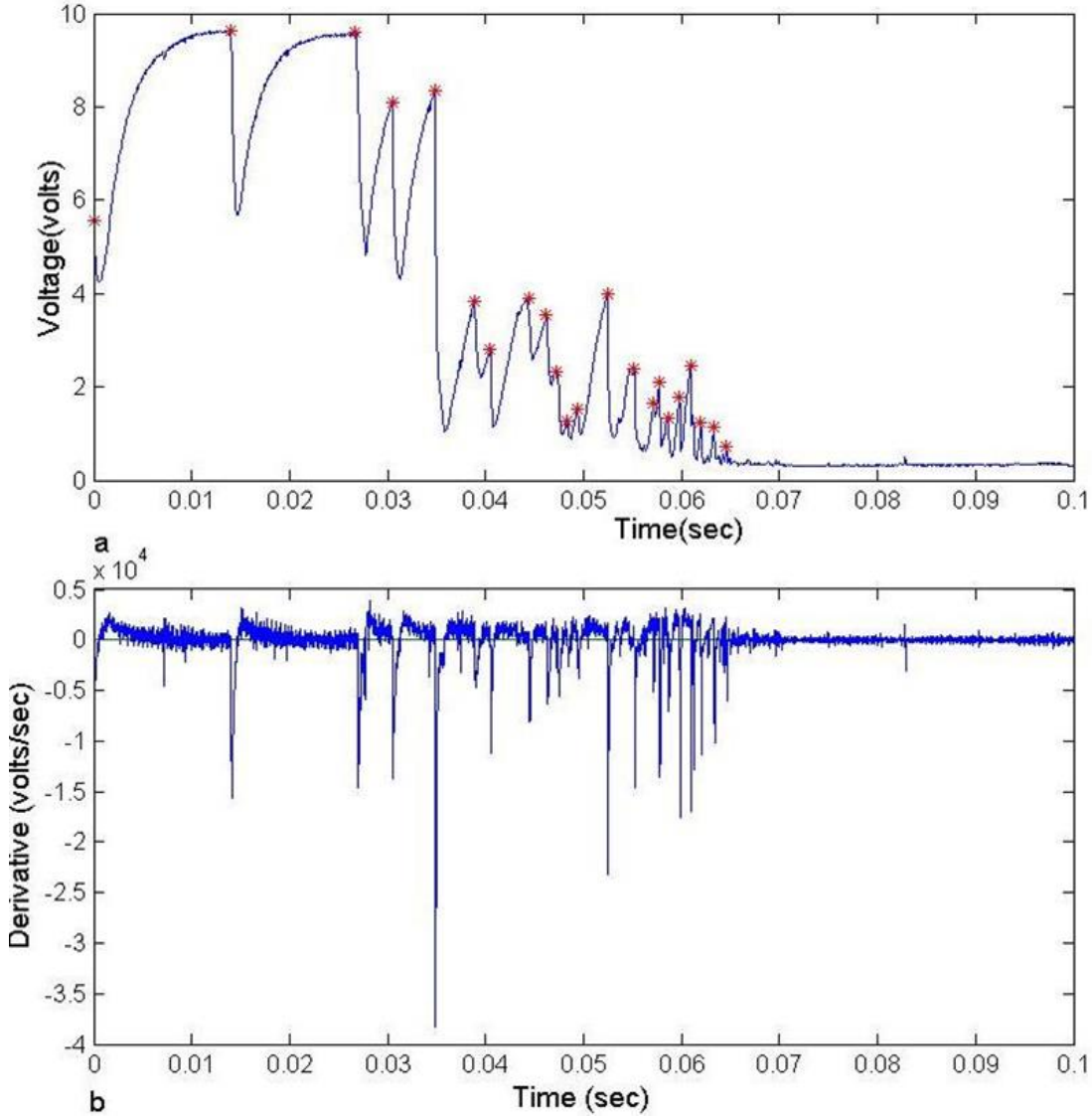

Figure 5.2: Typical bubble-sizer signal (a) and its derivative (b) IID measurements were taken 0.57cm/s gas flux and froth depth of 11cm.

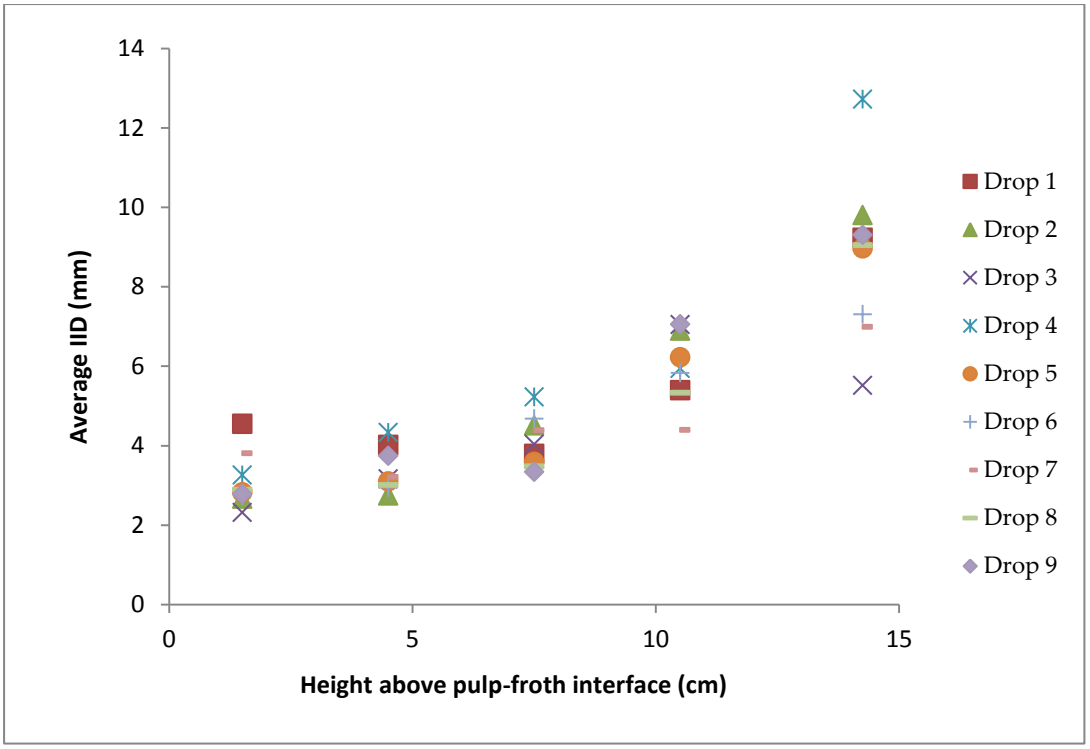

Figure 5.3a: Illustration of IID determination showing average IIDs for each of the nine drops

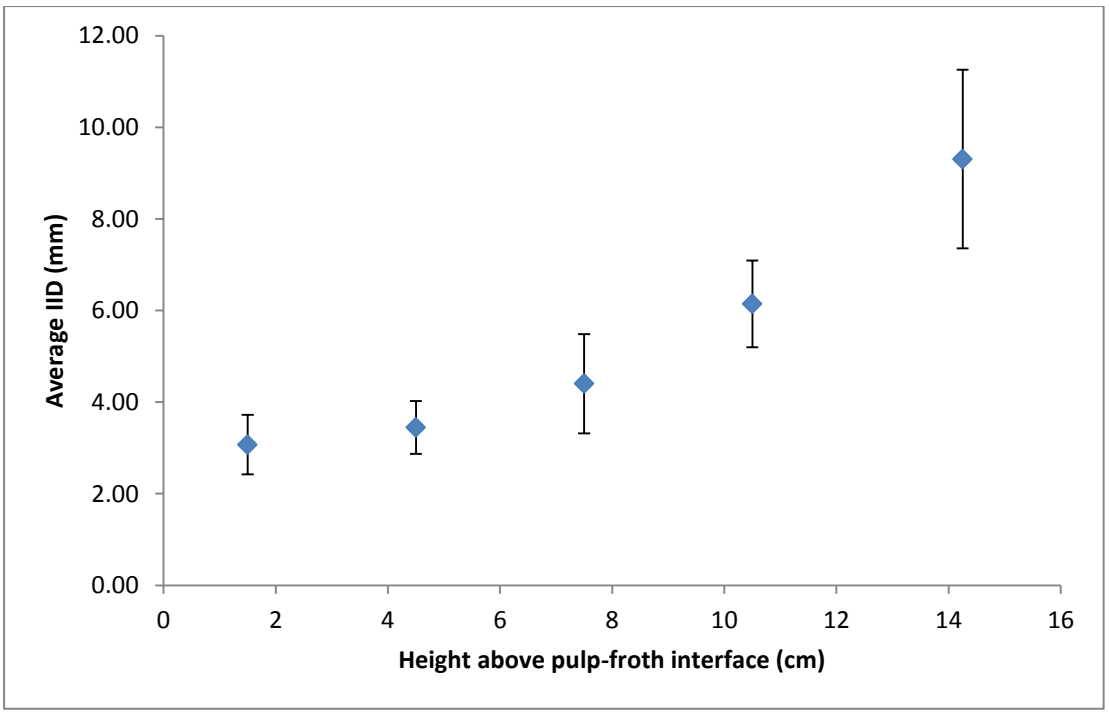

Figure 5.3b: Average IID for the nine drops shown in figure 5.3a, error bars based on standard deviations.

5.3.2.1 Variation of IID with height

Unlike measurements done in Chapter 4, where the IID vary linearly with height, measurements done with the industrial slurry (e.g. Figure 5.3b) show a non-linear variation of IID with height above the pulp froth interface. In fact a closer look reveals two regions of different rates of change of bubble sizes (gradients). In Figure 5.3b for instance, a straight-line can be fitted to average IIDs between the pulp-froth interface to height of 8cm while another straight-line can be fitted from 8cm and above. The gradients of these lines reveal two different rates of bubble coalescence, with the region close to the surface coalescing at a faster rate than the region below. This observation is also reinforced by the pictures of the froth taken from the side of the flotation cell. Consider Figure 5.4, it is easy to see that the region labelled (B) contains small bubbles that gradually increase in size while region labelled (A) has very large bubbles that are increasing in size rapidly. We suspect that this phenomenon depends on froth stability, and water drainage. Region A contains a significant amount of water when compared to region B; where the amount of water is little the susceptibility of bubbles to coalesce increases and vice versa. Of interest also is that most of the very large bubbles occur in the froth above the concentrate weir.

Figure 5.4: Picture showing variation in bubble sizes above the pulp-froth interface.

5.3.3 Effect of froth depth

Increasing froth depth increases average froth retention time and according to Feteris et al. (1987), it also reduces froth stability. It is thus expected that as froth depth is increased, the rate of increase in average bubble sizes should increase or more precisely values of IID close the froth surface should increase. Figure 5.5 and Figure 5.6 illustrate the IIDs that were obtained for the two gas velocity of 0.57 cm/s and 0.97cm/s at two froth depths of 6.7cm and 11cm measured to the concentrate weir lip. The height (HT) depicts froth height as measured from the pulp-froth to the top of the froth. This value cannot be fixed as it depends on operating conditions such gas rate and froth depth. As shown in Figure 5.5, the average IIDs when froth depth was set at 11cm are higher than the average IIDs obtained at a froth depth of 6.3cm at the same average gas flux of 0.97cm/s for all 3cm froth segments. Top of the froth IID value of 9.31mm was observed for the 11 cm froth depth when compared to 6.75mm obtained when froth depth was set at 6.3cm. Similar results are observed in

Figure 5.6, when superficial gas velocity was reduced to 0.57cm/s i.e. higher average IID at a larger froth depth especially close to the surface of the froth starting at 7.5cm above the pulp froth interface.

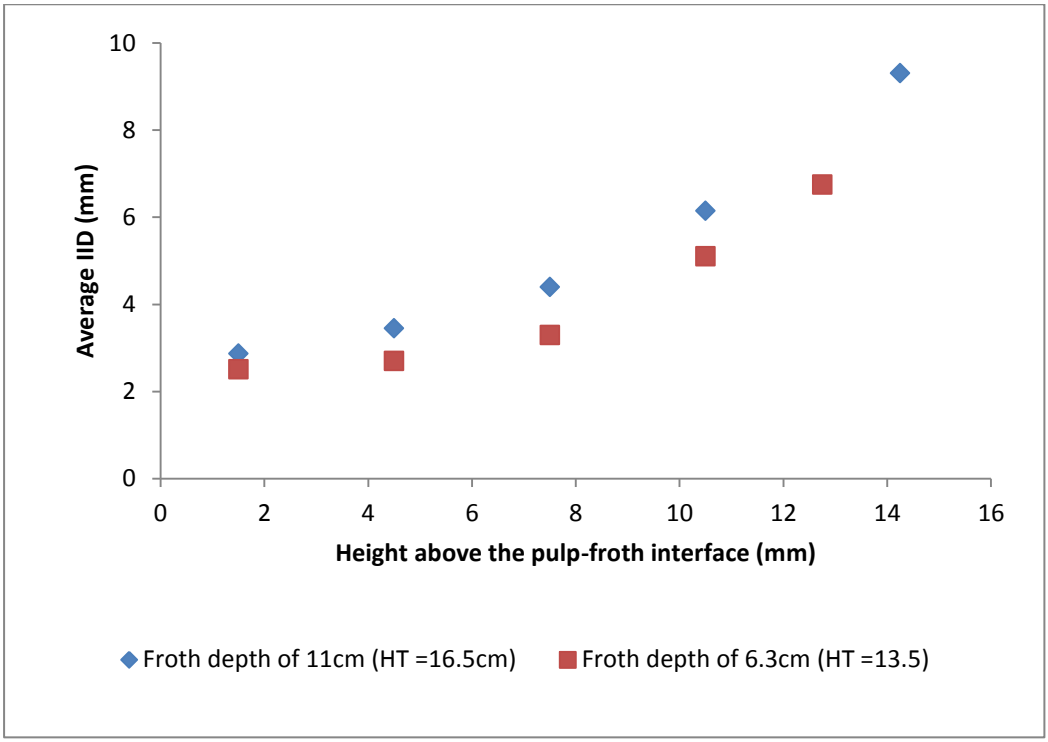

Figure 5.5: Graph illustrating effects of froth depth at a fixed superficial gas velocity of 0.97cm/s

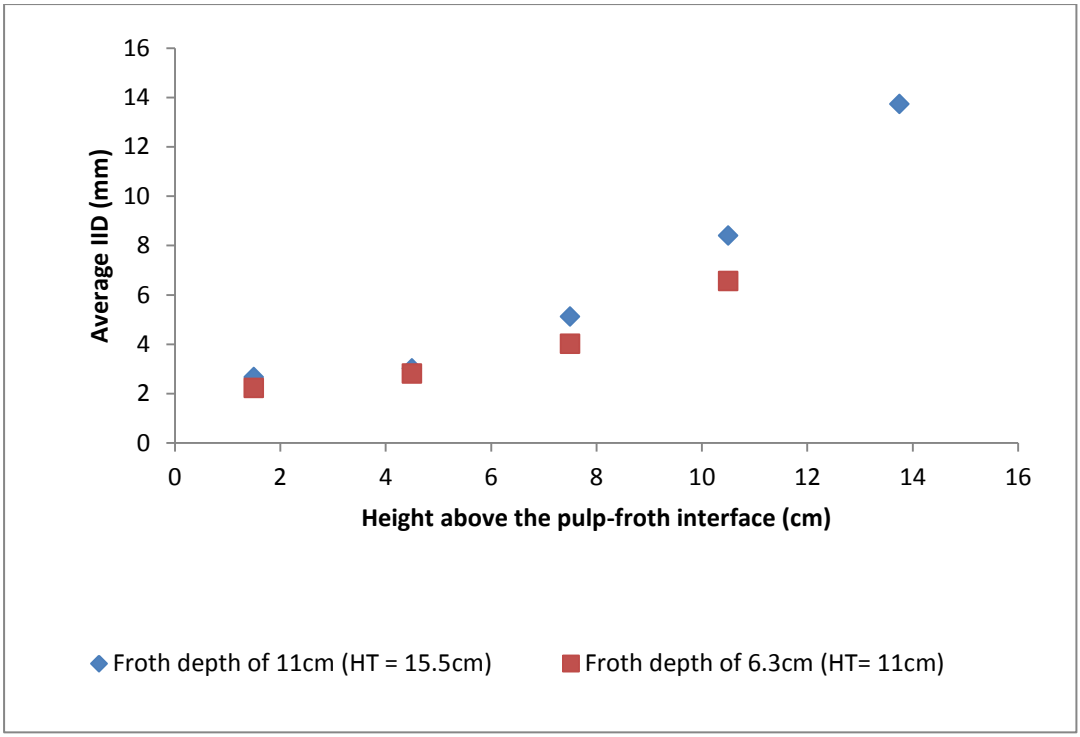

Figure 5.6: Graph illustrating effects of froth depth at a fixed superficial gas velocity of 0.57cm/s

5.3.4 Effect of gas rate on IID

Gas rate affects froth stability by altering froth residence times. At a fixed froth depth, changing superficial gas velocity is expected to have an effect on froth phase bubble sizes. Figure 5.7 and Figure 5.8 represent IIDs that were obtained at two superficial gas velocities of 0.57cm/s and 0.97cm/s at two fixed froth depths. When froth depth was fixed at 6.3cm, results shown in Figure 5.7 were obtained; they indicate that as gas velocity was increased from 0.57cm/s to 0.97 cm/s the average IID decreased. This can be attributed to change in average froth residence time, which means reduced bubble coalescence of bubbles. According to Tao et al. (2000) increasing gas rate also increases froth stability, thus increasing gas rate reduces bubble coalescence per given froth depth and fixed chemical conditioning. Similar results were obtained when froth depth was increased to 11cm (Figure 5.8) affirming that the measuring technique is able to follow the changes inside the froth phase when operating parameters were changed

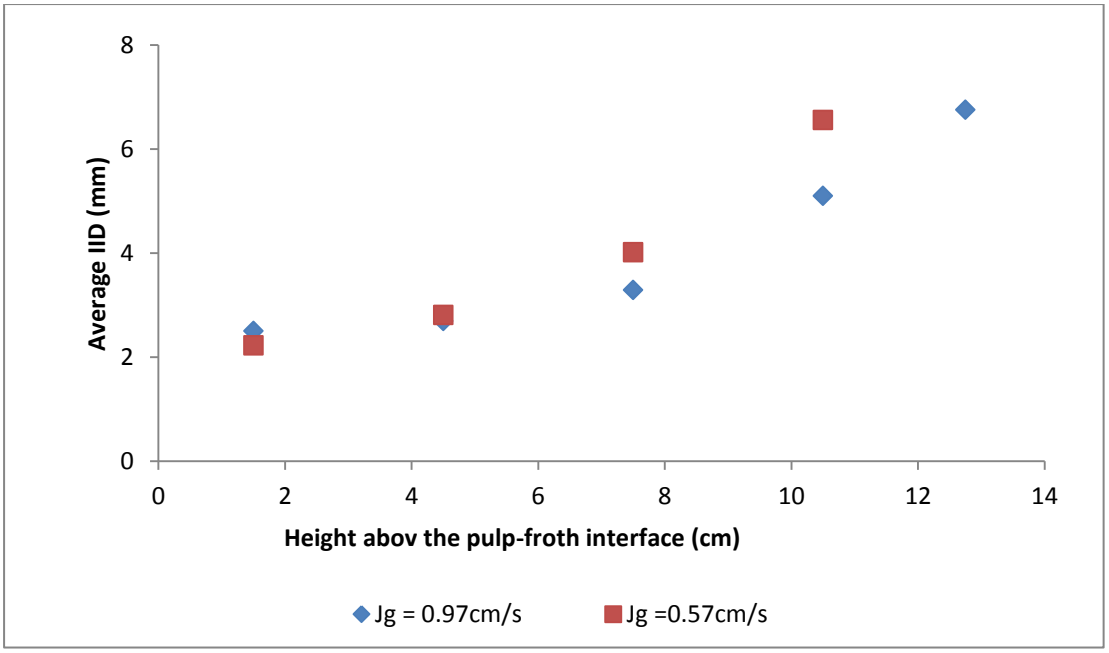

Figure 5.7: Effect of gas rate on IID when froth depth was fixed at 6.3cm

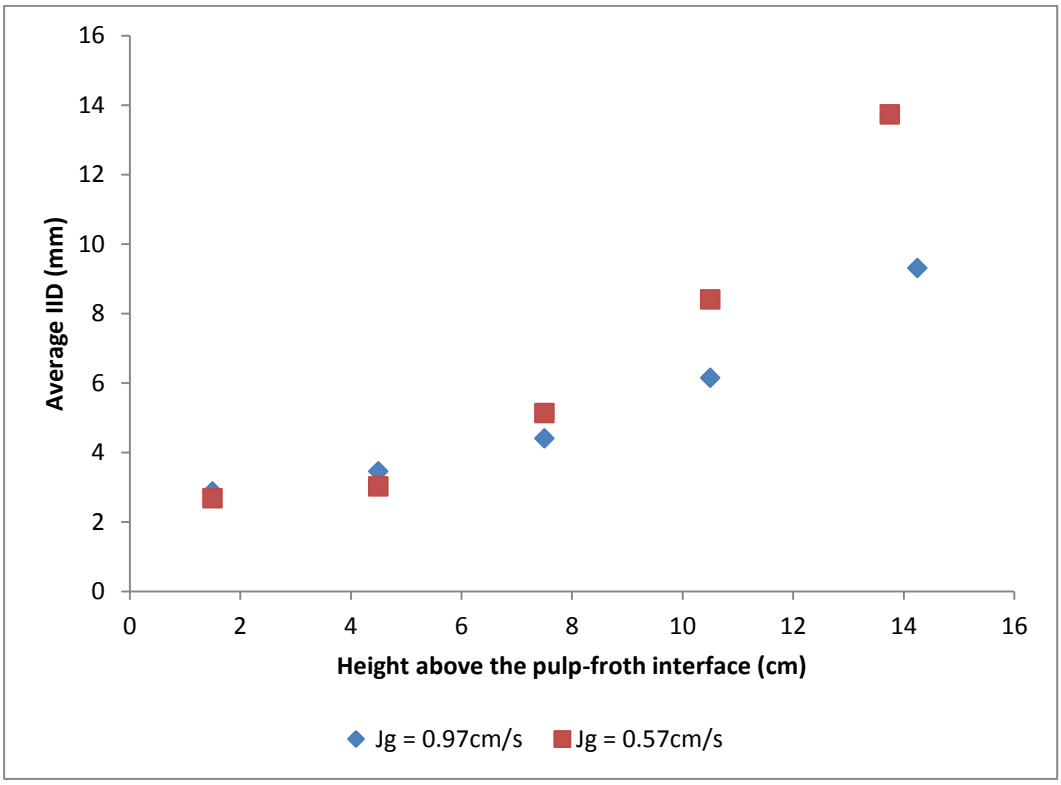

Figure 5.8: Effect of gas rate on IID when froth depth was fixed at 11cm

5.4: Conclusions

Increasing superficial gas velocity at fixed froth depth increases froth stability as revealed by a decrease in IID as superficial gas velocity was changed from 0.57cm/s

to 0.97cm/s, the increase in IID is greatest close to the surface of the froth. Fixing gas flux and changing froth depth results in an increase in average IID as froth depth is increased. Despite the seeming bias towards the larger bubble sizes especially close to the pulp-froth interface, this measuring technique provided an output that if related to froth stability; agrees with work done by other workers e.g. Moys et al. (1979), Feteris et al. (1987).

Overall, a new technique that can be used to study the froth phase in particular bubble coalescence and froth stability has been developed and tested. The technique has potential to be used for real-time control of froth phase performance.

Chapter 6

Effects of gas distribution profile to flotation cell performance

Work reported in this Chapter has been peer-reviewed and is under second review at the International Journal of Mineral Processing (IJMP)

6.1 Introduction

Control of the froth phase in flotation is usually achieved by manipulating froth residence times through variation of froth depth and gas rate. These variables have a profound effect on both flotation phases, such that they can only be changed within a limited range. The froth phase being rate limiting in most cases require critical attention, but because very few practical methods to manipulate its sub-process exist in literature most froth systems do not operate at optimum levels as exemplified by low froth recoveries such as those reported in literature .e.g. Vera (2002). Opportunities to optimise the performance of the froth phase lie in optimising froth residence time distribution. It is generally accepted in flotation that bubbles which enter the froth phase close to the concentrate weir spend less time in froth as compared to those that are generated further away. This has implications on froth phase performance. Froth residence time by definition is inversely proportional to superficial gas velocity such that for a given froth depth, the distribution of gas flux across the pulp-froth interface strongly influences the distribution of residence times in the froth. Thus, how gas is distributed across the pulp-froth interface offers an opportunity for optimising froth residence time distribution. Work described in this Chapter, is aimed at investigating the use of gas flux distribution across the pulp-froth interface as a way of optimising froth performance.

The research on gas dispersion properties ((bubble size, superficial gas velocity, gas hold up and bubble surface area flux) discussed in flotation literature (see section 2.2.2.1) assumes an average superficial gas velocity which is then taken to be uniform across the flotation cell. It does not take into account the effects of air

distribution across the pulp-froth interface. In simulating his two dimensional model for the froth phase Moys (1979) recognised the influence of air flux distribution across the pulp froth interface. He suggested that the air flux distribution in a flotation cell could be described by $g(x) = g_o \sin(\pi x / L)$ where $g(x)$ representing a superficial gas velocity a distance x from the back plate of a cell of length L and g_o being the air flux at the centre of the cell. Ross and van Deventer (1987) after taking measurements in industrial flotation cells supported this proposal. Moys *op cit*. simulations revealed that the sinusoidal form of gas distribution profile which is normally found in mechanically agitated vessels with impeller at the centre of the cell results in negative velocity profiles at the back of the cell that results in reduction of the effective froth volume. Thus though the importance of air distribution profile to froth performance has been recognised by early practitioners, work to characterise the best air distribution profiles in a flotation cell seems absent in the flotation literature.

In view of the above, work in this Chapter, presents results to answer whether or not profiling gas flux in a single flotation cell can optimise cell performance. An experimental approach that produces different gas fluxes across the pulp-froth interface was chosen as the basis of study as opposed to simulations as done by Moys *op cit*. Flotation performance is compared and results from video analyses are used as to explain the observed performance differences. If indeed air profiling within individual flotation cells can be an additional manipulated gas dispersion property, then the effect of this study on flotation cell design is significant. A distribution profile that reduce dead zones and optimises froth residence times in a flotation cell will increases the separation efficiency of each flotation cell and if it is coupled with an optimum air distribution profile on a flotation bank, it will increase flotation circuit performance.

6.2 Brief experimental description

The description of the flotation cell used for experiments reported in this Chapter is given in section 3.4.3. Three positions of the impeller shown in Figure 3.4 were investigated and superficial gas velocity measured using the specially designed (J_g) device described in section 3.3.2 on 25 positions on a 5 X 5 grid as shown in Figure 6.1. Flotation experiments were performed using ore comprising of 80% silica and 20% limestone as the gangue and floatable material respectively. The flotation cell

was operated in a continuous manner by connecting it to an 85 litre mixing tank with tails and concentrates from the flotation cell flowing back into the mixing tank as shown in Figure 3.4.

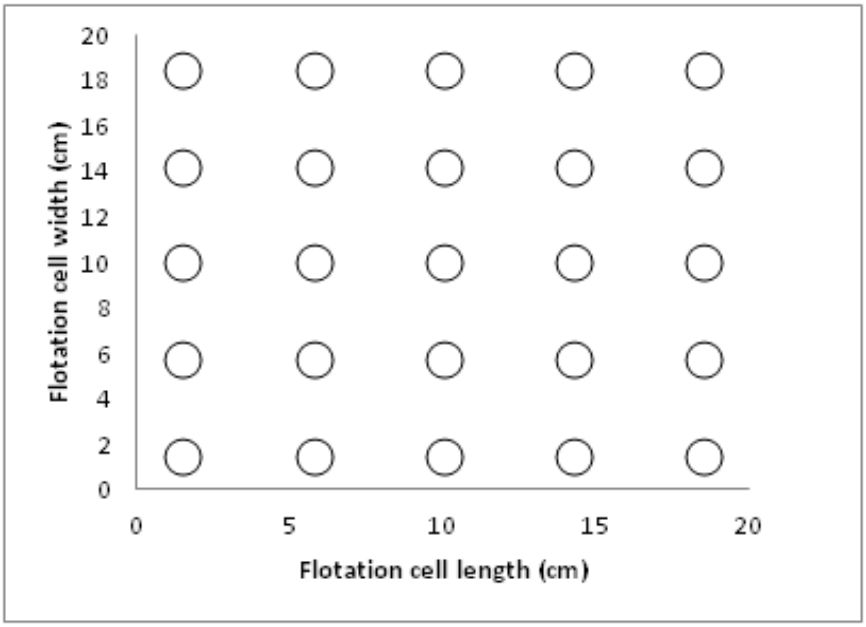

Figure 6.1: The plan view of the flotation cell showing points at which superficial gas velocity was measured.

6.2.1 Slurry preparation

The slurry was prepared according to the recipe described in section 3.3.3. Solids concentration was maintained at 15%w/w. Three different gas rates of 13.6, 21.5 and 30 litres/min were investigated, giving an average superficial gas velocity that ranges between 0.57 and 1.25cm/s. Impeller speed was set at 1200rpm; a scaled down Outotec agitator was used for this purpose. Pump rate was set to provide a slurry residence time of 3.0minutes; froth depth as measured from the pulp-froth interface to the concentrate weir lip was set two different values of 6.3cm and 10.1cm. Sampling procedure described in section 3.4.1.

6.3 Results

6.3.1 Variation of superficial gas velocity with impeller position

When the position of the impeller is changed relative to the concentrate launder the gas flux distribution across the flotation cell changes as well. Three positions were investigated and superficial gas velocity measurements were taken at points

indicated in Figure 6.1; the results are plotted in Figure 6.2. Figure 6.2a shows the gas flux distribution when the impeller was moved to the back of the flotation cell. Notable on this figure, is the high gas flux at the back of the cell, superficial gas velocities as high as 1.7cm/s were recorded which gradually decrease towards the concentrate weir with an average decrease of about 35percent. Figure 6.2b, is a representation of the gas flux across the pulp-froth interface when the impeller was at the centre of the flotation cell. It shows that gas flux is relatively uniform across the bulk of the of the pulp-froth interface although the right side of the flotation cell shows higher values than the left side. An average difference of about 7% was measured between the left and the right side of the flotation cell. This was caused by the air distribution mechanism; the air supply pipe is inclined to the right and the agitator rotates in an anti-clockwise direction such that most of the finer bubbles of air are pumped to the right. When the agitation mechanism was moved to the front i.e. close to the concentrate weir, gas flux distribution shown in Figure 6.2c was obtained. High gas flux was recorded at the front position and decreased towards the back of the flotation cell. An average change of 33% from the front to the back was i.e. from 1.8 to 1.2cm/s was recorded. It was also observed during J_g measurement that the gas flux distribution profile in addition to being strongly affected by gas rate was also a function of the impeller speed and frother dosage rate or more directly the bubble size distribution produced by the impeller and the impeller pumping rate. At high frother dosages and high impeller speed, higher values of J_g were recorded away from the impeller and vice-versa. Thus superficial gas velocity measurements recorded in this work were done at frother dosage of 20mg/litre of water and impeller speed of 1200 rpm and a gas rate 35l/min resulting in an average J_g of 1.45cm/s. Measurements were also taken without a crowder and without solids. Presence of solids in the pulp phase is not expected to affect the pulp phase bubble size distribution although it is known to affect froth phase bubble size distribution. Thus all measurements were done below the pulp-froth interface

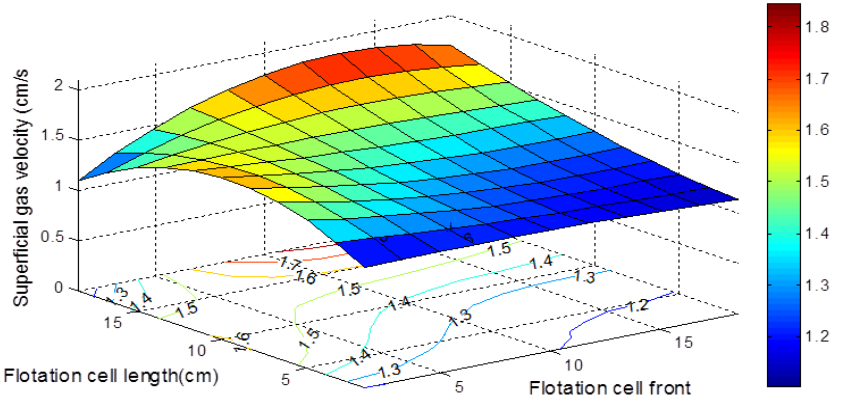

a) Agitator at the back of the flotation cell

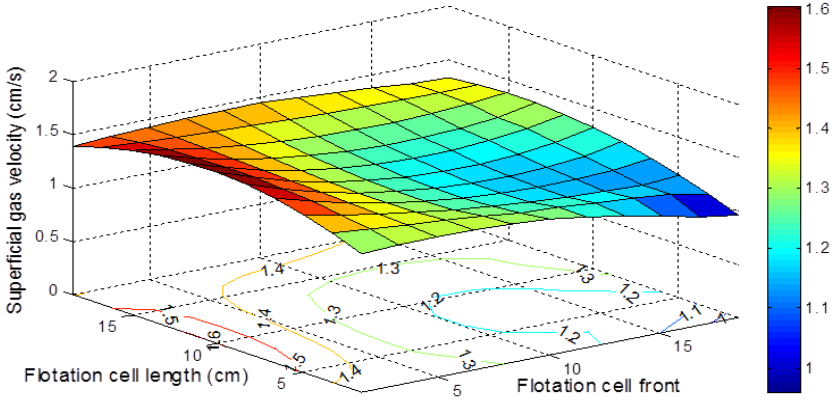

b) Agitator at the centre of the flotation cell

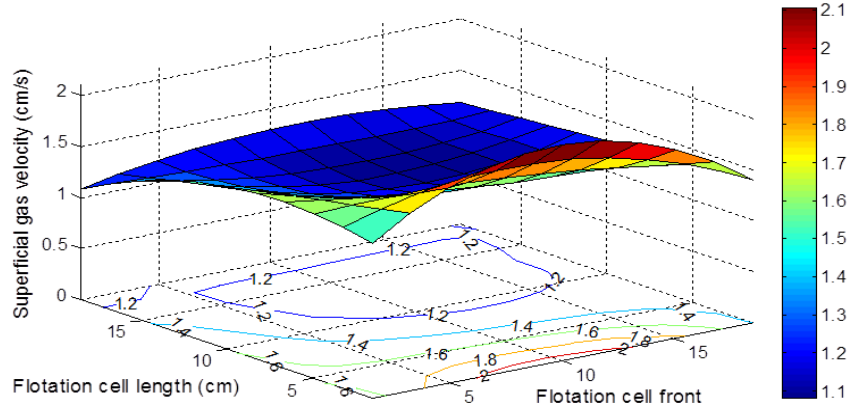

c) Agitator close to the concentrate weir

Figure 6.2: Variation of superficial gas velocity with agitator position (a) representing gas flux profile when the agitator is at the back of the flotation cell (b) agitator at the centre (c) agitator close to the concentrate weir

6.3.2 Effect of impeller position on limestone recovery

The changes in limestone grade and recovery that were observed when the impeller position was changed relative to the concentrate launder are shown in Figure 6.3. Figure 6.3a and 6.3b shows how limestone recovery varied with agitation mechanism position for froths height of 6.3cm and 10.1cm respectively. Measurements were taken at three different gas rates for the shallower froth depth and two gas rates for the deeper froth depth. In all measurements, impeller speed was maintained constant at 1200rpm and average pulp residence time maintained at 3.07minutes. Noticeable in Figure 6.3a and 6.3b is the increase in limestone recovery as the impeller position was changed from the conventional impeller at the centre position. Highest recoveries were obtained when the impeller was positioned at the back followed by recoveries when the impeller was near the front of the flotation cell for both froth heights and for all gas rates. Significantly lower recoveries were obtained when the impeller was positioned at the centre of the flotation cell and especially at deeper froths and low gas rate (Figure 6.3 b, c and d). Although the differences in recovery appear smaller i.e. the maximum difference for 6.3cm froth depth of 10.5% and 10.6% for the 10.1cm froth depth, a two way analysis of variance at α= 0.05 proved that these differences are statistically significant. F -statistic values of 188.26 and 138.39 were obtained and compared to F_{crit} values of 3.89 and 4.75 for the two factors i.e. the impeller positions and froth height respectively. Table 6.1 is a summary of the ANOVA results. To enable identification of the limestone recoveries that are different within each factor, a Post-Hoc Test based on Tukey's honestly significant difference (HSD) was performed and results are shown in Table 6.2a and 6.2b. As shown in both tables, the differences in the means are greater than the HSD critical value implying that the observed recoveries are statistically different from each other for a given froth height and fixed air flux of 0.567cm/s.

Table 6.1: Statistical analysis for limestone recovery

Two way ANOVA for Limestone recovery						
Source of Variation	SS	df	MS	F	P-value	F crit
Impeller position	333.62	2	166.81	188.26	8.68E-10	3.89
Froth height	122.62	1	122.62	138.39	6.03E-08	4.75
Interaction	0.09	2	0.05	0.05	0.95038	3.89
Within	10.63	12	0.89			
Total	466.97	17				

Table 6.2: Post hoc analysis for limestone recovery

Table 6.2a:Tukey's HSD test for limestone recovery at froth depth 6.3cm			Difference in Means	Tukey HSD Value	Outcome
Back (μ1)	56.68	μ1-μ2	10.46	**2.36**	**Different**
Centre (μ2)	46.21	μ1-μ3	5.16		**Different**
Front(μ3)	51.52	μ3-μ2	5.30		**Different**

Table 6.2b:Tukey's HSD test for limestone recovery at froth depth 10.1cm			Difference in Means	Tukey HSD Value	Outcome
Back (μ1)	51.63	μ1-μ2	10.63	**2.36**	**Different**
Centre (μ2)	41.00	μ1-μ3	5.51		**Different**
Front(μ3)	46.12	μ3-μ2	5.12		**Different**

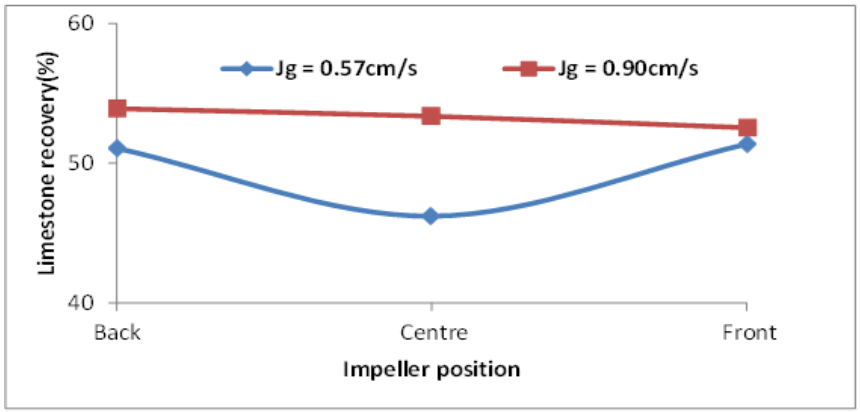

a) Limestone recovery as a function of agitator position and Jg for a froth depth of 6.3cm

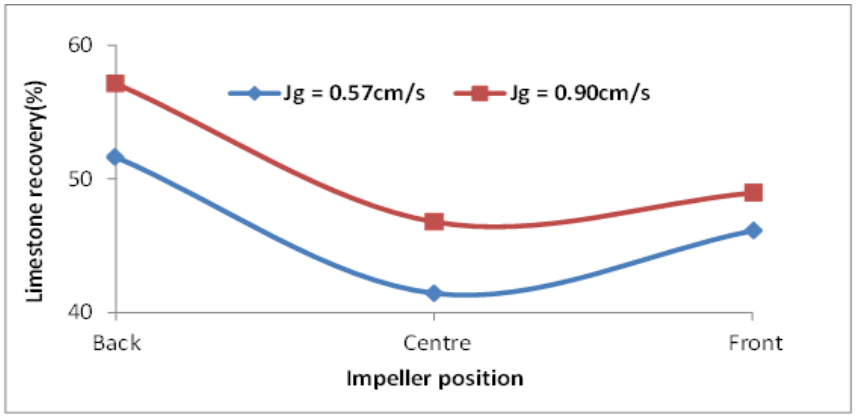

b) Limestone recovery as a function of agitator position and Jg for a froth depth of 10.1cm

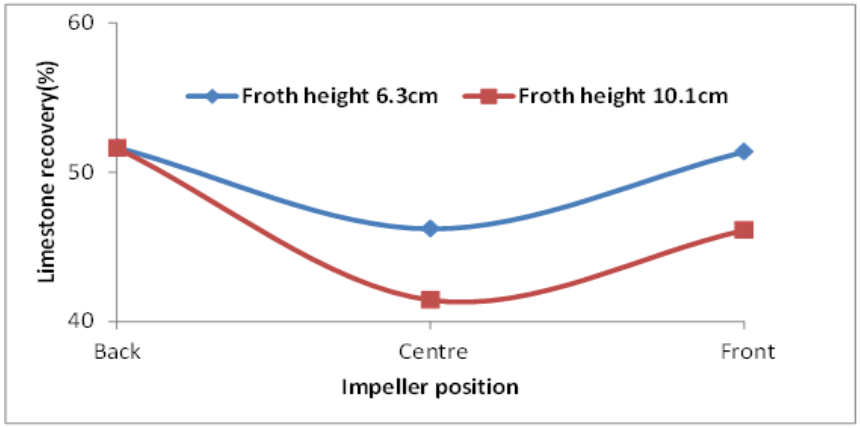

c) Limestone recovery as a function of agitator position and froth height at Jg = 0.57cm/s

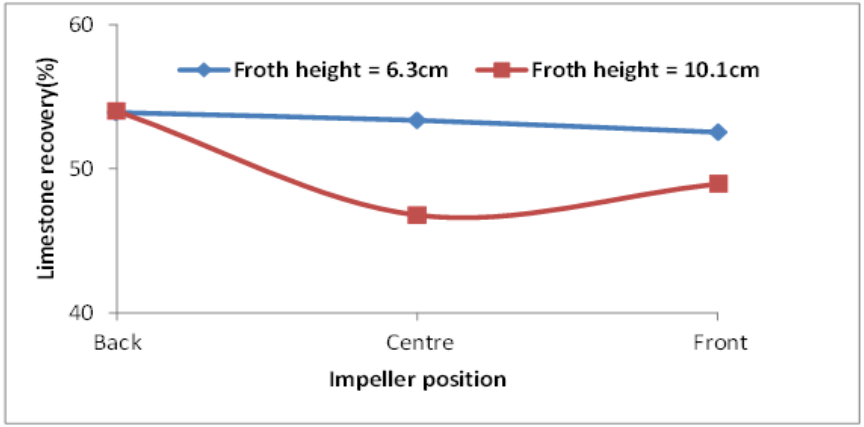

d) Limestone recovery as a function of agitator position and froth height at Jg = 0.90cm/s

Figure 6.3: Variation of limestone recovery with impeller position and gas rate at two froth depth (a, b) and with impeller position and froth height (c, d) at different air flowrates.

6.3.3: Effect of impeller position on limestone grade (concentrate)

Changing impeller position also impacted on the grade of limestone in concentrate; Figure 6.4 shows how limestone grade varied as impeller position was changed. It is clear that the grade of limestone was highest when the impeller was at the back and when it was close to the concentrate weir. The lowest grade was recorded when the impeller was at the centre. This is contrary to our expectation that limestone grade should have been lowest when impeller was closest to the concentrate weir. The maximum grade change observed when froth height was set at 6.3cm and 10.1 cm was 4.82% and 2.11% respectively. Of interest in Figure 6.4a and 6.4b also is the interaction of air rate and froth height. At lower froth depth (Figure 6.4a) the grade of limestone decreased as air flux was increased from 0.57cm/s to 1.24cm/s for all impeller positions. When froth height was increased to 10.1cm, as expected the limestone grade obtained was higher than that obtained when froth height was set at 6.3cm. Increasing gas rate at this froth height increased the grade of limestone, thus higher grade was obtained at higher gas rate and vice versa (Figure 6.4b). This is the opposite of what was observed at lower froth height. This observation is probably as a result of limestone losses due to drainage and froth collapsing at high froth depth and low gas rate. Variation of limestone grade with froth height at the two superficial gas velocities is shown in Figure 6.4c and 6.4d. For all gas rates and impeller positions a higher grade was obtained at deeper froth.

Limestone grade data was also subjected to a two way ANOVA at an alpha value of 0.05, with impeller position and froth depth as factors. Results obtained indicated that indeed the average grade is different in at least two of the limestone recoveries at the air flux of 0.57cm/s and the two froth depths. It also revealed that there was no interaction of these two factors at this gas rate however, interaction of the parameters was observed at higher gas rates and the ANOVA test also proved it. At a gas flux of 0.90cm/s, an F value of 25.57 compared to an F_{crit} of 3.89 was obtained for the interaction of parameters as shown in Table 6.3. The post hoc test at this air flux is shown in Table 6.4. Table 6.4a reveals that there is no significant difference between limestone grade obtained when the impeller is at the back or close to the concentrate weir at a higher froth height. This may point to the dwindling effect of gas flux distribution on the froth phase as froth height is increased.

Table 6.3: Statistical analysis for limestone grade

Two way ANOVA for Limestone grade						
Source of Variation	SS	df	MS	F	P-value	F crit
Impeller position	36.67	2	18.33	122.79	1.02226E-08	3.89
Froth height	169.74	1	169.74	1136.82	2.94332E-13	4.75
Interaction	7.64	2	3.82	25.57	4.70881E-05	3.89
Within	1.79	12	0.15			
Total	215.84	17				

Table 6.4: Post-Hoc Test for limestone based on Tukey's honestly significant difference (HSD)

Table 4a:Tukey's HSD test for limestone grade at froth depth 6.3cm			Difference in Means	Tukey HSD Value	Outcome
Back (μ1)	73.90	μ1-μ2	4.82	0.97	Different
Centre (μ2)	69.08	μ1-μ3	1.40		Different
Front(μ3)	72.50	μ3-μ2	3.42		Different

Table 4b:Tukey's HSD test for limestone grade at froth depth 10.1cm			Difference in Means	Tukey HSD Value	Outcome
Back (μ1)	78.36	μ1-μ2	1.65	0.97	Different
Centre (μ2)	76.72	μ3-μ1	0.47		No difference
Front(μ3)	78.83	μ3-μ2	2.11		Different

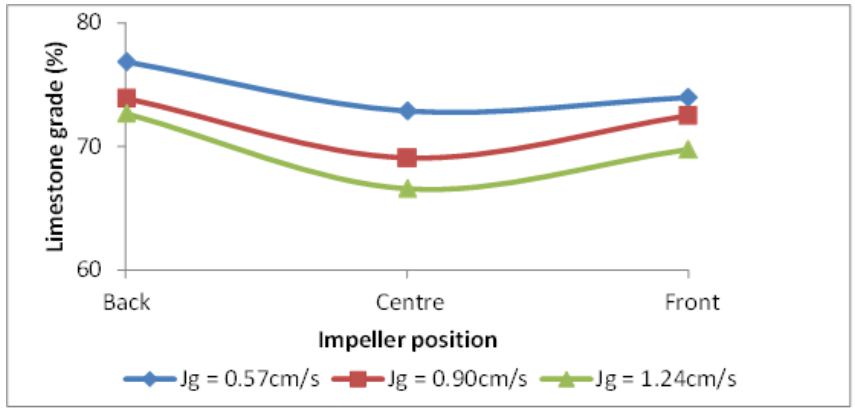

a) Limestone grade as a function of agitator position and Jg for a froth depth of 6.3cm

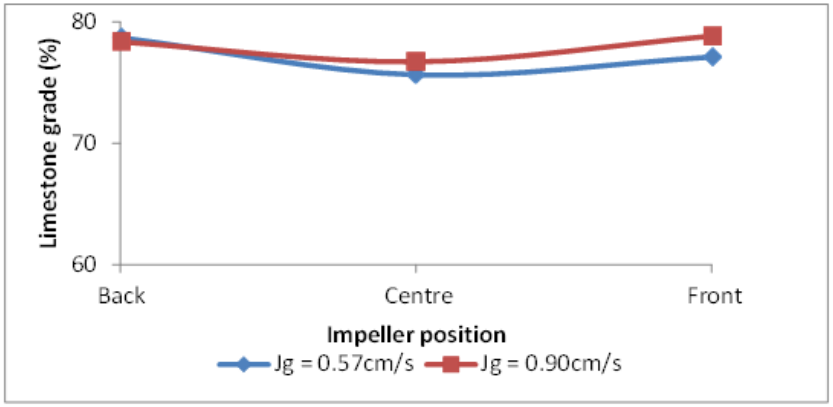

b) Limestone grade as a function of agitator position and Jg for a froth depth of 10.1cm

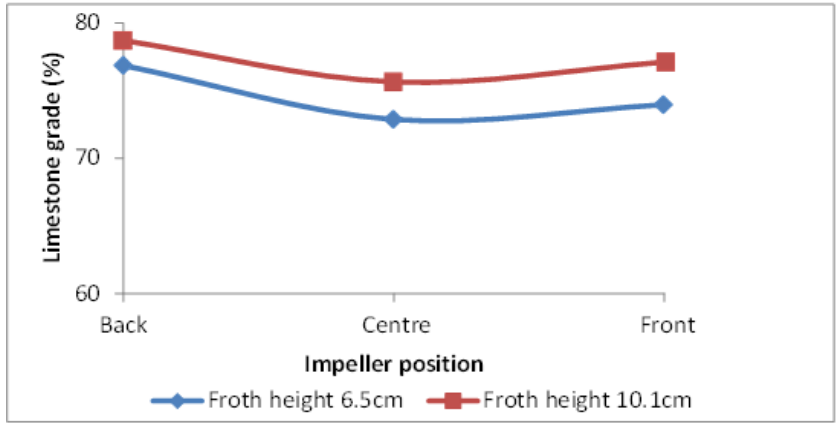

c) Limestone grade as a function of agitator position and froth depth at Jg = 0.57cm/s

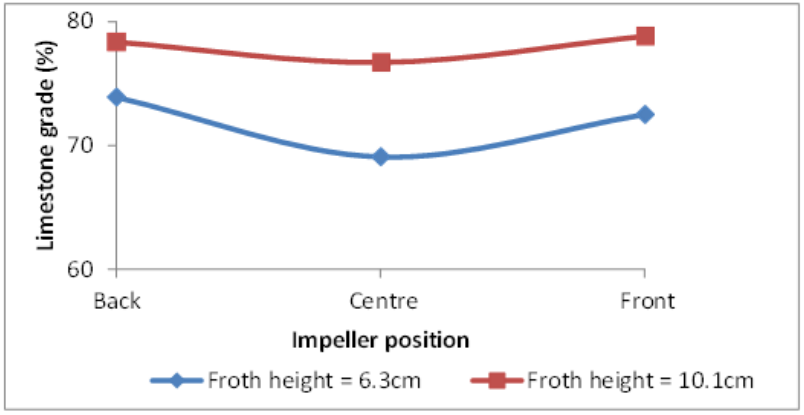

d) Limestone grade as a function of agitator position and froth depth at Jg = 0.90cm/s

Figure 6.4: Variation of limestone grade with impeller position and gas rate at two froth depths (a, b) and with impeller position and froth height at two superficial gas velocities (c, d)

6.3.4: Effect of impeller position on silica recovery, water recovery and entrainment.

Figure 6.5a and 6.5b show how silica recovery changed with air rate and impeller position for the two froth depths while 6.5c and 6.5d show how silica recovery varied with impeller position and froth height as a function of gas rate. Under these experimental conditions, silica which is non-floatable was added as the gangue material and its recovery is by entrainment. Generally the recovery of silica is at its minimum when the impeller is at the front i.e. when high gas rate is supplied close to the concentrate weir and highest when the impeller is at the centre and back for the 6.3cm froth depth and at higher superficial gas velocities. For all froth depths and at low gas rate the changes in silica recovery were found to be very low and statistically insignificant. When gas rate was increased to 0.90m/s and 1.24cm/s a trend showing low silica recoveries when the impeller was in front and high silica recoveries when the impeller was placed at the centre and at the back emerged. Subjecting the silica recovery data at froth depth of 6.3cm and a gas flux of 0.90cm/s to a two-way ANOVA and Tukey's Post hoc analysis revealed the significance of the observed silica recovery differences as shown in Table 6.5a. Table 6.5b shows the results for the Tukey analysis at a froth depth of 10.1cm and gas flux of 0.90cm/s affirming that high silica recoveries were obtained when the impeller was at the back or on the centre of the flotation cell while low silica recoveries were obtained when agitator was in front. For all gas rates and all impeller positions, high entrainment values were obtained at low froth depths and vice versa (Figure 6.5c and 6.5d).

Table 6.5: Statistical analysis for silica recovery

a) Tukey's HSD test for silica recovery at froth depth 6.3cm			Difference in Means	Tukey HSD Value	Outcome
Back (μ1)	7.76	μ1-μ2	-0.48	0.59	No difference
Centre (μ2)	8.24	μ1-μ3	1.31		Different
Front(μ3)	6.45	μ2-μ3	1.79		Different

b)Tukey's HSD test for silica recovery at froth depth 10.1cm			Difference in Means	Tukey HSD Value	Outcome
Back (μ1)	5.27	μ1-μ2	0.84	0.59	Different
Centre (μ2)	4.43	μ1-μ3	1.23		Different
Front(μ3)	4.04	μ2-μ3	0.39		No difference

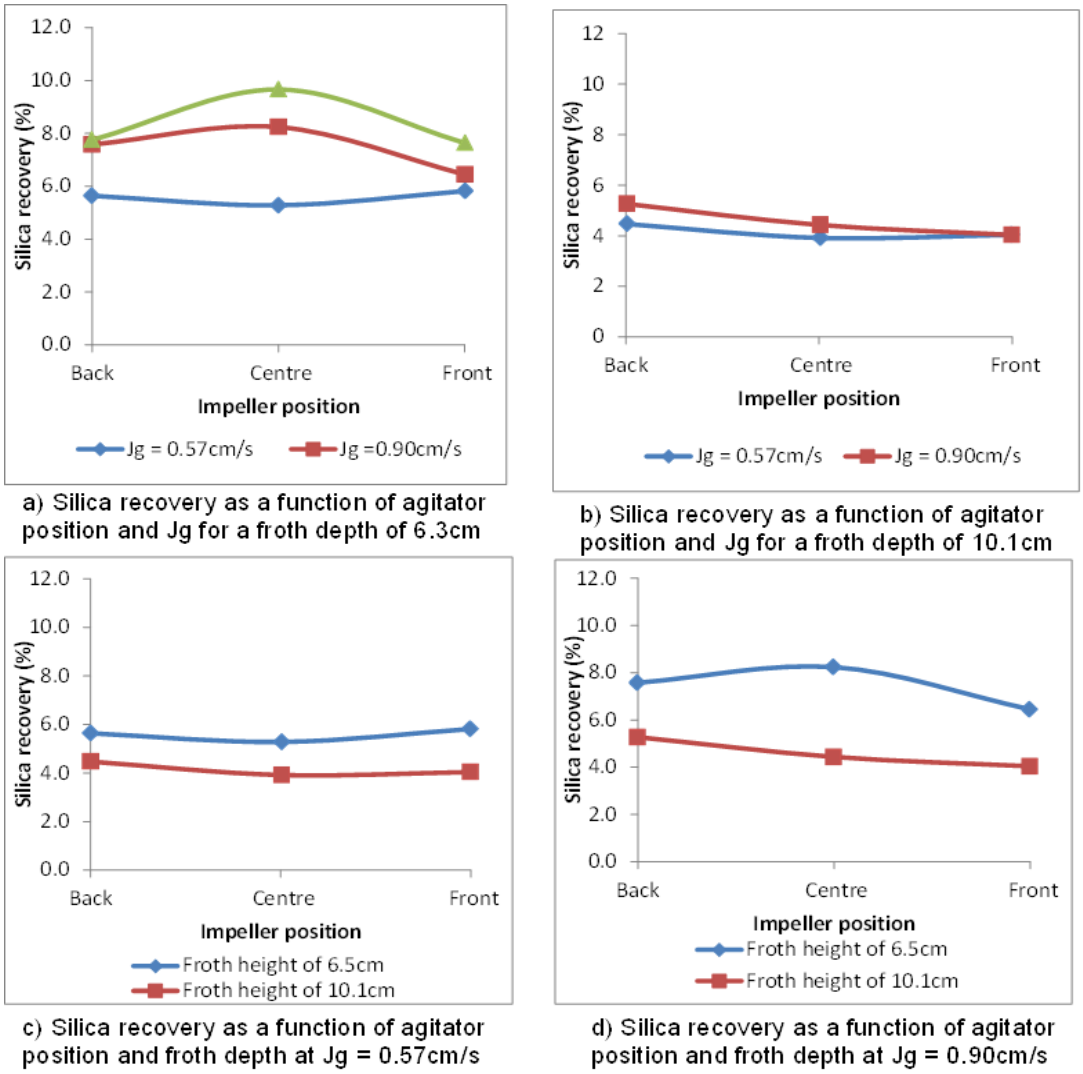

Figure 6.5: Variation of silica recovery with impeller position and gas rate at two froth depths (a &b) and variation of silica recovery with froth height at two fixed gas rates (c &d)

6.3.4.1 Effect of impeller position on entrainment

Hydraulic entrainment of gangue material is an important consideration in flotation process. Silica was used to evaluate entrainment as it was non-floatable under our experimental conditions. According to Smith & Warren (1989) entrainment is only significant for particles below 50µm; this was also reinforced by our results which show that 88% of the silica recovered to the concentrate was less than 50µm when compared to 42% in feed (Figure 6.6). The recovery of silica as a function of size class for a froth depth of 6.3cm and gas flux of 1.24cm/s is shown in Figure 6.7a while Figure 6.6b shows the silica recovery data fitted to the Yianatos et al. (2010) entrainment factor model. Silica entrainment is high at lower size classes and decreases as particle sizes increases. Thus the cumulative silica recovery is mainly

(94%) constituted of particles less than 50µm. Consequently, the silica recoveries plotted in Figure 6.4 are a strong indication of entrained silica.

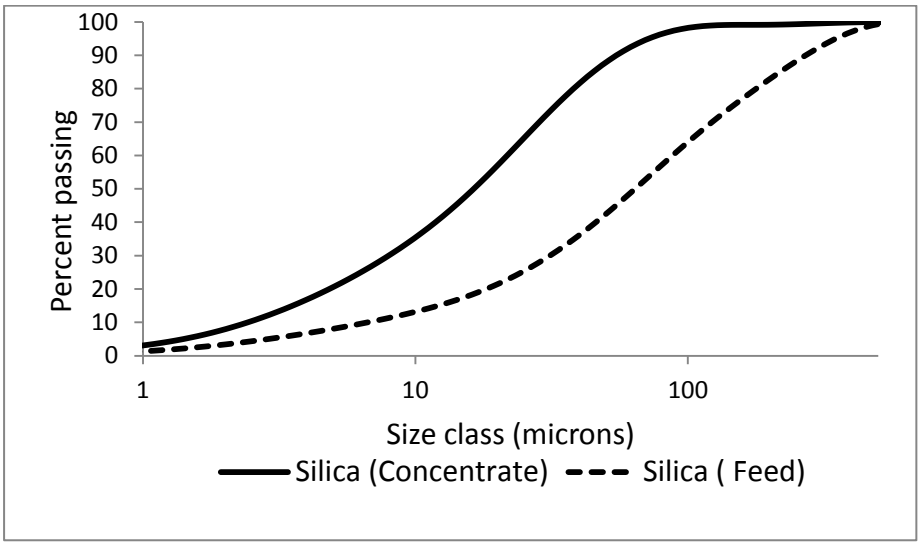

Figure 6.6: Typical silica PSDs for the concentrate and feed when impeller was at the centre.

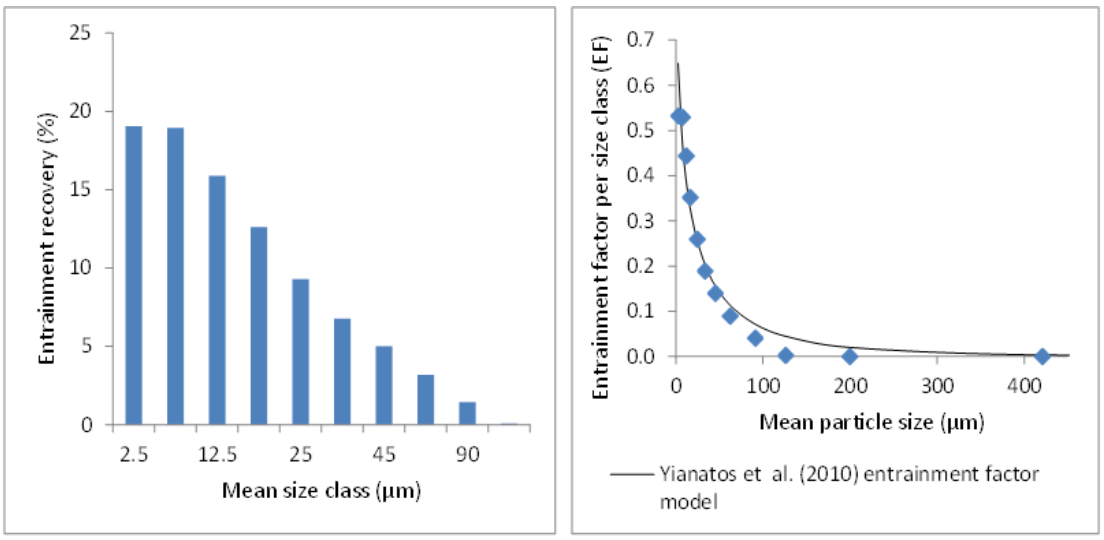

a) Silica recovery as a function of size class b) Silica recovery as a function of size class

Figure 6.7: (a) Typical silica recovery/Entrainment recovery as a function of particles size and (b) Entrainment factor per size class obtained at a gas flux of 0.90cm/s and a froth depth of 6.3cm when the impeller was at the central position fitted onto the Yianatos et al. (2010) entrainment model.

6.3.4.1 Effect of impeller position on water recovery

The relationship between water recovery and entrainment of fine material has been used in modelling recovery of gangue in flotation systems (Savassi et al., 1998;

Zheng et al., 2006). Figure 6.8a and 6.8b show how water recovery changed with gas rate at the three impeller positions for the two froth depths. As can be seen, water recovery increases with increase in gas rate at all froth depth which is consistent with results obtained by other flotation workers e.g. Moys (1979). It is again evident at high gas rates that low water recoveries are obtained when the impeller is positioned at the front of the flotation cell, with higher water recoveries observed when the impeller is at the back and centre. This observation dovetails with observation made on silica recovery and the accepted variation of water recovery with entrainment recovery e.g. Zheng *op cit*. Figure 6.9 illustrates the variation of water recovery and silica recovery based on silica feed particles less than 50µm at froth height of 6.3cm and superficial gas velocities of 0.57, 0.90 and 1.24cm/s for all impeller positions.

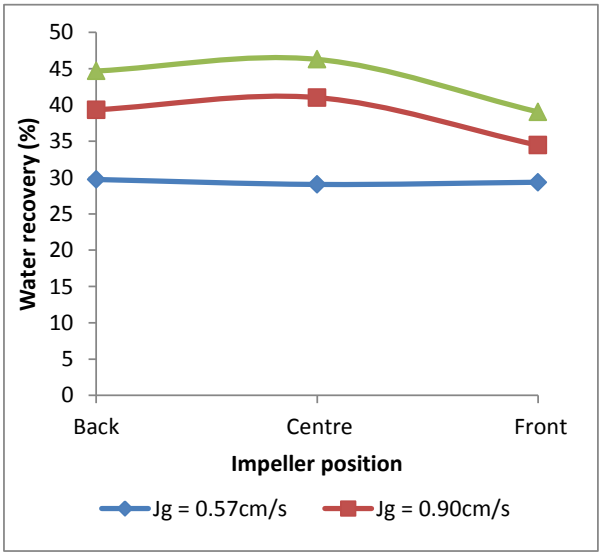

a) Water recovery as a function of agitator position and Jg for a froth depth of 6.3cm

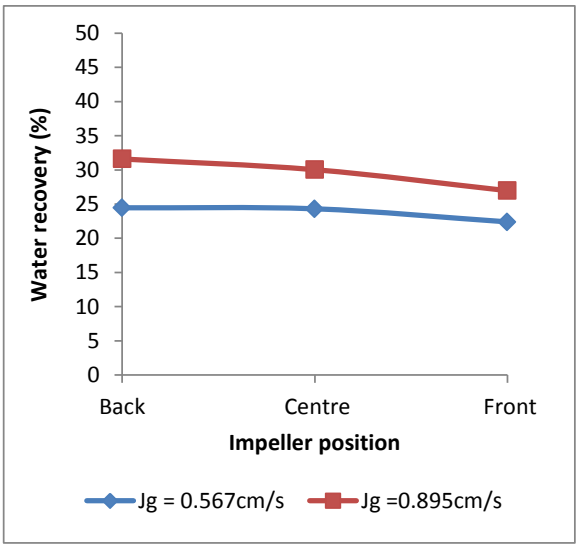

b) Water recovery as a function of agitator position and Jg for a froth depth of 10.1cm

Figure 6.8: Variation of water recovery with impeller position and gas rate at (a) froth height of 6.3cm and (b) froth height of 10.1cm

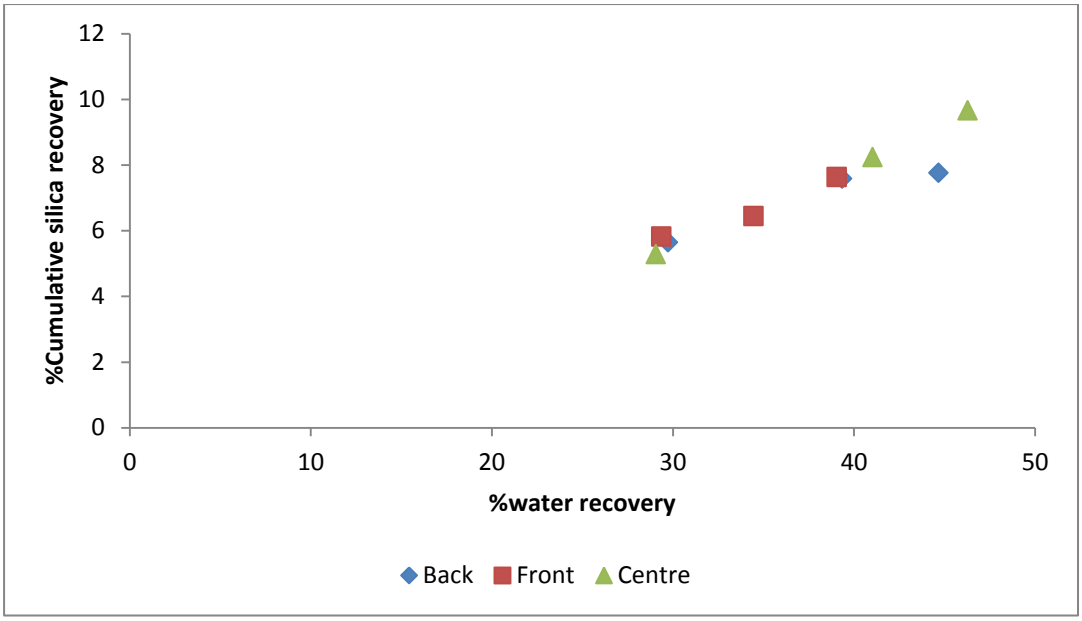

Figure 6.9: Plot of silica recovery as a function of water recovery for the three impeller positions at froth height of 6.3cm and three different gas rates (0.57, 0.90 and 1.24cm/s).

6.3.5: Summary of the effects impeller position, gas rate and froth height on flotation performance

It is evident from the experiments performed that profiling gas flux within a flotation cell has significant impact on flotation performance. High gas rate at the back of the flotation cell results in high limestone recovery at a grade comparable to the high gas flux close to the concentrate weir. Although the symmetric gas flux (impeller at the centre) is more common, results found herein reveal that for a flotation cell with a concentrate weir on one side, it produces the worst performance in terms of limestone recovery and grade. Distributing air in such a way that there is high gas flux close to the concentrate weir gave the lowest silica or entrainment recovery values. A summary of the observations is given in Table 6.

Table 6.6: Summary of the effects of impeller position, gas rate and froth height on flotation performance

Impeller/ agitator position	Air distribution profile	Effect on limestone recovery and grade	Effect on entrainment/silica and water recovery
Back	High J_g at the back of the flotation cell that decreases towards the concentrate weir. The range of superficial gas velocities was from -15% to +20% relative to the average value.	High recoveries were recorded for all gas rates and froth height when compared to the other positions (centre and front). At both froth heights recovery when the impellor was at the back was 10.5% higher than the recovery recorded when the impeller was at the centre. The recovery was also on average 6% higher than recovery when the impeller was in front Limestone grade when impeller was at the back was higher than those at the other two impeller positions especially at low froth depth. It was 5% higher than limestone grade obtained when impeller was at the centre and 1.4% higher than limestone grade obtained when impeller was in front. At higher froth depth, grade was 1.6% higher than when the impeller was at the centre and 0.5% lower than when the impeller was in front. This value was found to be statistically insignificant.	Silica recovery values were relatively lower when compared to those obtained when impeller was on the centre but were higher than values obtained when the impeller was close to the concentrate weir for shallow froth depth. Water recovery values were generally higher than those obtained with the impeller in front but less that those obtained when the impeller was at the centre
Centre	Superficial gas velocity J_g seems even with maximum change around 7%, the left side of flotation cells had on average higher gas rates than the right side of the flotation cell. This was attributed to the air supply mechanism.	Lower recoveries were recorded for all gas rates and froth height when compared to the other positions. Limestone grades obtained were also lower than the other positions especially at low froth depth. The lowest limestone grade obtained was 69% at a froth depth of 6.3cm and J_g =1.24cm/s and the highest grade obtained was 77% at froth depth 10.1cm and J_g =0.90cm/s.	Highest values of silica recovery were recorded at shallow froth depth Water recovery values when agitator was at the centre-were found to be statistically similar to water recoveries recorded when the impeller was at the back. All values were higher than those obtained when the impeller was close to the concentrate weir.
Front	High J_g values were measured at the front of the flotation cell and they decreased towards the back of the flotation cell. The range of superficial gas velocities was from -17% to +21% relative to the average value.	Recovery higher than that obtained when the impeller was at the centre but relatively lower than that obtained when the impeller was at the back was recorded for all gas rates and froth heights. Limestone grade obtained was higher than that obtained when impeller was at the centre and lower than that obtained when impeller was at the back for a shallow froth. At deeper froth depth grade similar to that obtained when the impeller was at the back was recorded though they it was still higher than that obtained when the impeller was at the centre	Performed best in terms of silica recovery as lower values of silica recovery and water recovery were obtained for all froth depths and for the high gas rates**.**

6.3.5.1 Conclusions

An experimental set-up that enables the study of the effects of gas flux on flotation performance in a single mechanically agitated flotation cell was designed. Experiments that were performed in this cell using an artificial ore comprising of silica (gangue) and limestone (floatable component) have shown that gas flux profiling in a single flotation cell with a concentrate launder on one side has a significant impact on flotation performance. Results indicate that providing a high gas flux away from the concentrate launder can result in increased grade and recovery. Providing high gas flux close to concentrate launder resulted in lower water and silica recovery and high limestone grade. The results also strongly suggest that the conventional design of placing the impeller at the centre result in a non-optimum flotation performance. Despite the fact that experiments reported above were performed in a flotation cell with a concentrate launder on one side, profiling gas across the pulp-froth interface can also be important in industrial flotation cells with concentrate launders on at least two sides (rectangular cells) or around the flotation cell (cylindrical cells). This maybe important if one considers large diameter cells with capacities of up to 600m3 that are being manufactured currently. The large diameters means that bubbles have to travel a relatively long distances before they reach the concentrate weir especially in absence of internal launders. Consequently, regions around the centre of the flotation cell maybe rendered partially inactive and do not contribute to concentrate flow optimally. In fact froth regions around the impeller in flotation cells are known to be stagnant regions where froth collapses as a result of overloading or because of the rotating shaft especially in the absence of a shroud. See work by Zheng et al. (2004). Increasing gas flux at these regions may activate them to increase their contribution to concentrate recovery. Thus an optimum distribution of gas across the interface can be a way of reducing the inactive regions in froth the same way they were reduced in our flotation cell by supplying high gas flux at the traditional ‘dead zone’ which is the back part of the flotation cell.

The flotation performance changes witnessed from the experiments suggest that there are some processes that change as the air distribution profile across the entire flotation cell is changed. It was decided that video recordings should be analysed. Results of that endeavour are presented in section 6.4.

6.4: Using froth surface velocities to explain flotation performance changes.

The changes in flotation performance witnessed as the impeller position was changed relative to the concentrate weir can be attributed to some change in both the pulp and the froth phase. In this section an explanation of why the changes in flotation performance occurred is advanced. The explanation is based on an analysis of velocity profiles of the froth phase from recorded videos of the surface of the flotation cell. It is important to note that we assumed that air flux profiling has a significant impact on froth phase sub-processes when compared to its effect on pulp-phase sub-processes. This assumption may not be true as the number of bubble-particle collisions in the bulk of the pulp-phase may change as gas flux profile changes.

On a macroscopic level sanding of the flotation cell base was used to gauge whether there were major changes in mixing regime in the pulp. Excessive sanding would mean that there is a significant change in the hydrodynamics of the pulp phase and vice versa. Excessive sanding also renders pulp level control within the flotation cell impossible as solids accumulate and interfere with the level control mechanism. Thus as a rule of thumb; experiments without sanding were assumed to have similar hydrodynamic conditions. All experiments were done without problems of level control so it was assumed that the changes as a result of the mixing were minimal and any flotation performance change was largely attributed to changes in froth flow patterns. Videos of both the surface of the froth and from the sides of the flotation cell were taken with the sole intent of analysing the trajectories/ bubble streamlines and velocity profiles as bubbles rise and as they flow across the surface of the froth. An open source software, Tracker (http://www.cabrillo.edu/~dbrown/tracker) was used to track both polystyrene beads that were sprinkled on to the froth surface as well as trace bubbles as they rise in the froth phase. Figure 6.10 is a screenshot of how bubble trajectories and bubble velocities were determined using tracker.

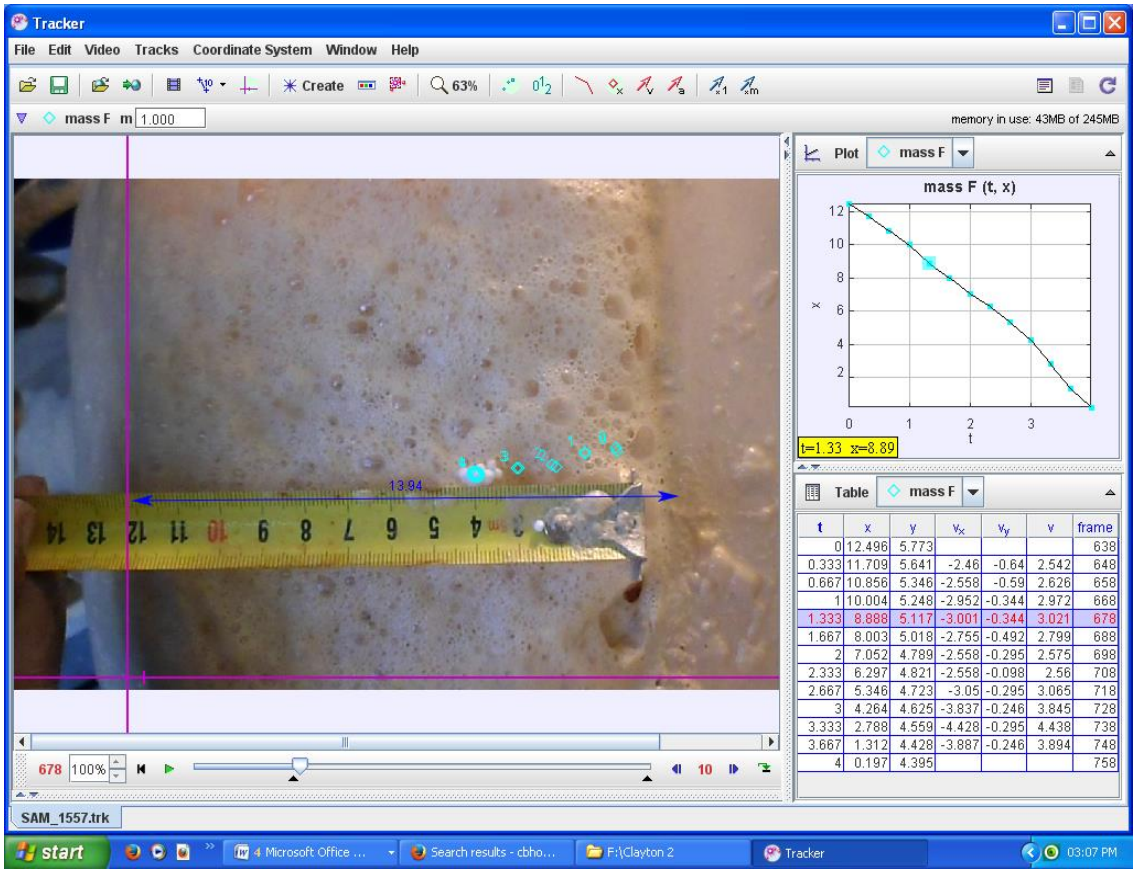

Figure 6.10: A picture illustrating how froth surface velocities and streamline position was determined using Tracker

6.4.1. Froth surface trajectories and velocities profiles for the three gas flux distribution at froth height of 6.3cm and gas flux of 0.90cm/s

Tracking of the Polystyrene beads that were sprinkled on to the surface of the froth provided some clues which can be used to explain the differences that were observed on limestone grade and recovery. Figure 6.11 summarizes the results of surface trajectories and surface velocities that were obtained at a superficial gas velocity of 0.90cm/s and froth depth of 6.3cm. For all impeller positions, the right side of the flotation cell shows the lowest surface velocities, this is in agreement with results obtained on characterisation of superficial gas velocity across the pulp-froth interface where the gas flux was on average 7% lower than the left side because of the gas distribution mechanism adopted. The central part of flotation cell exhibits the highest surface velocity for all impeller positions. This is probably because it is further away from the walls where wall effects are significant.

6.4.1.1 Surface velocity profiles when impeller was at the back

When the impeller was moved to the back, the velocity profile shown in Figure 6.10 was obtained. It shows high velocities at the back which decreases towards the centre of the flotation cell and then increases towards the concentrate launder, this unique surface flow pattern was observed under all conditions when the impeller was at the back. High values of surface velocities were obtained at the back mainly because a large fraction of the gas fed to the flotation cell was being supplied at the back of the flotation cell (according to the Jg profiles shown in Figure 6.1). Increasing gas rate at a fixed froth depth increase froth stability thereby reducing bubble coalescence and break-up, this means that air recovery at the back was high resulting in most of the air flowing with the concentrate. The crowder at the back of the flotation cell also helped in directing the froth towards the concentrated launder. Surface velocities decreased mild-way toward the concentrate weir probably because of bubble coalescence and break-up. High rates of bubble break-up mid-way towards the concentrate weir can be attributed to a number of factors e.g. high gas rates at the back and the presence of a froth crowder means that residence time of the bubble at the back is low and the water content associated with bubbles is high such that as the concentrate flows towards regions with low gas rate, drainage of the froth would commence which then results in bubbles coalescing and breaking up. This means that air recovery in centre section is low and consequently surface velocities decrease. An increase in surface velocity close to the concentrate weir is attributed to increased volume of froth as a result of contributions from the rest of the flotation cell. The complex surface velocity profile as described above can have a profound effect of flotation performance. High surface velocity at the back of the flotation cell result in an increase in recovery as it means that the froth at back of the flotation cell which is usually dormant can now actively contribute towards recovery. A decrease in surface velocity mid-way towards the concentrate weir points to a possible region where enrichment of the concentrate through froth drainage takes place while the increase in surface velocity observed towards the concentrate weir helps to maintain recovery.

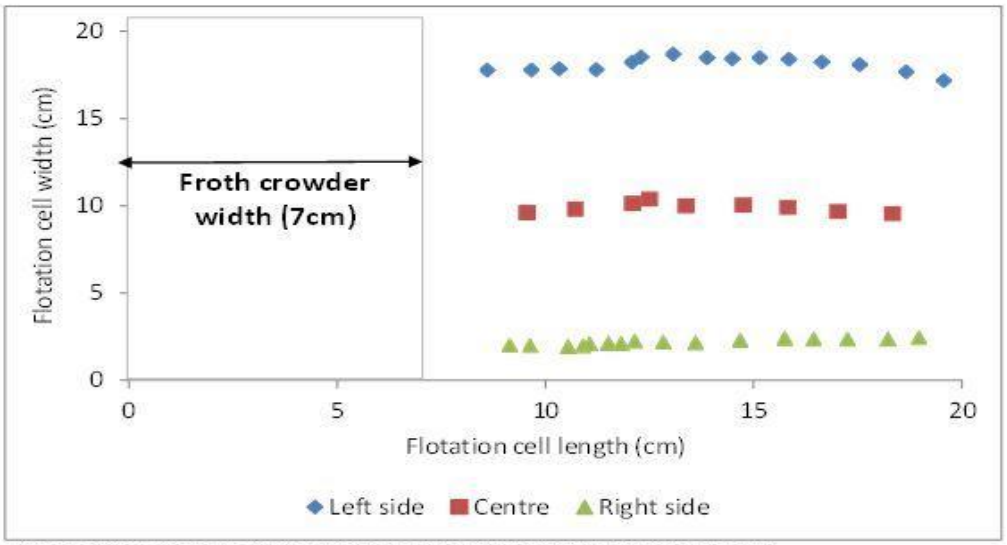

a)Tracer trajectories on the surface of the froth (agitator at the back)

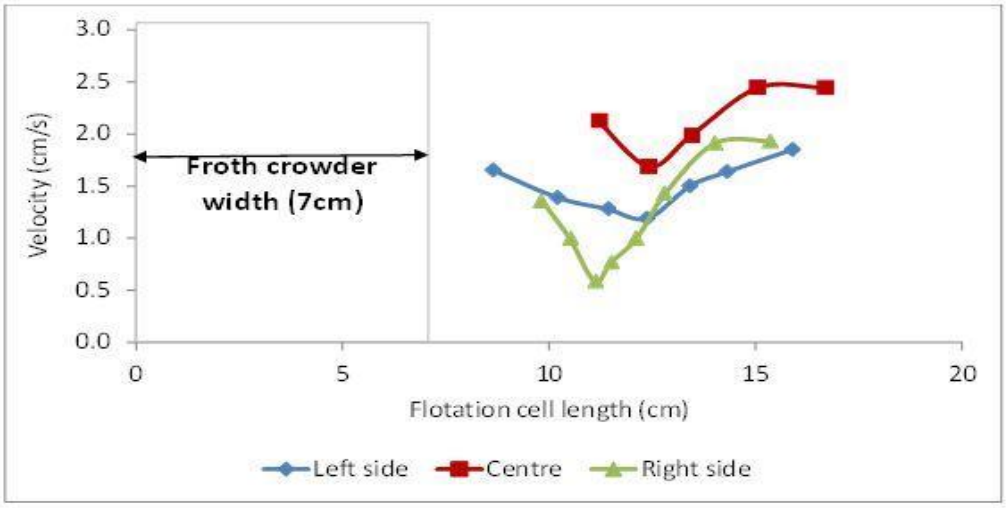

b)Surface velocity distribution profile for the trajectories in (a)

Figure 6.10: Surface trajectories (a) and velocity profiles (b) when impeller was at the back of the flotation cell for a gas flux of 0.90cm/s and froth depth 6.3cm

6.4.1.2 Surface velocity profiles when impeller was at the centre of the flotation cell

Changing the impeller to the centre shows surface velocity profiles and surface streamlines presented in Figure 6.11. The surface velocity profile shows a general increase in velocity from the back of the flotation cell to the concentrate weir. Very low velocities as low as 0.5cm/s were measured at the back of the flotation cell implying a dead zone. Higher surface velocities with values up to 3cm/s were measured close to the concentrate weir. Given the uniform gas flux distribution obtained when the impeller was at the centre as shown in Figure 6.1, this velocity profile may imply high entrainment regions close to the concentrate weir. High entrainment is possible in this

case because the well-drained high grade concentrate from the back of the flotation cell has limited chances of being recovered leaving the bulk of the concentrate to coming from regions close to the concentrate weir.

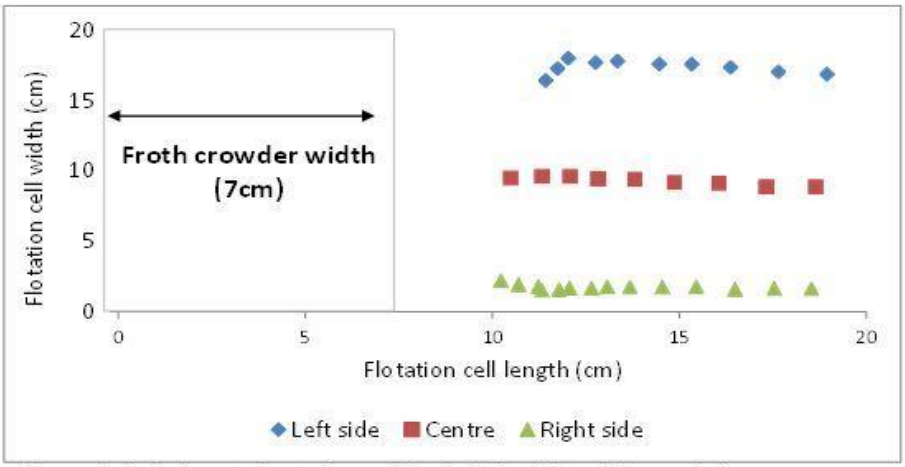

a)Tracer trajectories on the surface of the froth (agitator at the centre)

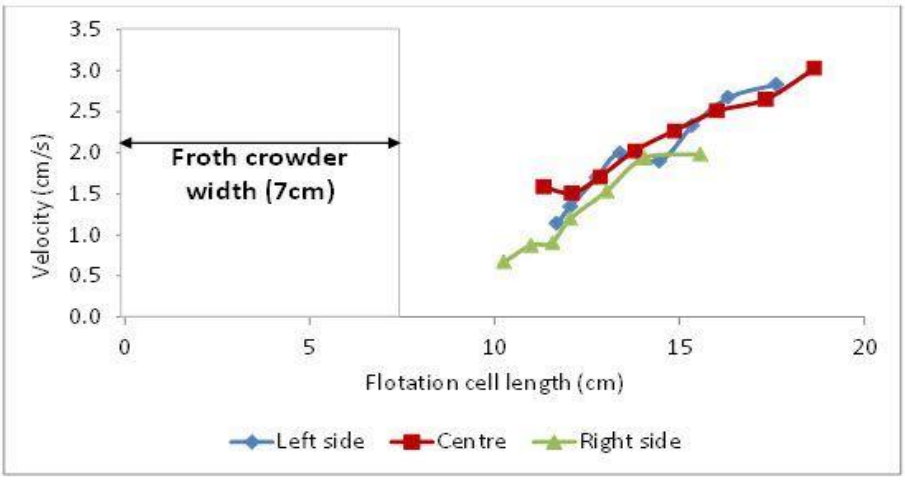

b)Surface velocity distribution profile for the trajectories in (a)

Figure 6.11: Surface trajectories (a) and velocity profiles (b) when impeller was at the centre of the flotation cell for a gas flux of 0.90cm/s and froth depth 6.3cm

6.4.1.3 Surface velocity profiles when impeller was near the concentrate weir.

When the gas flux was changed such that high gas fluxes were recorded close to the concentrate weir, froth surface trajectories and surface velocities shown in Figure 6.12 were obtained. A trend similar to the one observed when agitation mechanism was at the centre is observed, although in this case high gas flux was supplied close to the concentrate weir

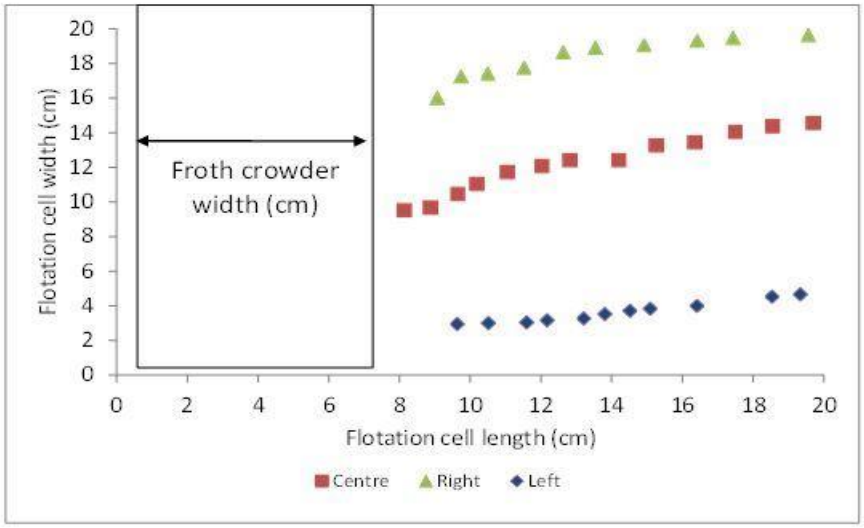

a)Tracer trajectories on the surface of the froth (agitator close to the concentrate weir)

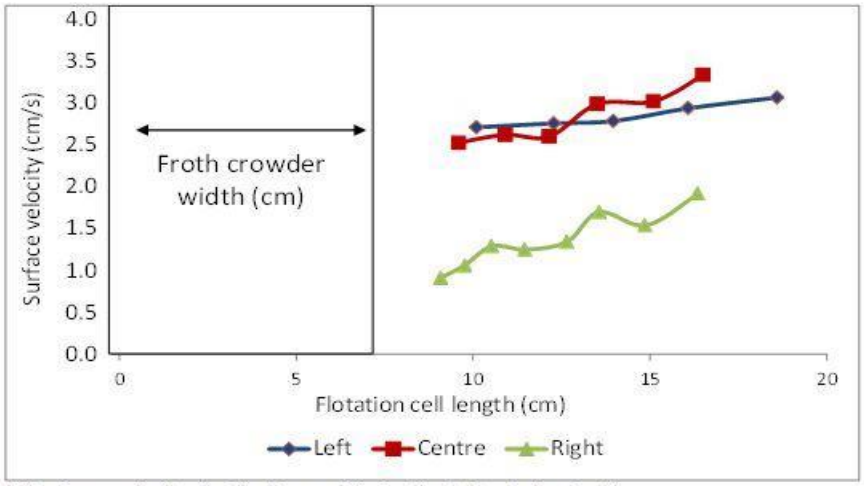

b)Surface velocity distribution profile for the trajectories in (a)

Figure 6.12: Surface trajectories (a) and velocity profiles (b) when impeller was close to the concentrate weir for a gas of flux 0.90cm/s and froth depth 6.3cm

6.4.2. Recovery and grade- froth surface velocities link

A comparison of the average surface velocities for the three impeller positions investigated in this work is shown in Figure 6.13. These values were obtained by averaging the velocities from the three positions (left, centre and right) across the surface of the flotation cell. Seen in Figure 6.13 is that the average surface velocities obtained when the impeller was at the back of the flotation is higher than those obtained when the agitator was on the other two positions for the first 15cm from the back of the flotation cell. The lowest surface velocity was obtained when agitator was at the centre (uniform gas flux). Velocities were less than 2cm/s for 75% (measured from the back of the flotation cell) of the available froth surface area for uniform gas

flux distribution whereas for the other two gas fluxes velocities were all above 2cm/s with impeller at the back showing higher values. This observation can be used to explain the low recoveries that were obtained when the impeller was at the centre as it points to possible dead zones close to the back of the cell. The presence of dead zones at the back of the flotation cell when a uniform gas flux is impressed on flotation dovetails with simulation results obtained by Moys (1979).

Interestingly the remaining 25% of the flotation cell surface that is close to the concentrate weir shows a different scenario all together. The average surface velocity when the impeller is at the centre is higher than the average surface velocities of the other two impeller positions with impeller close to the concentrate weir showing the lowest value. This change in velocity may explain the high water and entrainment recovery that was observed with impeller at the centre when compared to the other two impeller positions. Low silica and water recovery values were obtained when the impeller was close to the weir (Figure 6.4 and 6.7) which has the lowest surface velocity close to the concentrate.

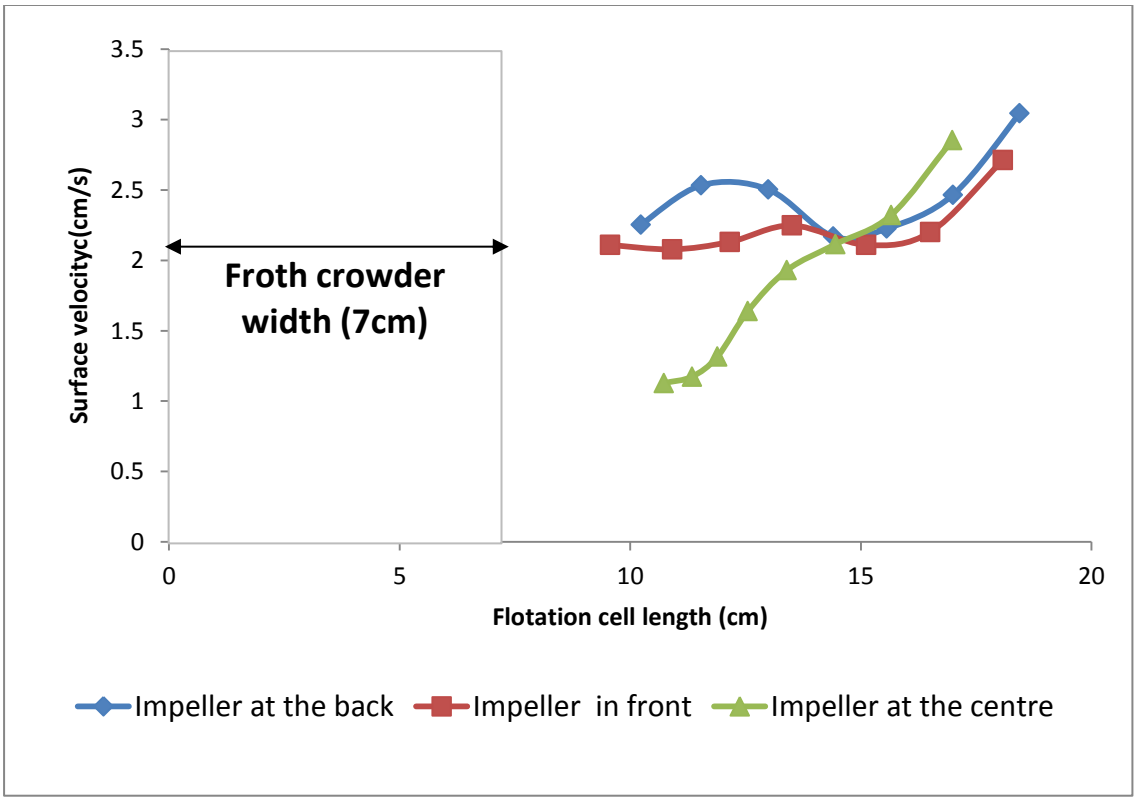

Figure 6.13: Comparison of average surface velocity at a froth height of 6.3cm for the three impeller positions at a superficial gas velocity of 0.90cm/s

6.4.2. Froth surface trajectories and froth surface velocities profiles for the three gas flux distribution at froth height of 10.1cm and 0.90cm/s gas flux

Increasing the froth height to 10.1cm and repeating froth surface velocity analysis resulted in Figure 6.14 and Figure 6.15. Figure 6.14 is summary of the trajectories and surface velocity trends that were obtained at a froth depth of 10.1cm and 0.90cm/s for all impeller positions. The trends obtained when froth depth was at 6.3cm can also be observed in Figure 6.14. The results of average velocities that were calculated are shown in Figure 6.15. Unlike at lower froth depth, the variations in average froth surface velocities are less obvious. It can be observed that the average velocity when the agitator was at the back and when the agitator was at the front of the flotation cell are almost similar with the only difference being the high values observed at the back of the flotation cell when the impeller was at the back. This reveals that the back part of the flotation cell was contributing significantly to concentrate when high gas rate was supplied at the back when compared to the other impeller positions. The lowest surface velocity values were recorded when the impeller was at the centre resulting in lower recoveries.

Now if we consider the grade obtained at this froth depth for the three different impeller positions, it is difficult to link the average surface velocity to the grades obtained for each gas distribution profile. Consider Figure 6.15 for instance, supplying high gas rate close to the concentrate weir results in higher surface velocities close to the concentrates weir, which intuitively should result in lower limestone grade. Experimental results contradict this hypothesis as high limestone grades were obtained when high gas rates were supplied to the concentrate weir. Consequently it is not possible to make conclusions on the relationship between limestone grade and surface velocity at this froth depth. This lack of clear cut relationship between gas flux distribution and surface velocity at high froth depths was also observed in Figure 6.3b. The accompanying ANOVA also revealed dwindling effect of gas flux distribution with froth height and high interaction between these two factors. This observation means that more information is required in order to explain experimental results especially at deeper froths. It thus suggested that froths rise velocity and bubble rise streamlines be obtained to facilitate elucidation of experimental results or alternatively use a froth transport model to explain the observed results.

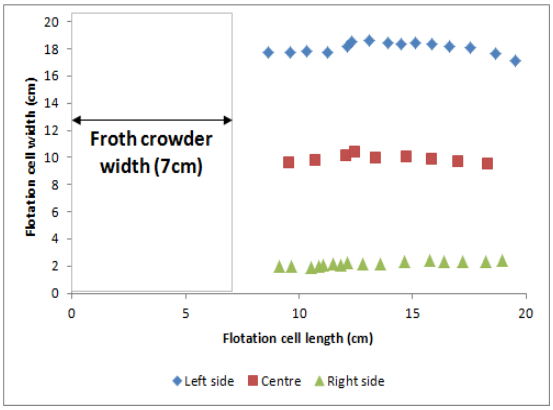

a) Tracer trajectories on the surface of the froth (agitator at the back)

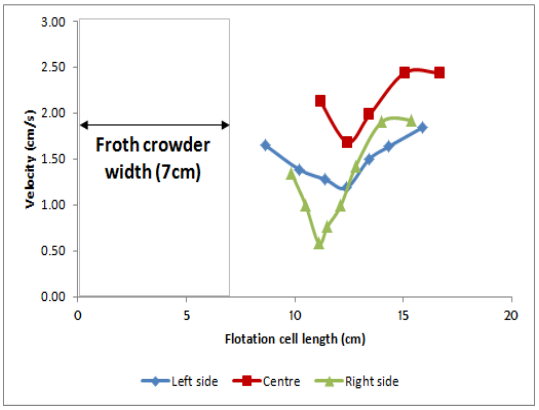

b) Surface velocity distribution profile for the trajectories in (a)

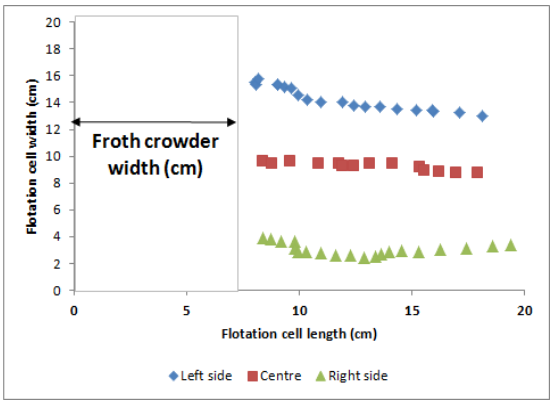

c) Tracer trajectories on the surface of the froth (agitator at the center)

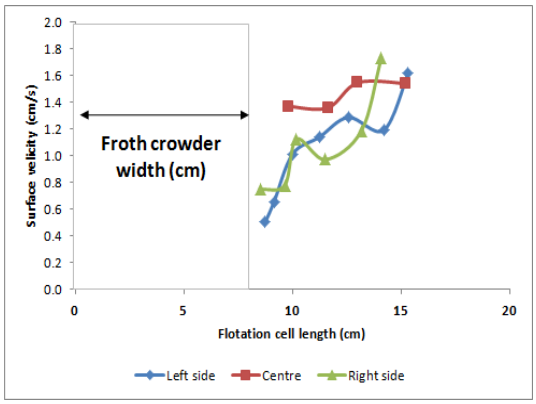

d) Surface velocity distribution profile for the trajectories in (c)

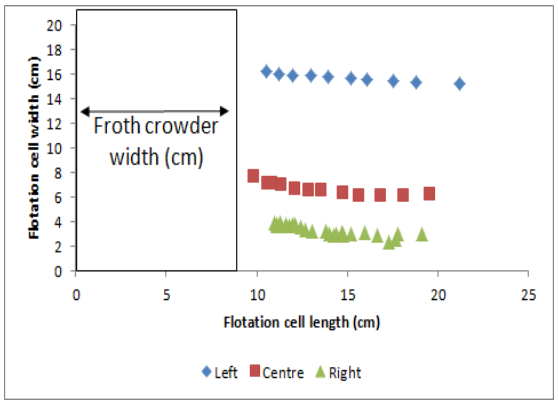

e) Tracer trajectories on the surface of the froth (agitator close to the concentrate weir)

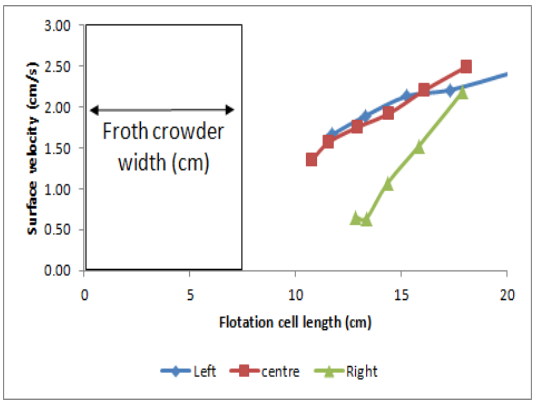

f) Surface velocity distribution profile for the trajectories in (e)

Figure 6.14: Surface trajectories and velocity profiles for the three impeller positions for gas rate 0.90cm/s and froth depth 10.1cm

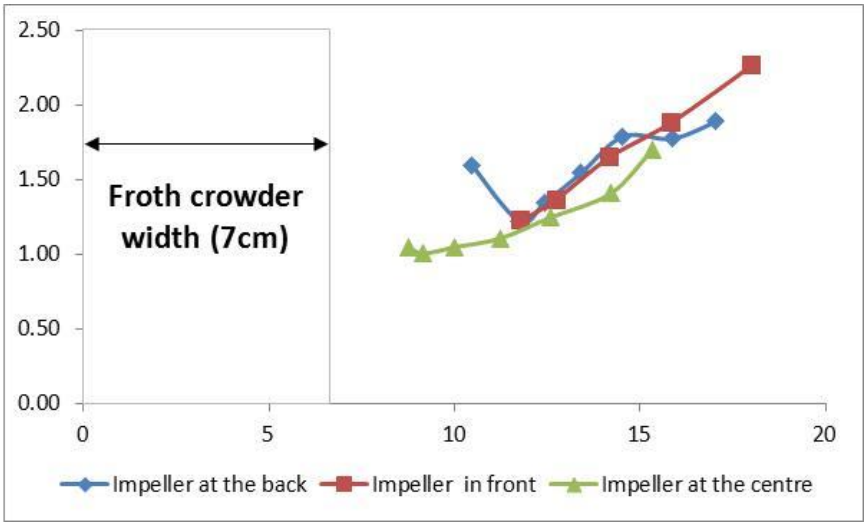

Figure 6.15: Comparison of average surface velocities for froth height of 10.1cm for the three impeller positions at a superficial gas velocity of 0.90cm/s

6.4.3. Effect of froth depth on surface velocity.

Froth depth also affects recovery and grade; data obtained herein has shown that at lower froth depth, recoveries obtained are high and grades are low and vice versa when froth depth is increased. Changing froth depth changes the average froth residence times by altering the vertical component of the residence time. Interestingly this work has also revealed that changing froth depth also alters the horizontal component of froth residence times. Analysis of average surface velocities for 6.3cm and 10.1cm froth depth is shown in Figure 6.16. At all impeller positions the average surface velocity at 6.3cm froth depth was higher than the average surface velocity at 10.1cm. This information may be important in modelling froth residence times if a solid link between the surface velocity and limestone grade and recovery is developed since surface velocity is easy to measure. Although surface velocity can provide partial insight into the froth performance, comprehensive information can be obtained if surface velocities are analysed in conjunction with rise velocities and bubble rise trajectories.

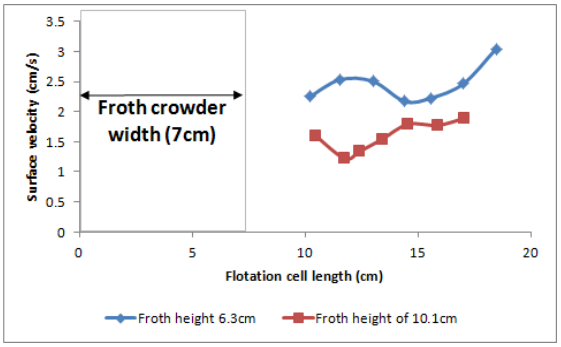

a) Impeller at the back

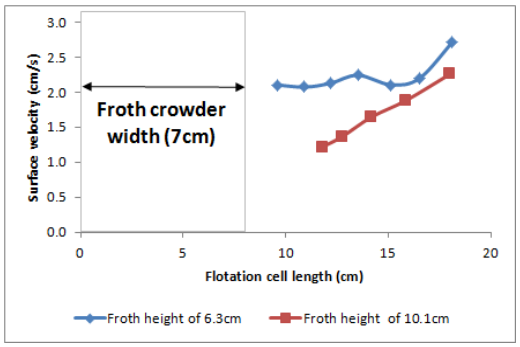

b) Impeller in front/ close the concentrate weir

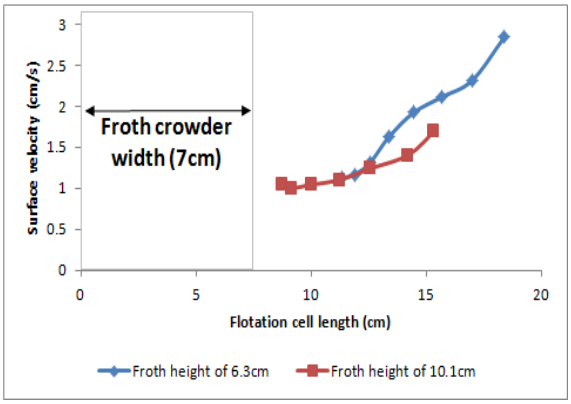

a) Impeller at the centre

Figure 6.16: Comparison of average surface velocities for froth height of 10.1cm and 6.3cm for the three impeller positions at a superficial gas velocity of 0.90cm/s

6.5 Summary and conclusions on surface velocity link

A number of important observations were extracted from the analysis of froth surface velocity profiles as a function of gas flux distribution; some of the important points are highlighted here and include that:

1) High surface velocity across the entire surface of the froth, results in high recoveries and vice versa. Consequently a gas distribution profile that ensures high surface velocity across the entire surface of the froth ensures high recovery.
2) High average froth surface velocity close to the concentrate weir means lower grades at low froth depth. When froth depth is increased, the link between surface velocities and concentrate grade disappears.

Point number two suggest that at high froth depths, surface velocities profiles alone cannot be used to explain the observed grade of the concentrate. Froth mobility which according to Cutting et al. (1986) can be described as the bubble stream profiles in the froth between the pulp-froth interface and the concentrate discharge should be used in

conjunction with surface velocities. Bubble streamlines indicate the distribution of residence times in the froth which in turn influences both froth recovery and grade. We thus conclude that surface velocities as applied in this Chapter can only partially explain the observed froth performance changes observed during experimentation. A complete picture can be obtained by additionally analysing rise velocities and the path taken by bubbles and their load as they rise from the pulp-froth interface to the surface of the froth. Tracking bubbles from the pulp-froth interface to the concentrate launder or until, they burst or coalesce is a very challenging process. Analysis of videos recorded during experimentation was done manually using Tracker and a number of factors made the process unreliable. For example at shallow froth depth, turbulence in the pulp phase generated by the agitator introduces shocks into the froth phase, thus at all times the froth oscillated up and down. This resulted in a distortion of the actual motion of the bubble and tracking of its path, especially close to the interface become highly subjective. Bubble coalescence within the froth phase or bursting on the surface cause sudden changes in the direction as the bubbles move in to occupy the cavity created when the bubble burst. Finer bubbles close to the interface were not clearly visible because of high slurry content. Consequently, it was decide that the 2D stream function equation be used to get an insight into flotation performance changes observed in experiments. It was important that surface velocity measured be included as boundary conditions when solving the stream function equation. The next Chapter is dedicated to explaining the flotation performance changes recorded in this Chapter, using the solution stream function equation subject to the measured superficial gas velocity distribution obtained for each impeller position and also the surface velocities.

Chapter 7

Use of 2D stream function equation to study the effect of gas distribution profile on flotation cell performance

7.1 Introduction

Chapter 6 describes effects of varying gas flux distribution gas across the pulp-froth interface on flotation performance in a single mechanical flotation cell. The results indicated a profound change in flotation performance as a function of gas flux distribution profile. Supplying high gas flux at the back of the flotation cell resulted in the highest recovery at intermediate grades while high gas flux at the centre produced low grades and low recoveries. Although surface velocities were used to explain these changes, a deeper understanding of the observed changes in flotation performance can be achieved through analysing bubble rise velocities, trajectories, froth residence time distribution and water drainage patterns within the froth.

Because of bubble coalescence, bubble bursting and the bulk oscillation of the froth as a result of turbulence in the pulp phase, accurate estimation of rise velocities of bubbles in absence of a suitable tracer was not possible. It was decided that a model which can describe the flows in the froth be used to facilitate a deeper understanding of the observed flotation performance changes. Work described in this Chapter used a model 2D stream function equation to provide an explanation of the observed performance changes. The 2D stream function equation/ Laplace equation was chosen for this purpose as it has been found to adequately describe the flow of froth by a number of researchers e.g. Moys (1979), Murphy et al.(1996), Neethling and Cilliers (1999) and Brito-Parada et al.(2012). Important process parameters such as froth residence time distributions, bubble streamline profiles and bubble velocity distributions were obtained from this equation. Its disadvantage though is that it does not account for drainage of water. A separate water drainage model is required.

Moys (1979) was the first to apply the Laplace equation to a simple rectangular froth flow domain in which an analytical solution was relatively easy to obtain. Murphy et al. (1996) followed after Moys *op cit*. and also applied the same equation on a simple rectangular flow domain but went further to compare the analytical solution similar to that of Moys *op cit*. to results obtained from a finite difference numerical scheme solved using successive relaxation techniques based on Gauss-Siedel method. For a complicated flow domain, obtaining an analytical solution becomes very complex and the numerical solution based on the finite difference discretisation may not be accurate. In such cases, numerical schemes based on finite element method have been applied. For example, Brito-Parada et al. (2012) applied finite element method to study the flow of foam in non-rectangular flow domain using both 2D and 3D Laplace equation. In this work, experiments reported in Chapter 6 were done in a flotation cell that has a crowder at the back making the flow domain non-rectangular, which precludes the application of the analytical solution and also puts the accuracy of numerical schemes based on finite difference to question. Consequently, we have opted for a semi-analytical approach based on the Method of Lines (MOL). The MOL is simple to code in Matlab and is also applicable to solve elliptic partial differential equations with complex boundaries.

7.2. Model

According to Moys (1979), Murphy et al. (1996) and Neethling and Cilliers (1999) the flow of foam can be adequately represented by equation [7.1] if the following assumptions are made (1) the froth is well drained (2) no frictional forces act in the froth. According to Neethling and Cilliers (1999), a well-drained froth implies that the change in internal pressure of the bubbles is small satisfying the incompressibility assumption while no friction implies that the flow is irrotational as no shear stress is introduced into the froth (Neethling and Cilliers, 2003). These assumptions are taken as true in this thesis. The advantage of equation [7.1] is that it leads to streamlines which are the isocontours of the stream function. Streamlines are important in trying to visualise the motion of bubbles and their associated load in the froth.

$$\frac{\partial^2 \psi}{\partial x^2} + \frac{\partial^2 \psi}{\partial y^2} = 0 \qquad [7.1]$$

The incompressible assumption implies that

$$u = \frac{\partial \psi}{\partial y} \quad \text{and} \quad v = -\frac{\partial \psi}{\partial x} \qquad [7.2]$$

where u and v represent x-velocity component and y-velocity component respectively.

7.2.1 Boundary conditions

The numerical solution to equations of the form of [7.1] is specific to a bounded region, thus to solve equation [7.1], boundary conditions specific to the current flow domain are required. Unlike Moys (1979) and Murphy et al. (1996) whose froth flow domains were rectangular, the flow domain herein is complicated by the presence of a froth crowder at the back of the flotation cell. Furthermore, gas distribution across the pulp-froth interface should reflect gas flux profiles that were experimentally determined in the previous Chapter. The froth chamber from which boundary conditions of the model are derived is shown in Figure 7.1. The convention of specifying boundary conditions presented by Murphy et al. (1996) is adopted where the general distribution of airflow across each boundary was defined as by equation [7.3]. This equation is then applied to each boundary depending on specific conditions on that boundary. It is important that we mention that some assumptions that contradict physical reality are made in order to simplify specification of boundary equations. For instance where wall effects play a significant role in froth flow as shown experimentally in Chapter 6, they are ignored in specifying boundary conditions on the solid walls.

$$\frac{\partial \psi}{\partial s} = g_i(s) \qquad [7.3]$$

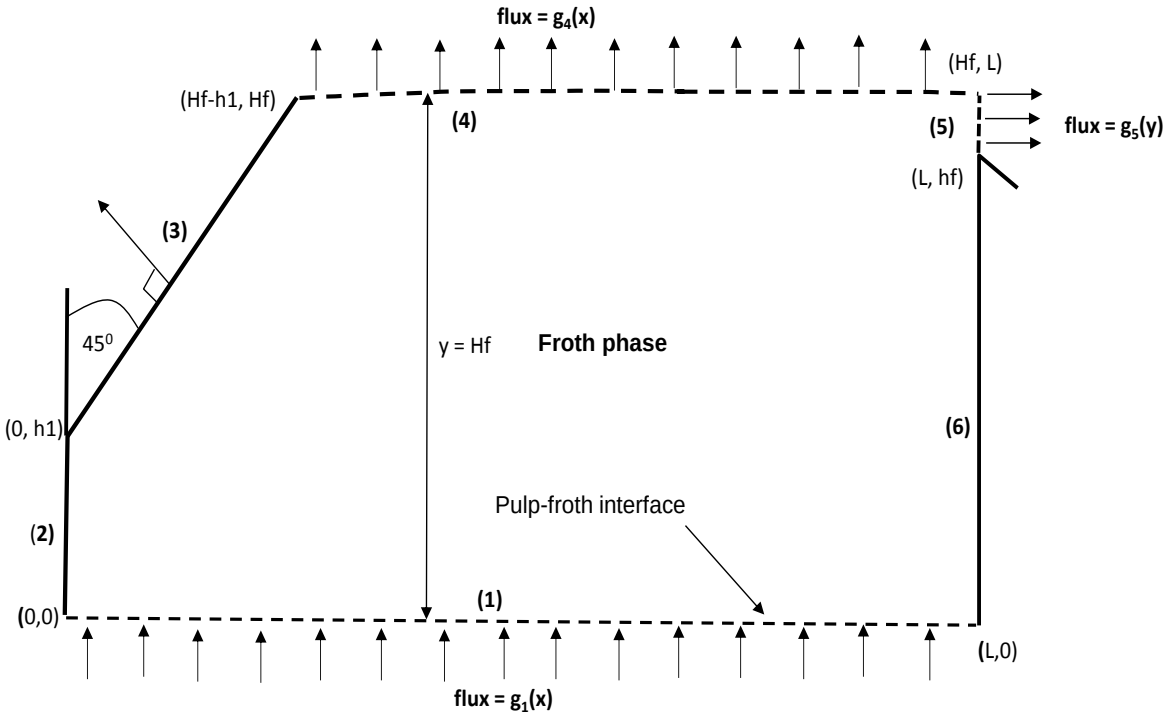

Figure 7.1: Two-dimensional flow domain showing the boundaries that need to be defined.

7.2.1 Solid walls (2), (3) and (6)

7.2.1.1 Boundary (2) Flotation back plate (0≤y≤h1)

The most obvious boundary condition that applies to all the solid boundaries is the no-penetration boundary condition. This means that the velocity normal to the wall is zero. Applying the no-penetration boundary condition on solid boundary (2) results in equation [7.7]. Note that for simplicity wall effects are ignored on all solid walls even though they play a significant role in reality.

$$\frac{\partial \psi}{\partial y}(0, y) = 0 \qquad [7.4]$$

7.2.1.2 Boundary (3) Flotation crowder (0≤x≤Hf-h1) and (h1≤y≤Hf)

This boundary is inclined at 45^0 to the horizontal and the velocity normal to this wall is a resultant of both the x and y components. Applying the no-penetration condition, a Neumann boundary condition for this wall is defined and is shown by equation [7.5].

$$\frac{\partial \psi}{\partial x}(x, h_1 + x) + \frac{\partial \psi}{\partial y}(x, h_1 + x) = 0 \qquad [7.5]$$

7.2.1.3 Boundary (6) concentrate weir wall (0≤y≤hf)

The no-penetration boundary condition on this solid wall results in equation [7.5].

$$\frac{\partial \psi}{\partial y}(L, y) = 0 \qquad [7.6]$$

7.2.2 Permeable walls (1), (4) and (5)

7.2.2.1 Pulp-froth interface boundary (1) $(0 \le x \le L, y = 0)$

Flux across this boundary is very crucial in quantifying the effects of gas flux distribution across the pulp-froth interface. In our previous work, experimental evaluation of the effects of gas flux distribution across the flotation cell was done by exploring three different gas flux regimes and these were (1) high gas flux at the back of the flotation cell (2) a uniform/ high gas flux at the centre and (3) high gas flux close to the concentrate weir. If the assumption made by Moys (1979) that the volume of liquid and solids is much less than the volume of gas is adopted, then a polynomial fit to the superficial gas velocities distributions obtained through measurements will provide a mathematical description of flux across the pulp-froth interface. In this case, if the value of stream function passing through points $\psi(0,0)$, $\psi(0, h_1)$ and $\psi(H_f - h1, H_f)$ is taken as zero and if a pseudo aeration rate Qs (cm^2/s) is defined as given by equation [7.7] then, the pseudo flux across this boundary is given by equation [7.8].

$$Qs = \frac{Q}{w} \qquad [7.7]$$

where Q is the actual air flowrate in cm^3/s and w is the width of the cell in the z direction.

$$Qs = \int_0^L g_1(x)\, dx \qquad [7.8]$$

For any stream function between 0 and L i.e. $\psi(x,0)$, flux is defined according to equation [7.9]

$$\psi(x,0) = \int_0^x g_1(x)\,dx \qquad [7.9]$$

At any point along the pulp-froth interface, the vertical component of the foam is assumed to be equal to the superficial gas velocity at that particular point, and is given by equation [7.10]. The horizontal component can be calculated from the stream function using equation [7.2]

$$\frac{\partial \psi}{\partial x}(x,0) = -\,g_1(x) \qquad [7.10]$$

The RHS of equation [7.10] assume different forms depending on the chosen superficial gas velocity profile. A polynomial of order two ($g_1(x) = ax^2 + bx + c$) was fitted to the gas distribution profiles obtained experimentally for three different gas fluxes i.e. high gas flux at the centre of the flotation cell (G-centre), high gas flux at the back (G-back) and high gas flux close to the concentrate weir (G-front). Coefficients of the polynomial differentiate the three gas fluxes.

7.2.2.2 Froth surface boundary (4) (Hf-h1≤x≤L)

The breakage of bubbles on the froth surface determines the flux across this boundary. To determine the fraction of bubbles that breaks at the surface, we define a froth stability parameter (α) according to Moys (1979) definition i.e. that it is the fraction of volumetric flowrate of concentrate to the volumetric flowrate across the pulp-froth interface. It is easy to see that the volumetric flow per unit cell width across this boundary is $(1-\alpha)Qs$ or as defined by equation [7.11]. The gradient of the resulting stream function provides the velocity components in the x and y direction. Since flux across this boundary is entirely as a result of bubble breakage, the vertical velocity component of the stream function which is equal to the bubble breakage flux $g_4(x)$ is given by equation [7.12]. The horizontal component at this boundary can be obtained by differentiating the stream function with respect to y.

$$(1-\alpha)Qs = \int_{H_f - h_1}^{L} g_4(x)\,dx \qquad [7.11]$$

$$\frac{\partial \psi}{\partial x}(x, H_f) = \frac{\partial (1-\alpha)Q}{\partial x} = -\,g_4(x) \qquad [7.12]$$

The RHS of equation [7.12] can also assumes various forms depending on the profile of bubble breakage flux on the surface of the froth. Bubble breakage rate at the surface of the froth was estimated from froth surface velocities. Zheng et al. (2004) proposed that horizontal surface velocity $(v_{fh}(r))$ at a point of radius (r) in a cell of diameter (R) can be modelled by equation [2.47] in Chapter 2 for a circular cell, this equation suggests that for fixed superficial gas velocity (Jg) and fixed froth height above the concentrate launder (hf), surface velocity is linearly dependant on the volume of froth burst per unit time per unit surface area (δ). Equation [2.47] was adapted to our rectangular cell as shown in equation [7.13]. Thus from the froth surface velocity measurements done, an approximation for RHS of equation [7.12] can be obtained.

$$v_{fh}(x) = \frac{J_g - \delta}{h_f . \varepsilon_f} . x \qquad [7.13]$$

where x is the distance from the back of the flotation cell.

7.2.2.3 Concentrate weir boundary (5) $(x = L, hf \le y \le H_f)$

The horizontal velocity component of the flow across this boundary is obtained from equation [7.14]. If this component is specified, its vertical component can easily be obtained from the stream function.

$$\frac{\partial \psi}{\partial y}(L, y) = g_5(y) \qquad [7.14]$$

Moys (1979) suggested several options for the RHS of equation [7.14] including that the flux $g_5(y)$ is invariant with y. in this work the form of equation that satisfies the RHS of equation [7.14] is obtained by satisfying equation [7.15].

$$\int_0^L \frac{\partial \psi}{\partial x}(x,0)dx = \int_{H_f - h_1}^{L} \frac{\partial \psi}{\partial x}(x, H_f)dx - \int_{h_f}^{H_f} \frac{\partial \psi}{\partial y}(L, y)dy \qquad [7.15]$$

7.2 Numerical solution development

7.2.1 Method of Lines (MOL)

The MOL is a technique that has been developed to solve PDE, by converting them into a system of ODEs. The conversion is achieved by discretising all variables except one; usually time (Schiesser and Griffiths, 2009). The system of ODEs generated can then be solved using standard ODE solvers. Thus the MOL involves two steps viz. discretising the space variables and integrating the resulting system of ordinary differential equations in time. Although the MOL is mostly suitable parabolic PDE, literature shows that it has also been applied to elliptic problems with complicated geometries. Its application to purely elliptic partial differential equations such as the stream function equation requires the addition of a time derivative of the dependent variable in a method called the method of false transients. The addition of the time derivative effectively converts the elliptic PDE into a parabolic PDE (Paul et al. 2013). Consider equation [7.1] for instance, a time dependent derivative of the stream function can be added to it such that a parabolic equation of the form shown in equation [7.16] is obtained.

$$\frac{\partial \psi}{\partial t} = \nabla^2 \psi \qquad [7.16]$$

If finite central differencing on the spatial variables is applied to the RHS of equation [7.16] and if a square grid in which the grid width (Δx) is chosen such that it is equal to the grid height (Δy) a system of ODEs represented by equation [7.17] is obtained.

$$\psi_{i+1,j} + \psi_{i-1,j} + \psi_{i,j+1} + \psi_{i,j-1} - 4\psi_{i.j} = \frac{\partial \psi_{i,j}}{\partial t} \qquad [7.17]$$

where $i = 1,2,3...n$

$j = 1,2,3...m$

The solution to the resulting system of ODEs can be obtained using standard ODE solvers such as ode45 in Matlab. The solution is obtained by marching in time until steady state conditions prevail. It is easy to see from equation [7.17] that as time approaches infinity $\frac{\partial \psi}{\partial t}$ approaches zero satisfying equation {7.1]. Thus the condition

for convergence when using the method of false transients is met when equation [7.18] is satisfied.

$$\lim_{t\to\infty} \frac{d\psi}{dt} = 0 \qquad [7.18]$$

7.2.1.1 Treatment of boundary conditions

All of the Neumann boundary conditions developed for the current domain have their RHS either as constant or as a polynomial. To incorporate these boundary conditions into the solution domain, and also to make coding easier in Matlab, the boundary conditions defined by generic equation [7.3] were converted into Drichelet type boundary conditions by integration. Integrating polynomials in Matlab is easy as such function as *polyin*t can be easily implemented.

7.3 Discussion of results

The code to implement the MOL was written in Matlab and is shown in Appendix C. Visualisation of the results i.e. plotting of bubble streamlines and velocity vector plot was done using Mathematica, using a code also shown in Appendix C. In addition to visualising the path that is most likely to be followed by bubbles and attached particles, the coding in this work was done in such a way that air recovery to the concentrate is calculated from conservation laws. This unique approach was made possible by the fact that rate of bubble breakage at the top of the froth was estimated from froth surface velocity data and also the gas flux distribution at the pulp froth interface was measured. Consequently comparison of the effect of gas distribution profile on froth performance entails comparison of the air recovery factors obtained for each gas distribution flux. During the discussion of the results, a link between air recovery values obtained for each gas distribution profile and experimental limestone recovery is inferred. It is important to note that we are aware that the relationship between air recovery and recovery of valuable minerals is not that simple. We decided to simplify this relationship because using equation [7.1] is already a simplified depiction of froth mobility and also what we are mostly interested in are trends

7.3.1 Permeable boundary specification

7.3.1.1 Pulp-froth interface flux

Gas flux across the pulp-froth interface g1(x) was obtained experimentally by measuring Jg at points indicated in Figure 6.1 in Chapter 6. By changing the position of the agitation and gas distribution mechanism to three locations viz. close to the concentrate weir, centre of the flotation cell and at the back of the flotation cell, three different gas flux distribution profiles shown in Figure 7.2 were obtained. A polynomial fit to the measured superficial gas velocities resulted in the equations shown in Figure 7.2. These equations were used as the flux across pulp-froth interface boundary conditions in simulations.

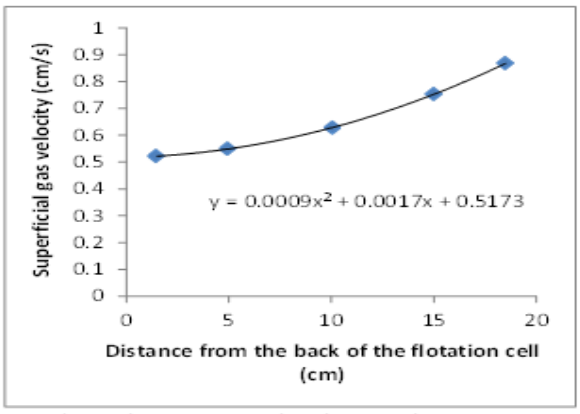

a) High gas rate at the close to the concentrate weir

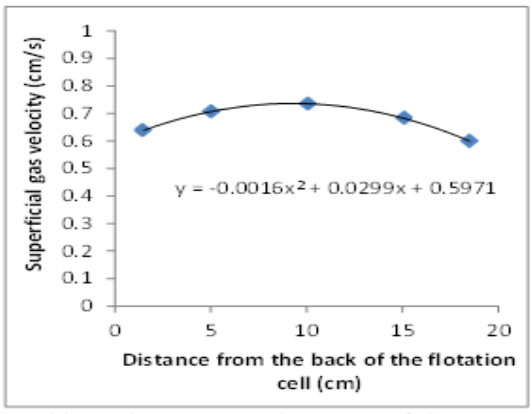

b) High gas rate at the centre of the flotation cell

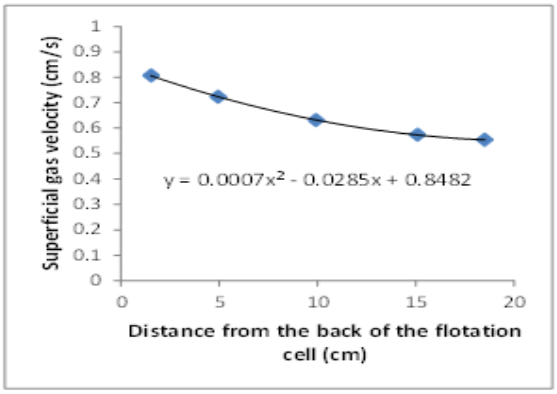

c) High gas rate at the back of the flotation cell

Figure 7.2: Gas flux distribution at the pulp-froth for (a) high gas rate close to the concentrate weir (b) high gas rate the centre (c) high gas rate at the back of the flotation cell

7.3.1.2 Bubble breakage flux

The flux across the surface of the froth as a result of bubble breakage $g_4(x)$ was obtained from measured froth surface velocities shown in Figure 7.3 a, b& c. Zheng et al. (2004) equation was fitted to the surface velocity data and the flux/bubble breakage per unit area at the froth surface was obtained and is shown in Figure 7.3 d, e & f. It is easy to see from Figure 7.3, that as surface velocity increases, bubble breakage at the top of the froth decreases and vice versa. The polynomial equations in Figure 7.3 d, e & f were taken as the equations that define boundary (4) in Figure 7.1. The flux across the concentrate launder boundary (5) is calculated from equation [7.18].

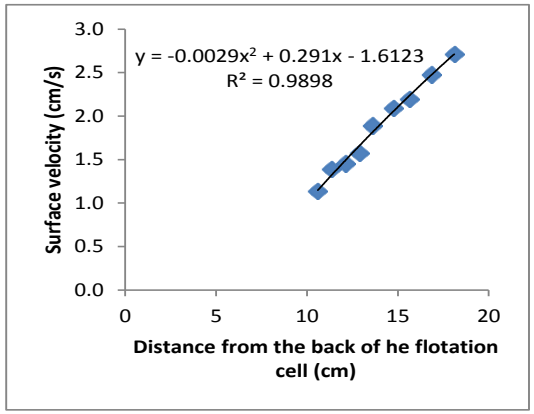

a) Froth surface velocity when high gas flux was supplied close to the concentrate weir

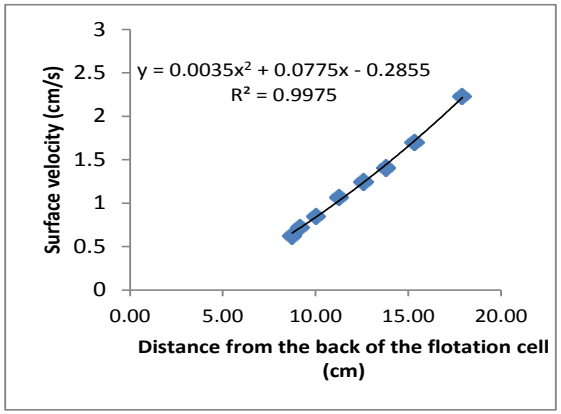

b) Froth surface velocity when high gas flux was supplied at the centre of the flotation cell

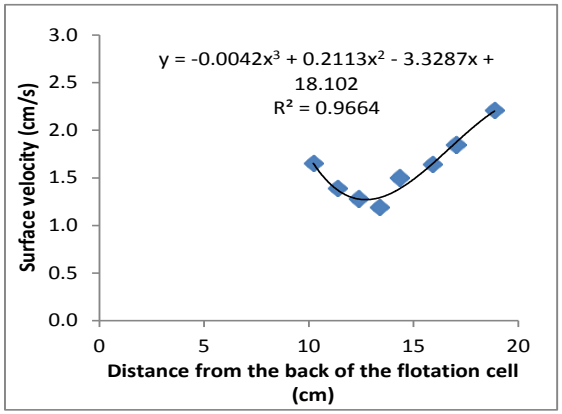

c) Froth surface velocity when high gas flux was supplied at the back of the flotation cell

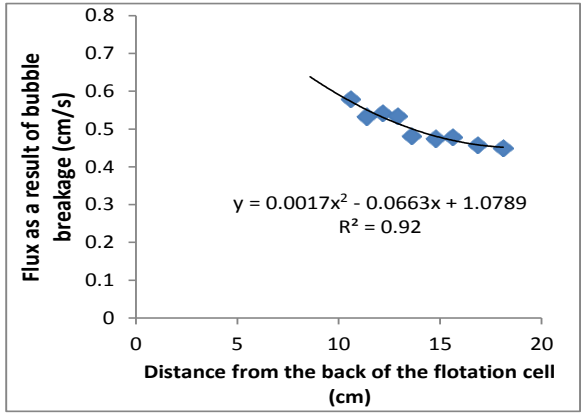

d) Flux across froth surface: high gas flux close to the concentrate weir

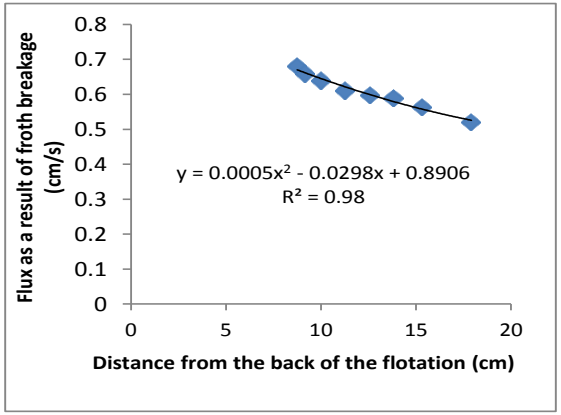

e) Flux across froth surface: high gas flux at the centre of the flotation cell

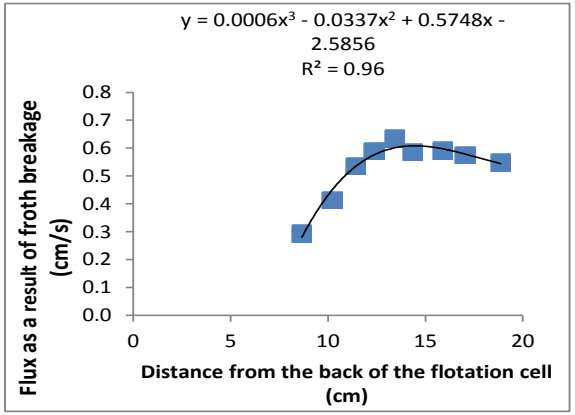

f) Flux across froth surface: high gas flux at the back of the flotation cell

Figure 7.3: Froth surface velocity as a function of distance from the back of the flotation (a,b,c) and fluxes across the surface of the froth (d,e,f) obtained for the three gas fluxes

7.3.2 Effect of gas distribution on air recovery

Applying the developed boundary equations and simulating the stream function equation resulted in streamline plots shown in Figure 7.4 a, b & c while Figure 7.4d compares the air recovery values obtained for each of the three gas flux distribution profiles. Figure 7.5 is a summary of actual experimental results obtained at froth height of 10.1cm and average superficial gas velocity of 0.9cm/s. Comparison of the resulting air recovery values shows that by supplying high gas flux at the back of the flotation cell (G-back) an air recovery factor (fraction of the inlet gas flow recovered to the concentrate) of 0.63 is found while high gas flux close to the concentrate weir (G-front) resulted in an air recovery value of 0.49. High gas flux at the centre of the flotation cell (G-centre) gave the lowest air recovery value as summarised in Figure 7.4d. These air recovery values show a similar trend to the experimental limestone recovery trends shown in Figure 7.5.

It is easy to deduce from the streamline plots (Figure 7.4 a, b & c) why G-back gives the highest air recovery value. As can be observed, the bubble streamlines for G-back shows majority of bubbles flowing to concentrate launder (Figure 7.4c), whereas Figure 4 b & c seems to suggest that bubbles from the back of the flotation cell have a lower chance of being recovered to the concentrate as a majority of these bubbles have higher chance of breaking at the surface of the froth. Furthermore, because these bubbles reach the surface of the froth close to the back of the flotation cell, they have to travel an extra horizontal distance to reach the concentrate weir. This means that they have more time to allow drainage of slurry. Particles attached to the bubbles are assumed either to flow horizontally when bubbles burst or drain back to the pulp phase. This also could be the reason why high limestone recovery was obtained when high gas flux was supplied close to the concentrate weir.

The streamline plots in Figure 7.4 do not offer a clear-cut explanation on why G-front gives a 5% higher air recovery and 8% higher limestone recovery when compared to G-centre. A possible explanation for this behaviour is obtained if Figure 7.6 is considered. It shows how velocity changes within the froth as a function of distance from the back of the flotation cell for the three gas flux distributions. From the actual velocity vector plots it may be difficult to readily see the differences in velocity until a closer look to the superimposed velocity density plots. The variation in the colours indicates different velocities. Consider the colourbar in Figure 7.6 for instance; it is easy to see that the

maximum velocity of 4.8cm/s (measured at the concentrate weir) was recorded for G-back followed by a value of 4cm/s for G-front and lastly a value of 3.6cm/s for G-centre. It is important to note that the maximum and minimum froth velocities for each gas flux distribution profile were used as the minimum and maximum values for the colourbars. Since the maximum velocities are registered at the concentrate weir, they determine the concentrate rates such that for a given time, concentrate flowrate would also follow the air recovery trend shown in Figure 7.4d. Consequently, the 11% difference in concentrate flux between G-centre and G-front could be the reason why high gas flux close to the concentrate weir has a higher air recovery and limestone recovery when compared to high gas flux at the centre of the flotation cell. This difference in fluxes across the concentrate weir points to high bubble breakage rate which reduces concentrate volumetric flowrate since the gas flowrate into the flotation cell was constant for the three gas flux distributions.

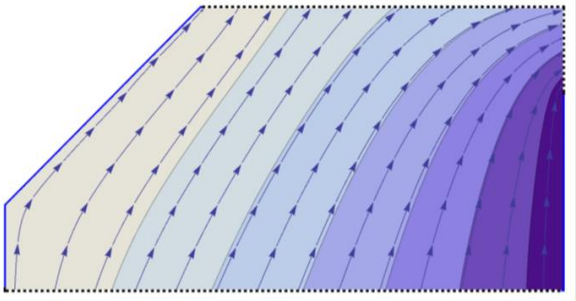

a) High gas flux close to the concentrate weir (G-front)

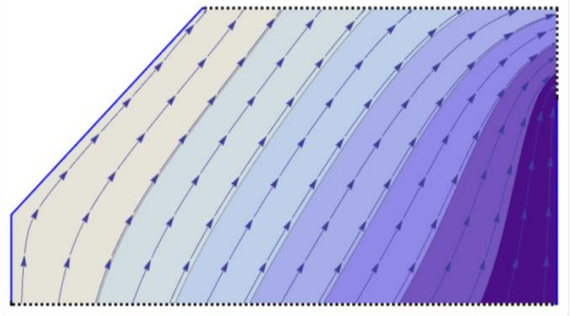

b) High gas flux at the centre of the flotation cell (G-centre)

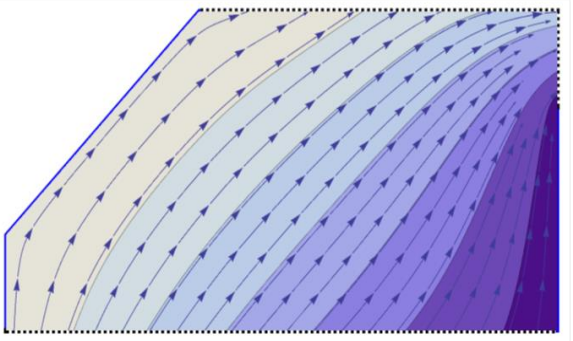

c) High gas flux at the back of the flotation cell (G-back)

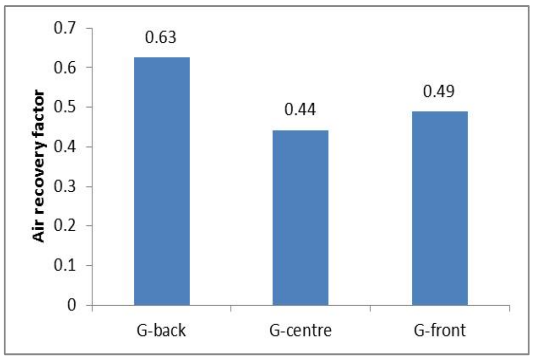

d) Air recovery

Figure 7.4: Bubble streamline plot for (a) high gas flux is supplied close to the concentrate weir (G-front) (b) high gas flux at the centre (Ge-centre) (c) high gas flux at the back of the flotation cell (G-back) and air recovery values for the three fluxes

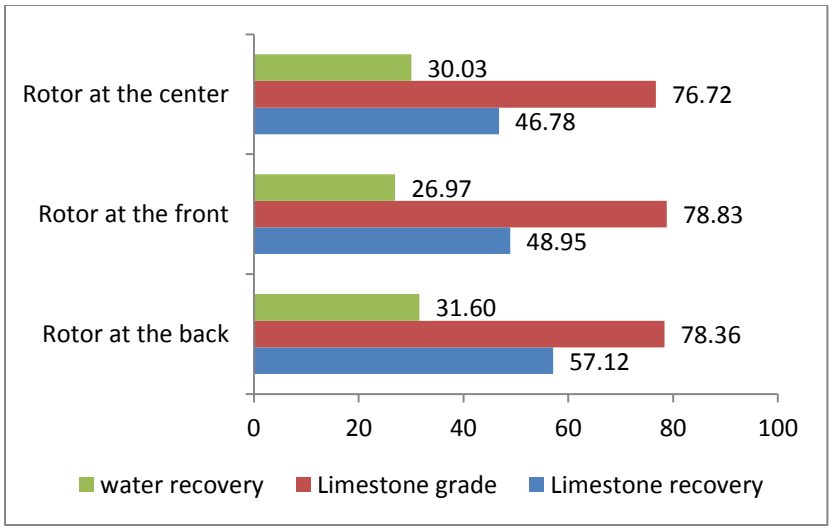

Figure 7.5: Summary of flotation performance obtained when froth depth and average gas rate was set at 0.9cm/s

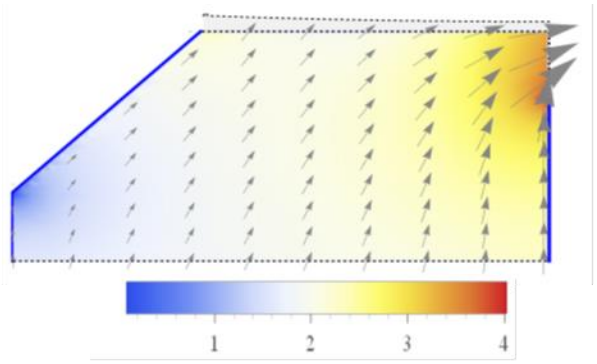

a) Velocity vector plot for G-front

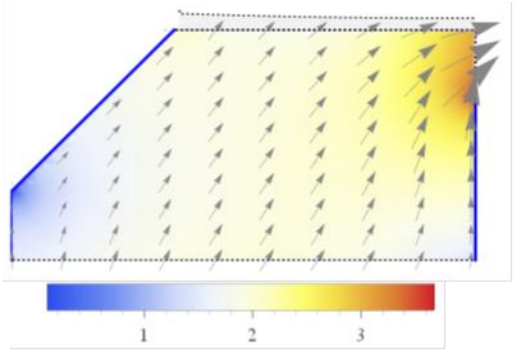

b) Velocity vector plot for G-centre

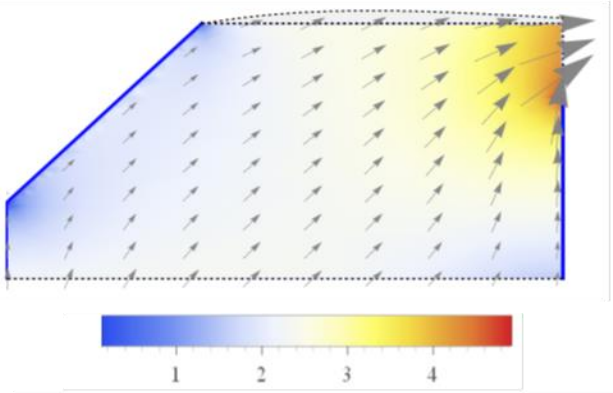

C) Velocity vector plot for G-back

Figure 7.6: Simulated velocity distributions in the froth phase for each of the gas distribution profiles.

7.3.3 Effect of gas distribution on froth residence time

7.3.3.1 Bubble residence time

The time that a loaded bubble spends in the froth phase is an important parameter in optimising froth phase performance. A distribution of these times termed froth residence time distribution has a profound impact on overall recovery through its influence on froth recovery. The relation between froth recovery and froth residence time has typically been expressed mathematically by equation [2.27] in Chapter 2. Concentrate grade also depends on froth residence time; with longer residence times providing ample time for unattached particles to drain back to the pulp phase which result in improved grade and vice versa. Thus longer residence times generally favour grade at the expense of recovery. In this section our working hypothesis is that the variation of gas flux across the pulp-froth interface has a profound impact on the distribution of residence times in the froth. Flotation performance will therefore depend on the distribution of residence times. A code that enables tracing and estimation of the time that a bubble takes from the pulp-froth interface until it reaches, the concentrate weir or it bursts at the top of the froth was written in Wolfram Mathematica and is shown in Appendix C. The code is based on equation [7.2]. Vertical and horizontal velocity components are calculated along a streamline until the bubble burst at the top or is recovered at the concentrate weir. These velocity components are then used to calculate the time taken for each bubble to travel from the interface until it burst or is recovered to the concentrate.

Figure 7.7 illustrates the distribution of bubble retention times as a function of distance from the back of the flotation cell. From this figure, a trend where bubbles that are generated at the back of the flotation showing longer residence times when compared to those generated close to the concentrate weir can be observed. Of interest also is the observation that the residence times obtained for G-front show higher values for the first 15cm from the back of the flotation cell than the other gas distribution profiles. The distribution obtained for G-centre shows the lowest values for the first 10cm from the back of the flotation cell. Converting the data in Figure 7.7 into a cumulative frequency curve (Figure 7.8) reveals interesting trends especially if the lowest and longest mean residence times are examined. It is easy to interpolate from Figure 7.8 that 50% of bubbles produced when high gas flux was supplied close to the concentrate weir (G-front) have residence times less than 15s while 50% of bubbles produced when high gas

rate was supplied close to the back (G-back) and G-centre have residence times less than 12s. All things being equal, this result should mean similar water recovery values and grade should be obtained for G-back and G-centre while G-front should produce low water recovery and high grade. But if we consider the shortest residence time i.e. less than 10s, we can see that G-back resulted in the highest frequency (39%) of bubbles with residence time less than 10s while G-centre and G-front produced 32% and 29% bubbles with less than 10s respectively. if we assume (Figure 7.7 supports the assumption) that bubbles with this mean residence time are generated close to the concentrate weir, its then safe to say that they are most likely to be recovered to concentrate. It is also important to note that these bubbles have the shortest time for drainage of entrained particles therefore they are most likely responsible for loss in concentrate grade and also results in high water recoveries. Consequently it is expected that recovery (values, entrainment and water) should decrease in the order high gas flux at back, centre and front while grade is expected to increase in that order.

Now let's consider the fraction of bubbles with the longest residence times by assessing the remaining 50% of all bubbles. For G-centre and G-back, these bubbles have a residence time (Tf) greater than 12s while for G-front they have Tf more than 15s. The distribution of the bubbles is shown in Table 7.1.

Table 7.1: Residence time distribution for 50% of bubbles with longest residence time

Point of high gas flux	12<Tf ≤15	15<Tf ≤ 20	20<Tf ≤ 25	25<Tf ≤ 30
Back	27	63	10	0
centre	54	42	4	0
Front	0	78	20	2

From the distribution shown in table 7.1, we can see that G-front results in larger number of bubbles with higher residence time when compared to the other gas distribution profiles. Of importance also is the observation that even though G-centre and G-back produces 50% of bubbles with residence times greater than 12s, the way in which the residence times are distributed is different.

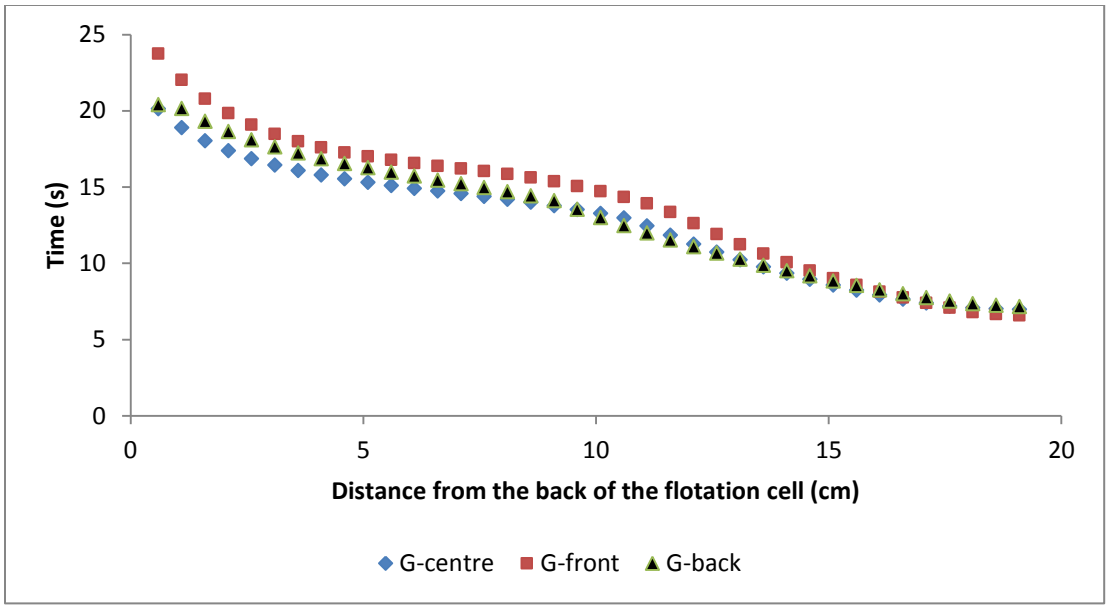

Figure 7.7: Variation of bubble residence times as a function of distance from the back of the flotation cell.

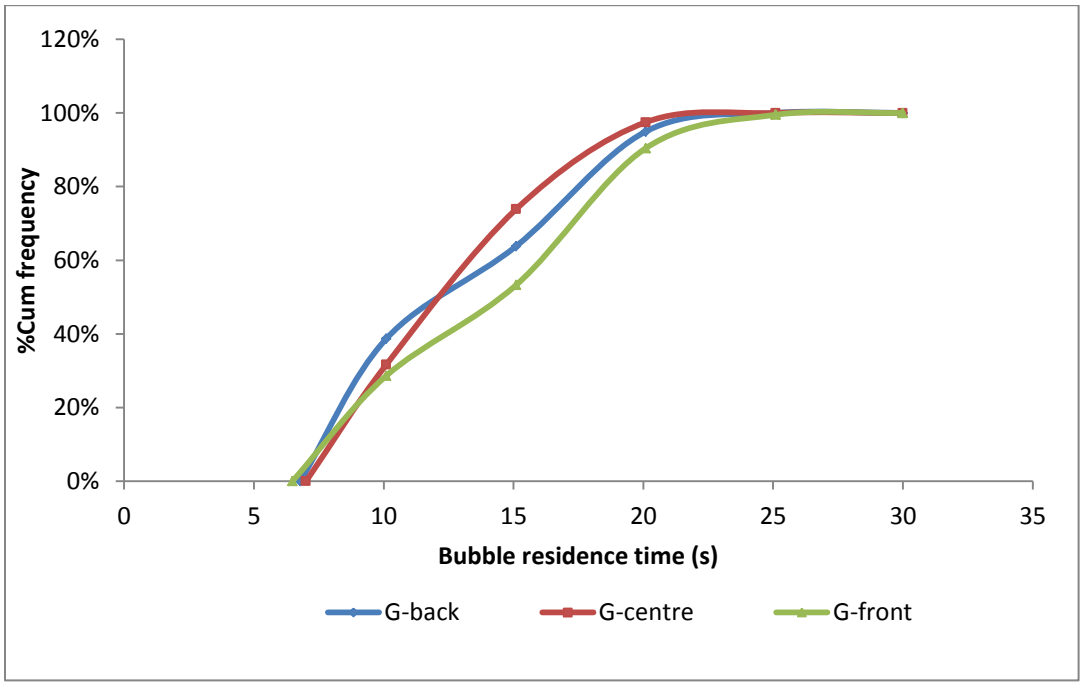

Figure 7.8: Cumulative bubble residence time distribution for the three gas flux distribution profiles.

7.3.1.1: Comparison of simulation data with experimental data

From the discussion presented above, it is very clear that the manner in which gas is distributed across the pulp-froth interface, changes froth residence time distribution. In this section we try to create a link between the residence time distributions obtained from simulations to the flotation performance observed experimentally. We emphasise that the stream function equation used to obtain the froth residence time distributions does not account for all the froth phase sub-processes that govern froth performance therefore where experimental results do not agree with simulation predications, points to the inadequacy of the current model. To circumvent using mean residence times, we instead opted to use the distribution of residence times of bubbles that have the minimum and maximum residence times. This resulted in us adopting a convention which says that bubbles with residence times lower than the median controls overall recovery while bubbles with residence times above the median controls grade. From Figure 7.8, it is easy to see that recovery would increase in the order G-front, G-centre and G-back. This agrees with experimental results except for G-centre which experimentally resulted in the lowest recovery. Intuitively this means that G-back should result in highest water recovery followed by G-centre and G-front; this agrees with the water recovery values shown in Figure 7.5.

Let's consider concentrate grade which according to our convention is largely controlled by residence time distribution of bubbles with residence times greater than the median residence time. From Table 1, the highest grade should then be obtained with G-front, G-back and lastly G-centre. Now consider Figure 7.5. The highest grade was obtained with G-front and G-back while the lowest grade was obtained with G-centre. This result again partly agrees with the predictions from residence time distributions although, where simulations seem to suggest a big difference in grade especially between G-back and G-front experimental results show a statistically insignificant difference. The partial agreement between residence time predictions and experimental data seems to suggest that although the use of number of bubbles with the minimum and maximum residence time can partly explain the observed performance differences, an improved understanding maybe accrued from using particle residence times instead of bubble residence times.

7.3.3.2 Effect of gas distribution on particle residence time

If the assumption previously used by Moys (1979) that particle residence time is always greater than or equal to bubble residence time is adopted, and if we further assume that when a bubble burst at the surface of the froth, its load will travel to the concentrate at a velocity equivalent to the froth surface velocity, particle residence times can be obtained for each gas distribution profile. The surface velocities plotted in Figure 7.3 a, b & c were used in conjunction with rise velocities to estimate particle residence times. Figure 7.9 shows the simulated particle residence times for the three gas distribution fluxes while Figure 7.10 is a cumulative residence time plot as a function of distance from the back of the flotation cell. It is clearly visible in Figure 7.9 that G-front produces particles with highest residence time for the first 14cm from the back of the flotation cell while the lowest residence times are obtained with G-back. Converting data in Figure 7.9 into a cumulative frequency curve (Figure 7.10) clearly reveals that G-back produces particles with lowest residence times while G-front produces particles with the highest residence times.

If particle residence times were solely responsible for froth performance, then G-front should produce high limestone grade and low recovery while G-back should produce, the highest recovery and the lowest grade, with G-centre producing intermediate grade and recovery. Now if we consider Figure 7.5 it is easy to see that highest recovery was obtained with G-back and low recoveries obtained for both G-centre and G-front albeit recovery obtained for G-centre being 2 percent lower than that for G-front. G-front produced the highest grade as predicted by the simulations; G-back also produced a grade statistically similar to the grade produced G-front contradicting simulations predictions. The lowest grade was found with G-centre.

From the comparison of experimental data to flotation performance based on froth residence times, it can be seen that froth residence times alone cannot completely account for all the froth phase sub-processes and therefore cannot accurately explain froth performance on it's on. Consequently, we suggest that an improved explanation can be accrued by coupling the residence time distributions with a froth drainage model. A froth drainage model will be able to capture the minute differences in froth drainage patterns that arise as a result of differences in superficial gas velocity distribution across the pulp-froth interface. Of importance also is the influence of gas rate on froth stability,

which then governs bubble breakage as exemplified by Figure 7.3 d, e & f. Results presented in Chapter 5 also reveal that indeed gas rate influences froth stability. In the current work the flux across the pulp-froth interface is not uniform, it is thus expected that different drainage patterns prevail on each section of the froth. Sections with low gas rate may produce well-drained froth than sections where the gas velocity is high. These minute variations in drainage patterns and froth stability across the entire froth maybe the source of the inconsistencies observed with the current model.

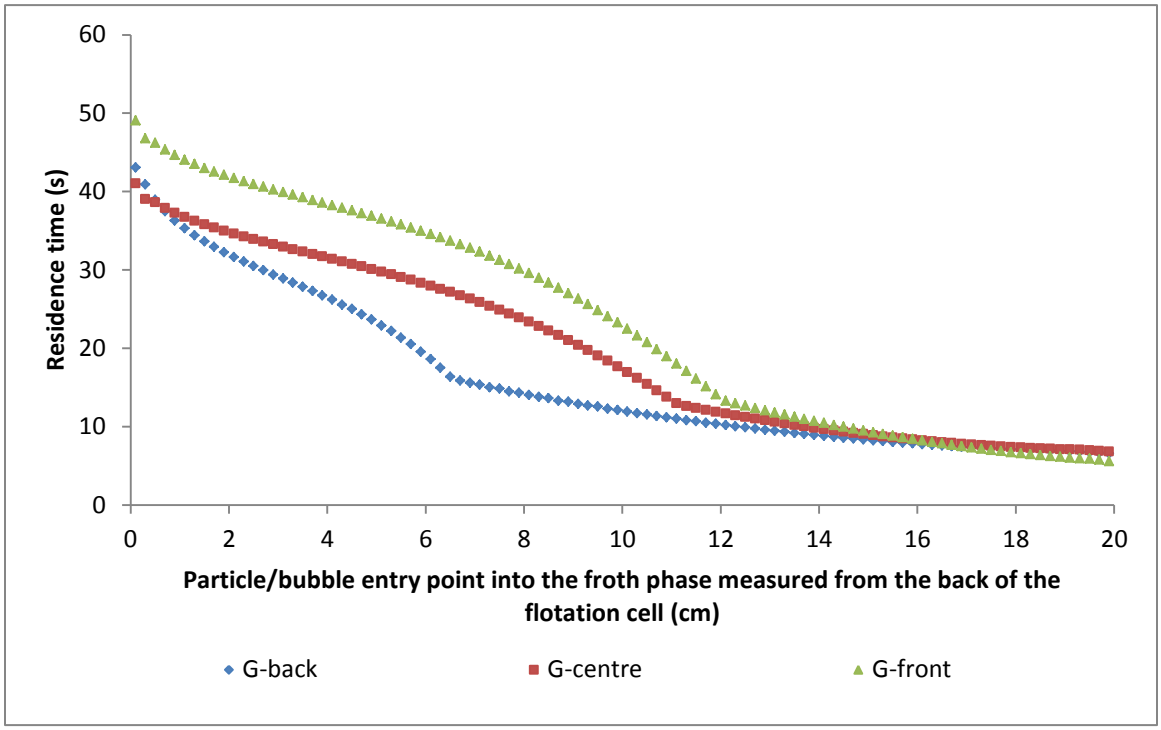

Figure 7.9: variation particle residence times as a function of distance from the back of the flotation cell.

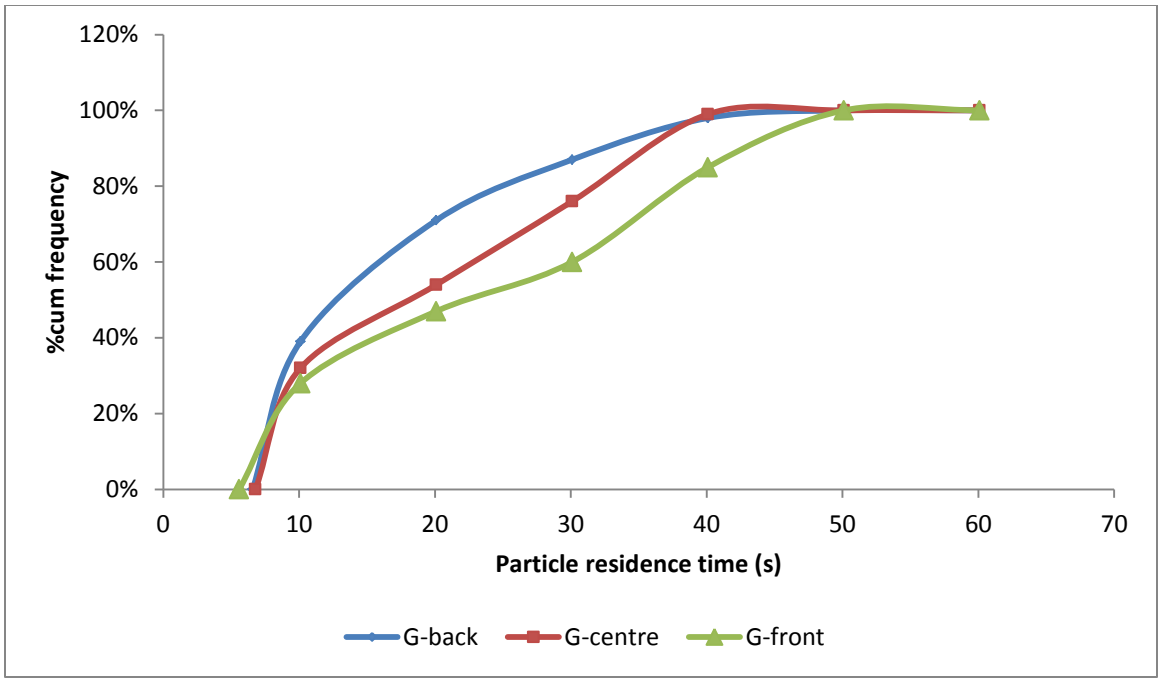

Figure 7.10: Cumulative bubble residence time distribution for the three gas flux distribution profiles

7.4: Summary and conclusions

Equation [7.1] was used to study the effects of gas distribution profile across the pulp-froth interface. A numerical technique based on the Method of Lines (MOL) termed the method of false transients was used to solve the equation for the stream function. Suitable boundary conditions were developed for each gas flux investigated. Of note on boundary conditions development was the use of surface velocities to generate a distribution of gas flux across the surface of the froth due to bubble breakage. To this end, an equation developed by Zheng et al. (2004) was adopted. This generation of flux across the surface of the froth enabled the setting of flux across the concentrate weir as an output variable during coding. Consequently, analysis of the results was done based on two aspects viz. air recovery and residence time distribution. Results from the simulations indicated that supplying high gas flux at the back of the flotation cell produces the highest air recovery factor, followed by high gas flux close to the concentrate weir and lastly supplying high gas flux at the centre. Analysis of bubble streamlines gave an adequate explanation on why high air recovery was possible with G-back but was inadequate in explaining the difference in air recovery values between G-centre and G-front. A sufficient explanation was reached after considering froth

velocity vector filed plot. The velocity density plot proved that flux across the concentrate weir with G-front was 11% higher than flux obtained with G-centre. This difference in flux across the concentrate weir can only mean high gas loss as a result of bubble breakage since total gas flowrate across the pulp-froth interface was maintained the same for three gas flux distributions. An attempt to relate air recovery values to concentrate recovery was carried out. A convention that states that high air recovery factor means higher limestone recovery to concentrate was adopted and experimental results reported affirmed the predictions from the modelling approach.

The impact of gas flux distribution on froth residence time distribution aspect was also considered. From both bubble and particle residence time distributions, it was clear that the manner in which gas is distributed across the pulp-froth interface hugely influences the distribution of residence times. Generally G-front produces highest number of bubbles and particles with higher residence times while G-back produces the largest number of both particles and bubbles with the minimum residence time. An attempt was then made to try and use the variations in residence time to make predictions and rankings in terms of flotation performance. To this end, a convention was also developed. It was based on analysing the percentage of bubbles with the shortest/minimum residence time and those with the longest residence time. A large percentage of bubbles with the minimum residence time would mean high recovery and low grade and vice versa while a higher percentage of bubbles with longest residence time would mean low recovery and high grade and vice versa. The output of this exercise did not wholly agree with all the experimental results. For instance where, according to simulations, G-back was expected to produce grade lower than G-front, experimentally similar grades where obtained (Figure 7.5) although recovery wise there was agreement. These discrepancies between residence time model predictions and real experimental data were attributed to the simplicity of the current model, especially that it does not take into account drainage patterns in the froth. Drainage patterns are expected to play a huge role as superficial gas velocity is varied.

Overall, this Chapter demonstrated that the way in which gas is distributed across the pulp-froth interface will change the distribution of residence times and also importantly bubble breakage at the surface of the froth. Simulation suggested that high gas flux at the back will produce high recoveries while high gas flux close to the concentrate weir produces high grade.

Chapter 8

Study of the effects of froth baffle on froth flotation performance: experimental investigation

8.1 Introduction

In Chapter 6 and Chapter 7, a method of manipulating froth residence time distribution in the froth was studied both experimentally and numerically. While Chapter 6 experimentally shows that gas flux distribution across the pulp-froth interface influences froth performance, Chapter 7 confirms some of the trends in Chapter 6 through simulations. It also goes on to show that indeed the distribution of residence times in the froth changes significantly as gas flux distribution across the pulp-froth interface is changed. This Chapter is a further attempt to optimize froth performance through manipulation of residence time distribution. It uses a technique that was proposed by Moys (1979) which involves the use of froth baffles or froth flow modifiers. The froth flow baffle alters froth mobility, by changing the path taken by bubble streamlines, significantly narrowing the range of both particle and bubble residence times.

Froth recovery has typically been used as a froth phase performance measure; its definition entails quantification of the fraction of particles attached to bubbles that enter the froth phase that are recovered as concentrate. Several methods to evaluate froth recovery have been established, these include changing the froth depth as described by Vera et al. (1999), use of specially designed devices that measures bubble loading in the pulp phase in conjunction with concentrate rate (Dyer, 1995; Seaman et al., 2006; Bhondayi and Moys., 2011). The dependence of froth recovery on froth residence time is well documented e.g. Vera *op cit*, Yianatos et al. (1998) and Vera et al. (2002). In most froth recovery models, the froth residence time is expressed in terms of froth depth and gas rate. Thus by manipulating these variables, froth residence time is changed and

consequently froth recovery is changed. Other froth properties such as froth stability and cell design also influences froth residence times. Although these properties may have a huge impact on flotation froth performance, they are not readily amenable to manipulation by flotation plant operators. Changing these properties may involve changing pulp chemical conditioning; which may prove costly in terms of reagent consumption in the long run. As a result, operating plants have typically manipulated froth residence times by changing froth depth and superficial gas velocity; with deeper froths generally producing high grade concentrates at lower recoveries and vice versa. High superficial gas velocities result in increased recovery at the expense of concentrated grade.

Although gas rate and froth depth can successfully be used to optimize froth phase performance, is it not desirable to have an additional manipulated variable that specifically targets sub-processes in the froth phase? An additional manipulated variable that targets froth mobility which can be changed for a given flotation cell without destabilizing the whole flotation circuit?

After proposing a froth transport model and comprehensive studies on froth residence times, Moys, (1979) developed a novel technique to manipulate froth residence times in addition to gas rate and froth height. This technique involves the use of froth baffles. The purpose of the froth baffles is to elongate the path taken by a bubble that enter the froth phase close to the concentrate weir as it travels from the pulp-froth interface until it is recovered to the concentrate at a fixed froth depth. Exciting results were obtained from Moys' technique. An increase in chalcopyrite grade that ranged between 10.4% and 22.1% was recorded for a given recovery. Despite the potential of this work to be used as a tool for manipulating froth residence time, no further work has been done on froth baffles/froth modifiers. Froth baffles can provide the flotation operator with an additional variable to manipulate when optimizing flotation performance. It is thus the objective of work discussed in this Chapter to further investigate the use of froth baffles as a way of optimizing flotation performance. The work focuses on the effects of a froth baffle and its inclination angle to the horizontal on recovery and grade. Comparison of a baffled froth system to the same flotation system without a baffle is done.

8.2 Review of froth transport models

In all the transport models that were discussed in Chapter 2 section 2.6.1, the back part of the flotation cell is taken as a ‘dead zone’ which seldom contributes to recovery. Particles that enter the froth phase in that region have an infinite residence time as they cannot be recovered to the concentrate. Also, bubbles generated close to the concentrate weir are subjected to the shortest residence time which means minimum drainage; consequently this region is known to contribute significantly to entrainment recovery. It appears that optimization of the froth should then include:-

(1) Activating the ‘dead zone’ so that it contributes towards recovery

(2) Increasing the residence time of bubbles that enter the froth phase close to the concentrate weir to reduce entrainment.

From froth residence time studies, Moys (1979) suggested and tested several froth chamber design options. Of concern to this work is the froth flow modifier herein termed the froth baffle. The froth baffle is a metallic or Perspex strip that effectively divides the froth phase into two sections as represented by Figure 8.1. The duty of the froth baffle is to alter the path followed by bubble streamlines as they rise from the pulp-froth interface. It is thus the objective of this work to further investigate the effect of a froth baffle and its inclination to the horizontal on flotation performance. Comparison of recovery on an un-baffled system with baffled systems with different inclination angles will be done.

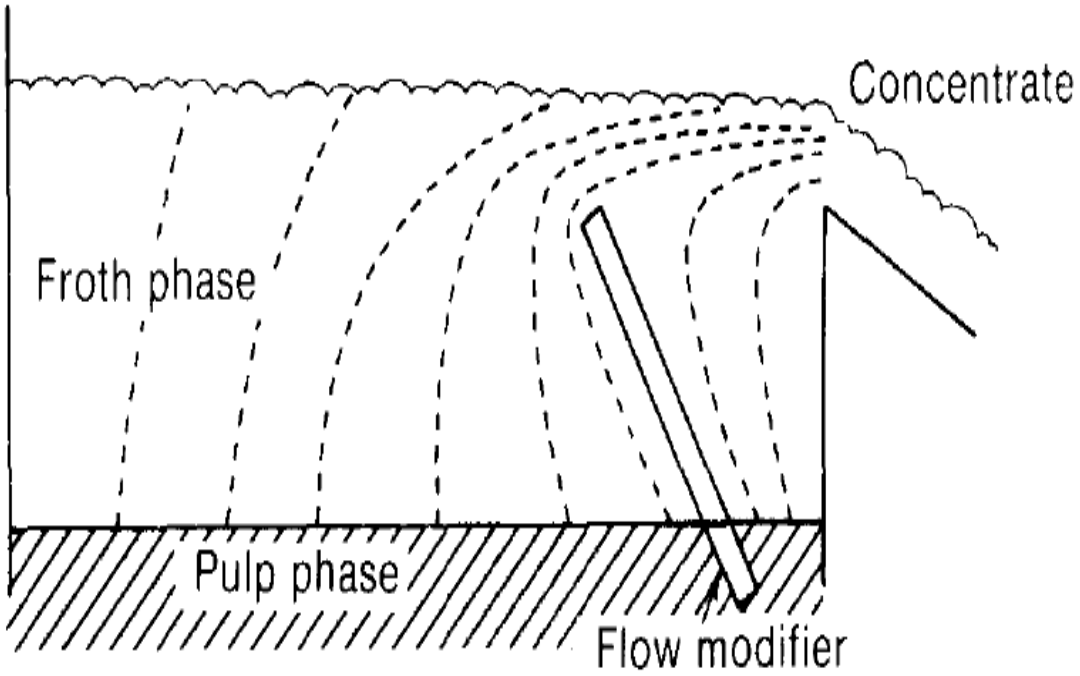

Figure 8.1: effect of flow modifiers on bubble streamlines in the froth phase (after Moys 1984)

8.2 Brief experimental description

Flotation tests were done using an artificial ore made up of 80% silica as gangue and 20% limestone as floatable component in a closed loop circuit described in Chapter 3 section 3.3.1 using the flotation cell also described in Chapter 3. These experiments were done to compare the effect of a froth baffle on flotation performance i.e. limestone recovery and grade. Three conditions were investigated at fixed froth depth of 10.1cm and average superficial gas velocity of 0.90cm/s. The conditions are (1) No baffle in the froth phase (2) baffle inclined at 67^0 and (3) baffle inclined at 45^0 to the horizontal as depicted in Figure 8.2. The baffle was inserted at a distance L_{baffle} equal to 2.5cm from the flotation cell concentrate weir wall and extended 2-5mm below the pulp-froth interface. The average pulp residence time in the flotation cell was maintained at 3.0 minutes by fixing feed flowrate into the 8 litre pulp volume flotation cell. Oleic acid and Dowfroth 250 were used as collector and frother with dosage rate of 20 mg/liter of water and 30 mg/100g limestone respectively. Pulp %solids was maintained at 15%w/w while agitation rate was kept constant at 1200rpm.

.

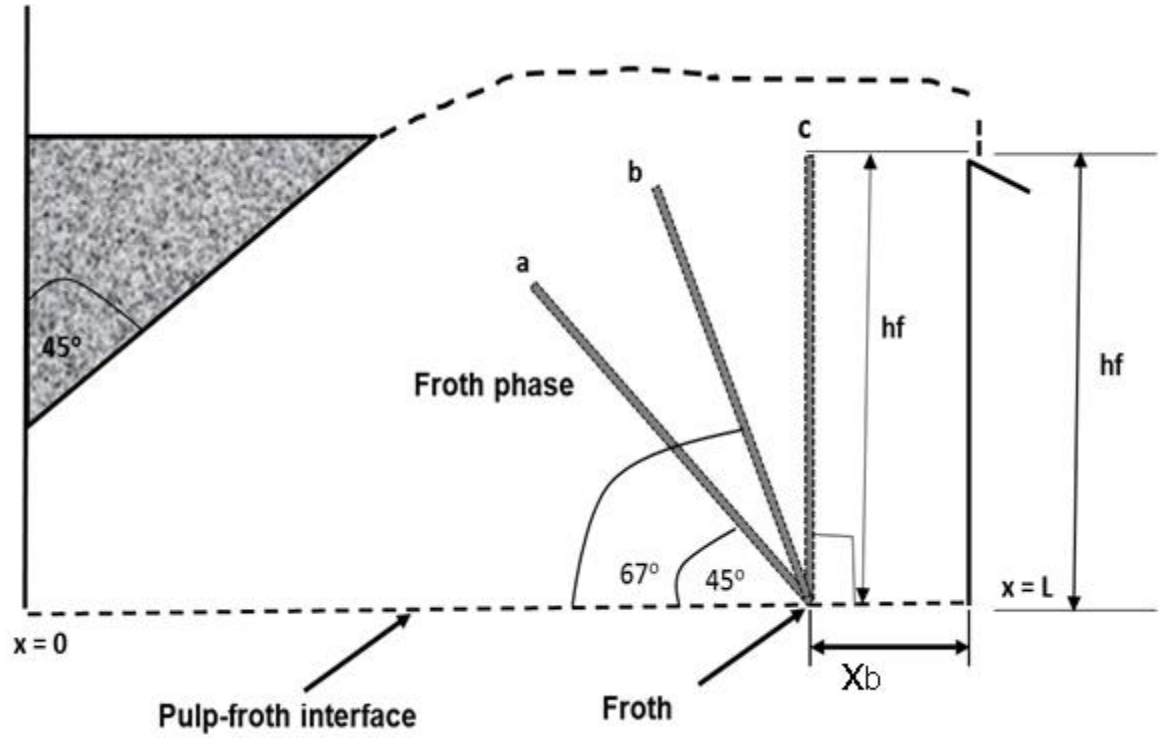

Figure 8.2: schematic representation of froth baffle positions investigated (a) baffle at 45^{o} to the horizontal, (b) baffle at 67^{o} to the horizontal and (c) baffle at 90^{0} to the horizontal

8.4 Results

As observed by Moys (1979), the introduction of a froth baffle has a notable effect on overall performance of a flotation system. Froth baffles were inserted in the froth with their bottom section just below the pulp-froth interface (2-5mm). Its positioning would impose little changes to the pulp phase sub-processes, thus it can be assumed that any change to the overall flotation performance (grade and recovery) is associated with the baffle geometry and changes in the froth mobility. Samples were collected and treated according to the procedure described in Chapter 3 section 3.4 and results are summarized in Figure 8.3

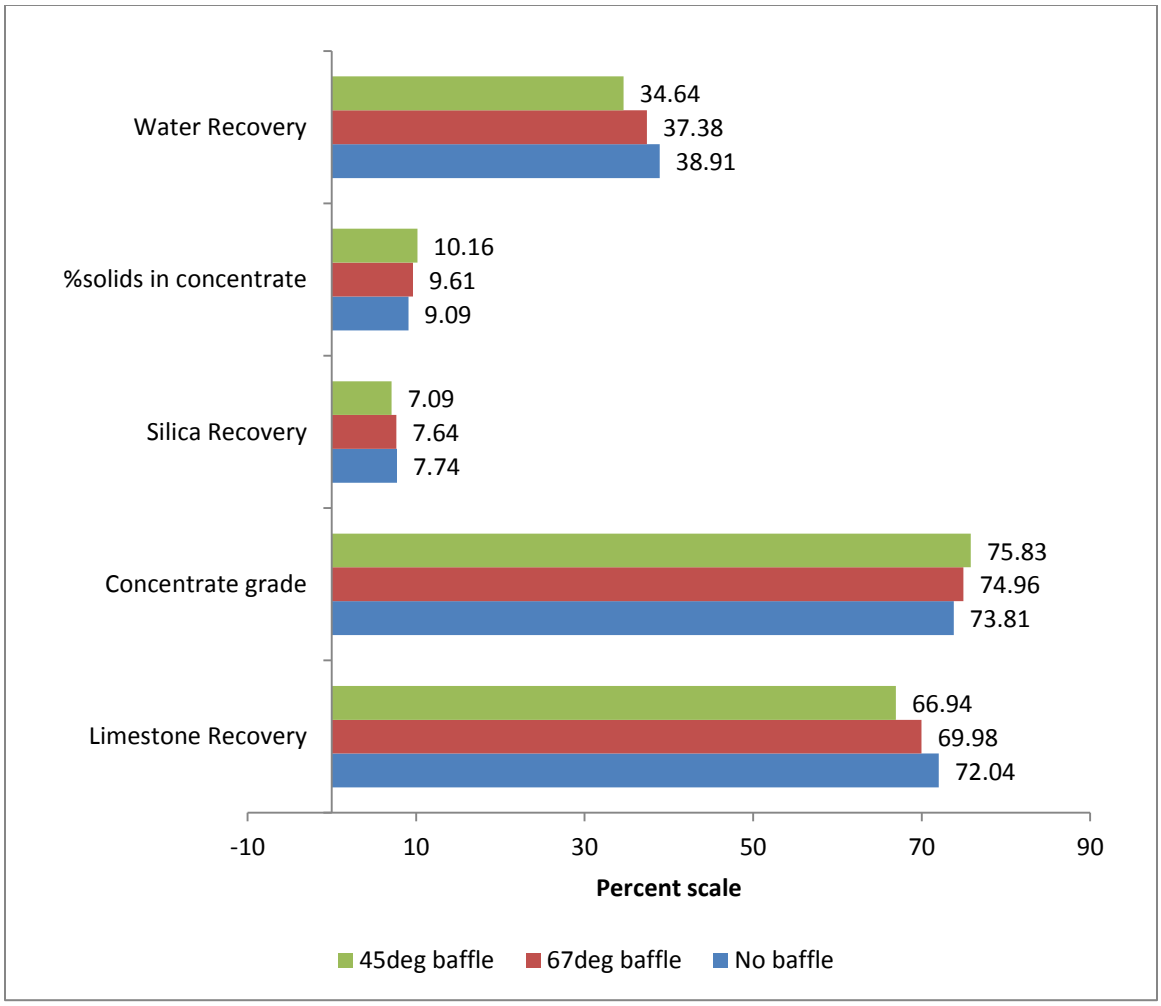

Figure 8.3: Comparison of the effect of a froth baffle and its inclination angle to the horizontal on flotation performance

8.4.1 Limestone recovery

The recovery of limestone decreased from 72.0% to 67% when froth baffles were introduced into the froth (Figure 8.3). The lowest recovery was recorded when the baffle angle was 45^{o} while the highest recovery was observed when there was no baffle in the froth. These changes in limestone recovery were expected since introducing a froth baffle will elongate the path followed by bubbles generated close to the concentrate weir increasing the average froth residence time. This gives the froth a longer time to drain in the process reducing froth and water recoveries according to equations [2.27] and [2.31] in Chapter 2. As the baffle angle becomes more acute (as measured according to Figure 8.2), the path taken by most bubbles becomes longer and therefore residence time

distribution become narrower i.e. shifted towards the mean value by narrowing the spread.

The range of limestone recoveries observed in these experiments is 5% which is small when compared to the range of recoveries reported by Moys (1979). Thus to be sure that the observed changes in recovery are indeed a result of the instituted process changes and not due to random variations, the data was subjected to statistical analysis. More so, the flotation process is very complex and any slight changes in solution chemistry or atmospheric conditions may affect the results leading to biased conclusions. One-Way ANOVA was performed on recovery. The following hypothesis was tested at α =0.05 using the analysis package in Microsoft excel.

Null hypothesis H_o: The means of limestone recoveries are equal for the three factors i.e. baffle positions.

Alternative hypothesis H_a: At least two of the recoveries are different.

The analysis at α = 0.05 and F_{crit} value of 5.14 resulted in the rejection of the null hypothesis because the calculated F statistic value of 72.74 is higher than the F_{crit} value; results are summarized in Table 8.1a. Rejection of the null hypothesis proves that there is some significant difference in at least two of the limestone recoveries that is due to the instituted process changes and not due to random errors. To enable identification of the limestone recoveries that are different, a Post-Hoc Test based on Tukey's HSD (Honestly significant difference) test was carried out. The test (Table 8.1b) concluded that the differences between the recoveries of limestone in all tests are statistically significant. The conclusion was reached at because the differences in the average limestone recoveries for all conditions were higher than the Tukey's HSD value of 1.38.

Table 8.1a: One-Way Anova for limestone recovery- results summary

Groups	Count	Sum	Average	Variance		
No baffle(μ_2)	3	217.13	72.38	0.43		
67deg baffle(μ_3)	3	208.95	69.65	0.24		
45deg baffle (μ_1)	3	200.82	66.94	0.24		
ANOVA						
Source of Variation	SS	df	MS	F	P-value	F crit
Between Groups	44.34	2	22.17	72.74	0.00006	5.14
Within Groups	1.83	6	0.30			
Total	46.17	8				

Table 8.1b: Tukey HSD test results summary

	Difference in Means	Tukey HSD Value	Outcome
μ2-μ1	5.44	1.38	Different
μ2-μ3	2.73		Different
μ3-μ1	2.71		Different

Now that it has been proven that the limestone recoveries obtained are statistically different and are not a consequence of random errors, it is important that we explain our results in relation to Moys *op cit.* results. Moys *op cit.* results show that the introduction of a froth baffle resulted in an increase in recovery while results reported herein indicate a loss in recovery as the froth baffle was introduced. This loss in recovery increases as the baffle angle becomes more acute. Before advancing an explanation for the trends observed, it is important to highlight that the flotation cell used by Moys did not have a froth crowder whereas experiments reported herein were done in a flotation cell with a inclined at 45^0 as shown in Figure 8.2. The crowder can introduce significant changes in froth flow patterns by directing the froth towards the concentrate launder thereby reducing significantly or eliminating the volume of inactive froth at the back of the flotation cell.

Our results can be explained by noting that introducing an inclined baffle reduces the vertical cross sectional area as a function of height above the pulp-froth interface on one side of the baffle while increasing it on the other (see Figure 8.4). The vertical cross sectional area between the flotation cell back plate/crowder and the baffle (Froth phase region B, in Figure 8.4) decreases with height while the area between the baffle and the concentrate weir-wall increases (Froth phase region A, in Figure 8.4). This means that superficial gas velocities in these sections vary differently; it increases with height in region B while decreasing in region A. Consequently froth drainage patterns are also different. Froth generated in region B is much less drained because of the high Jg when compared to the froth generated in the region A. The froth that is generated in region B is directed towards the concentrate launder by the froth crowder which means that it has to travel the horizontal distance Hd (shown in Figure 8.4) across region A. Intuitively significant drainage of this high water content froth is expected to take place as it travels across region A, because the decreasing Jg in region A may not be able to balance out the force of gravity acting on water and its associated load. This results in high downward water flux which carries with it smaller and heavily laden bubbles in this region (this phenomenon was noticed during tests). This process becomes more evident and dominant as the distance between the baffle and the concentrate weir wall at the pulp-froth interface is reduced.

The overall effect of such drainage pattern is that it can reduce the effective froth volume as one region's contribution to froth recovery decreases as it becomes predominantly a drainage region. Consequently recoveries will decrease as was observed experimentally. Additionally, introducing the froth baffle shifts the minimum residence time in the froth by elongating the streamlines of bubbles in froth region B and as a result of low Jg in region A (equation [2.26] in Chapter 2); this would inevitable increase the average froth residence time. Increasing average froth residence time reduces froth recovery (equation [2.27]) which in turn reduces overall recovery according to equation [2.34] in Chapter 2.

In the absence of a froth crowder, the back part of flotation cell is typically taken as a dead zone as exemplified by froth transport models suggested by Moys (1979), Ross (1990) and Zheng et al. (2006). This dead zone does not contribute to concentrate recovery. Inserting a froth baffle as was done by Moys (1979) in flotation cells without a crowder activates the dead zone by increasing superficial gas velocity at the back of the

flotation cell. When the dead zone is activated, the effective froth volume increases and recovery is expected to increase. This activation of the dead zone at the back of the flotation cell, in the absence of the froth crowder may have resulted in the increased recoveries observed by Moys (1979) after inserting a froth baffle.

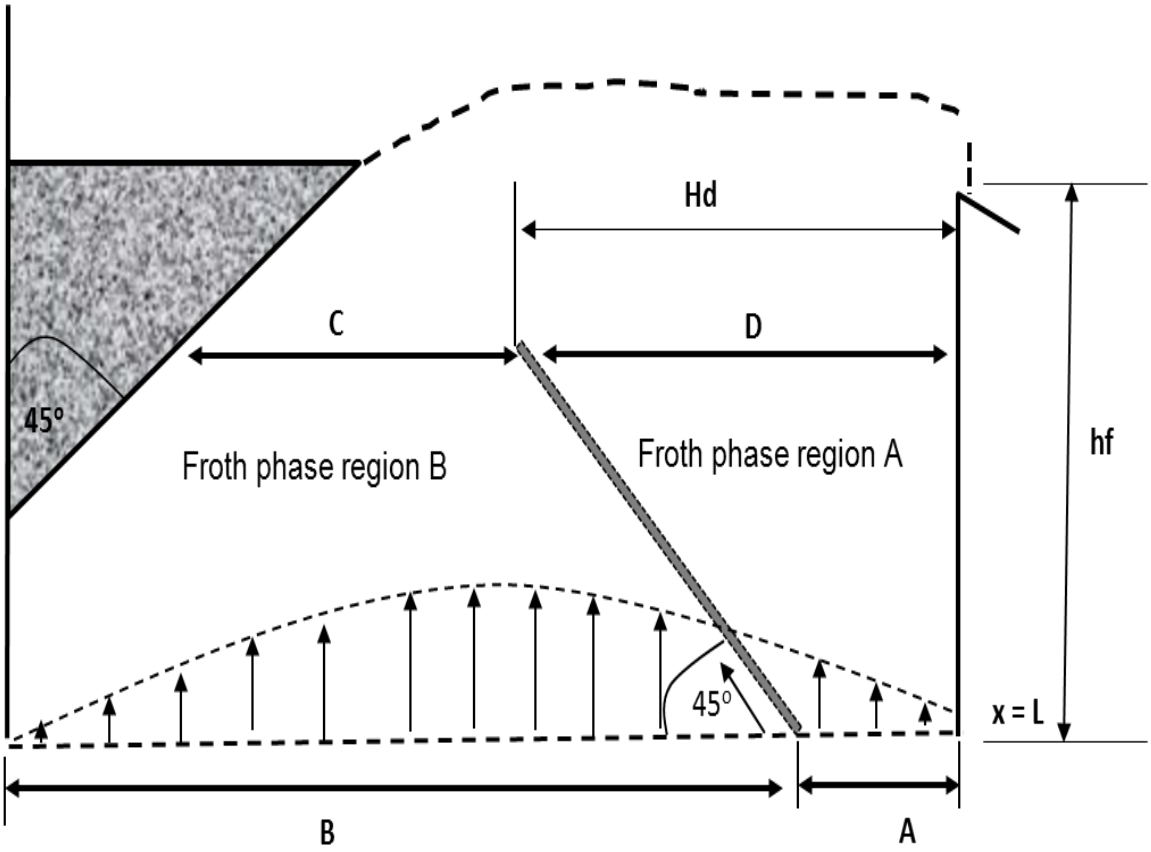

Figure 8.4: illustration of the most important regions and cross sectional areas when a froth baffle is inserted into the froth.

8.4.2 Concentrate grade

Limestone grade also changed when the froth baffles were introduced. From Figure 8.3; limestone grade increased from 74% when there was no baffle in the froth to 76% when the baffle angle was 45^0. The grade results trends agree with results reported by Moys *op cit* albeit at lower values of change. Subjecting the grade data to ANOVA produced results summarized in Table 8.2a while results from the Tukey Post hoc analysis are shown in Table 8.2b. The conclusion from the statistical analysis is that there is significant difference in limestone grade obtained when there was no baffle and when a

45^0 baffle was introduced. The values of grade obtained when there was no baffle and when a 67^0 baffle was introduced were found to be statistically similar although a difference of 0.86% was obtained. The grade trends can be explained as follows:-

The fact that as the baffle angle becomes more acute, the difference in J_g values of froth region A and B in Figure 8.4 increases helps us to hypothesis that:-

(1) The water content of the froth coming from froth region B increases as the baffle becomes more acute while the drainage of water in froth region A increases as well.

(2) The horizontal distance Hd shown in Figure 8.4 on which the froth from region B has to travel across the low Jg and high drainage region A increases with the decrease in baffle angle.

The consequences of the above points are a decrease in water recovery and subsequent increase in concentrate grade as baffle angle becomes more acute. It is also obvious that as the baffle angle becomes more acute, the average residence time of bubbles that enter the froth in region A increases allowing more drainage time and therefore improving concentrate grade. The effect of baffle angle on both recovery and grade can be summarized by plotting a grade recovery curve as shown in Figure 8.5; axis scales are suppressed for clarity.

Table 8.2a: One-Way Anova for limestone grade- results summary

Groups	**Count**	**Sum**	**Average**	**Variance**		
No baffle(g_2)	3	221.18	73.73	0.09		
67deg baffle(g_3)	3	223.99	74.66	0.20		
45deg baffle (g_1)	3	227.50	75.83	0.19		
ANOVA						
Source of Variation	**SS**	**df**	**MS**	**F**	**P-value**	**F crit**
Between Groups	6.67	2	3.33	21.06	0.0019	5.14
Within Groups	0.95	6	0.16			
Total	7.62	8				

Table 8.2b: Tukey HSD test results summary

	Difference in Means	**Tukey HSD Value**	**Outcome**
g1-g2	1.17	1.00	different
g1-g3	2.10		Different
g2-g3	0.93		No difference

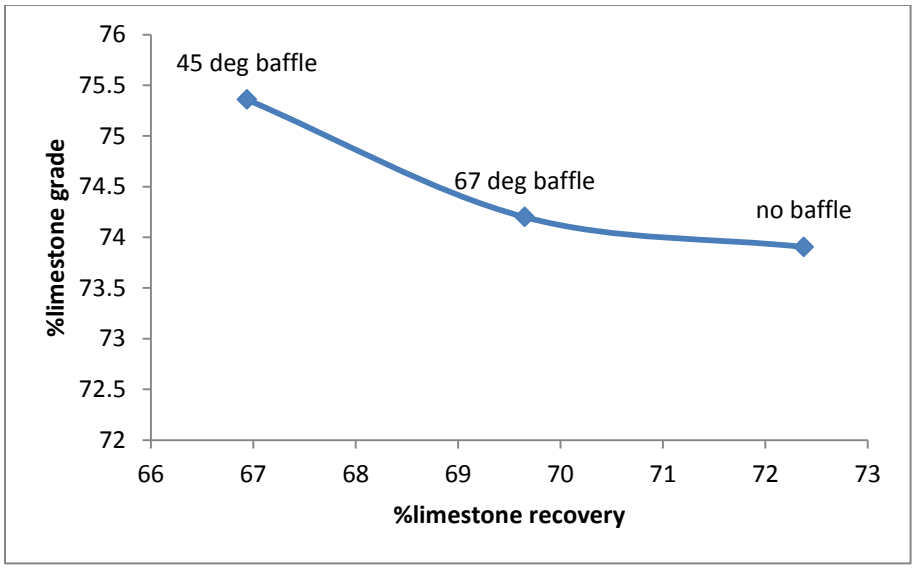

Figure 8.5: Grade-recovery plot of the three baffle positions.

8.4.3 Silica recovery

Silica was used as non-floatable gangue material in these experiments, as such its recovery is deemed solely due to entrainment. From Figure 8.3, we can see that the gangue/silica recovery values are almost similar, although a trend showing lower values of silica recovery in the presence of a baffle is visible. The difference in %silica recovery needs to be statistically tested to assess whether it is as a result of a random errors in sampling or it's a result of the froth interventions. Table 8.3a and 8.3b shows the results of F-test and the accompanying Tukey test for silica recovery at 5% level i.e. $\alpha = 0.05$. Results indicate that there is a statistically significant difference in silica recovery in at least two of the variables. The Tukey test (Table 8.3b) shows that a statistically significant difference in silica recovery exists between that obtained with a 45^0 baffle and that obtained when there was no baffle. A significant difference also exists between the recovery obtained when there was a 45^0 baffle and that obtained when the baffle angle was 67^0. The results also reveal that silica recovery difference obtained when there was no baffle and when the baffle angle was 67^0 is statistically insignificant. These results follow the same trend that was observed on limestone grade.

Table 8.3a: One-way ANOVA for Silica recovery results summary

Groups	**Count**	**Sum**	**Average**	**Variance**		
No baffle(s_2)	3.00	23.23	7.74	0.03		
45deg baffle (s_1)	3.00	22.93	7.64	0.07		
67deg baffle(s_3)	3.00	21.27	7.09	0.03		
ANOVA						
Source of Variation	**SS**	**df**	**MS**	**F**	**P-value**	**F crit**
Between Groups	0.74	2.00	0.37	8.66	0.02	5.14
Within Groups	0.26	6.00	0.04			
Total	1.00	8.00				

Table 8.3b: Tukey HSD test results for silica recovery.

	Difference in Means	Tukey HSD Value	Outcome
s2-s1	0.65	0.52	Different
s2-s3	0.10		No difference
s1-s3	0.55		Different

8.4.4 Water recovery

Water recovery is another important parameter that can be used together with an entrainment factor to evaluate the recovery of gangue material. Where water recovery is high, entrainment recovery is also expected to be high. The variation of water recovery as a function of baffle position is shown in Figure 8.6. The introduction of a 67^0 baffle decreases water recovery by 1.52% while a further 2.74% decreases in water recovery was observed as the baffle angle was further decreased to 45^0. Results of water recovery were also subjected to ANOVA analysis at an alpha value of 0.05 and a Tukey test. Output from Tukey test indicated that the mean water recoveries are all different from each other and the differences although small are statistically significant. A summary of the statistical analysis results is given in Table 8.4.

Table 8.4a: One-way ANOVA for water recovery results summary

Groups	*Count*	*Sum*	*Average*	*Variance*
45deg baffle (p_1)	3	116.73	38.91	0.37
67deg baffle(p_3)	3	112.15	37.38	0.32
No baffle(p_2)	3	103.92	34.64	0.18

ANOVA

Source of Variation	*SS*	*df*	*MS*	*F*	*P-value*	*F crit*
Between Groups	28.08	2	14.039	48.422	0.0002	5.14
Within Groups	1.74	6	0.290			
Total	29.82	8				

Table 8.4b: Tukey HSD test results for water recovery.

	Difference in Means	**Tukey HSD Value**	**Outcome**
p1-p2	-2.74	1.35	Different
p1-p3	-4.27		Different
p2-p3	-1.53		Different

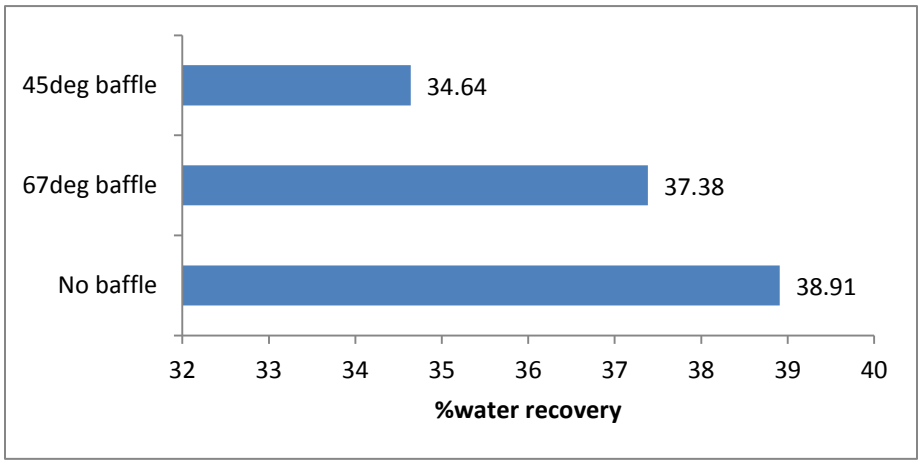

Figure 8.6: Variation of water recovery with baffle position and angle

The changes in residence time caused by the introduction of the baffle are responsible for the changes in water recovery summarized in Figure 8.6. Local variations in drainage

patterns that are a consequence of the presence of a baffle can also contribute significantly to the changes in water recovery.

8.5 Results summary

The results from the experimental data can be summarized as follows:

I. The recovery of limestone decrease with the introduction of a froth baffle; this decrease is also a function of the inclination angle of the baffle to the horizontal; recovery decreases as the inclination angle measured according to the convention shown in Figure 8.2 becomes more acute.
II. The grade of the concentrate increases with the introduction of the froth baffle, higher grades are also obtained as the angle of the baffle becomes more acute
III. Water recovery decreases with baffle angle; entrainment recovery herein represented by silica recovery also decreases with baffle angle. The high water recoveries (above 35%) measured indicates that the froth was highly stable. We suspect that with a slurry that is not as stable as the one used for these investigations, the changes in flotation performance can be quite significant.

Consequently the introduction of the froth baffle in this context has its own merits and demerits. Its use thus depends on the objectives of a particular operation. Where grade is the target, the froth baffle can be used to optimize it without changing gas rate and froth depth. If recovery is the target then the use of a froth baffle with an acute angle will not suffice.

8.6. Conclusion

In this work, the impact of a froth baffle on flotation cell performance has been experimentally tested and results from the experiments resulted in the following conclusions

(1) The introduction of an angled froth baffle leads to reduction in recovery of the floatable mineral; a maximum 5.4% change in recovery was measured. This conflict observations made by Moys (1979) whose results indicate an increase in recovery with the introduction of a froth baffle.

(2) The introduction of an angled froth baffle results in reduction in water recovery, the water recovery decreases as the baffle angle became more acute.

(3) Silica recovery which in this work is a proxy for entrainment recovery decrease with the introduction of a froth baffle. The decrease is in the order, No froth baffle, 67^0 baffle and 45^0 baffle; which is as expected.

(4) An angled froth baffle favors concentrate grade. Results have shown a statistically significant increase in grade as the baffle angle become more acute. The grade result agrees with observations made by Moys (1979). Consequently for a stable froth with particles of high floatability, introducing a froth baffle will increase grade at a compromised recovery.

The flotation performance results summarized above agrees with our working theory that the froth baffles shifts residence times towards higher values as they elongate the path followed by bubbles that enter the froth phase close to the concentrate weir. The conflict between Moys (1979) recovery results with our artificial slurry results is suspected to stem from the difference in flotation cells used. Experiments done by Moys *op cit*. were carried out in a flotation cell without a froth crowder whereas the current experiments were done in flotation cell with a froth crowder. The absence of a froth crowder in the flotation cell used by Moys *op cit*. means the volume fraction of the dead zone was large. Introducing a froth baffle then reduced this volume by inducing large velocities close to the back of the flotation cell resulting in increased recoveries. Froth baffles can therefore be used to optimize froth performance in large flotation cells that are currently being designed and used in industry.

8.7 Further remarks

Froth residence time is an important parameter in froth phase performance, almost all froth phase sub-processes depends on it. In this Chapter, one of the ways that were considered to be a viable option of manipulating froth residence time was studied and results presented. In addition to using froth residence time to explain our results, other parameters also came into focus and their effects seemed predominant. These factors are drainage patterns, bubble coalescence and froth stability.

8.7.1 Drainage patterns

Inserting an inclined baffle into the froth phase induces different drainage patterns in the two regions separated by the baffle; in region B, superficial gas velocity (Jg) increase with height while in region A it decreases. These variations of Jg as a function of height result in different drainage patterns. Froth generated in the region where Jg is increasing with height is expected to carry more water with it when compared to froth generated in the region where Jg is decreasing with height. To totally understand the effect of differential drainage patterns induced by froth baffles, it is recommended as a further study to simulate the foam drainage equation as described by Brito-Parada et al. (2012) under different vertical velocities and then comparing the water content as a function of height.

8.7.2 Bubble coalescence

The difference in the observed drainage patterns implies different rates of bubble coalescence. Furthermore, the fact that the froth flow channel B is narrowing suggest that bubbles are being squeezed together i.e. bubble crowding. Bubble crowding may lead to bubble coalescence and subsequent loss of attached particles. On the other hand it may be possible that it's only the velocity of the bubbles that increases at the constriction and the bubbles do not necessarily coalescence. This is a possibility in that as Jg increases a significant amount of water is carried with bubbles preventing rapid thinning of bubble lamellae there by reducing bubbles coalescence. The phenomena that take place at constriction i.e. section labeled C in Figure 8.4, can be experimentally quantified by measuring froth phase bubble sizes using the technique developed in Chapter 4. Unfortunately this was not done when experiments reported in this Chapter were done

8.7.3 Bubble coalescence

Indications in this Chapter suggest that the stability of the froth is a key parameter in choosing ways of optimizing the froth phase. A highly stable froth, may not respond very well to froth optimization techniques, it thus suggested tests with a froth baffle be done with a less stable froth.

Lastly, the increase in average residence time with introduction of froth baffles has not been proven or measured in this work. Our belief that a froth baffle increases froth residence time solely depends on the work by Moys (1979) which was done on a different froth chamber design. The changes in froth residence times need to be verified on the current froth chamber. Thus the next Chapter is dedicated to using mathematical modelling to quantify the changes in residence time as a function of baffle angle.

Chapter 9

Use of 2D stream function equation to study the effect of froth baffles

9.1 Introduction

In Chapter 8, the impact of a flow modifier/ froth baffle was investigated experimentally. Results from an artificial ore which produced a very stable froth as typified by the associated high water recovery suggested that inserting a froth baffle increases concentrate grade at the expense of recovery. Variation in both grade and recovery also depends on baffle's inclination angle, therefore like froth depth, a froth baffle can be used to optimise froth performance. Use of a froth baffle as froth optimisation technique is centred on the belief that it will change the distribution of froth residence times through changing the path followed by bubbles. Testing this assumption experimentally was not possible using the experimental setup described in Chapter 8. A froth transport model was used to ascertain the degree by which the distribution of residence time would change with the introduction of the baffle and its inclination angle to the horizontal. Of importance in the simulations also is velocity distribution in the froth. The introduction of an angled froth baffle is suspected to cause huge velocity differences in the sections separated by the baffle. These velocity differences are expected to cause different drainage patterns in each section of the froth; thus the overall drainage characteristics are expected to be different. The stream function equation was selected for this work and the solution technique used is based on conformal mapping. The Schwarz–Christoffel mapping in particular was chosen. The development of the model and boundary conditions is similar to that described in Chapter 7 except for the additional boundary conditions that represent the baffle.

9.2. Boundary conditions

In addition to the boundary conditions described in Chapter 7, the presence of the froth baffle introduces additional boundaries that need to be specified. In the experimental setup, the froth baffle was introduced at distance x_b cm from the concentrate launder wall, its height (hf) was chosen to be equal to the height of the froth from the pulp-froth interface to concentrate weir lip as shown in Figure 9.1. The inclination angle of the froth baffle was measured as depicted in Figure 8.2 in Chapter 8. In developing the boundary conditions for the baffle, it was assumed that the baffle just sits at the interface and its ends (Top and Bottom) are always parallel to the x-axis regardless of the baffle's inclination angle.

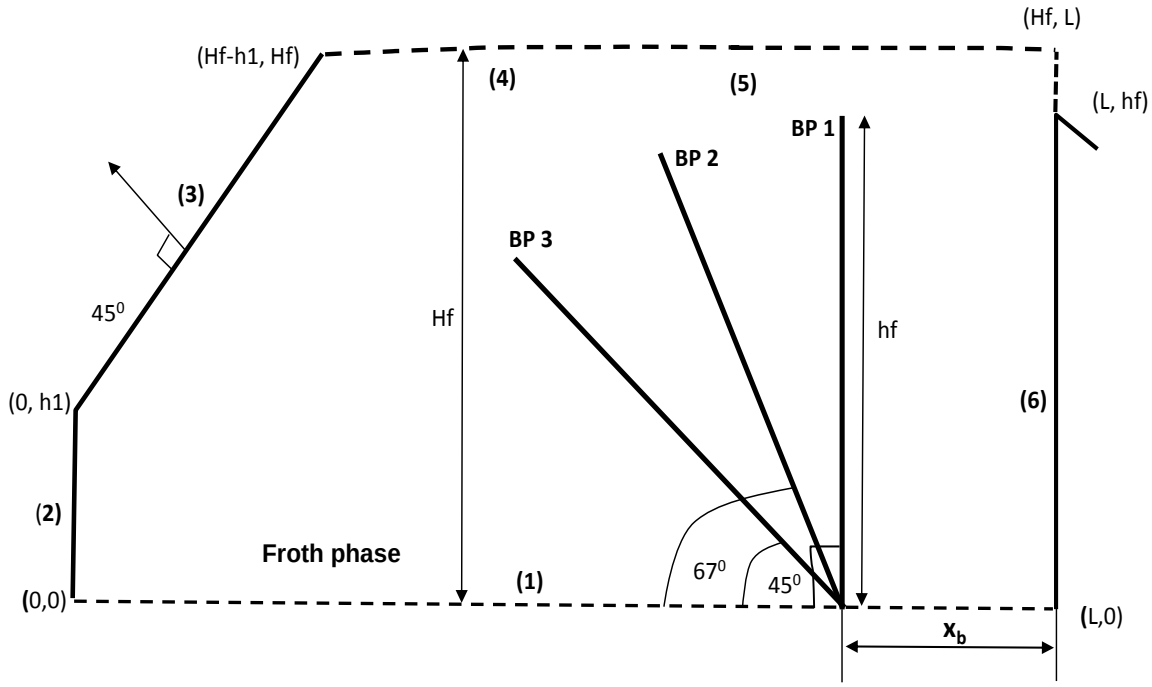

Figure 9.1: Flow domain showing all boundary position including the position of the froth baffles

9.2.1 Baffle position BP 1 ($L - x_b; 0 \le y \le hf$)

At this position the baffle was inserted at 90^0 to the horizontal and a distance x_b from the concentrate wall. Since there is no flow through the baffle, the no-penetration boundary condition is applicable on both side of the baffle. This means that flow into the baffle is zero. If the thickness of the baffle is taken as t cm then boundary condition equation on

the side of the baffle which is along coordinates $(L - x_b, 0)$ and $(L - x_b, h_f)$ is given by equation [9.1a]. Since the thickness of the baffle is t cm, the other boundary equation on this baffle which is along points $\left(L - (x_b + t), 0\right)$ and $\left(L - (x_b + t), h_f\right)$ is defined by equation [9.1b].

$$\frac{\partial \psi}{\partial y}(L - x_b, y) = 0 \qquad [9.1a]$$

$$-\frac{\partial \psi}{\partial y}\left(L - (x_b + t), y\right) = 0 \qquad [9.1b]$$

If the baffle is assumed to be sitting right at the interface at point $(L_2, 0)$ in Figure 9.2 and also if we further assume that the top-end of the baffle is parallel to the x-axis i.e.at point (L_1, hb). Velocity into the baffle at these points is also zero. The resulting boundary condition equations are;

$$-\frac{\partial \psi}{\partial x}(L_2, 0) = 0 \qquad [9.2a]$$

$$\frac{\partial \psi}{\partial x}(L_1, hb) = 0 \qquad [9.2b]$$

9.2.2 Angled baffle positions

Position BP 2 and BP 3 represent the baffle when inclined at 67^0 and 45^0 to the horizontal respectively. To develop the boundary equations when the baffle is inclined at any angle theta (θ), consider Figure 9.2. Since the baffle is a solid boundary, flux normal to this boundary ($g_n(s)$) is zero. If the x, y velocity components naming convention used in Chapter 7 is adopted, it is easy to deduce that $g_{n1}(s)$ and $g_{n2}(s)$ are represented by equation [9.3] and [9.4] respectively.

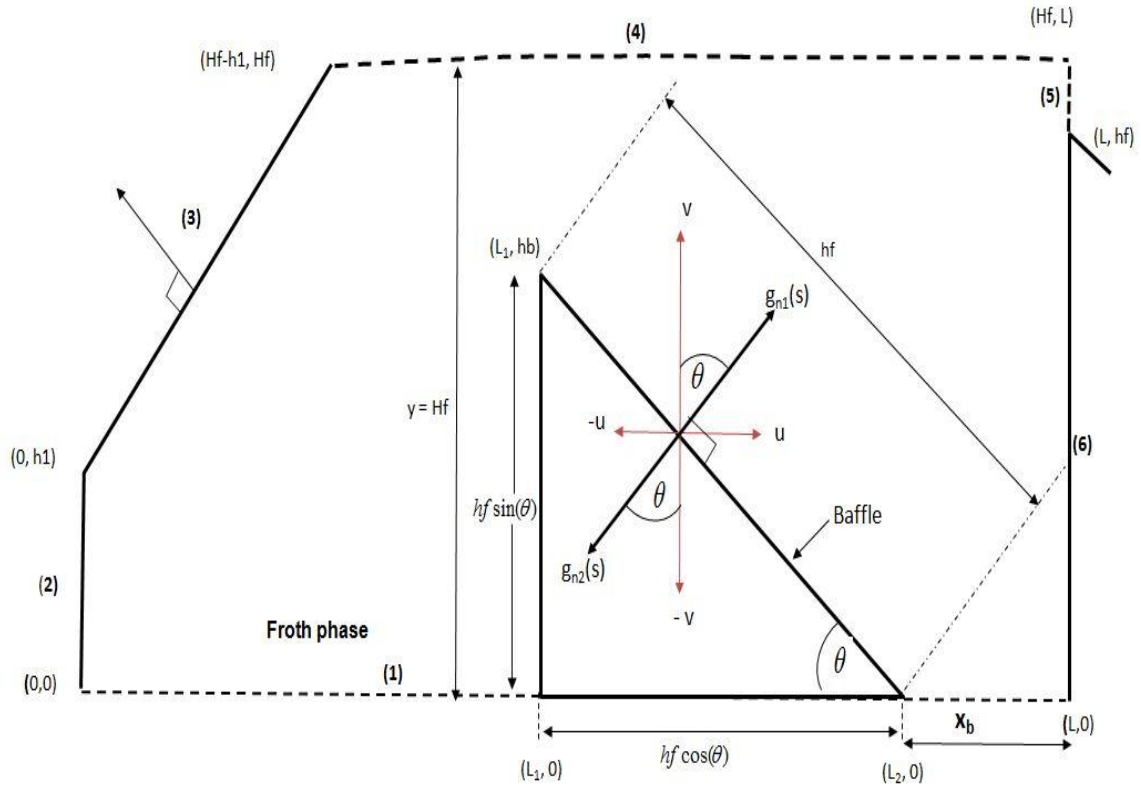

Figure 9.2: Illustration of the development of boundary conditions for angled froth baffle

$$g_{n1}(s) = v\cos\theta + u\sin\theta = 0 \qquad [9.3]$$

$$g_{n2}(s) = -v\cos\theta - u\sin\theta = 0 \qquad [9.4]$$

If equation [7.2] in Chapter 7 is substituted into equation [9.3] and equation [9.4] the resulting equations in terms of the stream function (ψ) are represented by equation [9.5] and equation [9.6] respectively.

$$-\frac{\partial\psi}{\partial x}\cos\theta + \frac{\partial\psi}{\partial y}\sin\theta = 0 \qquad [9.5]$$

$$\frac{\partial\psi}{\partial x}\cos\theta - \frac{\partial\psi}{\partial y}\sin\theta = 0 \qquad [9.6]$$

9.2.2.1 Baffle position BP 3

Now when $\theta = 45^0$, the coordinates $(L_1, 0)$, $(L_2, 0)$ and (L_1, hb) in Figure 9.2 can be represented on both sides of the baffle as follows

$$(L_1,\ 0) = \left(L - (x_b + \frac{\sqrt{2}}{2} h_f);\ 0 \right) \quad [9.7a]$$

$$(L_1,\ 0) = \left(L - (x_b + t + \frac{\sqrt{2}}{2} h_f);\ 0 \right) \quad [9.7b]$$

$$(L_2, 0) = (L - x_b,\ 0) \quad [9.8a]$$

$$(L_2, 0) = (L - (x_b + t),\ 0) \quad [9.8b]$$

$$(L_1, hb) = \left(L - (x_b + \frac{\sqrt{2}}{2} h_f),\ \frac{\sqrt{2}}{2} h_f \right) \quad [9.9a]$$

$$(L_1, hb) = \left(L - (x_b + t + \frac{\sqrt{2}}{2} h_f),\ \frac{\sqrt{2}}{2} h_f \right) \quad [9.9b]$$

where L is length of the flotation cell

Consequently for a 45^0 impermeable baffle, the velocity normal to the surface along coordinates represented by equation [9,8a] and equation [9.9a] when: $L - (x + \frac{\sqrt{2}}{2} h_f) \le x \le L - x_b$ and $0 \le y \le \frac{\sqrt{2}}{2} h_f$ is given by equations [9.10] while the velocity normal to the remaining side of the baffle which is along coordinates represented by equation [9.8b] and equation [9.9b] is given by equation [9.11].

$$-\frac{\partial \psi}{\partial x}(x, y) + \frac{\partial \psi}{\partial y}(x, y) = 0 \quad [9.10]$$

$$\frac{\partial \psi}{\partial x}(x, y) - \frac{\partial \psi}{\partial y}(x, y) = 0 \qquad [9.11]$$

Since the ends of the baffle at coordinates ($L_2, 0$) and (L_1, hb) are considered parallel to the x-axis, boundary condition equations for these ends are similar to equation [9.2a] and [9.2b] respectively.

9.2.2.2 Baffle position BP 2

When the baffle is moved to baffle position BP 2 as depicted in Figure 9.1, the angle is increased to 67^0, now if we approximate $\cos(67)$ and $\sin(67)$ by 0.92 and 0.39 respectively, the coordinates (L1, 0), (L2, 0) and (L1, hb) in Figure 9.2 can also be represented as follows

$$(L_1, 0) = (L - (x_b + 0.92hf), 0) \qquad [9.12a]$$

$$(L_1, 0) = (L - (x_b + t + 0.92hf), 0) \qquad [9.12b]$$

$$(L_2, 0) = (L - x_b, 0) \qquad [9.13a]$$

$$(L_2, 0) = (L - (x_b + t), 0) \qquad [9.13b]$$

$$(L_1, hb) = (L - (x_b + 0.92hf),\ 0.39hf) \qquad [9.14a]$$

$$(L_1, hb) = (L - (x_b + t + 0.92hf),\ 0.39hf) \qquad [9.14b]$$

Thus for $L - (x_b + 0.92hf) \le x \le L - x_b$ and $0 \le y \le 0.39hf$ equation [9.9] and equation [9.10] also apply on both sides of the 67^0 baffle.

9.2.3 Boundaries (1) to (6) shown in Figure 9. 2

In addition to the baffle boundary conditions defined above, the stream function equation is solved with boundary equations [7.4] to [7.16] defined in Chapter 7. The only

exception is that the polynomial $g_1(x)$ and $g_4(x)$ represented by equation [7.9] and [7.11] respectively can only take coefficients obtained when the impeller was at the centre.

9.3 Numerical solution development

The solution to the 2D stream function equation under the boundary conditions defined above was developed using numerical techniques based on Finite Difference (FD) discretisation of the solution region. Because of the complexity of the flow domain, applying FD techniques directly to the flow domain was avoided because of its lack of flexibility in complex domains. Consequently conformal transformation techniques which map the complicated flow domain onto a rectangle in the complex plane were applied. The FD method would then be applied on the rectangle before mapping the solution back to the complicated flow domain. Specifically, our flow domain which is a region in the Cartesian plane can be viewed instead as a region in the complex z-plane. Due to the celebrated *Riemann Mapping Theorem*, there exists an analytical map, $w = f(z)$, that transforms the z-plane into another complex plane (the w-plane) such that the flow domain is mapped to a rectangle. Since the stream function equation is invariant under the action of a complex map, it will not change under this map. Therefore a solution can be developed in the w-plane by solving the stream function equation on the simple rectangle domain. This solution is transformed back into the z-plane by the inverse transformation $z = f^{-1}(w)$.

In the case of a polygonal domain, the map from this domain to a rectangle is known as a Schwarz-Christoffel (SC) mapping. Efficient numerical methods have been developed to approximate Schwartz-Christoffel mappings for arbitrary polygonal domains, and several good packages exist that implement these methods such as SCPACK, a FORTRAN library developed by Trefethen (1989), and the SC toolbox in Matlab by Driscoll (1996) – a descendent of SCPACK. This latter toolbox can easily be used even without deeper knowledge of the numerical methods behind conformal mapping.

9.3.1 Schwarz-Christoffel (SC) mapping

A significant amount of work has been done on SC mapping due to its application in solving the Laplace's equation e.g. Driscoll and Trefethen (2002), Brown and Churchill (2009). Before discussing the basic theorem behind the SC mapping, let us consider

conformal mapping in general. According to Sultan (2013), a complex mapping $w = f(z)$ defined in a region D is conformal at a point z_0 in D if for every pair of smooth oriented curves C_1 and C_2 in D intersecting at z_0 the angle between C_1 and C_2 is equal to the angle between their images C'_1 and C'_2 at $f(z_0)$ in both magnitude and sense. This definition leads to a key result: it implies that if the stream function equation is satisfied on a domain D, it is also satisfied on the transformed domain $f(D)$. Another important result is that the function $f(z)$ is conformal on a region if and only if it is analytic (complex derivative exists) everywhere on that region and its derivative is not equal to zero anywhere on the region. The reader interested in the mathematics behind conformal mapping and the proofs of the various theorems is referred to a book by Brown and Churchill (2009).

For the solution to the stream function equation, this definition implies that the equation is also satisfied in the transformed plane. The function $f(z)$ is conformal if it is analytic and its derivative is not equal to zero i.e. ($f'(z) \neq 0$). A function is said to be analytic in a given complex region if it has a derivative at each point in that particular region. The reader interested in the mathematics behind conformal mapping and its proof is referred to a book by Brown and Churchili (2009).

According to Reira et al. (2008) the Schwarz-Christoffel transformation formula provides conformal mappings of the upper half plane onto domains with a finite number of line segments. More precisely, SC formula results in conformal mapping of upper half plane onto the interior of a polygon. The typical Schwarz-Christoffel theorem is written as follows (Bergonio, 2003)

Theorem: Let P be the interior of a polygon D in the complex plane with vertices $w_1, w_2, w_3 ... w_n$ and interior angles $\alpha_1\pi$, $\alpha_2\pi$, $\alpha_3\pi ... \alpha_n\pi$ in counter-clockwise order. Let f be any conformal one-to-one map from the upper half plane onto P satisfying $f(\infty) = w_n$ then f can be written in the form

$$f(z) = A + C\int_{z_0}^{z} \prod_{k=1}^{n-1} (\zeta - z_k)^{\alpha_n - 1} \, d\zeta \qquad [9.15]$$

where A and C are complex constants and $z_0 < z_1 < z_2 .... z_{n-1}$ are real numbers satisfying $f(z_k) = w_k$ for $k = 1, 2 .... n-1$

Equation [9.15] can be adapted for maps from different region such as unit disks, triangles etc. In particular if f_1 maps region 1 to the upper half-plane and f_2 maps region 2 to the upper half-plane, then $f_2^{-1} \circ f_1$ maps region 1 to region 2. This way we can build maps between any two simply-connected regions in the complex plane. For a rectangle, according to Driscoll and Trefethen (2002), the function $f(z)$ is given by equation [9.16]

$$f(z) = C \int_0^z \frac{d\zeta}{\sqrt{(\zeta^2 - m^{-1})(\zeta^2 - 1)}} \qquad [9.16]$$

The solution to the stream function equation is developed in the w-plane on the map before using an inverse mapping function to get $z(w)$. The inverse of the map can be calculated by solving an initial value problem (IVP) shown by equation [9.17] as recommended by Driscoll and Trefethen (2002). Thorough Mathematical descriptions of mapping functions and how to calculate the inverse of the map can be found in the book by Driscoll and Trefethen (2002).

$$\frac{dz}{dw} = \frac{1}{f(z)} \text{ and } z(w) = z_0 \qquad [9.17]$$

Instructions on how to use the SC pack in Matlab can be found in the SC user guide developed by Driscoll (1996).

In this work the Matlab toolbox developed by Driscoll (1996) was used to compute the mapping and its inverse. We then discretized the transformed rectangle and used the forward map to populate the boundary values on this rectangle. The resulting Finite Difference Problem on the rectangle was solved numerically using Successive Over-Relaxation. The solution was then obtained at points in the original domain by first using the inverse map to obtain corresponding points in the rectangle, and then using

numerical interpolation within the rectangle approximate the solution value (since the transformed points usually would lie in between grid points).

9.4 Discussion of results

The output from the simulation exercise is discussed below. The discussion is mainly centred on explaining the experimental results reported in Chapter 8 by using simulation outputs. We will discuss the effect of froth baffle and its inclination to the horizontal on froth residence time distribution at a fixed distance (x_b = 5cm) between the baffle and the concentrate weir wall at the pulp-froth interface. The distance x_b is measured as described in Figure 8.2 in Chapter 8. After establishing the effect of the froth baffle and its inclination angle on residence time, we test the effect of the distance x_b on residence time distribution. Streamlines that bubbles follow as they rise from the pulp-froth interface until they are recovered to the concentrate are also important in understanding the froth performance. They are also discussed in this section.

9.4.1 Effect of froth baffles on bubble streamlines

The codes to implement Schwarz-Christoffel mapping and calculate the solution to the stream function equation in the rectangular domain are shown in Appendix C from C.6 to C.11. The resulting bubble streamlines from the simulations are shown below in Figure 9.3. Observe that the introduction of the froth baffle shifts the path taken by a loaded bubble in region B as it rises from the pulp-froth interface. Bubble streamlines in region B are elongated further as the baffle angle becomes more acute. Interesting also in the same figure is the observation that bubbles that are generated in the immediate vicinity of the froth baffle in region B tend to flow downwards on the other side of the baffle in region A. This is probably because of the decreasing Jg in region A as a function of height above the pulp-froth interface. The distance travelled by the bubbles in the downward direction tends to increase as the baffle angle is reduced. A possible consequence of this downward flow of bubbles is that bubbles with low rise velocity (small and heavily laden bubbles) may never make it to the concentrate launder especially if we consider the additional downward push on the bubbles by draining water. This can lead to loss in recovery which should increase as baffle angle becomes more acute. Experimental results reported in Chapter 8 affirmed this loss in recovery with the introduction of a baffle and also with the decrease in baffles' inclination angle.

9.4.2 Effect of froth baffles on velocity distribution

As mentioned in section 8.4.1 the introduction of a froth baffle results in different froth velocities across the entire froth. From simulations, the variation of velocities inside the froth was calculated and is represented as vector plots (arrows) and velocity density plot (colour) in Figure 9.4. It is obvious that introducing a froth baffle changes the velocity distribution drastically in the froth. Without a baffle (Figure 9.4a) the greater percentage of the region close to the back of the flotation cell has velocity less than 2cm/s whereas when a baffle was introduced, velocity ranged from 2cm/s and above, see Figure 9.4 b, c & d. The introduction of a froth baffle also creates a low velocity point (dead zone) along the length of the baffle where flow is nearly zero. That region is labelled C in Figure 9.4 b, c & d. It tends to increase in size as the inclination angle becomes more acute and it also moves down with decrease in baffle angle. When the froth is un-baffled this region is observed at the back of the froth chamber point C in Figure 9.4 a. Thus the introduction of the froth baffle largely activates the back part of the froth chamber. The creation of drainage region when a baffle is introduced can also be noticed in Figure 9.4 b, c & d, in region labelled A. Low velocity values are recorded above the pulp-froth interface up to the height labelled (h). Froth above this height, has higher velocity than that below it, this is presumably because of the bulk flow of froth from region B that has to flow across region A. If this froth carries with it a significant amount of water, that water is most likely to drain in this region. This may render this region to be predominantly a drainage region resulting in loss in recovery.

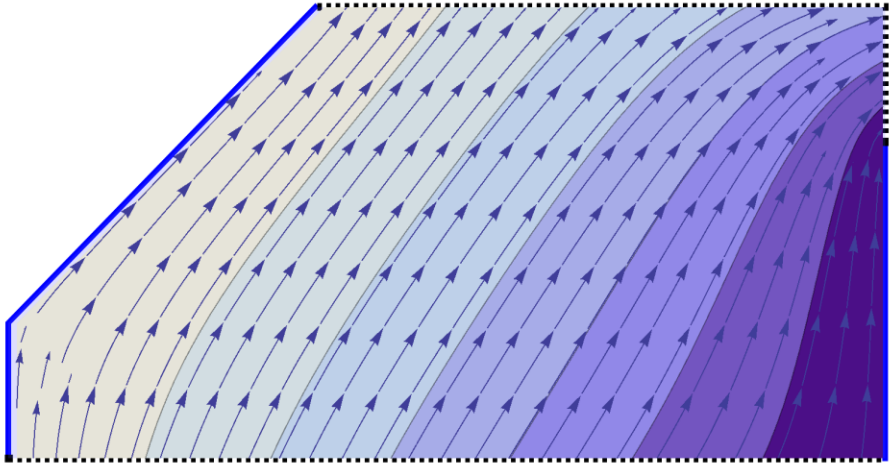

a) Bubble streamlines for no baffle in the froth

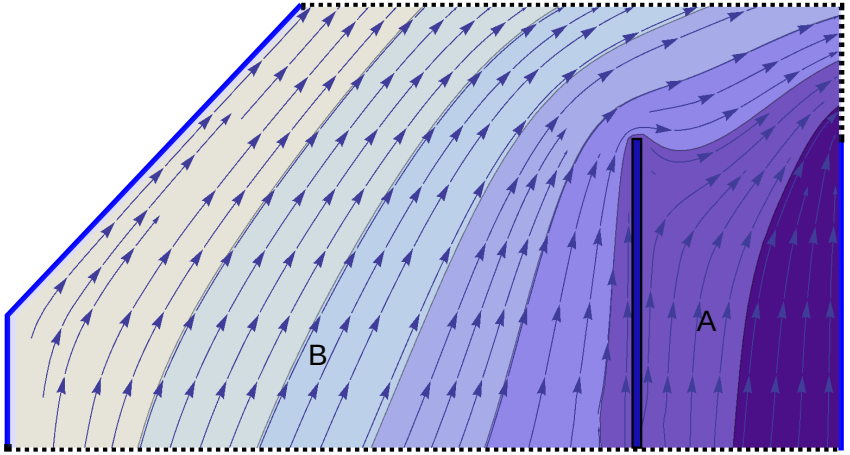

b) Bubble streamlines for a 90 Deg baffle

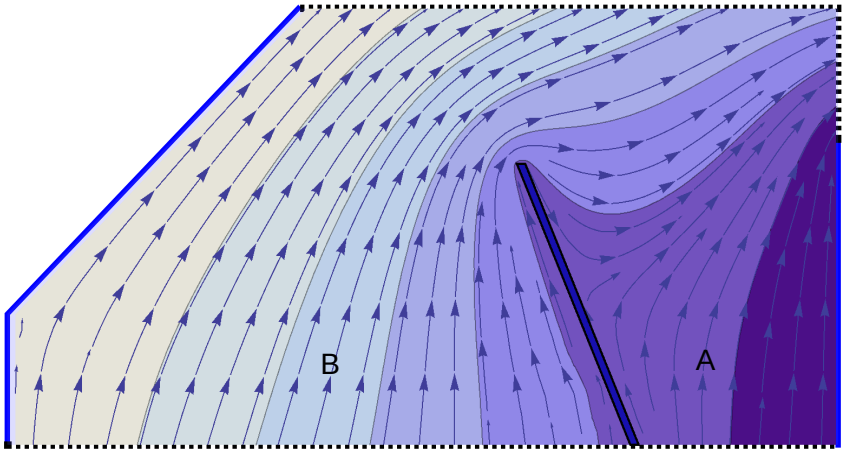

c) Bubble streamlines for a 67 Deg baffle

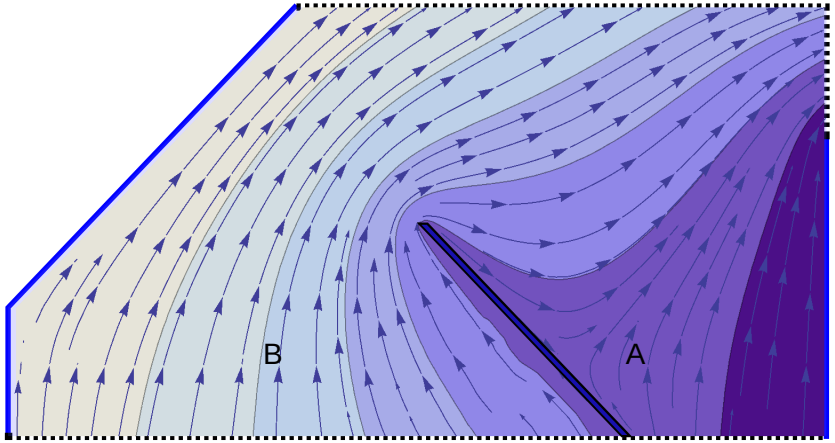

d) Bubble streamlines for a 45 Deg baffle

Figure 9.3: Bubble streamlines when there was (a) No baffle in the froth (b) 90^0 baffle in the froth (c) 45^0 in the baffle and (d) 67^0 baffle in froth, with (x_b) set at 5cm.

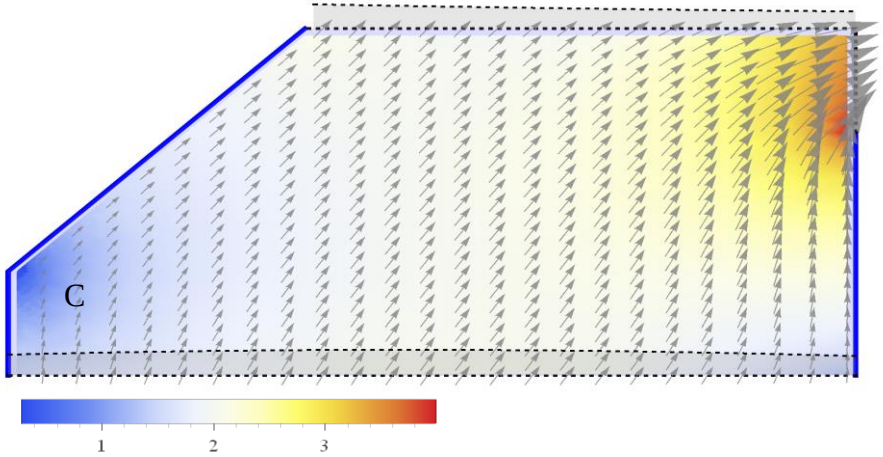

a) No baffle in the froth

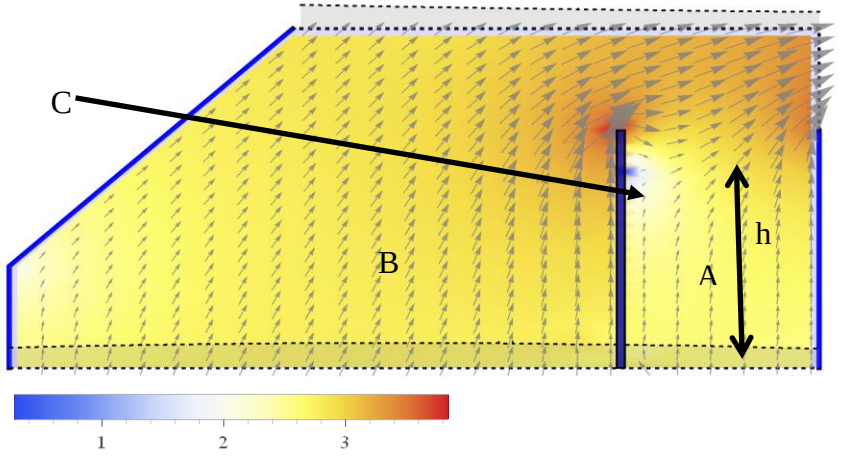

b) 90 Deg baffle in the froth

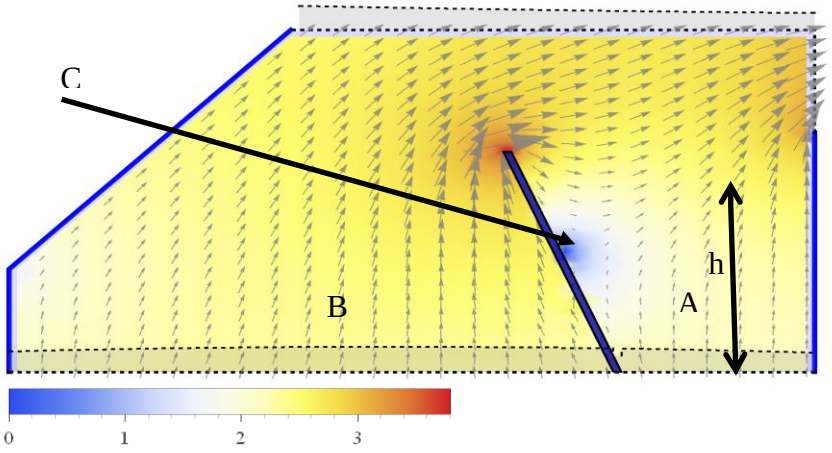

c) 67 Deg baffle in the froth

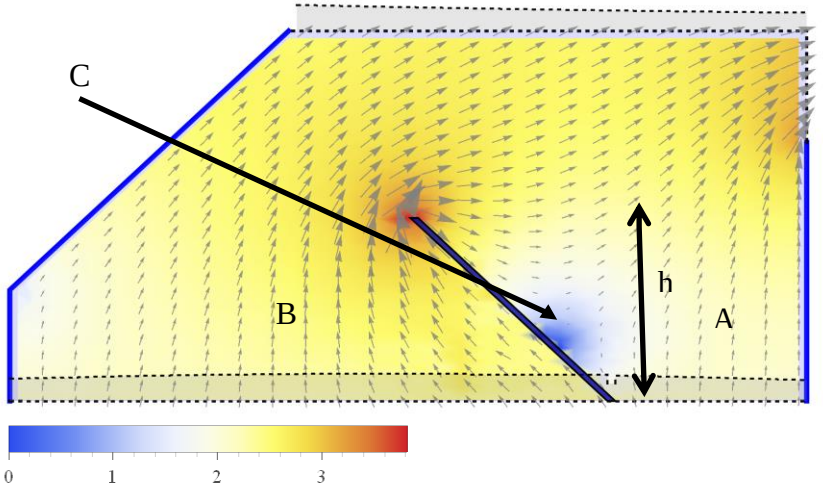

b) 45 Deg baffle in the froth

Figure 9.4: Velocity distribution when there was (a) No baffle in the froth (b) 90^0 baffle in the froth (c) 45^0 in the baffle and (d) 67^0 baffle in froth with x_b set at 5cm

9.4.3 Effect of froth baffles on particle residence time distribution

In order to get a clear understanding of what transpires to froth residence time distribution when a froth baffle is introduced into the froth, particle residence times were calculated for each of the conditions under discussion by tracing a bubble from the pulp-froth interface until it bursts or is recovered to the concentrate. If the bubble bursts at the froth surface its particles are assumed to flow to the concentrate at a velocity equivalent to the froth surface velocity. Surface velocity polynomial shown in Figure 7.3b was used in this work. The bubble residence time distributions were calculated using a Mathematica code shown in Appendix C section C.11.

Figure 9.5 represents the variation of particle residence time as a function of distance from the back of the flotation cell. Notice the change in residence time values for bubbles that are generated between 11cm and 15 cm from the back of the flotation cell in the presence of a baffle. In this region, particle residence times increase in the order no baffle, 90^0 baffle, 67^0 with the longest residence times observed is with a 45^0 baffle. The distribution in this region is suspected to be purely as a result of elongation of the path followed by the bubbles. Inserting a baffle also changes the distribution of residence times for particles that are generated in first 5cm from the back of the flotation cell. It is easy to see that the baffle with the most acute angle produced particles with relatively lower residence times as compared to the others. Residence times increased as the angle becomes larger. Highest values were obtained with no baffle. This type of particle residence time distribution is ascribed to the increase in velocity at the back of the flotation cell in the presence of a baffle see Figure 9.4 and most importantly this reduction in particle residence times may mean that the back part of the flotation cell has been activated by the presence of a baffle. Froth baffle activation of the back part of the flotation cell could be the reason why an increase in recovery in the absence of a crowder was observed by Moys (1979).

If the data in Figure 9.5 is converted into a cumulative frequency polygon, Figure 9.6 is obtained. From this figure, interesting observations can be made. For instance if we consider particles with residence times lower than the median residence time to positively influence recovery of water and valuable mineral and those with residence time above the median to negatively influence impact recovery but positively impact grade, the following deductions regarding flotation performance can be made from

Figure 9.6. if we consider the distribution of residence time of particles with residence times lower than the median residence time, recovery is expected to decrease in the order no baffle, 90^0 baffle, 67^0 baffle and 45^0 baffle while grade is expected to decrease in the reverse order. This agrees with experimental results. Notable in Figure 9.6 is that the presence of a baffle, tends to shift particle residence times lower than the 50^{th} percentile up i.e. towards higher values while shifting those above the 50^{th} percentile lower i.e. towards the median time. This narrows/decreases spread of the froth residence time distribution, thus it is expected that the loss in recovery should result in a gain in grade and most importantly, the loss in recovery is not expected to be drastic since an increase in residence times for particles generated close to the concentrate weir is compensated by a marginal decrease in residence time for particles generated at the back of the floatation cell. In the absence of a froth crowder, the residence time distribution obtained in the presence of a baffle is expected to increase both grade and recovery if optimally positioned as was observed by Moys (1979).

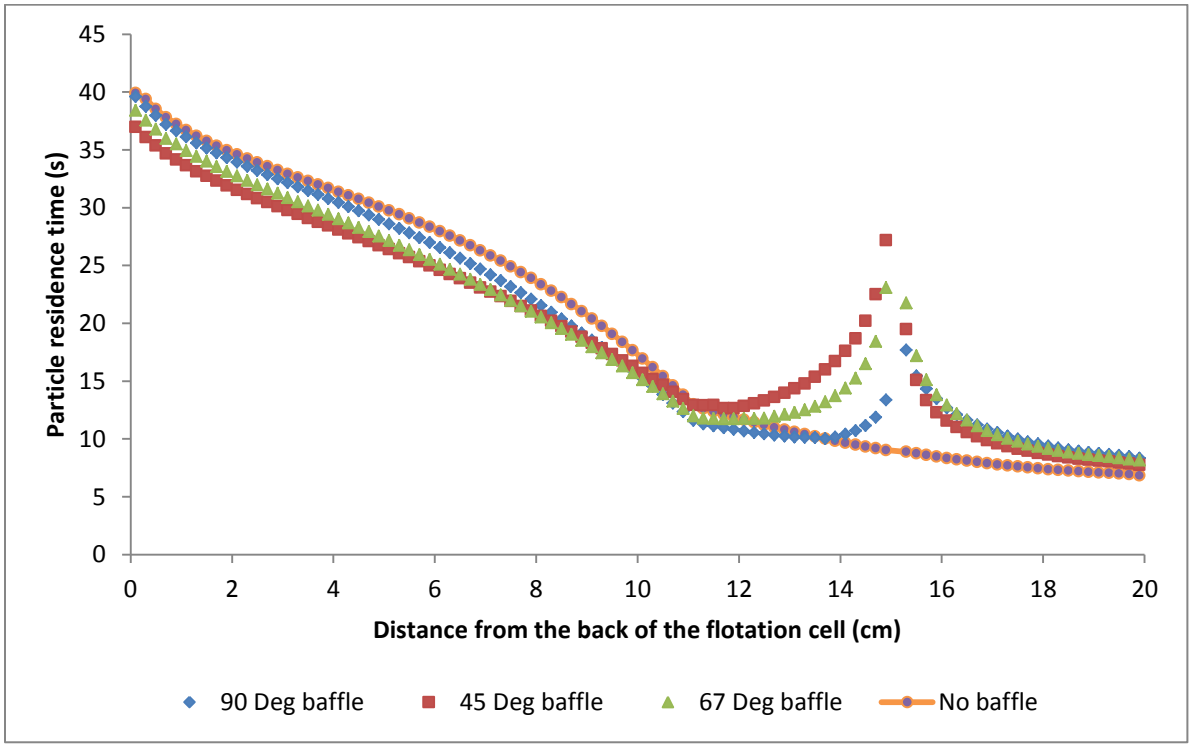

Figure 9.5: Variation of bubble residence times as a function of distance from the back of the flotation cell.

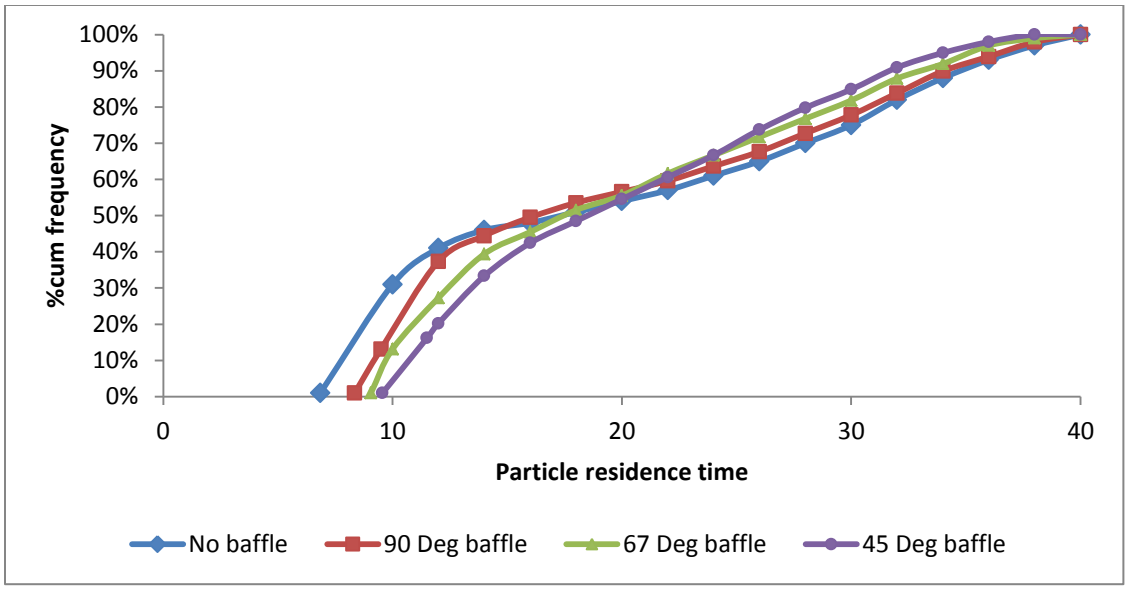

Figure 9.6: Cumulative particle residence time distributions for the four baffle positions when L_B was 5cm

9.4.4 Effect of distance x_b on residence time distribution

Simulation results presented above show that inserting a baffle has an impact on froth flow pattern, froth velocity distribution and most importantly froth residence time distribution. Flotation performance predictions from froth flow patterns and the residence distribution agreed with experimental results shown in Chapter 8. However, observations during experiments suggested that the distance (x_b) between the baffle and the concentrate weir wall at the pulp-froth interface is very important as it dictates the amount of gas flow and ultimately the drainage pattern in region A. The effect of x_b on flotation performance was not tested experimentally thus it was decided to test it numerically. Results in Figure 9.7 compare the effect of x_b on residence time distribution. Three values of x_b were compared viz. 2.5cm, 5cm and 7.5cm. Comparison of velocity distribution and bubble flow profile is shown in Appendix B. While Figure B.1 to B.3 compares bubble streamline profiles at different x_b values, Figure B.4 to B.7 show velocity profile comparison at those x_b values.

From Figure 9.7 changes in residence time distribution with changes in x_b are visible. As x_b increases from 2.5cm to 7.5cm, a trend which shows a reduction in residence time of particles that are generated close to the concentrate weir is seen, the residence times are increasing i.e. moving those obtained when there was no-baffle. At the same time,

the residence times of particles generated close to the back of the flotation cell tend to decrease i.e. move away from the distribution obtained when there was no baffle. This means that having a large x_b favours recovery at the expense of grade while lower x_b favours grade. It appears like optimum performance is obtained when x_b is 5cm for all baffle angles because it increases residence times of particles close to the concentrate weir wall while reducing that of particles generated close to the back of the flotation cell decreasing the spread of particle residence time distribution.

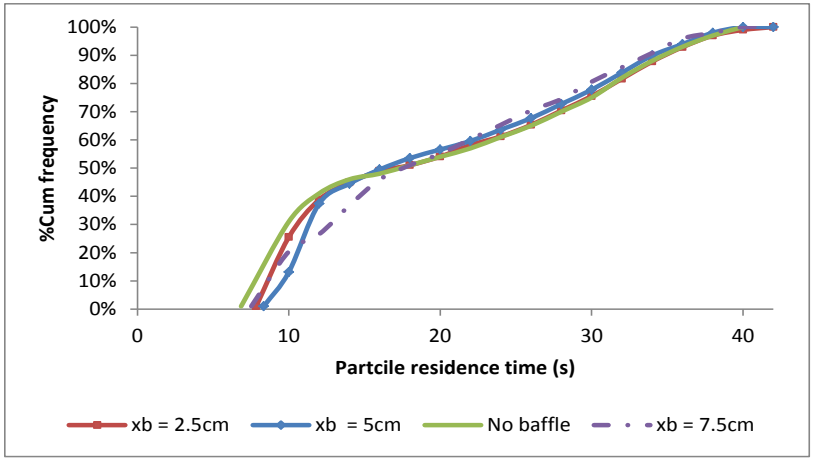

a) 90 degree baffle

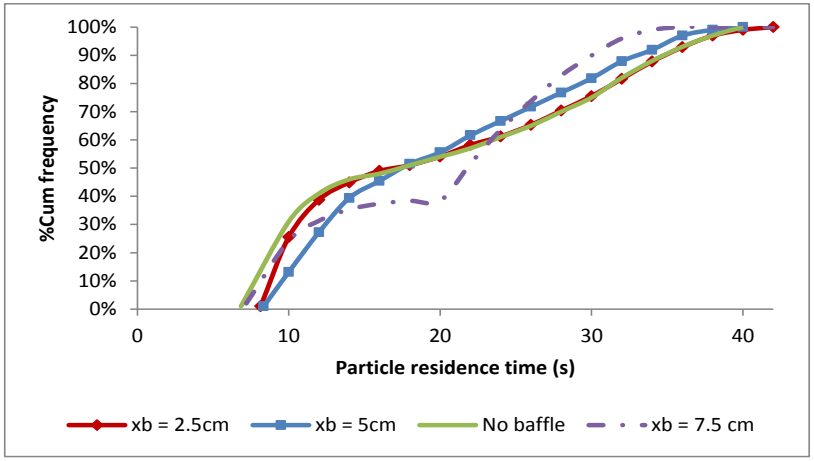

b) 67 degree baffle

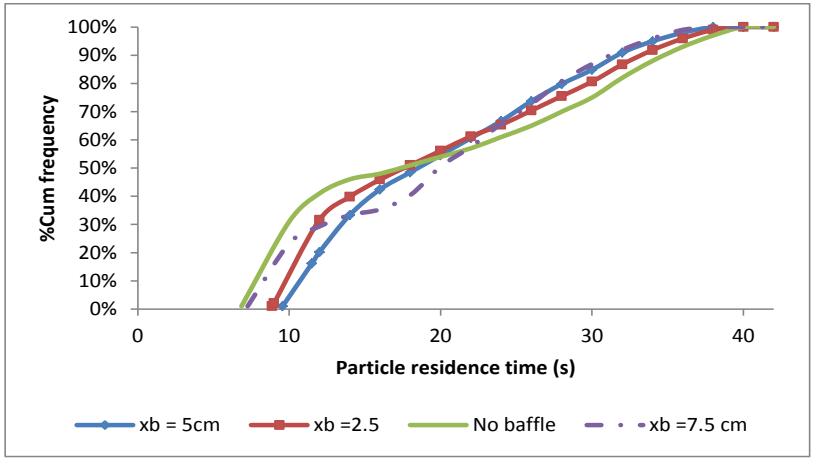

c) 45 degree baffle

Figure 9.7: Variation of particle residence time distribution with distance between baffle and concentrate weir wall (x_b) for (a) 90^0 baffle (b) 67^0 baffle and (c) 45^0 baffle

9.5 Conclusions

Schwarz-Christoffel mapping was used in generating a numerical solution to the 2D stream function equation. A specialized Matlab toolbox developed by Driscoll (1996) was used to effect the rectangular transformation from which finite difference methods was used to discretise the domain. Solution in the rectangular map was achieved by successive relaxation methods. The resulting bubble streamlines and velocity vector distribution obtained helped in developing an explanation of the experimental results. Of particular interest especially to the work in Chapter 8, is the confirmation of changes in residence time distribution with the introduction of the froth baffle and its inclination to the horizontal. Flotation performance trends deducted from the residence time distribution agreed with experimental results reported in Chapter 8. The effect of the distance between the baffle and the concentrate weir wall at the pulp-froth interface (x_b) was also investigated. The overall conclusion from that exercise is that increasing (x_b) favours recovery through reduction of residence times of particles generated both close to the back and close to the concentrate weir. Reducing to 2.5cm shifts the graph towards no baffle residence times especially for particles with residence times above the median residence time. Placing the baffle at 5cm seems to be the optimum position as it increases residence times of particles close to the concentrate weir while reducing that of particles generated at the back of the flotation cell.

Chapter 10

Conclusions and Recommendations

10.1 introduction

It is generally agreed that the froth phase is to-date not well-understood despite the enormous amount of research effort expended towards it. This has led to the froth operating at sub-optimal levels with froth recoveries as low as 10% reported in literature e.g. Vera et al. (2002). Factors that exacerbate the situation include, lack of measurement techniques to train models of our current understanding of the froth phase and also operational limits imposed on gas rate and froth depth which are typically used to optimize the froth phase per given chemical conditioning, particle size and floatability distribution. Work reported in this thesis is a small contribution towards understanding the froth. It addresses challenges posed by the lack of measurement techniques by providing a novel method to estimate froth phase bubbles sizes. In addition, techniques to optimize the froth outside of using the conventional gas rate and froth depth are discussed albeit in a laboratory environment. Overall conclusions and recommendations from this thesis are summarized in this Chapter.

10.2 Conclusions from froth phase bubble-sizer development and testing

Chapter 4 and Chapter 5 of this thesis are dedicated to the development of a technique to estimate froth phase bubble sizes as a response to one of the constraints identified as exacerbating our lack of understanding of the froth phase. This technique provides valuable information on how bubble coalescence changes as a function of height above the pulp-froth interface. Estimates of bubble sizes from the technique can be used to train bubble coalescence models and also infer froth stability. The technique which is based on the electro-resistive properties of the air inside the bubble and the water making up the bubble lamellae to measure a proxy for froth phase bubble sizes (IID) was

developed and tested with and without solids, under various slurry chemical conditions. Results reported in Chapter 4 gave us the confidence to conclude that a method to estimate froth phase bubble sizes that is comparable to the photographic method was developed. Bubble size measurement in the development section was done in slurry rich in Cu^{2+} ions. The second section of the work involved testing the concept under different slurry chemical conditions. Signals obtained with various chemicals that alter the electrical conductivity of water were found to be amenable to froth bubble size proxy (IID) estimation. A baseline condition of tap water dosed with frother also produced a signal from which IIDs were calculated. Addition of solids did not affect the bubble size signal, however the same limitation revealed in the development section was also observed in the testing phase i.e. the new technique over-estimates Sauter-mean diameter. Of importance though is that chemical composition of water that makes bubble lamella does not have a significant impact on bubble size estimation technique.

In Chapter 5 the froth bubble size measurement technique was tested in a mechanical flotation cell with solids content of up to 35%. Effect of froth depth and gas rate on froth phase bubble size as a function of height above the pulp-froth interface was tested. Results indicated that increasing superficial gas velocity at fixed froth height increases froth stability as revealed by a decrease in IID as superficial gas velocity was changed from 0.57cm/s to 0.97cm/s. The rate of increase in IID was greatest close to the surface of the froth and insignificant close to the interface. Fixing gas flux and changing froth depth resulted in an increase in average IID (close to the froth surface) as froth depth was increased. Thus the froth bubble size measuring technique provided an output that is related to froth stability and agrees with work done by other workers e.g. Moys et al. (1979), Feteris et al. (1987).

This measurement technique can be used for the optimization of froth performance if developed further. For example it can be used to obtain real-time data on how froth bubbles sizes are changing within the froth. If the rate of change of bubble sizes deviates from a preset optimum value, then mitigating action such as adding more frother, increasing or reducing gas rate, increasing or decreasing froth depth can be done to keep froth performance optimum. Consequently it is recommended that the new technique be tested further in industrial flotation cells with a view of developing an online froth stability and froth performance monitoring technique.

10.3 Conclusions from techniques to optimize froth phase performance through altering froth residence times

The second objective of this thesis was to develop and study ways of manipulating froth phase performance through manipulating froth residence time distribution. Two distinctive methods were chosen and studied experimentally and numerically by solving the 2D stream function equation which has been found to adequately describe froth transport by a number of flotation workers e.g. Moys (1979), Murphy et al. (1996), Neethling and Cilliers (1999) and Brito-Parada et al.(2012). The techniques studied include:

(1) Variation of gas flux distribution across the pulp-froth interface

(2) Use of froth baffles/ froth flow modifiers as suggested by Moys (1979)

Experiments were performed using artificial slurry comprising of 20% limestone as the floatable component and 80% silica as the gangue mineral in a pseudo steady state flotation environment. Conclusions from each of these techniques are summarised below.

10.3.1 Conclusions on the effect of gas flux distribution across the pulp-froth interface.

While Chapter 6 report results of experimental work done to investigate the effect of gas flux distribution across the pulp-froth interface on flotation performance, Chapter 7 is dedicated to using solution to the Stream function equation to explain changes in flotation performance observed in Chapter 6. A novel method to obtain various gas flux distributions across the pulp-froth interface was developed and tested. It involved designing a flotation cell with a false bottom that enabled both gas distribution mechanism and agitation mechanism to be moved relative to the flotation cell center. At each position a different gas distribution profile flux was obtained. Three gas profiles were investigated viz. high gas flux at the center (agitation and gas supply mechanism at the center), high gas flux at the back (agitation and gas supply mechanism at the back) and high gas flux close to the concentrate weir (agitation and gas supply mechanism close to the concentrate weir). Flotation experiments show that providing high gas flux at

the back of the flotation cell results in increased recovery while supplying high gas flux close to the concentrate launder resulted high grade which is contrary to our expectations. The results also strongly suggest that the conventional design of placing the impeller at the centre results in a sub-optimal flotation performance.

The flotation performance changes witnessed in Chapter 6 were explained in Chapter 7 by studying the stream function equation with boundary conditions that represent the various gas flux distribution profiles. A numerical technique based on the Method of Lines (MOL) termed the method of false transients was used to solve the stream function equation. Analysis of the results was done based on two aspects viz. air recovery and residence time distribution. Simulations indicated that supplying high gas flux at the back of the flotation cell produces the highest air recovery factor, followed by high gas flux close to the concentrate weir and lastly supplying high gas flux at the centre. An attempt to relate air recovery values to concentrate recovery was carried out. A convention that states that high air recovery factor means higher limestone recovery was adopted and experimental results reported affirmed the predictions from the modelling approach. The impact of gas flux distribution on froth residence time distribution was also considered. From both bubble and particle residence time distributions, it was clear that the manner in which gas is distributed across the interface influences the distribution of residence time substantially. Generally high gas flux close to the concentrate weir produces highest average bubble recovery and particles with higher residence times while high gas flux at the back produces the largest number of both particles and bubbles with the minimum residence time.

An attempt to link froth residence time distribution to flotation performance was made and the output of this exercise did not wholly agree with all the experimental results. The discrepancies between flotation performance predictions based on calculated residence times and real experimental data were attributed to the simplicity of the current model, especially which for example does not take into account drainage patterns in the froth. Drainage patterns play a huge role as superficial gas velocity is varied. Consequently using a froth model that includes a drainage equation is recommended if a complete explanation of how gas flux distribution across the interface influences flotation performance is to be accrued.

10.3.2 Conclusions on the froth baffles

The second and final technique of manipulating froth residence time distribution and ultimately froth performance that was studied in this thesis is the use of froth baffles as proposed by Moys (1979). Experimental results reported in Chapter 8 led to the following conclusions: (1) recovery of limestone decreases with the introduction of a froth baffle. The decrease is a function of the inclination angle of the baffle to the horizontal i.e. it decreases as the inclination angle (measured according to the convention in Figure 8.2) becomes more acute. (2) The grade of the concentrate increases with the introduction of the froth baffle, higher grades are obtained as the angle of the baffle becomes more acute (3) Water recovery decreases with baffle angle. Entrainment recovery represented by silica recovery also decreases with decrease in baffle inclination angle. Simulation of the Stream function equation in the presence of froth baffles was performed in Chapter 9. A method that involves conformal mapping and the Schwarz-Christoffel mapping in particular was used to convert the complicated flow domain into a rectangle. A solution to stream function was developed in the rectangular map and the mapped back to the physical domain. Results from the simulations affirmed changes in residence time distributions in the presence of a baffle and flotation performance predictions from these resulting residence time distributions agreed with results from Chapter 8. Activation of the back part of the froth in the presence of the baffle was also evident in the residence time distributions as exemplified by the decrease in residence time of particles generated close to the back of the flotation cell. Thus froth baffles can be used to optimize froth performance, both grade and recovery can be optimized by including a froth baffle with an inclination angle that can be changed to suit a particular concentrator's operating philosophy. Testing of froth baffles in a larger flotation cell operating with less stable froth as compared to the stability of froth used in this work is recommended.

10.4 Overall conclusions and recommendations

The primary objectives of work reported in this thesis was to use both experimental and numerical techniques to advance understanding of the froth phase and to develop non-conventional techniques that can be used to optimize froth performance through manipulation of froth residence time distribution. The objectives set out at the beginning

of the thesis have been achieved. A method to measure froth phase bubbles sizes has been developed. Data from the bubble sizer is vital in understanding the froth and can also be used for optimizing froth performance if developed further. Methods to manipulate froth residence time and froth phase sub-processes were developed and tested in a laboratory environment, encouraging results were obtained which warrants further studies in pilot plant or full scale plant. Thus while the development of the froth bubble size measuring technique can enhance understanding of important froth phase sub-processes such as bubble coalescence and froth stability, data on froth residence time manipulation techniques also reveal that froth performance can be optimized without changing gas rate and froth depth as done conventionally.

Appendix A

Pump Calibration data

A1: Pump calibration

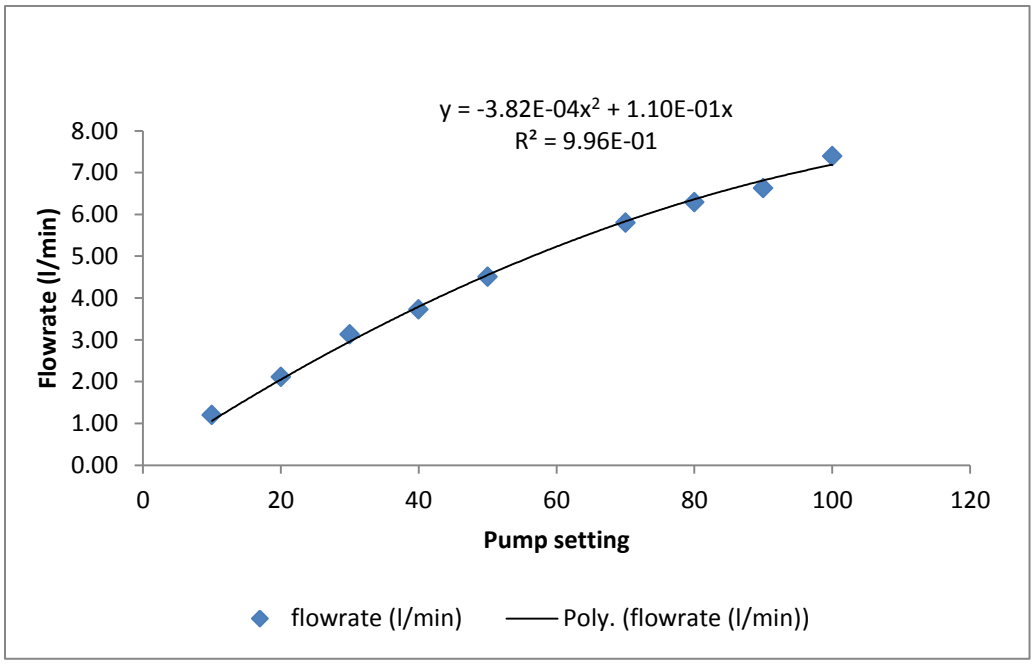

Figure A.1: Pump calibration curve

Table A1.1: Pump calibration data, with mean residence times for 8litre pulp volume

%flowrate	Volume(ml)	Time to fill	Flowrate (l/min)	Cell residence time	Pipe slurry velocity (cm/s)
10	1500	74.78	1.20	6.65	**9.98**
20	1500	42.66	2.11	3.79	**17.49**
30	2000	38.31	3.13	2.55	**25.96**
40	3500	56.28	3.73	2.14	**30.93**
50	2000	26.63	4.51	1.78	**37.35**
70	2500	25.84	5.80	1.38	**48.12**
80	4000	38.12	6.30	1.27	**52.19**
90	4000	36.21	6.63	1.21	**54.94**
100	4000	32.44	7.40	1.08	**61.33**

A1.1: Testing pump delivery consistence

The pump's ability to deliver a constant flowrate at a given pump setting was tested. Peristaltic pumps with Silicon rubbers are known to change delivery capacity as the rubber gets worked due to prolonged use. Table A1.2 show results obtained after running the pump for 1.5hrs

Table A1.2: Pump consistence test results

Time	Volume	Time (s) to fill 5000ml	Flowrate (l/min)
5	5	63.46	4.73
13	5	63.5	4.72
33	5	63.47	4.73
53	5	63.65	4.71
67	5	63.53	4.72
79	5	63.59	4.72
88	5	63.78	4.70
103	5	63.57	4.72
		Average	**4.72**
		Standard deviation	**0.008**

A2: Air rotameter calibration

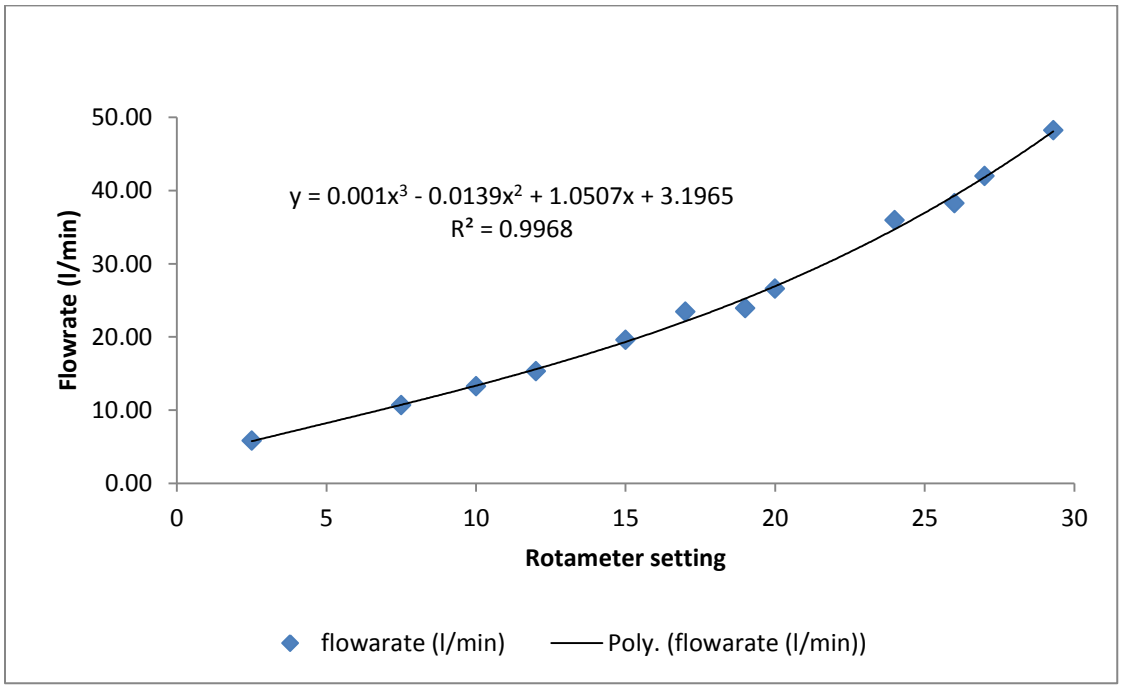

A.2: Air rotameter calibration curve

Table A.2: Air rotameter calibration data

SETTING	AVERAGE FLOWRATE (ml/sec)	AVERAGE FLOWRATE (l/min)
2.5	96.86	5.81
7.5	177.83	10.67
10	221.04	13.26
12	255.19	15.31
15	326.79	19.61
17	390.55	23.43
19	399.24	23.95
20	443.08	26.58
24	599.06	35.94
26	638.11	38.29
27	699.70	41.98
29.3	804.24	48.25

Appendix B

Miscellaneous graphs and plots

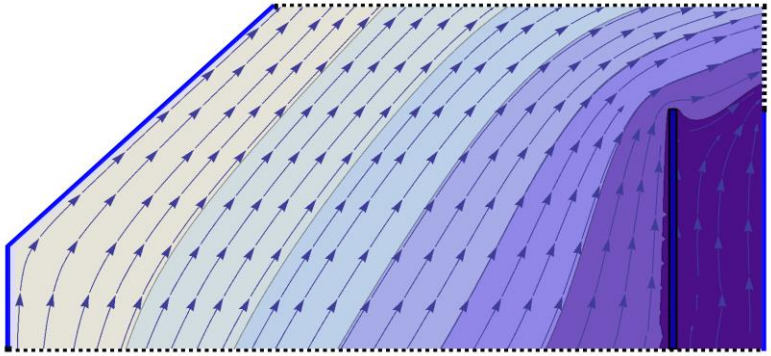

a) Distance between baffle and concentrate wier wall x_b =2.5cm

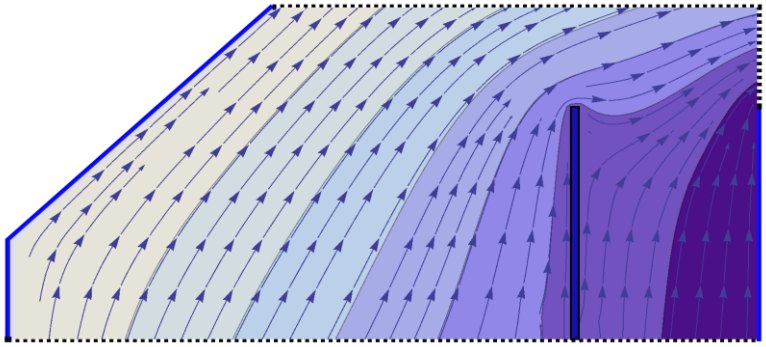

b) Distance between baffle and concentrate wier wall x_b = 5cm

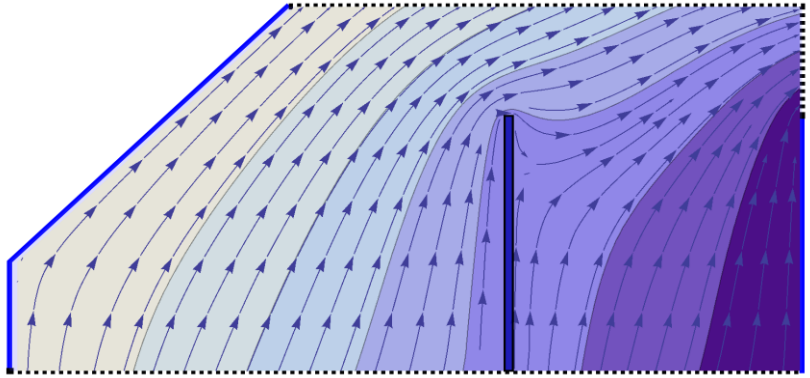

c) Distance between baffle and concentrate wier wall x_b = 7.5cm

B.1 Simulated bubble streamlines comparison for 90^0 baffle (a) x_b = 2.5 (b) x_b = 5 (c) x_b = 7.5

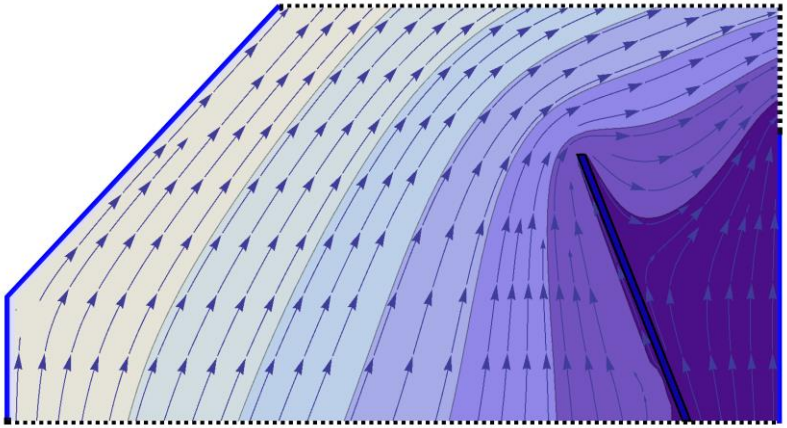

a) Distance between baffle and concentrate wier wall x_b =2.5cm

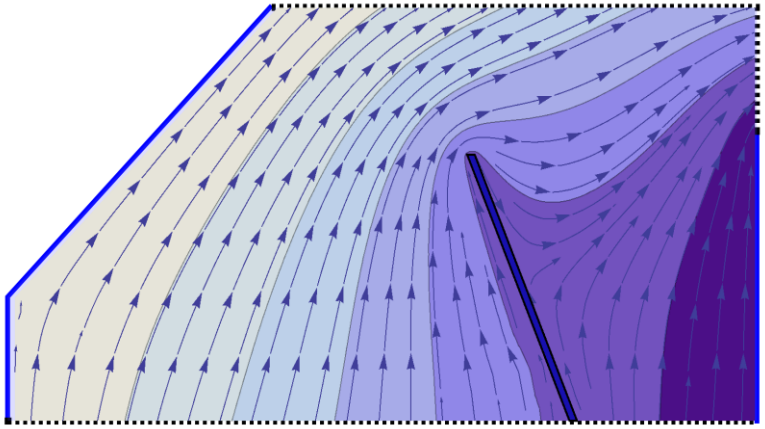

b) Distance between baffle and concentrate wier wall x_b = 5cm

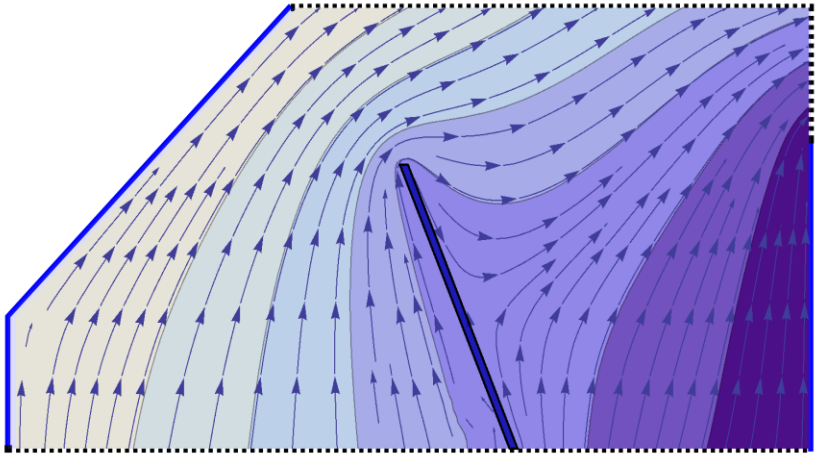

b) Distance between baffle and concentrate wier wall x_b = 7.5cm

B.2 Simulated bubble streamlines comparison for 67^0 baffle (a) x_b = 2.5 (b) x_b = 5 (c) x_b = 7.5

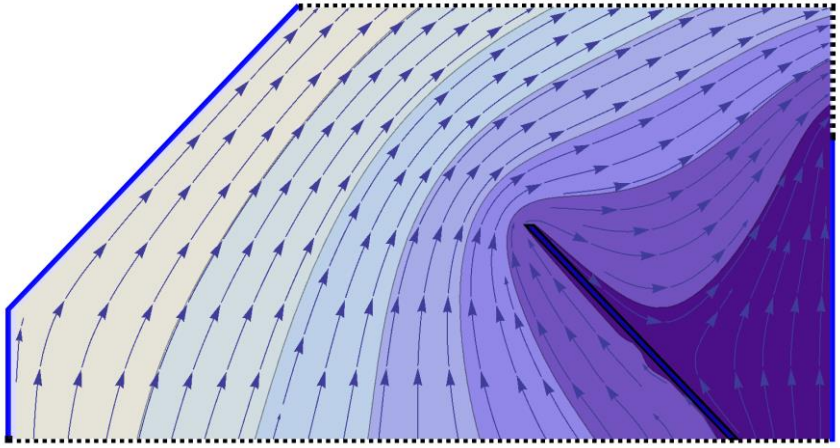

a) Distance between baffle and concentrate wier wall x_b =2.5cm

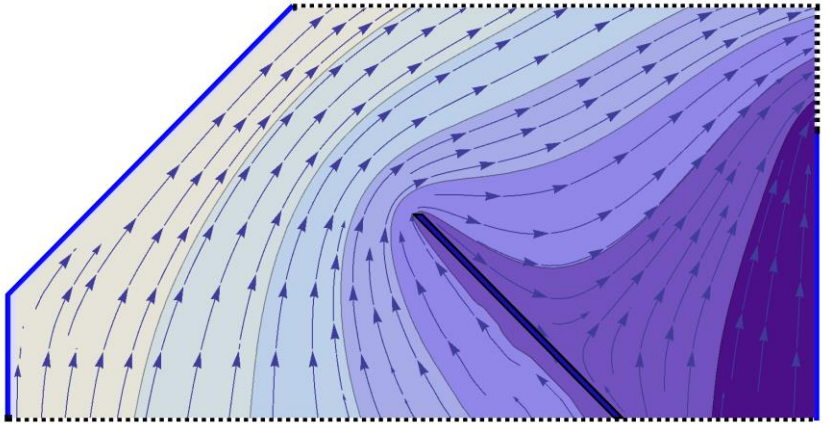

b) Distance between baffle and concentrate wier wall x_b = 5cm

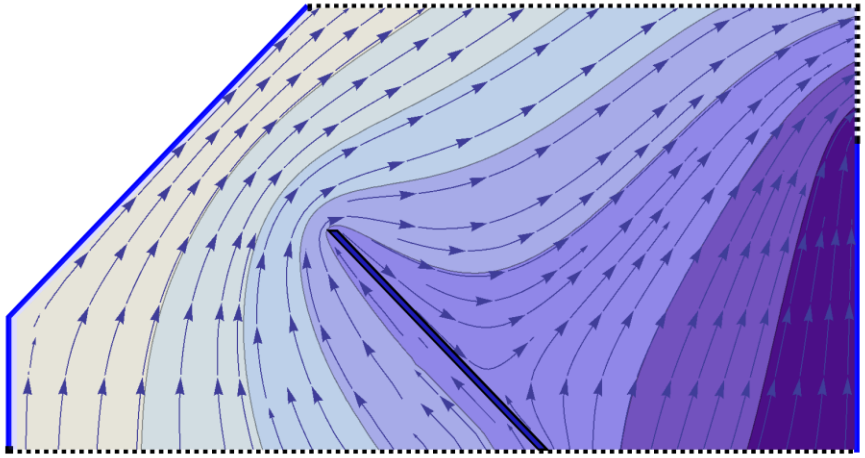

c) Distance between baffle and concentrate wier wall x_b = 7.5cm

B.3 Simulated bubble streamlines comparison for a 45^0 baffle (a) x_b = 2.5 (b) x_b = 5 (c) x_b = 7.5

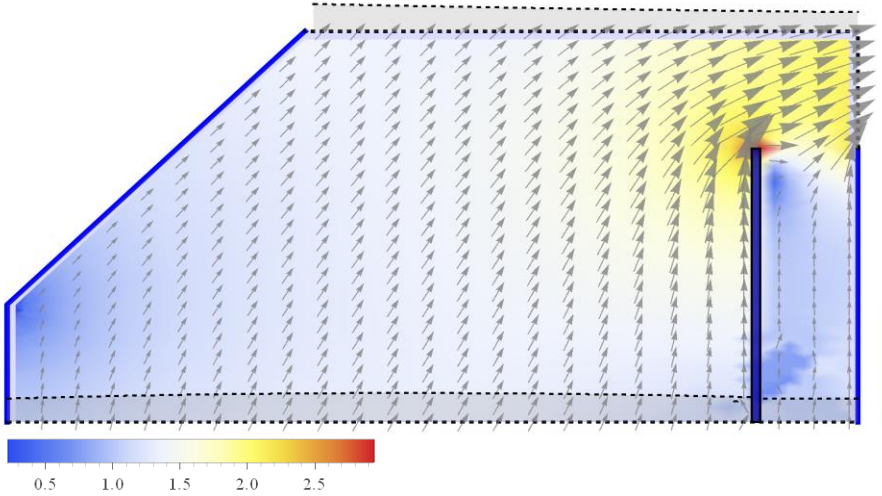

a) Distance between baffle and concentrate wier wall x_b =2.5cm

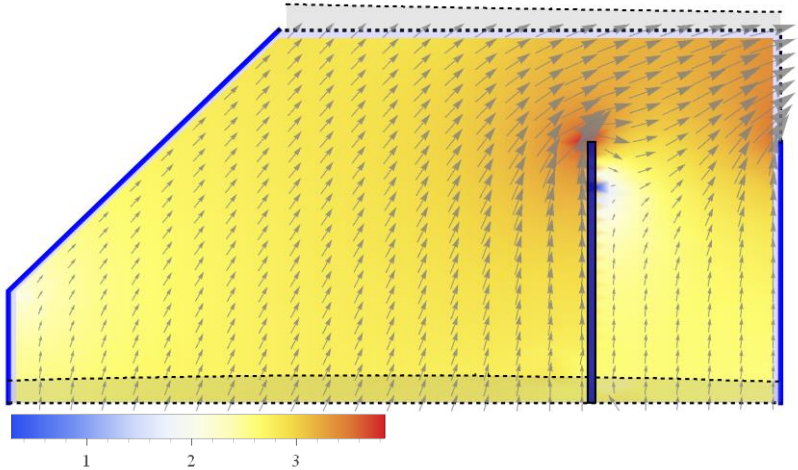

b) Distance between baffle and concentrate wier wall x_b = 5cm

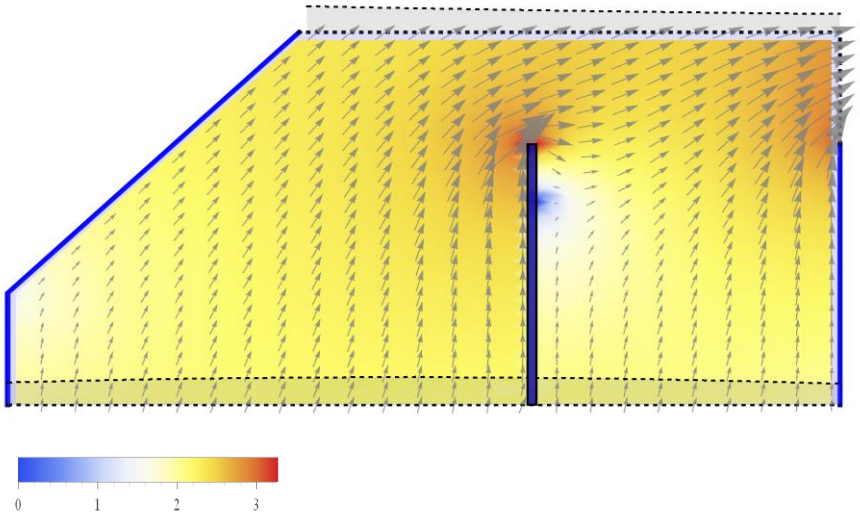

c) Distance between baffle and concentrate wier wall x_b = 7.5cm

B.4 Velocity profile comparison at 90^0 baffle angle (a) x_b = 2.5 (b) x_b = 5 (c) x_b = 7.5

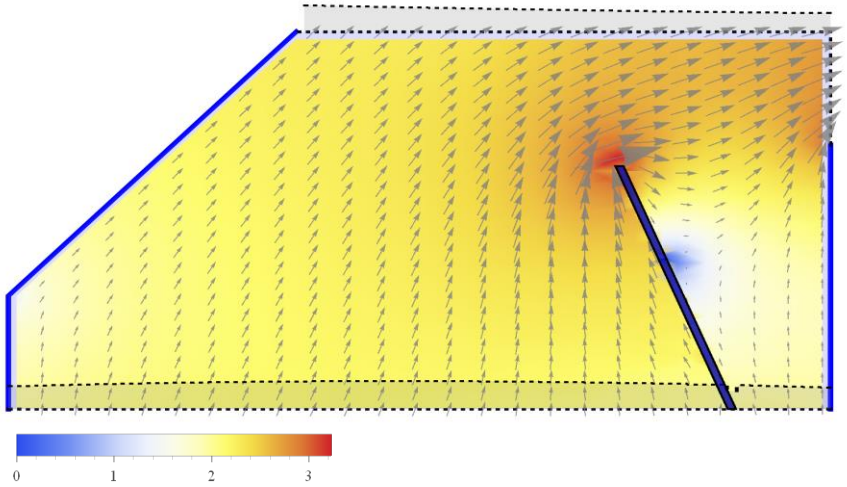

a) Distance between baffle and concentrate wier wall x_b =2.5cm

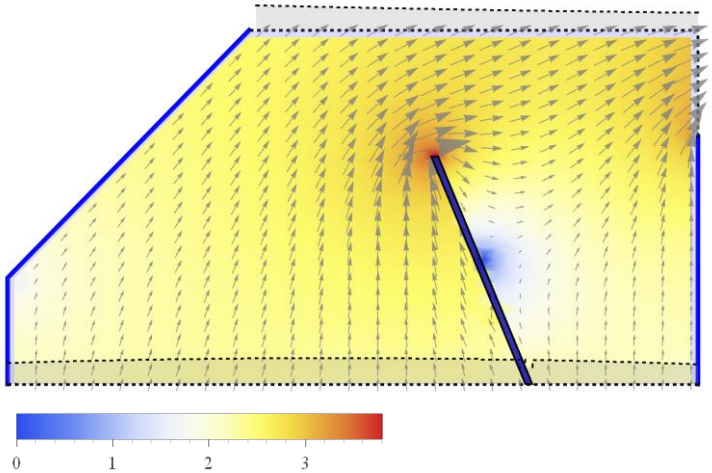

b) Distance between baffle and concentrate wier wall x_b =5cm

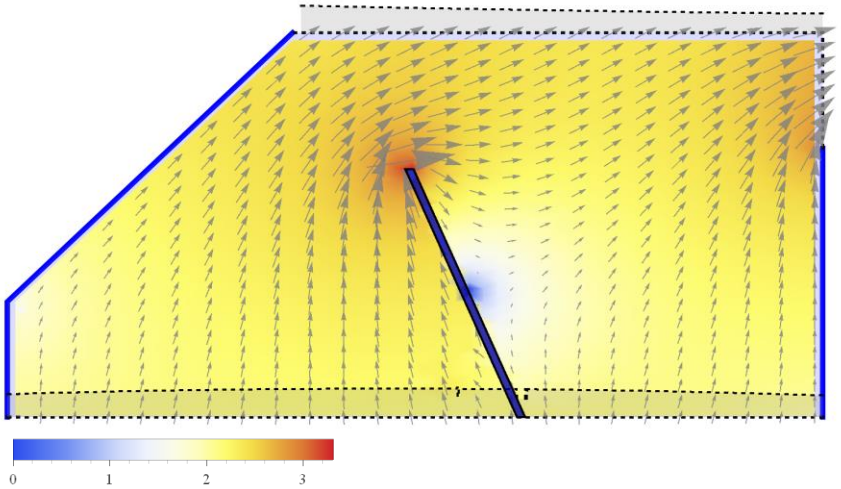

b) Distance between baffle and concentrate wier wall x_b=7.5cm

B.5 Velocity profile comparison at 67^0 baffle angle (a) x_b= 2.5 (b) x_b = 5 (c) x_b = 7.5

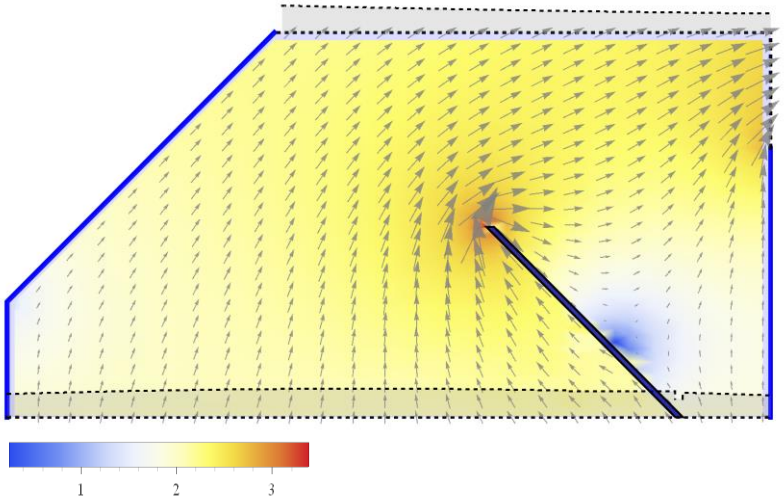

a) Distance between baffle and concentrate wier wall x_b =2.5cm

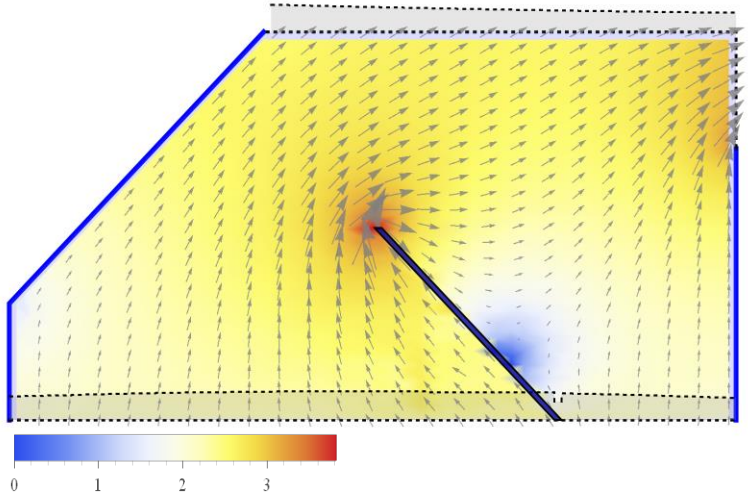

b) Distance between baffle and concentrate wier wall x_b =5cm

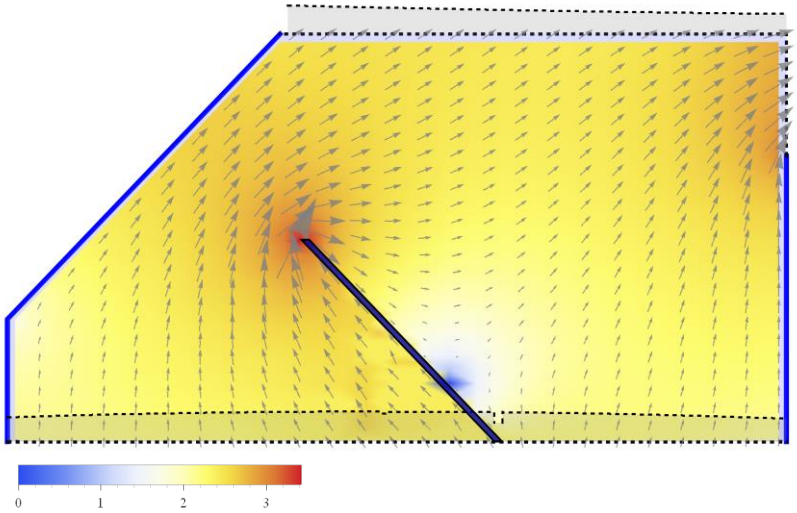

c) Distance between baffle and concentrate wier wall x_b =7.5cm

B.6 Velocity profile comparison at 45^0 baffle angle (a) x_b = 2.5 (b) x_b = 5 (c) x_b = 7.5

Appendix C

MATLAB and Mathematica Programs

C.1 Matlab function file to find local minima and maxima

This code was adapted from a code written by Eli Billauer for locating local maxima or minima from a signal.

```
function [maxtab, mintab]=peakdet(v, delta, x)
%PEAKDET Detect peaks in a vector
%        [MAXTAB, MINTAB] = PEAKDET(V, DELTA) finds the local
%        maxima and minima ("peaks") in the vector V.
%        MAXTAB and MINTAB consists of two columns. Column 1
%        contains indices in V, and column 2 the found values.
%        With [MAXTAB, MINTAB] = PEAKDET(V, DELTA, X) the indices
%        in MAXTAB and MINTAB are replaced with the corresponding
%        X-values.
%
%        A point is considered a maximum peak if it has the maximal
%        value, and was preceded (to the left) by a value lower by
%        DELTA.

% Eli Billauer, 3.4.05 (Explicitly not copyrighted).
% This function is released to the public domain; Any use is allowed.

maxtab = [];
mintab = [];

v = v(:,2); % Just in case this wasn't a proper vector

if nargin < 3
  x = (1:length(v))';
else
  x = x(:);
  if length(v)~= length(x)
    error('Input vectors v and x must have same length');
  end
end

if (length(delta(:)))>1
  error('Input argument DELTA must be a scalar');
end

%if delta <= 0
 % error('Input argument DELTA must be positive');
%end

mn = Inf; mx = -Inf;
```

```
mnpos = NaN; mxpos = NaN;

lookformax = 1;

for i=1:length(v)
  this = v(i);
  if this > mx, mx = this; mxpos = x(i); end
  if this < mn, mn = this; mnpos = x(i); end

  if lookformax
    if this < mx-delta
      maxtab = [maxtab ; mxpos mx];
      mn = this; mnpos = x(i);
      lookformax = 0;
    end
  else
    if this > mn+delta
      mintab = [mintab ; mnpos mn];
      mx = this; mxpos = x(i);
      lookformax = 1;
    end
  end
end
```

C.2.0 Matlab script file to calculate the derivative of a signal

```
clear all
%importing data from excel file
A = xlsread('result-40-10','result-40-10');
t =A(:,1);
v =A(:,2);
n=length(v);

%calculating the derivative of the signal at constant delta time

delT = t(2)-t(1);
 for i = 1:n-1
       d(i) = (v(i+1)-v(i));
       dd =d/delT;
 end

 m = length(dd);
 T = [0;t(1:m)];
 Y =[T,[dd(1);dd']];

[maxtab, mintab] = peakdet(Y, 1000);
tt =t(mintab(:,1));
tp =t(maxtab(:,1));
figure; plot(Y(:,1),Y(:,2));xlabel('Time(sec)');ylabel('Signal derivative (volts/sec)');
hold on; plot( tt,mintab(:,2), 'g*');
%plot( tp,maxtab(:,2) ,'r*');
figure;plot(t,v);xlabel('Time(sec)');ylabel('Voltage(volts)')
```

```
%CALCULATING TAKEN FROM PEAK TO PEAK
y = diff(tt);
%CALCULATING VELOCITY OF PROBE

% vp is calculated from the equations of motion by calculating the time
% the probe take to move a distance s to the bottom of the froth
% s = ut +0.5*g*T^2; u is initial velocity, g is acceleration due to
% gravity, T is time so travel a distance s. the probe starts at
% rest therefore its initial velocity u is zero

Hd = input('Please enter the value of s in meters Hd = ');
Hf = input ('Please enter froth depth Hf in meters Hf =  ');
Vt = sqrt(2*Hd*9.81); %velocity at the top of the froth
Vb = sqrt(2*(Hd+Hf)*9.81); %velocity at the bottom of the froth
Tf = sqrt(2*Hd/9.81); %time take to reach surface of froth
Tb =sqrt(2*(Hd+Hf)/9.81); %time taken to bottom of froth.
Thf=(Tb-Tf); %time taken to cut across the froth based on Newton's laws of motion
 %CALCULATING VELOCITY AT EACH GIVEN TIME PERIOD
 %vp = Vt + g*deltaT, this form
%%%%CALCULATING INSTANTANIOUS VELOCITY BASED OM TIME AND TIME OBTAINED
FROM
%%%%THE THE SIGNAL
 k = length(tt);
for j =1:k;
        deltaT(j) = tt(j)-t(1:1); %calculating incremental times from time at the top of the froth
end
  deltaT = deltaT(:);
  mn =length(deltaT);
for i =1:mn-1;
%vp = Vt + 9.81.*deltaT';
vp = Vt + 9.81.*tt';
vp = vp(:);
va(i) = ( vp(i)+ vp(i+1))/2; %calculating average velocity between two consecutive peaks
end
 %CALCULATING PEAK TO PEAK DISTANCES IN MILLIMETERS, THESE REPRESENT
BUBBLE
%SIZES
s = length(y);
va = va(1:s);
Db = va'.* y; %calculating bubble sizes

%PLOTTING BUBBLE SIZE AS A FUNCTION OF FROTH DEPTH
D = 1000*Db;
hf = linspace(0,Hf*100,length(D));
figure;plot(hf,D,'g*')
xlabel('Depth below surface of froth');
ylabel('Bubble size index (mm)')

%CALCULATING AVEARGE VELOCITY AFTER A GIVEN FROTH DEPTH
%PLOTTING AVERAGE BUBBLE SIZE INDEX AS A FUCTION OF DEPTH
BB = [hf',D];
Vinfroth = sqrt(Vt*Vt + 0.02.*hf'*9.81);%variation of velocity based on equations of motion
instantaneous velocity can be calculated by differentiating calculating the derivative of the signal
at constant delta time
s =hf';
q=length(hf');
```

```
for i = 1:q-1
    h =Hd+Hf;
    Ttot = Tf+tt(k);
    a =2*(h)/(Ttot^2);
    vpf = Vt + a*tt';

end

%CALCULATING PEAK TO PEAK DISTANCES IN MILLIMETERS (IID),USING CORRECTED
ACCELLERATION
s = length(y);
vpf = vpf(1:s);
Db = vpf'.* y; %calculating bubble sizes
%PLOTTING BUBBLE SIZE AS A FUNCTION OF FROTH DEPTH
D2 = 1000*Db;
```

C.3 Matlab function file to solve Stream function equation using the method of lines (MOL)

```
function [ X,Y, A ] = setUpLaplace( m, g1, g2, g3, c )

% Solves Laplace's Equation on the domain with mesh size m
% INPUTS:
%       m       - mesh size (20m x 10m grid will be created)
%       g1      - Polynomial in x gives gas flow on the bottom; dmn (0,20)
%       g2      - Polynomial in x gives gas flow at the top; dmn (7,20)
%       g3      - Polynomial in y gives gas flow on side; dmn (7, 10)
%       c       - Value of psi in the bottom-left corner (default = 0)
%      NOTE: g1, g2 and g3 are represented by coefficient arrays so that
%           [a,b,c,d] represents ax^3 + bx^2 + cx + d.
% OUTPUTS:
%       A       - steady-state solution
% METHOD:
%

   if nargin < 5
      c = 0;
   end

   tmax = 20; % M

   delta = 1/m;
   invsqdelta = m*m;
   x = 0:delta:20;
   y = 0:delta:10;

   % Finite Difference Method

   % To get the Dirichlet Boundary conditions, we need to integrate the
   % derivative conditions around the boundary
   % Since the functions are polynomials, integrating them is easy:
```

```
    g1I = polyint(g1);  % coefficient array for the integral of g1
    g2I = polyint(g2);  % coefficient array for the integral of g2
    g3I = polyint(g3);  % coefficient array for the integral of g3

     c1 = c;                                    % bottom-left corner
    c2 = c1 - (polyval(g1I,20)-polyval(g1I,0));     % bottom-right corner
    c3 = c2 + (polyval(g3I,10)-polyval(g3I,7));     % top-right corner
    c4 = c3 - (polyval(g2I,7)-polyval(g2I,20));       % top of diagonal - should be same as bottom corner = c1

    % Requirement for consistency:
    % c4 = c1, implies g1I(0)-g1I(20)+g3I(10)-g3I(7)+g2I(7)-g2I(20) = 0

    if abs(c4-c1) > 1e-10
      %  error('Polynomials on boundaries are not consistent! The integral around the loop must be zero!\nThe condition you neerd ');
    end

    % some important indices and dimensions
    x7 = 7*m + 1;      % index in grid of x = 7
    y7 = 7*m + 1;      % index in grid of y = 7
    Nx = 20*m+1; Ny = 10*m+1;
    [X,Y] = meshgrid(x,y);

    % Feasible Region
    R = Y - X <= 3;                                         % The region R

    Rbar = false(size(R)+[2,2]);Rbar(2:end-1,2:end-1) = R;              % Framed R

    dR = xor(R,Rbar(3:end,2:end-1))     |   xor(R,Rbar(1:end-2,2:end-1))| ...
        xor(R,Rbar(2:end-1,1:end-2))   |   xor(R,Rbar(2:end-1,3:end));     % Boundary of R

    %iR = R & ~ dR;                                          % Interior of R

       % Initial and boundary values
    A0 = repmat((c1+c4)/2, size(R)); % c1=c4, averaging just to reduce numerical error

    A0(1,:)         = c1 - (polyval(g1I, x)         -   polyval(g1I,0));       % Bottom Boundary
    A0(1:y7,Nx)     = c2;                                       % Right wall
    A0(y7:Ny,Nx)    = c2 + (polyval(g3I, y(y7:Ny))  -   polyval(g3I,7));       % Right porous part
    A0(Ny,x7:Nx)    = c1 - (polyval(g2I, x(x7:Nx))  -   polyval(g2I,7));       % Top porous part

    u0 = reshape(A0, numel(A0), 1); % current solution reshaped to a column vector

    dfn = @(t, y) mol(t, y, invsqdelta, Nx, Ny, dR);

    [~, U] = ode45(dfn, [0, tmax], u0);

    A = reshape(U(end,:), Ny, Nx);
    A(~R) = -inf;

    disp('done');

end
```

```
% METHOD OF LINES
function dudt = mol(~, u, invsqdelta, N, M, dR)
   u = reshape(u, M, N);
   dudt = zeros(size(u));

   % Middle Points
   dudt(2:end-1, 2:end-1) = invsqdelta*( -4*u(2:end-1, 2:end-1)+ u(1:end-2, 2:end-1) + ...
                                    u(3:end, 2:end-1) +  u(2:end-1, 1:end-2) + ...
                                    u(2:end-1, 3:end));

   dudt(dR) = 0; % No change on the boundary

   % Reshape to vector
   dudt = reshape(dudt, numel(dudt), 1);

end
```

C.4 Matlab script file to solve Stream function equation using the method of lines (MOL)

```
clc
g1 = [0.8492, -0.0286, 6.8276e-4];       % Currently: (2 + 2 x + 3 x^2)
g2 = [-1.1058, 0.2273, -0.0075];         % Currently: 2 +3 x + 4x^2)

n = length(g1);

g1 = fliplr(g1);    % MATLAB treats [a,b,c] as a x^2 + b x + c, not as a + b x + c x^2. I have it the
other way around above
g2 = fliplr(g2);
G1 = polyint(g1);
G2 = polyint(g2);
g3 = ((polyval(G1,20)-polyval(G1,0))-(polyval(G2,20)-polyval(G2,7)))/3;
R3 =3*g3;
R1 =polyval(G1,20)-polyval(G1,0);
R2 = polyval(G2,20)-polyval(G2,7);
R1=R2+R3;
alpha = R3/R1

[X,Y,A] = setUpLaplace(4, g1, g2, g3, 0);            % The "8" here is for 8x grid size. You can go
lower for speed or higher for granularity
 subplot(1,2,1); surf(X,Y,A,'EdgeColor','none','LineStyle','none','FaceLighting','phong');
set(gca, 'DataAspectRatio', [repmat(min(diff(get(gca, 'XLim')), diff(get(gca, 'YLim'))), [1 2])
diff(get(gca, 'ZLim'))]);
%axis([-1, 21, -1, 11, min(min(A)), max(max(A))]);
axis([-1, 21, -1, 11]);
axis vis3d
subplot(1,2,2); contourf(X,Y,A); axis([-1 20 -1 10]); axis equal;

save psi.mat X Y A
figure; hold on
plot(7:0.1:20, polyval(g2, 7:0.1:20));
xlabel ('Flotation cell length (cm)');ylabel ('Gas flux (cm/s)')
```

```
plot(0:0.1:20, polyval(g1, 0:0.1:20), '--')
%plot(0:0.1:20, repmat(g3, length(0:0.1:20), 1), 'r');
legend('Flux at the froth surface','Flux at pulp-froth interface');
```

C.5 Mathematica code to plot bubble streamline.

```
Initializations
SetDirectory[NotebookDirectory[]]
{X,Y,psi} = Import["psi.mat"];
ClearAll[psiI, vx, vy]
edgeVal = X[[1,1]];
psiI[x_, y_] := Evaluate[Interpolation[Flatten[Table[{X[[i,j]], Y[[i,j]], psi[[i,j]]/.-Infinity→edgeVal}, {i, 1,
Length[X]}, {j, 1, Length@X[[i]]}], 1]][x,y]];
vx[x_, y_] := Evaluate[D[psiI[x,y], y]];
vy[x_,y_] := Evaluate[-D[psiI[x,y], x]];
H:\Drobox 2
Visualization of Stream function
Show[
 Graphics[
  Flatten@{
    Blue,Thickness[0.006],
    Line[{{20,0}, {20, 7}}],
    Line[{{7, 10}, {0, 3}, {0,0}}],
    Black, Dashed,Thickness[0.008],
    Line[{{0,0}, {20,0}}],
    Line[{{20, 7}, {20, 10}, {7, 10}}],
    EdgeForm[],
    FaceForm[Directive[Lighter@Blue, Opacity[0.2]]],
    Polygon[{{0,0}, {20,0}, {20,10}, {7, 10}, {0,3}, {0,0}}],
    },
  ImageSize→800
  ],
 StreamPlot[{vx[x,y],vy[x,y]}, {x, 0, 20}, {y, 0, 10}, AspectRatio→1/2]
]
```

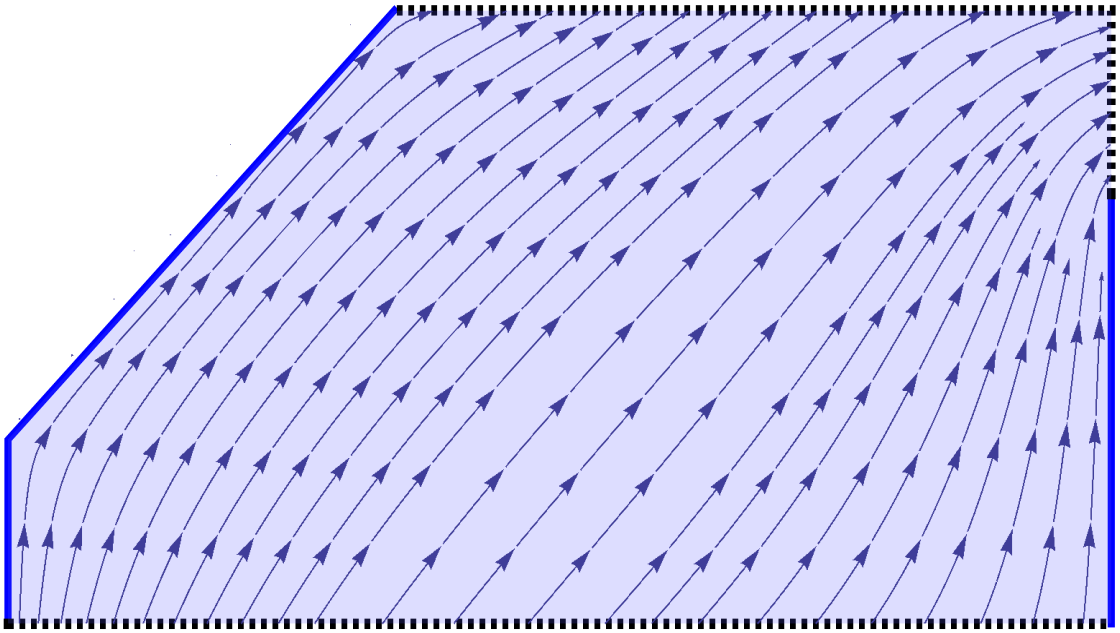

```
Show[
 Graphics[
  Flatten@{
    Blue,Thickness[0.006],
    Line[{{20,0}, {20, 7}}],
    Line[{{7, 10}, {0, 3}, {0,0}}],
    Black, Dashed,Thickness[0.008],
    Line[{{0,0}, {20,0}}],
    Line[{{20, 7}, {20, 10}, {7, 10}}],
    EdgeForm[],
    FaceForm[Directive[Lighter@Blue, Opacity[0.2]]],
    Polygon[{{0,0}, {20,0}, {20,10}, {7, 10}, {0,3}, {0,0}}],
    },
  ImageSize→800
  ],
 ContourPlot[psiI[x,y],     {x,  0,  20},  {y,  0,  10},  RegionFunction→Function[{x,y},  x>y-3],
AspectRatio→1/2, ImageSize→500], (* Line for contours *)StreamPlot[{vx[x,y],vy[x,y]}, {x, 0, 20},
{y, 0, 10}, AspectRatio→1/2] (* Line for streamlines *)
 ]
```

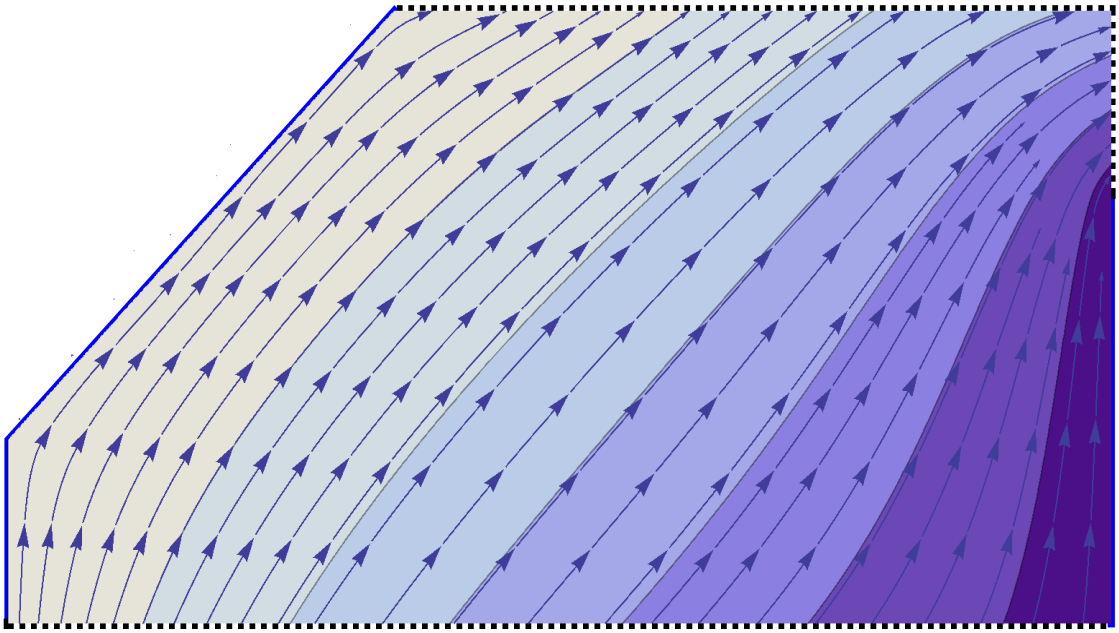

Bubble Transit Times

```
getTransitTime[x0_] :=
 Reap[NDSolve[{
    D[x[t], t] == vx[x[t], y[t]],
    D[y[t], t] == vy[x[t],y[t]],
    x[0] == x0,
    y[0] == 0,
    WhenEvent[(y[t]>9.9 && x[t] ≥  7) || (x[t] > 19.5 && y[t] ≥ 7), Sow[t];"StopIntegration"]
    },
   {x[t], y[t]},
   {t, 0, 100}
   ]
  ][[2,1,1]]
transitTimeList =Table[{x0, getTransitTime[x0]}, {x0, 0.1, 19.5, 0.5}];
ListPlot[transitTimeList[[1;;-1;;1,;;]], Frame→True,FrameLabel→{"x starting position (cm)", "transit time (seconds)"}, PlotStyle→PointSize[Large]]
```

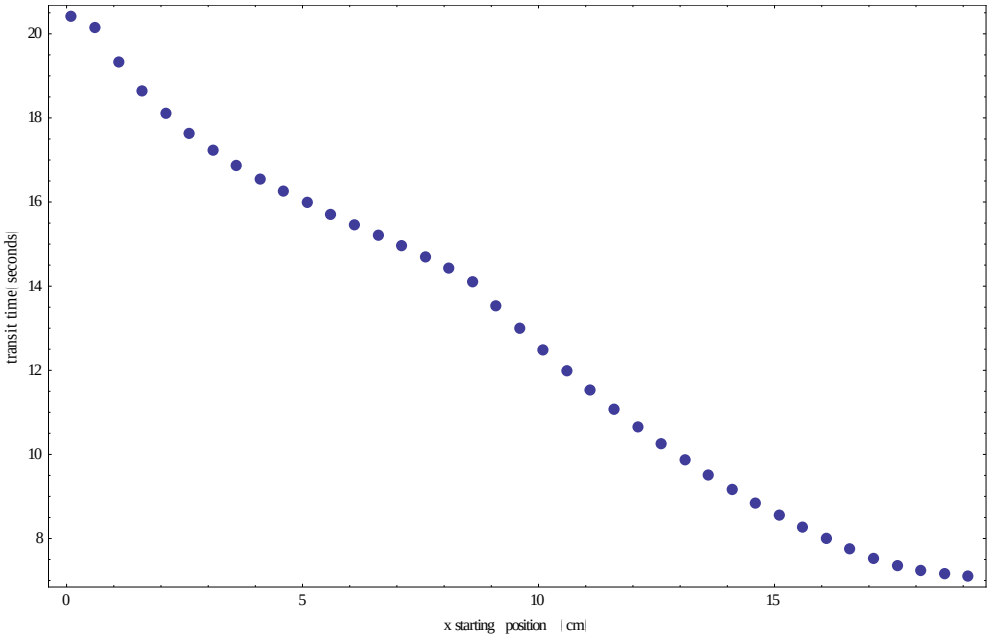

SetDirectory[NotebookDirectory[]]
Export["highgasback.xlsx", transitTimeList]
H:\frothphase
highgasback.xlsx

C.6 Matlab function file to implement Schwarz-Christoffel Mapping in the presence of a froth baffle

The function file given below performs the SC mapping of the physical domain to a rectangular map for the three baffle positions. It does not apply to a situation when there is no baffle in the froth.

```
function [xvals, yvals, zvals, bndDat, confMap] = solveRegionGeneral(g1, g2, divTheta, divStart, divLen, divWid, M, N)

%% Default values for input
if nargin < 1
    g1 = [0.5971, 0.03, -0.0016];
end
if nargin < 2
    g2 = [0.0889, -0.0352, 0.0008];
end

if nargin < 3
    divTheta = pi/2;%67*pi/180;
end

if nargin < 4
    divStart = 15;
end
if nargin < 5
    divLen  = 7;
end
if nargin < 6
```

```
    divWid = 0.2;
end

if nargin < 7
    M = 200;
end

if nargin < 8
    N = 100;
end

%% Set up the region & Boundary functions
x1 = divStart - divLen*cos(divTheta);
y1 = divLen*sin(divTheta);

polypts = [0 divStart x1+y1*1i x1+divWid+y1*1i divStart+divWid 20
20+10i 7+10i 3i];
Region2 = polygon(polypts);

% FUNCTION FOR BOUNDARY ALONG EACH LEG OF THE BOUNDING POLYNOMIAL
g1 = fliplr(g1);
g2 = fliplr(g2);
g1I = polyint(g1);
g2I = polyint(g2);
g3              =              (polyval(g1I,20-divWid)-polyval(g1I,0)-
polyval(g2I,20)+polyval(g2I,7))/3;
g3I = polyint(g3);

p10 = polyval(g1I, 0);
p1s = polyval(g1I, divStart);
p37 = polyval(g3I, 7);
p220 = polyval(g2I, 20);

c1 = 0;                                        % bottom-left corner
c15 = c1 - (p1s - p10);                        % Baffle
c2 = c15 - (polyval(g1I,20-divWid)-p1s);       % bottom-right corner
c3 = c2 + (polyval(g3I,10)-p37);               % top-right corner
c4 = c3 - (polyval(g2I,7)-p220);                 % top of diagonal - should
be same as bottom corner = c1
if abs(c4-c1) > 1e-10
    error('Polynomials on boundaries are not consistent! The integral
around the loop must be zero!\nThe condition you neerd ');
end

bndFn = cell(9,1);
bndFn{1} = @(x) c1 - ( polyval(g1I, divStart*x)  -   p10 );
bndFn{2} = @(x) repmat(c15, size(x)); % Baffle: up
bndFn{3} = @(x) repmat(c15, size(x)); % BAFFLE: accross
bndFn{4} = @(x) repmat(c15, size(x)); % BAFFLE: back down
bndFn{5} = @(x) c15 - ( polyval(g1I,divStart+(20-divStart-divWid)*x) -
p1s);
bndFn{6} = @(x) c2.*(x<.7) + (c2 + (polyval(g3I, 7+10*(x-.7)) -
p37)).*(x>=.7);
bndFn{7} = @(x) c3 - (polyval(g2I,20*(1-x)+7*x)-p220);
bndFn{8} = @(x) repmat(c1, size(x));
```

```
bndFn{9} = @(x) repmat(c1, size(x));

%% Solution
% GET THE MAP TO A RECTANGLE
confMap = rectmap(Region2, [1,6,7,8]);

% SOLVE LAPLACE'S EQUATION!
[xvals, yvals, zvals] = solveLaplace(Region2, bndFn, confMap, M, N);
xBnd = real(polypts); xBnd = [xBnd(1:6) 20 xBnd(7:end) xBnd(1)];
yBnd = imag(polypts); yBnd = [yBnd(1:6) 7 yBnd(7:end) yBnd(1)];
zBnd = [c1 c15 c15 c15   c15   c2  c2 c3  c1 c1 c1];
bndDat = [xBnd; yBnd; zBnd];
```

C.7 Matlab function file to solve stream function equation on the rectangular map and transforming it back to the physical domain

```
function [xvals, yvals, zvals] = solveLaplace(polyReg, bndFn, confMap, M, N)
%solveLaplace - solve's laplace's equation on the transformed rectangle
%           and transforms the solution back to the original polygon
% INPUTS:
%     polyReg    - The polygon object (scpack) for the boundary region
%     bndFn      - The boundary function for the boundary region
%                A cell of functions for each edge mapping [0,1]->R
%     confMap    - The chosen conformal map from polyReg to a rectangle
%     M          - The number of points to discretize with in the imaginary direction
%     N          - The number of points to discretize with in the real direction
% OUTPUTS:
%     xvals      - a matrix of x-values indicating x positions in the
%                original polygon
%     yvals      - a matrix of y-values indicating y positions in the
%                original polygon1
%     zvals      - a matrix of z-values indicating the solution function
%                at the corresponding x and y values
%     (the sizes of these three matrices correspond to the transformed
%     rectangle)

V = vertex(polyReg); V = reshape(V, 1, length(V));
Vlng = abs([V(2:end) V(1)]-V);
R = rectangle(confMap);

% SET UP THE RECTANGLE WITH BOUNDARY (and record transformation back to
% poly)
A = zeros(M, N);
rlst = linspace(imag(R(1)), imag(R(2)), M);
clst = linspace(real(R(2)), real(R(3)), N);
[gC, gR] = meshgrid(clst, rlst);
tpts = confMap(gC+1i*gR); % WHERE EACH POINT IN THE GRID MAPS TO

for i = 1:4
   if mod(i, 2) == 1
      npts = M;
   else
```

```
        npts = N;
    end
    bndR = linspace(real(R(i)), real(R(mod(i,4)+1)), npts);
    bndI = linspace(imag(R(i)), imag(R(mod(i,4)+1)), npts);
    [mapCplx, vmap]  = nearestPtPoly(V, confMap(bndR+1i*bndI));
    vdst = abs(V(vmap)-mapCplx)./Vlng(vmap);

    for k = 1:length(vmap)
        if i==1
            r = k;
            c = 1;
        elseif i==2
            r = M;
            c = k;
        elseif i==3
            r = M-k+1;
            c = N;
        else
            r = 1;
            c = N-k+1;
        end
        A(r,c) = bndFn{vmap(k)}(vdst(k));
    end
end

% SOLVE LAPLACE'S EQUATION ON THE RECTANGLE WITH BOUNDARY
A = laplaceRectDirichlet(A, abs(R(2)-R(1))/M, abs(R(3)-R(2))/N);

% TRANSFORM BACK TO THE ORIGINAL POLYGON
xvals = real(tpts);
yvals = imag(tpts);
zvals = A;
```

C.8 Matlab function file to visualize the solution in Matlab

```
function visualizeSolution(xvals, yvals, zvals, bndDat, confMap)

[M, N] = size(xvals);

nstepsR = ceil(M/40); pieceR = 2:nstepsR:M; % only show a subset (of most 40 in each direction
of points)
nstepsC = ceil(N/40); pieceC = 2:nstepsC:N;
xvalVis = xvals(pieceR, pieceC);
yvalVis = yvals(pieceR, pieceC);
zvalVis = zvals(pieceR, pieceC);

 %xBnd = [xvals(1,:) xvals(2:end,end)' xvals(end, end-1:-1:1) xvals(end-1:-1:1,1)'];
%yBnd = [yvals(1,:) yvals(2:end,end)' yvals(end, end-1:-1:1) yvals(end-1:-1:1,1)'];
%zBnd = [zvals(1,:) zvals(2:end,end)' zvals(end, end-1:-1:1) zvals(end-1:-1:1,1)'];

xR = reshape(xvalVis, numel(xvalVis), 1);
yR = reshape(yvalVis, numel(yvalVis), 1);
zR = reshape(zvalVis, numel(zvalVis), 1);
```

```
cols = 1+round(127*(zR - min(zR(:)))/(max(zR(:))-min(zR(:))));
cmap = hsv(128);

subplot(1,2,1); scatter3(xR, yR, zR, [],cmap(cols, :), 'filled');
set(gca, 'DataAspectRatio', [repmat(min(diff(get(gca, 'XLim')), diff(get(gca, 'YLim'))), [1 2])
diff(get(gca, 'ZLim'))]);
axis([-1, 21, -1, 11, min(min(zR)), max(max(zR))]);
axis vis3d
hold on;
plot3(bndDat(1,:), bndDat(2,:), bndDat(3,:), 'LineWidth', 3);
subplot(1,2,2); plot(confMap);
```

C.9 Matlab script file that calls functions C.6 to C.9 to solve flows when there is baffle in the froth.

This script allows changes in permeable region changes and also baffle angles and the distance the baffle and the concentrate launder wall at the pulp-froth interface. It also saves the solution which is the exported to Mathematica where elegant visualization of the solution is done and aslo calculation of residence time distributions.

```
g1 = [0.5971, 0.03, -0.0016];
g2 = [0.891, -0.0298, 0.0005];
M = 200;
N = 100;

% Region 2
divTheta = pi/2;
divStart = 15;
divLen  = 7;
divWid = 0.2;

[xvals2, yvals2, zvals2, bndDat2, confMap2] = solveRegionGeneral(g1, g2, divTheta, divStart,
divLen, divWid, M, N);
save reg2.mat xvals2 yvals2 zvals2 bndDat2

% Region 3
divTheta = pi/4;
divStart = 15;
divLen  = 7;
divWid = 0.2;

[xvals3, yvals3, zvals3, bndDat3, confMap3] = solveRegionGeneral(g1, g2, divTheta, divStart,
divLen, divWid, M, N);
save reg3.mat xvals3 yvals3 zvals3 bndDat3

% Region 4
divTheta = 67*pi/180;
divStart = 15;
```

```
divLen  = 7;
divWid = 0.2;

[xvals4, yvals4, zvals4, bndDat4, confMap4] = solveRegionGeneral(g1, g2, divTheta, divStart, divLen, divWid, M, N);
save reg4.mat xvals4 yvals4 zvals4 bndDat4
```

C.10 Matlab script file that calls functions C.6 to C.9 to solve flows when there is no baffle in the froth

Codes represented above implements the SC mapping and also solve the Lapalce equation in the presence of a froth baffle. Implementation of SC mapping in froth without a baffle was achieved by the code given below.

```
clear all
M = 200; N = 100;

% SET UP THE REGION
x1 = 13 - 7*sqrt(2)/2;
y1 = 7*sqrt(2)/2;

x2 = 13 - 7*cos(67*pi/180);
y2 = 7*sin(67*pi/180);

Region1 = polygon([0 20 20+10i 7+10i 3i]);

% FUNCTION FOR BOUNDARY ALONG EACH LEG OF THE BOUNDING POLYNOMIAL
g1 = [1.192, 0.074, -0.0036];          % Currently: ? + 2 x + 3 x^2
g2 = 2*[1.22, -0.1345, 0.004];         % Currently: 2 - x
n = length(g1);
g1 = fliplr(g1);    % MATLAB treats [a,b,c] as a x^2 + b x + c, not as a + b x + c x^2. I have it the other way around above
g2 = fliplr(g2);
g1I = polyint(g1);
g2I = polyint(g2);
g3 = (polyval(g1I,20)-polyval(g1I,0)-polyval(g2I,20)+polyval(g2I,7))/3;
g3I = polyint(g3);

p10 = polyval(g1I, 0);
p37 = polyval(g3I, 7);
p220 = polyval(g2I, 20);
c1 = 0;                                % bottom-left corner
c2 = c1 - (polyval(g1I,20)-p10);     % bottom-right corner
c3 = c2 + (polyval(g3I,10)-p37);     % top-right corner
c4 = c3 - (polyval(g2I,7)-p220);     % top of diagonal - should be same as bottom corner = c1
if abs(c4-c1) > 1e-10
   error('Polynomials on boundaries are not consistent! The integral around the loop must be zero!\nThe condition you neerd ');
end
```

```
bndFn = cell(5,1);
bndFn{1} = @(x) c1 - ( polyval(g1I, 20*x)  -   p10 );
bndFn{2} = @(x) c2.*(x<.7) + (c2 + (polyval(g3I, 7+10*(x-.7))  -  p37)).*(x>=.7);
bndFn{3} = @(x) c3 - (polyval(g2I,20*(1-x)+7*x)-p220);
bndFn{4} = @(x) repmat(c1, size(x));
bndFn{5} = @(x) repmat(c1, size(x));

% GET THE MAP TO A RECTANGLE
confMap = rectmap(Region1, [1,2,3,4]);

% SOLVE LAPLACE'S EQUATION AND TRANSFORM BACK TO THE ORIGINAL SPACE
[xvals, yvals, zvals] = solveLaplace(Region1, bndFn, confMap, M, N);
% VISUALIZE THE SOLUTION
nstepsR = ceil(M/40); pieceR = 1:nstepsR:M; % only show a subset (of most 40 in each direction
of points)
nstepsC = ceil(N/40); pieceC = 1:nstepsC:N;
xvalVis = xvals(pieceR, pieceC);
yvalVis = yvals(pieceR, pieceC);
zvalVis = zvals(pieceR, pieceC);

xBnd = [xvals(1,:) xvals(2:end,end)' xvals(end, end-1:-1:1) xvals(end-1:-1:1,1)'];
yBnd = [yvals(1,:) yvals(2:end,end)' yvals(end, end-1:-1:1) yvals(end-1:-1:1,1)'];
zBnd = [zvals(1,:) zvals(2:end,end)' zvals(end, end-1:-1:1) zvals(end-1:-1:1,1)'];

xR = reshape(xvalVis, numel(xvalVis), 1);
yR = reshape(yvalVis, numel(yvalVis), 1);
zR = reshape(zvalVis, numel(zvalVis), 1);

cols = 1+round(127*(zR - min(zR(:)))/(max(zR(:))-min(zR(:))));
cmap = hsv(128);

subplot(1,2,1); scatter3(xR, yR, zR, [],cmap(cols, :), 'filled');
set(gca, 'DataAspectRatio', [repmat(min(diff(get(gca, 'XLim')), diff(get(gca, 'YLim'))), [1 2])
diff(get(gca, 'ZLim'))]);
axis([-1, 21, -1, 11, min(min(zR)), max(max(zR))]);
axis vis3d
hold on;
plot3(xBnd, yBnd, zBnd, 'LineWidth', 3);
subplot(1,2,2); plot(confMap);

save reg1.mat xvals yvals zvals
```

C.11 Mathematica code to plot bubble streamline, velocity vector and density plots and calculate froth residence times.

```
Initialization
ClearAll[x,y,data1, data2, data3, data4, remDuplicates, fullDat1, fullDat2, fullDat3, fullDat4, fn1,
fn2, fn3, fn4, vx1,vy1, vx2, vy2, vx3, vy3]

SetDirectory[NotebookDirectory[]]
data1 = Import["reg1.mat"];
data2 = Import["reg2.mat"];
```

```
data3 = Import["reg3.mat"];
data4 = Import["reg4.mat"];
remDuplicates[dat_] := With[{sdat = Sort[dat]},
  sdat[[
    Sort[Flatten@Append[Select[Range[Length@sdat-1], (sdat[[#, 1]] ≠ sdat[[#+1, 1]]) || (sdat[[#,
2]] ≠ sdat[[#+1,2]])&], Length@sdat]]
   ]]
  ]
fullDat1 = remDuplicates[Transpose@(Flatten/@data1)];
fullDat2 = remDuplicates@Join[Transpose@(Flatten/@data2[[1;;3]]), Transpose@data2[[4]]];
fullDat3 = remDuplicates@Join[Transpose@(Flatten/@data3[[1;;3]]), Transpose@data3[[4]]];
fullDat4 = remDuplicates@Join[Transpose@(Flatten/@data4[[1;;3]]), Transpose@data4[[4]]];

fn1 = Interpolation[fullDat1, InterpolationOrder→1];
fn2 = Interpolation[fullDat2, InterpolationOrder→1];
fn3 = Interpolation[fullDat3, InterpolationOrder→1];
fn4 = Interpolation[fullDat4, InterpolationOrder→1];

vx1[x_, y_] := Evaluate[D[fn1[x,y], y]];
vy1[x_,y_] := Evaluate[-D[fn1[x,y], x]];
vx2[x_, y_] := Evaluate[D[fn2[x,y], y]];
vy2[x_,y_] := Evaluate[-D[fn2[x,y], x]];
vx3[x_, y_] := Evaluate[D[fn3[x,y], y]];
vy3[x_,y_] := Evaluate[-D[fn3[x,y], x]];
vx4[x_, y_] := Evaluate[D[fn4[x,y], y]];
vy4[x_,y_] := Evaluate[-D[fn4[x,y], x]];

Poly2 = Polygon[Transpose@data2[[4, 1;;2, 2;;5]]];
Poly3 = Polygon[Transpose@data3[[4, 1;;2, 2;;5]]];
Poly4 = Polygon[Transpose@data4[[4, 1;;2, 2;;5]]];

div2start = Poly2[[1,1,1]]; div2end = Poly2[[1,-1,1]];
div3start = Poly3[[1,1,1]]; div3end = Poly3[[1,-1,1]];
div4start = Poly4[[1,1,1]]; div4end = Poly4[[1,-1,1]];

C:\Users\USER\Desktop\Dropbox 5
Visualizations
ClearAll[visStream, visStream2, x, y]
visStream[psi_,vx_, vy_ , dividerPoly_:Polygon[{}]] := Show[
  Graphics[
   Flatten@{
     Blue,Thickness[0.006],
     Line[{{20,0}, {20, 7}}],
     Line[{{7, 10}, {0, 3}, {0,0}}],
     Black, Dashed,Thickness[0.008],
     Line[{{0,0}, {20,0}}],
     Line[{{20, 7}, {20, 10}, {7, 10}}],
     EdgeForm[],
     FaceForm[Directive[Lighter@Blue, Opacity[0.2]]],
     Polygon[{{0,0}, {20,0}, {20,10}, {7, 10}, {0,3}, {0,0}}],
     },
   ImageSize→800
   ],
  ContourPlot[psi[x,y],  {x, 0, 20}, {y, 0, 10}, RegionFunction→Function[{x,y}, x>y-3+.2 &&  .2≤ x≤
19.95], AspectRatio→1/2, ImageSize→500], (* Line for contours *)StreamPlot[{vx[x,y],vy[x,y]}, {x,
```

```
0, 20}, {y, 0, 10}, AspectRatio→1/2,  RegionFunction→Function[{x,y}, x>y-3+.2 && .2≤ x≤ 19.95]],
(* Line for streamlines *)
  Graphics[{Blue,  EdgeForm[Directive[Thick,  Black]],  FaceForm[Directive[Opacity[0.8],
Darker@Blue]],dividerPoly}],
  PlotRange→All
  ]

visStream2[vx_, vy_, dividerPoly_:Polygon[{}]] := With[{
   minVel = NMinimize[{If[x≥ y-3+.2,Sqrt[vx[x,y]^2 + vy[x,y]^2],   100], 0≤x ≤ 20, 0≤ y ≤ 10, x ≥ y-
3+.2}, {x,y} , PrecisionGoal→3][[1]],
   maxVel = NMaximize[{If[x≥ y-3+.2,Sqrt[vx[x,y]^2 + vy[x,y]^2],-100], 0≤x ≤ 20, 0≤ y ≤ 10, x ≥ y-
3+.2}, {x,y}, PrecisionGoal→3 ][[1]]},
  Show[
   Graphics[
    Flatten@{
      Blue,Thickness[0.006],
      Line[{{20,0}, {20, 7}}],
      Line[{{7, 10}, {0, 3}, {0,0}}],
      Black, Dashed,Thickness[0.004],
      Line[{{0,0}, {20,0}}],
      Line[{{20, 7}, {20, 10}, {7, 10}}],
      EdgeForm[],
      FaceForm[Directive[Lighter@Blue, Opacity[0.2]]],
      Polygon[{{0,0}, {20,0}, {20,10}, {7, 10}, {0,3}, {0,0}}],
      },
    ImageSize→800
    ],
   DensityPlot[
    If[x>y-3,Log@Sqrt[vx[x,y]^2 + vy[x,y]^2], 0],
    {x, 0.05, 19.8}, {y, 0.03, 9.8},
    RegionFunction→Function[{x,y}, x>y-3+.2 &&  .2≤ x≤ 19.95],
    PlotRange→All,  AspectRatio→1/2,  ColorFunction→"Temperature",
PlotLegends→BarLegend[{"Temperature", {minVel, maxVel}}]
    ],
   VectorPlot[{If[x>y-3,vx[x,y],0],If[x>y-3,vy[x,y],0]},  {x,  0,  19.8},  {y,  0,  10},  AspectRatio→1/2,
VectorPoints→Fine,  VectorScale→.1,  VectorStyle→Directive[Gray,  Opacity[0.8]],
RegionFunction→Function[{x,y}, x>y-3+.2 &&  .2≤ x≤ 19.95]], (* Line for streamlines *)
   Plot[vy[x,0], {x, 0, 20}, Axes→False,  Filling→0,PlotStyle→Directive[Thick, Black, Dashed],
FillingStyle→Directive[Gray,Opacity[0.2]], AspectRatio→1/2],
   Plot[10+vy[x,10], {x, 7.2, 20}, Axes→False, Filling→10,PlotStyle→Directive[Thick,Black, Dashed],
FillingStyle→Directive[Gray,Opacity[0.2]], AspectRatio→1/2],
   Graphics[{Blue,  EdgeForm[Directive[Thick,  Black]],  FaceForm[Directive[Opacity[0.8],
Darker@Blue]],dividerPoly}],
   PlotRange→All
   ]
  ]

visStream[fn1, vx1, vy1]
```

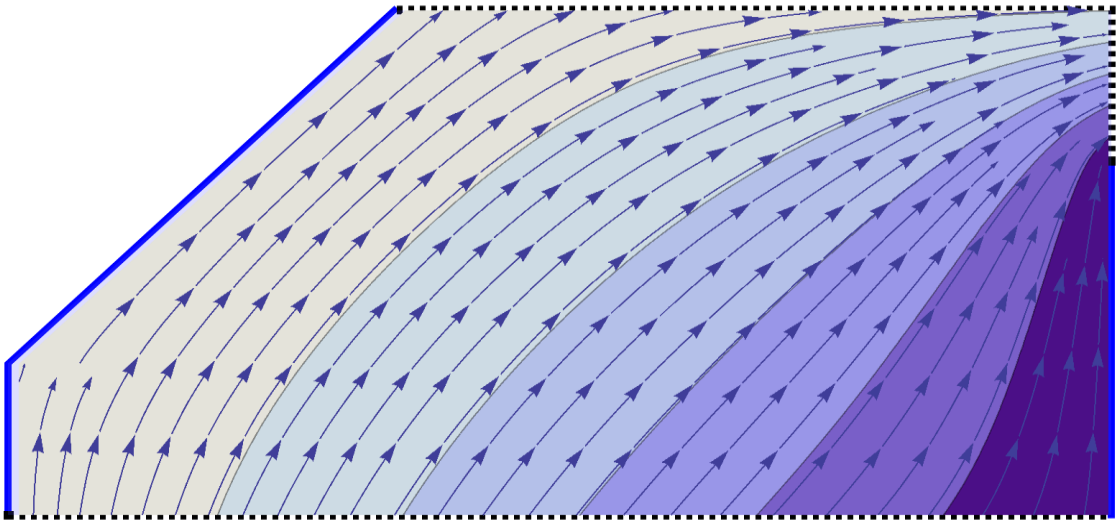

visStream[fn2, vx2, vy2, Poly2]

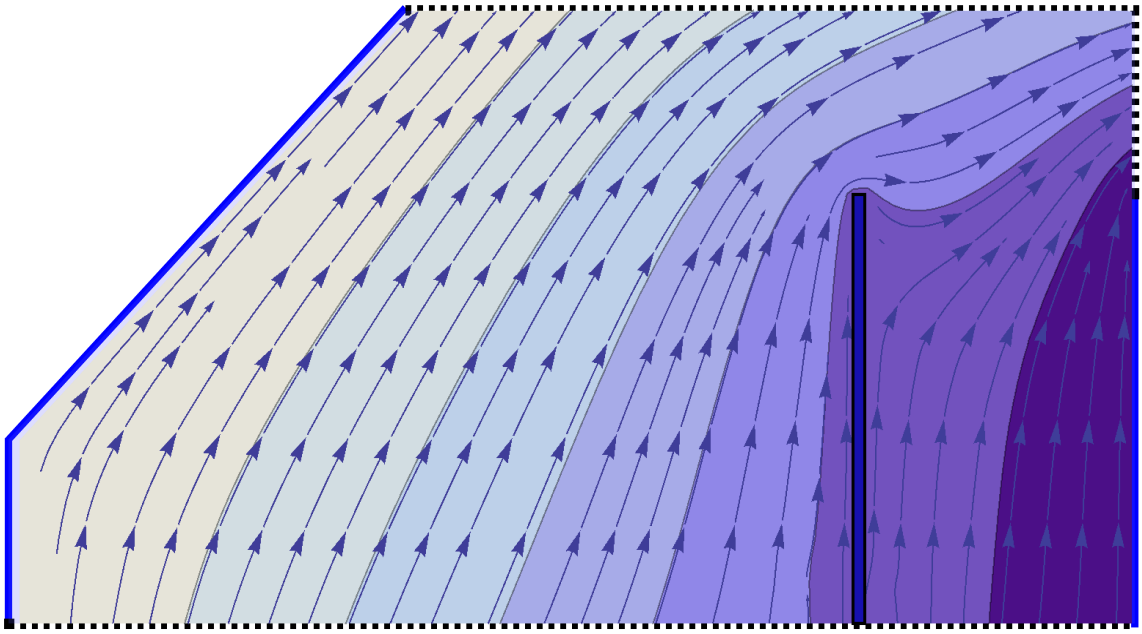

visStream[fn4, vx4, vy4, Poly4]

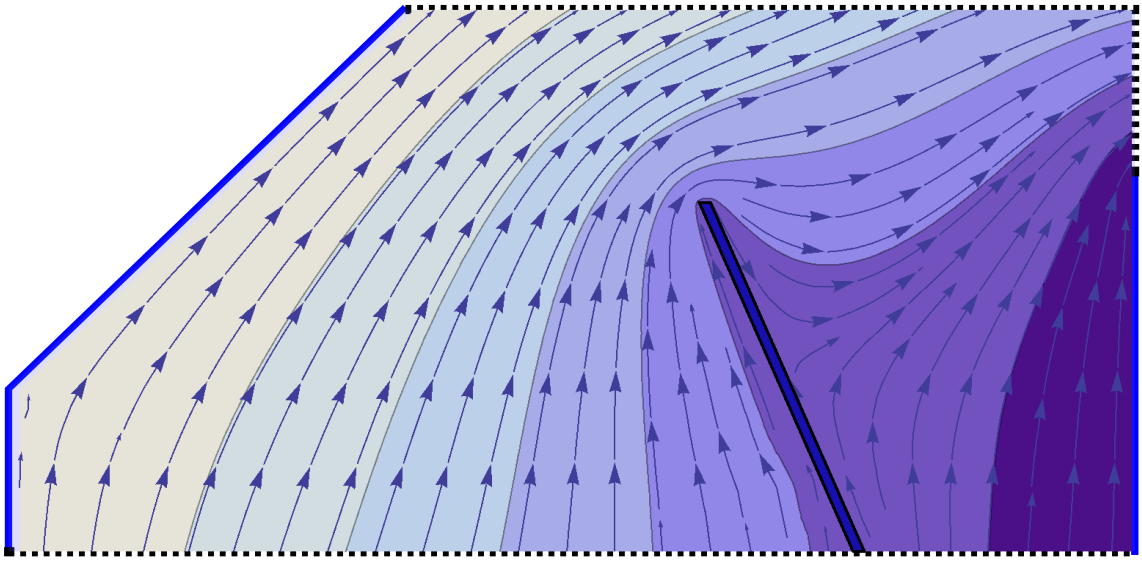

visStream[fn3, vx3, vy3, Poly3]

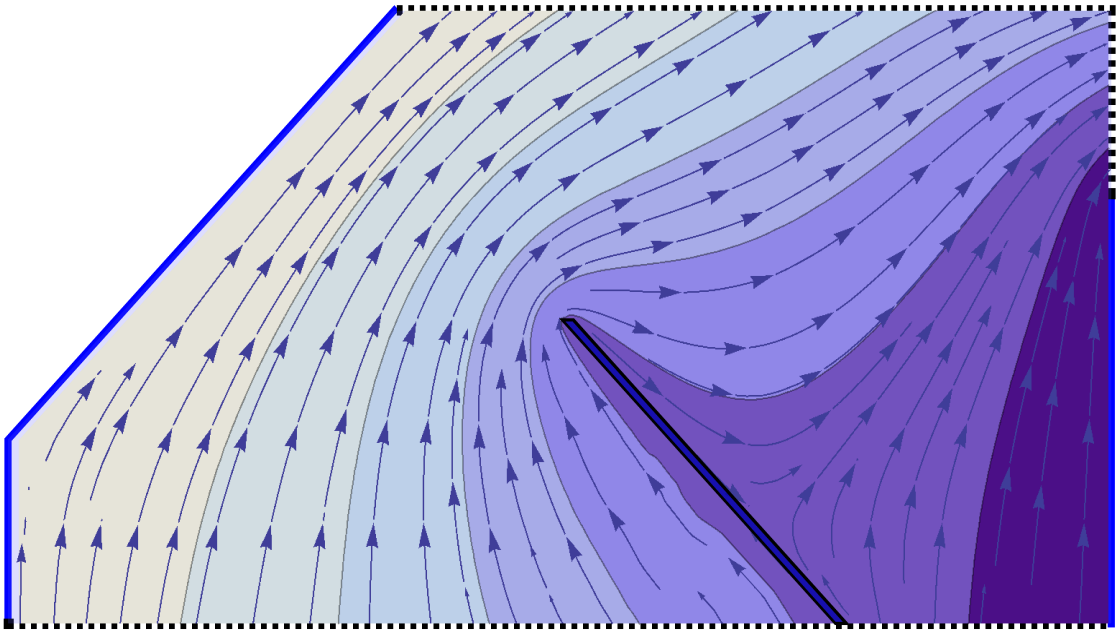

visStream2[vx1, vy1]
{

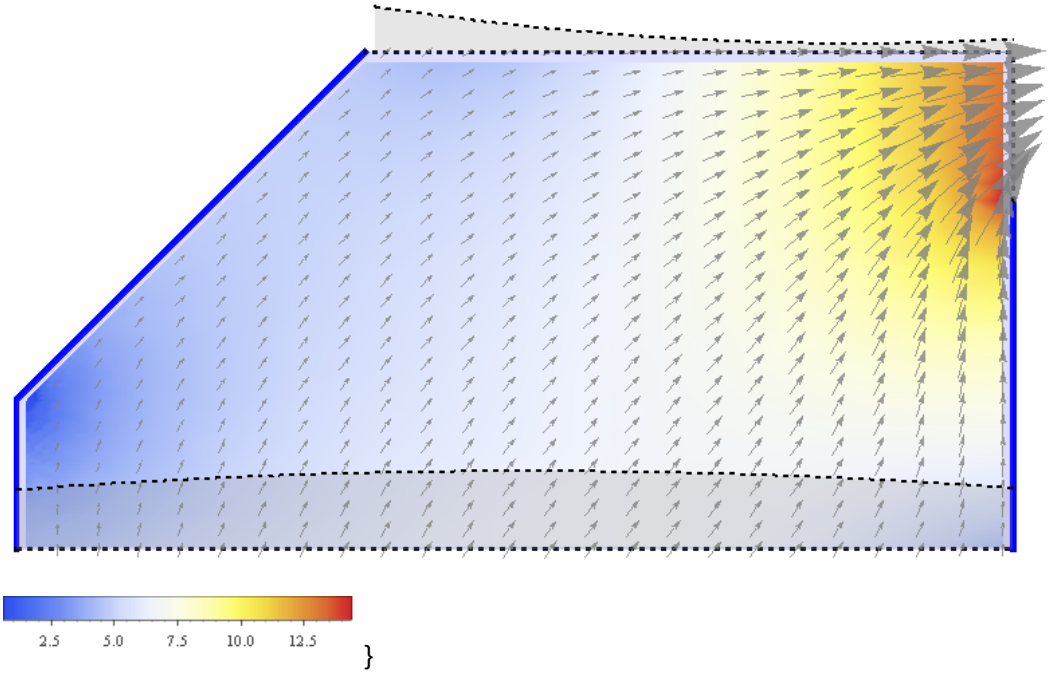

{ },

{ }

}

visStream2[vx2, vy2, Poly2]

{

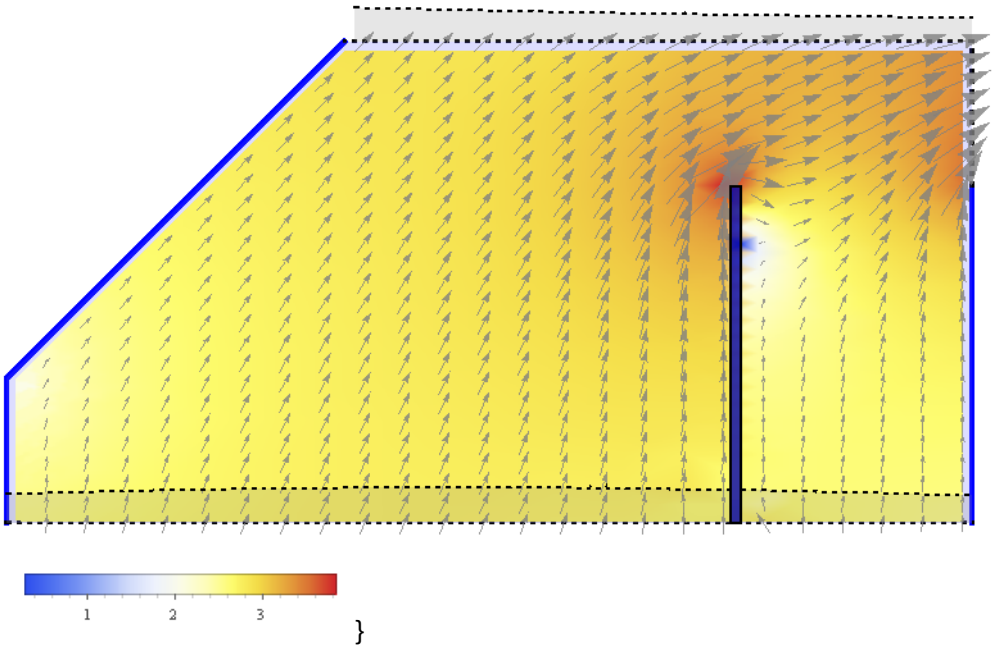

{ },

{ }

visStream2[vx4,vy4, Poly4]

{

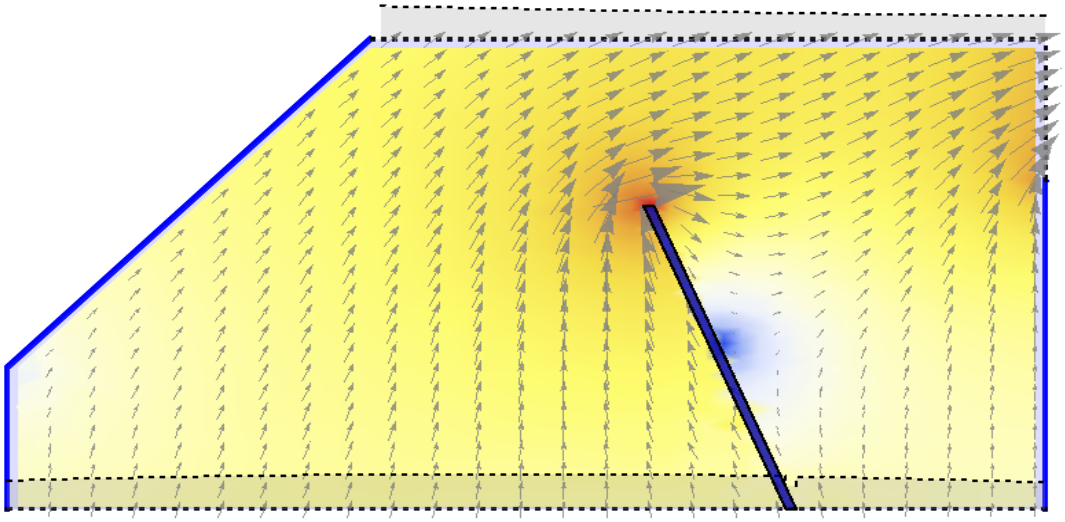

{ },

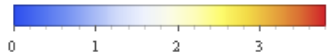

{ }

visStream2[vx3, vy3, Poly3]

{ {

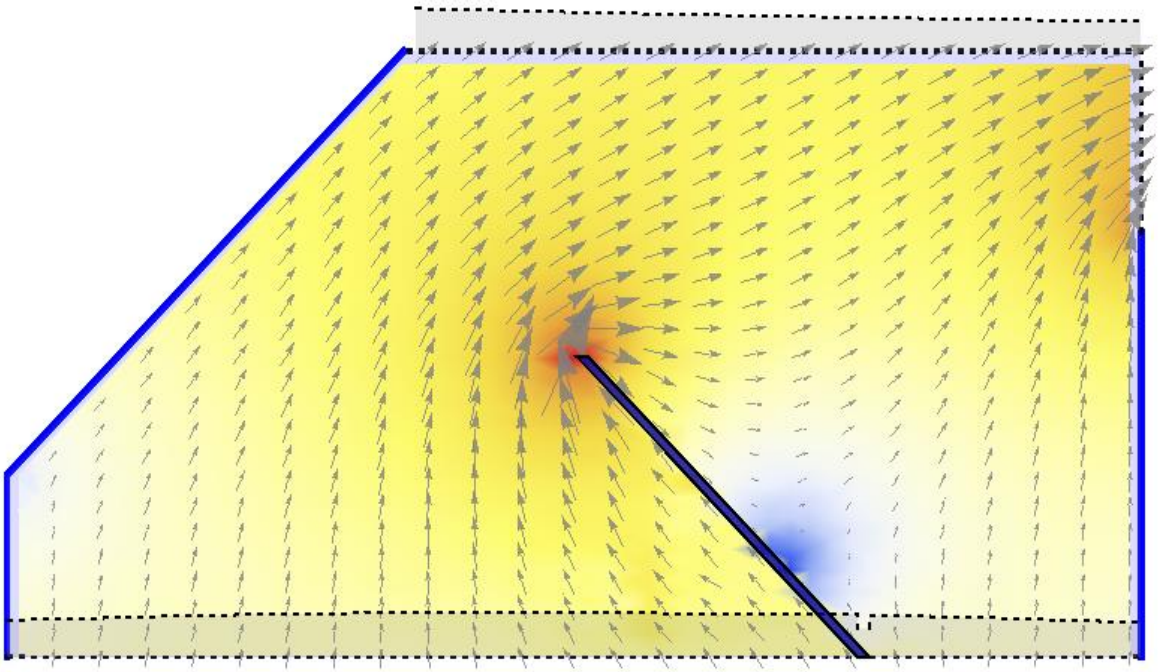

},

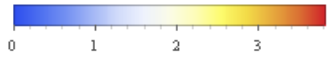

{ }

}

Transit Times

```
ClearAll[x,y,getTransitTimeAndPos, getFullTransitTime, getTransitTime]
getTransitTimeAndPos[vx_, vy_, x0_] :=
 Reap[NDSolve[
    With[{xval = Min[20,Max[x[t],0]],yval = Min[10,Max[y[t],0]]},
```

```
    {
     D[x[t], t] == vx[xval, yval],
     D[y[t], t] == vy[xval,yval],
     x[0] == x0,
     y[0] == 0,
     WhenEvent[(y[t]>9.95 && x[t] ≥  7) || (x[t] > 19.95 && y[t] ≥ 7), Sow[{t,x[t]}];"StopIntegration"]
     }
    ],
   {x[t], y[t]},
   {t, 0, 20}
   ]
  ][[2,1,1]]

getFullTransitTime[vx_, vy_,velfn_, x0_] :=
 Reap[NDSolve[
   With[{xval = Min[20,Max[x[t],0]],yval = Min[10,Max[y[t],0]]},
    { D[x[t], t] == vx[xval, yval],
     D[y[t], t] == vy[xval,yval],
     x[0] == x0,
     y[0] == 0,
     WhenEvent[(y[t]>9.9 && x[t] ≥  7) || (x[t] > 19.9 && y[t] ≥ 7), Sow[t+Integrate[velfn[p], {p, x[t],
19.9}]];"StopIntegration"]
     }
    ],
   {x[t], y[t]},
   {t, 0, 100}
   ]
  ][[2,1,1]]

getTransitTime[vx_, vy_, x0_] :=
 Reap[NDSolve[
   With[{xval = Min[20,Max[x[t],0]],yval = Min[10,Max[y[t],0]]},
    {
     D[x[t], t] == vx[xval, yval],
     D[y[t], t] == vy[xval,yval],
     x[0] == x0,
     y[0] == 0,
     WhenEvent[(y[t]>9.9 && x[t] ≥  7) || (x[t] > 19.9 && y[t] ≥ 7), Sow[t];"StopIntegration"]
     }
    ],
   {x[t], y[t]},
   {t, 0, 100}
   ]
  ][[2,1,1]]
```

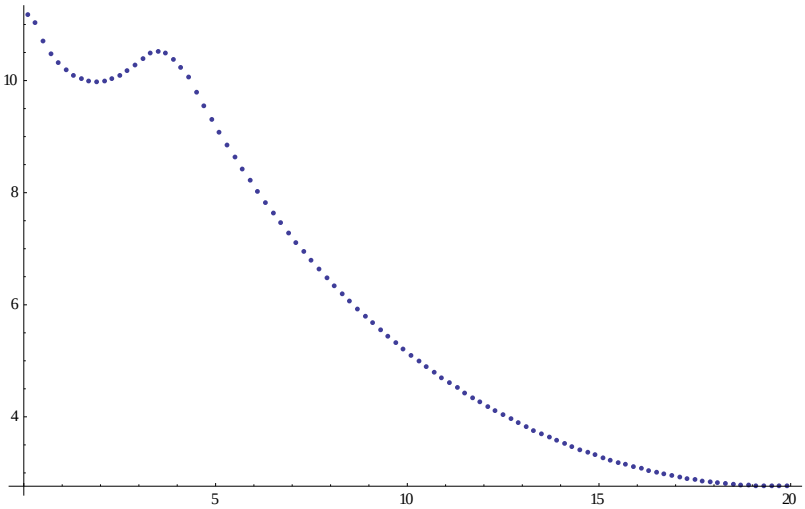


```
transitTimeList2 =Join[Table[{x0, getTransitTime[vx2n, vy2n, x0]}, {x0, 0.1, div2start-.1, 0.2}],
   Table[{x0, getTransitTime[vx2n, vy2n, x0]}, {x0, div2end+.1, 20, 0.2}]];
ListPlot[transitTimeList2
 ,Epilog→{Rectangle[{div2start, 0}, {div2end, 10}]}, ImageSize→500
 ]
```

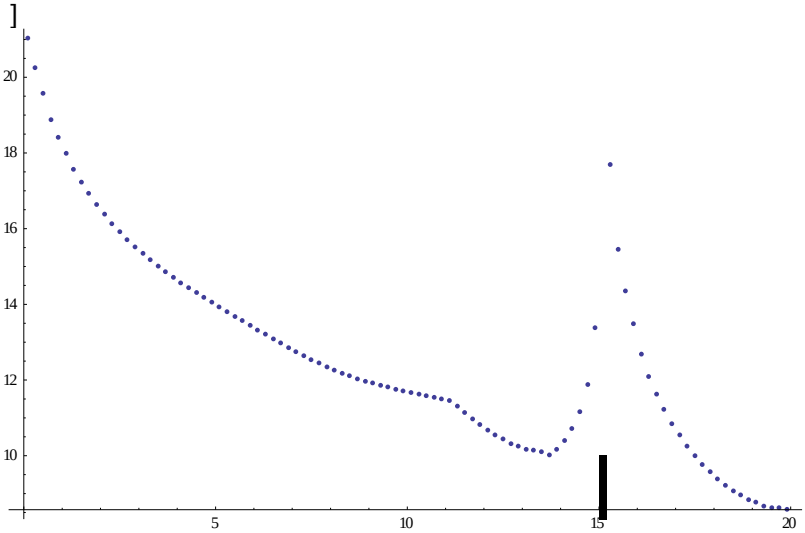


```
Export["transitTime2.xlsx", transitTimeList2]
transitTime2.xlsx
transitTimeList3 =Join[Table[{x0, getTransitTime[vx3n, vy3n, x0]}, {x0, 0.1, div3start-.1, 0.2}],
   Table[{x0, getTransitTime[vx3n, vy3n, x0]}, {x0, div3end+.1, 20, 0.2}]];
ListPlot[transitTimeList3
 , Epilog→{Rectangle[{div3start, 0}, {div3end, 10}]}, ImageSize→500
 ]
```

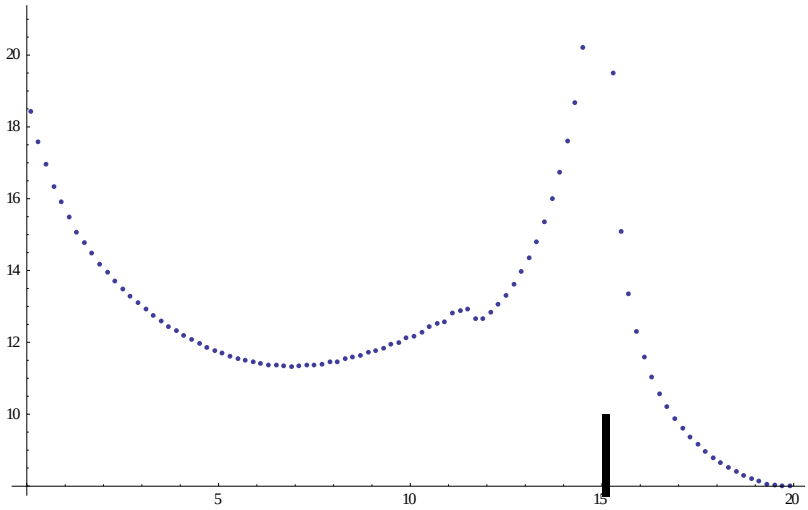


```
Export["transitTime3.xlsx", transitTimeList3]
```

transitTime3.xlsx

```
transitTimeList4 =Join[Table[{x0, getTransitTime[vx4n, vy4n, x0]}, {x0, 0.1, div4start-.1, 0.2}],
   Table[{x0, getTransitTime[vx4n, vy4n, x0]}, {x0, div4end+.1, 20, 0.2}]];
ListPlot[transitTimeList4
 , Epilog→{Rectangle[{div4start, 0}, {div4end, 10}]}, ImageSize→500
 ]
```

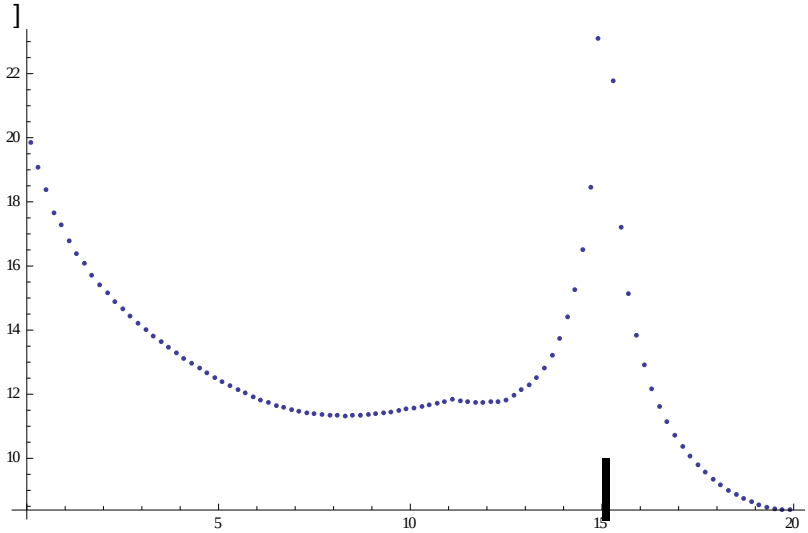


```
Export["transitTime4.xlsx", transitTimeList4]
```

transitTime4.xlsx

```
ListPlot[{transitTimeList1,transitTimeList2,transitTimeList3,transitTimeList4},
 Frame→True,
 PlotStyle→PointSize[Large],
 ImageSize→800,
 PlotLegends→{"No Divider", "90° Divider", "67° Divider", "45° Divider"},
 PlotLabel→Style["Transit Time (to vent) as a function of Starting Position\nfor four different
setups", 18, Bold],
 FrameLabel→{Style["Streamline starting position (x) at the bottom of the boiler", 14],Style["Full
Transit Time",14]},
 GridLines→Automatic,
 GridLinesStyle→Directive[Gray,Dashed],
 Epilog→ {Opacity[0.6], Rectangle[{div2start, 0}, {div2end, 15}]}
```

```
fullTTimes1= Table[{i,getFullTransitTime[vx1n, vy1n, Function[{r},0.0032 r^2+0.12 r-0.4473],i]}, {i, 0.1, 19.9, 0.2}];
ListPlot[fullTTimes1,Frame→True, PlotStyle→PointSize[Medium], ImageSize→500]
```

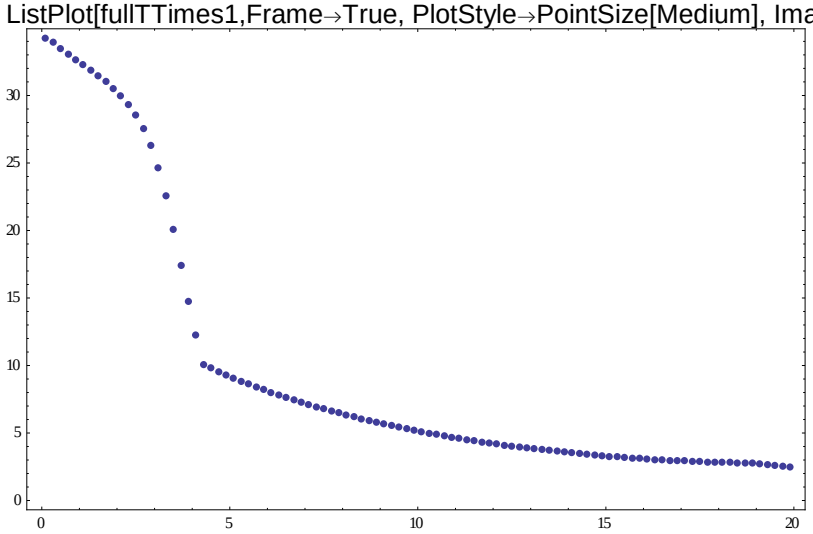


```
Export["fullTTimes1.xlsx", fullTTimes1]
fullTTimes2= Join[
  Table[{i,getFullTransitTime[vx2n, vy2n, Function[{r},0.0035 r^2+0.0775 r-0.2855],i]}, {i, 0.1, div2start-.1, 0.2}],
  Table[{i,getFullTransitTime[vx2n, vy2n, Function[{r},0.0035 r^2+0.0775 r-0.2855],i]}, {i, div2end+.1, 19.9, 0.2}]
  ];
ListPlot[fullTTimes2,Frame→True, PlotStyle→PointSize[Medium], ImageSize→500]
```

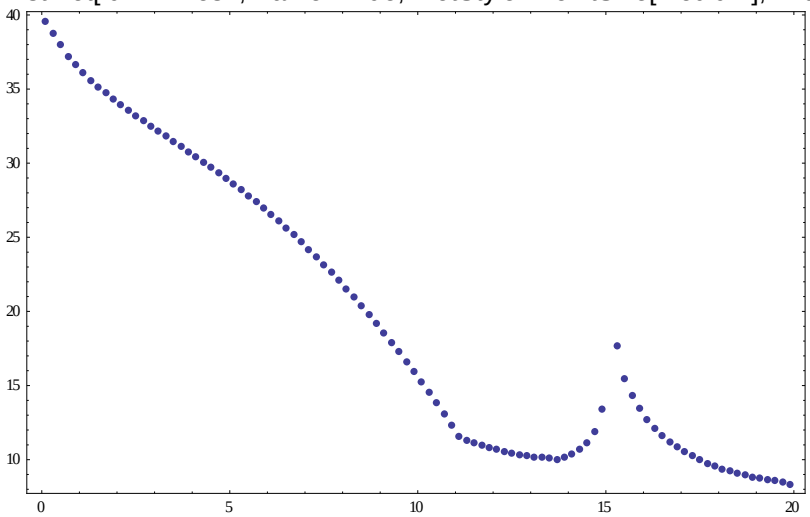


```
Export["fullTTimes2.xlsx", fullTTimes2]
fullTTimes2.xlsx

fullTTimes3= Join[
  Table[{i,getFullTransitTime[vx3n, vy3n, Function[{r},0.0035 r^2+0.0775 r-0.2855],i]}, {i, 0.1, div3start-.1, 0.2}],
  Table[{i,getFullTransitTime[vx3n, vy3n, Function[{r},0.0035 r^2+0.0775 r-0.2855],i]}, {i, div3end+.1, 19.9, 0.2}]
  ];
ListPlot[fullTTimes3,Frame→True, PlotStyle→PointSize[Medium], ImageSize→500]
```

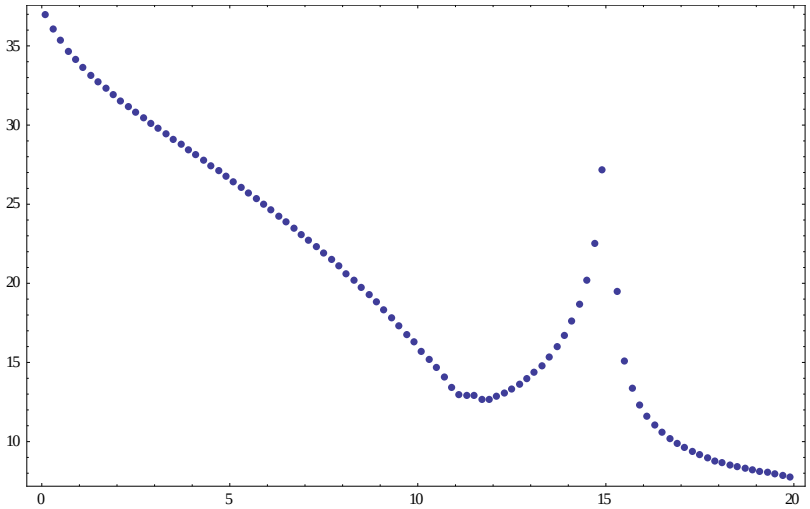


```
Export["fullTTimes3.xlsx", fullTTimes3]
fullTTimes3.xlsx
fullTTimes4= Join[
  Table[{i,getFullTransitTime[vx4n, vy4n, Function[{r},0.0035 r^2+0.0775 r-0.2855],i]}, {i, 0.1, div4start-.1, 0.2}],
  Table[{i,getFullTransitTime[vx4n, vy4n, Function[{r},0.0035 r^2+0.0775 r-0.2855],i]}, {i, div4end+.1, 19.9, 0.2}]
  ];
ListPlot[fullTTimes4,Frame→True, PlotStyle→PointSize[Medium], ImageSize→500]
```

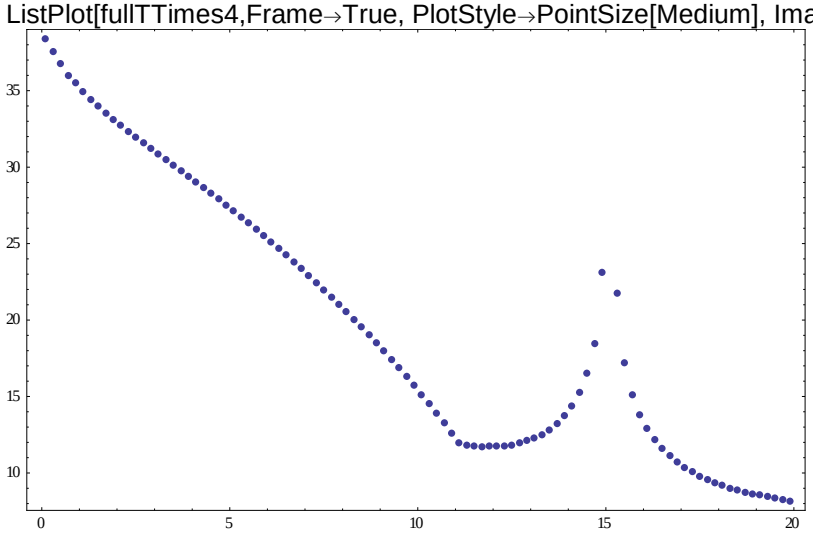


```
Export["fullTTimes4.xlsx", fullTTimes4]
fullTTimes4.xlsx
}
```

References

Ahmed, N., and Jameson, G.J., 1985. The effect of bubble size on the rate of flotation of fine particles. Int.J. Of Miner.Proc., 14, 195-215.

Alexander, D., Franzidis, J.-P., Manlapig, E., 2003. Froth recovery measurement in plant scale flotation cells. Minerals Engineering 16, 1197–1203.

Alford, R.A., 1990. An improved model for design of industrial column flotation circuits in sulphide applications. In: Gary, P.M.J. (Ed.), Sulphide Deposits—Their Origin and Processing. IMM, London.

Arbiter N.,1952. Flotation rates and flotation efficiency, AIME Trans, 190, 791-796.

Arbiter, N. and Harris, C.C., 1962. Flotation kinetics. Froth flotation 50th Anniversary Volume, ed. D. W. Fuerstenau, AIME, New York

Ata, S., Ahmed, N., Jameson, G.J., 2002. Collection of hydrophobic particles in the froth phase. Int. J. Miner. Process. 64, 101–122.

Ata, S., Ahmed, N., Jameson, G.J., 2003. A study of bubble coalescence in flotation froths. Int. J. Miner. Process. 72, 255–266.

Ata, S., Ahmed, N., Jameson, G.J., 2003. A study of bubble coalescence in flotation froths. Int. J. Miner. Process. 72, 255–266.

Ata,S., 2012. Phenomena in the froth phase of flotation — A review. Int J. Miner. Process., (102–103) 1–12.

Barbian, N., Hadler, K., Cillers, J.J., 2006. The froth stability column: measuring froth stability at an industrial scale. Minerals Engineering 19, 713–718.

Barbian, N., Hadler, K., Cilliers, J.J., 2005. The froth stability column – Measuring froth stability at an industrial scale. In: Proceedings of the Centenary of Flotation Symposium, Brisbane, pp. 315-319.

Barbian, N., Ventura-Medina, E., Cilliers, J.J., 2003. Dynamic froth stability in froth flotation.

Bennett A.J.R., Chapman W.R. and Dell C.C., 1960. Studies in froth flotation of coal, Third Int. Coal Preparation Congress 19S8, National de L'Industrie Charbonniere, Liege, 452-62.

Bergonio, P.P., (2003). Schwarz-Christoffel Transformations. Master of Arts Thesis. Georgia Southwerstern State University.

Bhondayi, C., 2010. Measurement of particle loading on bubbles in froth flotation. Msc thesis. University of the Witwatersrand

Bhondayi, C., Moys, M.H., 2011. Determination of sampling pipe(riser) diameter for a bubble load measuring device. Minerals Engineering 24, 1664-1676

Blanchard, D.C., "The Electrification of the Atmosphere by Particles from Bubbles in the Sea," Reference 61-9, Woods Hole. Oceanographic Institution, 1961.

Brito-Parada, P.R., Kramer, S.C., Wilson, C.R., Pain, C.C., Neethling, S.J., Cilliers, J.J.,2012. A finite element formulation to model the flow of foams. Chemical Engineering Science 69 (1), 279–286

Brown, J.W., Churchill, R.V., 2009.Complex variables and applications. McGraw-Hill, ISBN 978–0–07–305194–9

Burgess, F.L., 1997. OK100 tank cell operation at Pasminco—Broken Hill. Minerals Engineering 10 (7), 723–741.

Bushell C.H.G., 1962. Kinetics of flotation, AIME Trans., 223, 266-78.

Carlon, H.R., "Ion content of air humidified by boiling water," J. Appl. Phys. Vol. 51(1), pp 171-173 (1980).

Cliek, E.C., Yilmazer, B.Z., 2003. Effects of hydrodynamic parameters on entrainment and flotation performance. Miner. Eng. 16, 745–756.

Cillers, J., 2006. Understanding froth behaviour with CFD. In: Fifth International Conference on CFD in the Process Industries, CSIRO, Melbourne, Australia, 13–15 December 2006

Collins, G.L. and Jameson, G.J., 1976. Experiments on the flotation of fine particles the influence of particle size and charge. Chem. Eng. Sci., 31: 985--991.

Cooper, M., Scott, D., Dahlke, R., Finch, J.A.,Gomez, C.O., 2004. Impact of air distribution profile on banks in a Zn cleaning circuit. CIM Bull, 97, 1–6.

Cutting, G.W., Barber, S.P. and Newton, S., 1986. Effects of froth structure and mobility on the performance and simulation of continuously operated flotation cells. Int. J. Miner. Process.,16: 43-61.

Cutting, G.W., 1989. Effect of froth structure and mobility on plant performance. Miner. Process. Extr. Metall. Rev. 5, 169–201.

Cutting, G.W., Watson, D., Whitehead, A., Barber, S.P., 1981. Froth structure in continuous flotation cells: relation to the prediction of plant performance from laboratory data using process models. Int. J. Miner. Process. 7 (4), 347–369.

Driscoll, T. A., and Thefethen, L. N., (2002). Schwarz-Christoffel Mapping, Cambridge Monographs on Applied and Computational Mathematics.

Driscoll, T. A..(1996). A MATLAB toolbox for Schwarz–Christoffel mapping. ACM Trans. Math. Soft., 22:168–186.

Dyer, C., 1995. An investigation into the properties of the froth phase in flotation process. Msc thesis. University of the Witwatersrand.

Engelbrecht, J.A., Woodburn, E.T., 1975. The effect of froth height, aeration rate and gas precipitation on flotation. J. South Afr. Inst.Min. Metall. 76, 125–132.

Falutsu, M., Dobby, G.S., 1989. Direct measurement of froth drop back and collection zone recovery in a laboratory flotation column. Miner. Eng. 2 (3), 377–386.

Falutsu, M., Dobby, G.S., 1989. Direct measurement of froth drop back and collection zone recovery in a laboratory flotation column. Miner. Eng. 2 (3), 377–386.

Falutsu, M., Dobby, G.S., 1992. Froth performance in commercial sized flotation columns. Minerals Engineering 5 (10– 12), 1207–1223.

Farrokhpay, S., 2011. The significance of froth stability in mineral flotation — a review. Adv. Colloid Interface Sci. 166 (1–2), 1–7.

Feteris, S.M., Frew, J.A., Jowett, A., 1987. Modeling the effect of froth depth in flotation. Int. J. Miner. Process. 20 (1–2), 121–135.

Fichera, M.A. and Chudacek, M.W. 1992. Batch cell flotation models-A review. Miner.Eng.5, 41-55

Finch, J.A., Dobby, G.S., 1990. Column Flotation. Pergamon Press: Oxford Pergamon

Finch, J.A., Xiao,J.,Hardie, C.,Gomez, C.O.,2000. Gas dispersion properties: Bubble surface area flux and gas holdup.

Forbes, G., 2007. Texture and Bubble size measurements for modelling concentrate grade in flotation froths systems. PhD thesis. University of Cape Town.

Frew J.A. and Trahar W.J., 1981. Roughing and cleaning flotation behaviour and the realistic simulation of complete plant performance, Int. J. Miner. Process, 9, 101-20.

Fuerstenau,M.C., Yoon, R.-H., Jameson, G.J., 2007. Froth flotation : a century of innovation. Society for Mining, Metallurgy, and Exploration, Littleton, Colo., ix, p. 710.

Gaudin A.M., 1957. Flotation, 2nd Ed, McGraw-Hill Book Co., New York.

Gaudin, A. M., Groh, J.O., and Henderson, H. B.,1931. The effect of particle size on flotation. AIME. Tech.Pub.,414, pp.3-23.

Gaudin, A.M., Schuhmann, R. and Schlecten, W., 1942. Flotation kinetics. II, The effect of size on the behaviour of galena particles, J. Phys. Chem., 46, 902-10.

Gorain, B.K., Burgess, F., Franzidis, J.P., Manlapig, E.V., 1997a. Bubble surface area flux—a new criterion for scale-up. In: AusIMM Sixth Mill Operators' Conference,Madang, pp. 141–148.

Gorain, B.K., Franzidis, J.P., Manlapig, E.V., 1996. The effect of gas dispersion properties on the kinetics of flotation. Column-96: Proceedimgs of the 35th Annual conference of Metallurgists.CIM, Montreal, Canada, 26-28., pp .299-313.

Gorain, B.K., Franzidis, J.P., Manlapig, E.V., 1997b. Studies on impeller type, impeller speed and air flow rate in an industrial scale flotation cell. Part 4: effect of bubble surface area flux on flotation performance. Minerals Engineering 10, 367–379.

Gorain, B.K., Napier-Munn, T.J., Franzidis, J.P., Manlapig, E.V., 1998. Studies on impeller type, impeller speed and air flowrate in an industrial scale flotation cell. Part 5: validation of k–Sb relationship and effect of froth depth. Minerals Engineering 11, 615–626.

Grau, R., Laskowski, J.S., Heiskanen, K., 2005. Effect of Frothers on Bubble Size, Int. J. Mineral Processing, Vol. 76, 225-233.

Hadler, K., Cilliers, J.J., 2009. The relationship between the peak in air recovery and flotation bank performance. Minerals enginerring 22:451-455

Hadler, K.; Smith, C.D.; Cilliers, J.J., 2010. Recovery vs. mass pull: The link to air recovery. Miner. Eng, 23, 994–1002.

Hanumanth, G.S. and Williams, D.J.A., 1992 A three-phase model of froth flotation. Int. J. Mineral Process, 1992, 34, 261-273.

Hanumanth, G.S., Williams, D.J.A., 1990. An experimental study of the effects of froth height on flotation of China clay. Powder Technology 60, 131–144.

Harris C.C. and Chakravarti A., 1970. Semi-batch froth flotation kinetics: species distribution analysis, Trans. Soc. Min. Eng. AIME, 247, 162-72.

Harris, C. C.,1978. Multiphase models of flotation machine behavior. Int. J. Miner. Process. 5, 107-129.

Harris, T. A.,2000.The development of a flotation simulation methodology towards an optimisation study of UG2 platinum flotation circuits. PhD thesis. University of Cape Town.

Hukki R.T.,1953. Discussion on paper measurement and evaluation of the rate of flotation as a function of particle size" by T.M. Morris, AIME Trans, 196, 1122-4.

Iglesias E, Anderez J, Forgiarini A, Salager JL. 1995. A new method to estimate the stability of short-life foams. Colloids Surf A Physicochem Eng Asp 98:167–174.

Imaizumi T. and Inoue T., 1965. Kinetic consideration of froth flotation, 6th Int, Mineral Processing Congr., Cannes, 1963, Pergamon Press Ltd., London, 581-93.

Jafari, R., Tanguy P. A., and Chaouki, J., 2012. A comprehensive review of just suspended speed in Liquid-solid and gas-liquid-solid stirred tank reactors. International Journal of chemical Reactor Engineering 10: R1

Johansson, G., Pugh, R.J., 1992. The influence of particle size and hydrophobicity on the stability of mineralized froths. Int. J. Miner. Process. 34 (1–2), 1–21.

Jowett A. and Ghosh S.K.,1965. Flotation kinetics: Investigations leading to process optimization, 7th Int. Mineral Processing Cong. New York, 1964, Gordon & Breach, 175-84.

Jowett A. and Safvi S.M.M.1960. Refinements in methods of determining flotation rates, AIME,217, 351-7

Kelsail D.F., 1961. Application of probability in the assessment of flotation systems, Trans.Instn. Min. Metall. 70, 191-204

Khandpur R.S., 2003. Handbook of Biomedical instrumentation. Tata McGraw Hill Publishing Co Ltd

King, R.P., 1973. Model for the design and control of flotation plants. Society of Mining Engineering of AIME Transactions 274, 341–350.

King, R.P., 2001. Modelling and Simulation of mineral Processing Systems, Butterworth-Heinemann, pp 290

Kirjavainen, V.M., 1996, Review and analysis of factors controlling the mechanical flotation of gangue minerals. Int. J. Miner. Process., 46: 21-34.

Klassen, V.I., Mokrousov, V.A., 1963. An Introduction to the Theory of Flotation. Butterworth, London.

Laplante, AR., Toguri, J.M. and Smith, H.W., 1983a. The effect of air flow rate on the kinetics of flotation. Part I: The transfer of material from the slurry to the froth. Int. .I. Miner. Process., 11: 203-219.

Le Goff, A., Courbin, L., Stone, H, A., Qu´er´e, D., 2008. Energy absorption in a bamboo foam. Europhys. Lett. 84, (36001).

Maachar, A., Dobby, G.S., 1992. Measurement of feed water recovery and entrainment solids recovery in flotation columns, Canadian Metallurgical Quarterly, 31:167-172

Maldonado, M.; Araya, R.; Finch, J, 2011. Optimizing flotation bank performance by recovery profiling. Miner. Eng, 24, 939–943.

Malysa, E., Malysa, K., Czarnecki, J., 1987. A method of comparison of the frothing and collecting properties of frothers. Colloids Surf. 23, 29–39.

Mathe, T.Z., Harris, M.C., O'Connor, C.T., 2000b. A review of methods to model the froth phase in non-steady state flotation systems. Minerals Engineering 13 Ž2., 127–140.

Mehrotra,S.P. and Kapur, P.C.,1974. The effects of aeration rate, particle size and pulp density on the flotation rate distributions. Powder Technology, 9, 1974, pp. 213-219.

Meyer, G.H., 1978. The method of lines for poisson's equation with nonlinear or free boundary conditions., Numer. Math. 29, 329- 344

Morris T.M., 1952. Measurement and evaluation of the rate of flotation as a function of particle size, AIME Trans.,193, 794-8.

Moys, M.H., 1979. A study of processes occurring in flotation froths. PhD thesis. University of Natal, South Africa

Moys, M.H., 1984. Residence time distributions and mass transport in the froth phase of the flotation process. International Journal of Mineral Processing 13, 117–142.

Moys, M.H., Yianatos, J.B., Larenas, J., 2010. Measurement of particle loading on bubbles in the flotation process. Minerals Engineering Journal 23,131-136

Murphy, D.G., Zimmerman, W., Woodburn, E.T., 1996. Kinematic model of bubble motion in a flotation froth. Powder technology 78, 3-12

Neethling, S.J., 1999. A mathematical model of flowing foams and froths. Ph.D. thesis, University of Manchester Institute of Science and Technology, UK.

Neethling, S.J., Cilliers, J.J., 2003. Modelling flotation froths. International Journal of Mineral Processing 72 (1–4), 267–287.

Neethling, S.J., Lee, H.T., Cilliers, J.J., 2003. Simple relationships for predicting the recovery of liquid from flowing foams and froths. Minerals Engineering 16, 1123–1130.

Neethling, S.J.,Cilliers, J.J.,1998. The effect of weir angle on bubble motion in a flotation froth: visual modelling and verification. Minerals Engineering, 11, 1035-1046,

Neethling, S.J.,Cilliers, J.J.,2002. The entrainment of gangue into a flotation froth. Int J.Miner.Process, 123-134.

Nolan, J.J., and Enright, J., 1922. Experiments on the electrification produced by breaking-up water with special reference to Simpson's theory of the electrification of thunderclouds," Proc. R. Dublin Soc. Vol. 17, pp 1-11

Pacho, D., Davies, G., 2003. Detection and monitoring of oil foams using raw capacitance data. Ind. Eng. Chem. Res. 42, 636–645

Paul W.C.Northrop, P.W.C., Ramachandran, P.A., Schiesser, W.E., Subramanian, V.R., 2013. A robust false transient method of lines for elliptic partial differential equations. Chemical Engineering Science 90,32–39

Rahman, R.M., Ata, S., Jameson, G.J., 2012. Froth recovery in industrial flotation cells. XXVI International Mineral Processing Congress, New Delhi, India.

Rasband, W.S., ImageJ, US National Institutes of Health, Bethesda, Maryland, USA, http://imagej.nih.gov/ij/, 1997-2012.

Riera, G., Carrasco,H., Preiss,R., (2008). The Schwarz-Christoffel conformal mapping for ″Polygons″ with Infinitely Many Sides. International Journal of Mathematics and Mathematical, Sciences, Hindawi Publishing Corporation, doi:10.1155/2008/350326

Ross, V.E. & Van Deventer, J.S.J.,1988, Mass transport in flotation column froths, Column Flotation '88. Proc. Inter. Symp. Column Flotation, A.I.M.E

Ross, V.E., 1990. Interpretation of froth data to study the detachment of floating particles in flotation froths. Minerals Engineering 3 (5) 525-531

Ross, V.E., 1991. Comparison of methods for evaluation of true flotation and entrainment. Trans. Min. Metall. (sect. C: Mineral Process. Extr. Metall.) 100, C121-170.

Runge, K., Crosbie, R., Rivett, T., McMaster, J., 2010. An evaluation of froth recovery measurement techniques. XXV International Mineral Processing Congress, Brisbane, Australia, Brisbane, Australia.

Savassi, O., Alexander, D., Johnson, N., Franzidis, J.-P., Manlapig, E.,1997. Measurement of froth recovery of attached particles in industrial floatation cells. In: Sixth Mill Operators Conference. Madang, Papua New Guinea, pp. 149–156.

Savassi, O.N., Alexander, D.J., Franzidis, J-P., Manlapig, E.V., 1998. An empirical model for entrainment in industrial flotation plants. Miner. Eng. 11 (3), 243–256.

Schiesser, W.E., Griffiths, G.W., 2009. A compendium of Partial Differential Equation Models: Method of Lines Analysis with Matlab. Cambridge University Press, New York, ISBN: 9780521519861.

Schubert, H. and Bischofberger, C., 1978. On the hydrodynamics of flotation machines.Int. J. Miner. Process., 5: 131-142.

Schuhmann, R. 1942. Flotation Kinetics I: Methods for steady-state study of flotation problems. J. Phys. Chem., 46, 891-902.

Seaman, D., Franzidis, J., Manlapig, E., 2004. Bubble load measurement in the pulp zone of industrial flotation machines—a new device for determining the froth recovery of attached particles. International Journal of Minerals Processing 74 (1–2), 1–13.

Seaman, D.R., Manlapig, E.V., Franzidis, J.P., 2006. Selective transport of attached particles across the pilp-froth interface. Minerals Engineering 19 841-851

Simpson, G.C., "On the Electricity of Rain and Its Origin in Thunderstorms," Phil. Trans. A. Vol. 209, pp 379-4131'. (1909).

Smith, P.G and Warren, L.J., 1989, Entrainment of particles into flotation froths, in Frothing in Flotation, Gordon and Breach, New York, 123-145

Subrahmanyam, T.V., Forsberg, E., 1988. Froth stability, particle entrainment and drainage in flotation — a review. Int. J. Miner. Process. 23 (1–2), 33–53.

Sultan, A. I., (2013). Schwarz-Christoffel transformation on a half plane. International Refereed Journal of Engineering and Science (IRJES) 2319-1821 Volume 2, PP.25-29

Sutherland, K.L.,1948. Kinetics of the flotation process. Journal of Phys. Chem. 52, pp. 394-424

Szatkowski, M., 1987. Factors influencing the behaviour of flotation froth. Transactions of the Institution of Mining and Metallurgy (Sect. C: Mineral Process. Extr. Metall.) 96, C115– C122.

Tao, D., Lutrell, G.H., Yoon, R.H., 2000. A parametric study of froth stability and its effect on column flotation of fines. Int. J. Miner.Process. 59, 25-43.

Tomlinson H.S. and Fleming M.G., 1965. Flotation rate studies, 6th Int. Mineral Processing Congr., Cannes, 1963, Pergamon Press Ltd, London, 563-79).

Trahar, W.J. and Warren, L.J., 1976. The floatability of very fine particles. Int. J. Miner. Process, Vol.3, pp, 103-131.

Trahar, W.J., 1981. A rational interpretation of the role of particle size in flotation. Int.J.Miner.Proc.,Vol.8, pp.289-327.

Trefethen, L. N., (1989). SCPACK user's guide. MIT Numerical Analysis Report 89-2,

van Deventer, J.S.J. / Feng, D. / Burger, A.J., 2001. The use of bubble loads to interpret transport phenomena at the pulp-froth interface in a flotation column *Chemical Engineering Science* **56** (1 and 2):6313-6319.

Van Deventer, J.S.J., Feng, D., Burger, A.J., 2004. Transport phenomena at the pulp – froth interface in a flotation column: II. Detachment. International Journal of Mineral Processing 74, 217– 231.

Ventura-Medina, E., Cilliers, J.J., 2002. A model to describe flotation performance based on physics of foams and froth image analysis. International Journal of Mineral Processing 67, 79– 99.

Vera, M., Franzidis, J.-P., Manlapig, E., 1999a. Simultaneous determination of collection zone rate constant and froth zone recovery in a mechanical flotation environment. Minerals Engineering 12 (10), 1163– 1176.

Vera, M., Franzidis, J.-P., Manlapig, E., 1999b. The JKMRC high bubble surface area flux flotation cell. Minerals Engineering 12 (5), 477–484

Vera, M.A., Franzidis, J.P., Manlapig, E.V., 1999. Simultaneous determination of collection zone rate constant and froth zone recovery in a mechanical flotation environment. *Minerals Engineering.,* **12** (10): 1163–1176.

Vera, M.A., Mathe, Z.T., Franzidis, J.P., Harris, M.C., Manlapig, E.V., O'Connor, C.T., 2002. The modelling of froth zone recovery in bath and continuously operated laboratory flotation cells. Int. Miner. Process. 64, 135–151.

Volkova Z., 1946. The bubble mineralization process in flotation, Compt. Rend. Acad. 5ci.URSS,51,449-52

Warburg, E., 1899. Ueber das verhalten sogenannter unpolarisbarer elektroden gegen wechselstrom. Annalen der Physik und Chemie. 67, 493–499.

Watson, D. and Grainger-Allen, T.J.N., 1974. Study of froth flotation using a steady state technique. Trans.Soc.Min.Eng.AIME,256: 242-247

Wills. B.A.,1992. Mineral Processing Technology. Fifth ed. pp 491

Wilson, S.D.R., 1982. The drag-out problem in film coating theory. J. Eng. Math. 16, 209.

Woodbum, E.T. and Wallin, P.J., 1984. Decoupled kinetic model for simulation of flotation networks-. Trans. Instn. Min. Metall. (Sect. C." Mineral Process. Extr. Metall.), 93, C153-C161.

Woodburn E.T. and Loveday B.K., 1965. The effect of variable residence time on the performance of a flotation system, J. South African Inst. of Mining & Met., 65,612-28.

Woodburn, E.T.; Austin, L.G.; Stockton, J.B., 1994. A froth based flotation kinetic model. Chem. Eng.Res. Des, 72, 211–226.

Xie, W., Neethling, S.J. and Cilliers, J.J., 2004. A novel approach for estimating the average bubble size for foams flowing in vertical columns *Chemical Engineering Science*, Volume 59, issue 1; p. 81-86.

Yianatos, J., Bergh, L., Cortes, G., 1998. Froth zone modelling of an industrial flotation column. Minerals Engineering 11 (5), 423–435.

Yianatos, J.B., Finch, J.A. & Laplante, A.R., 1986. Apparent hindered settling in a gas-liquid-slurry counter-current column, Int. J. Miner. Process. 18:155-165.

Yianatos, J.B., Finch, J.A., Laplante, A.R., 1986a. Holdup profile and bubble size distribution of flotation column froths. Canadian Metallurgical Quarterly 25 (1), 23– 29.

Yianatos, J.B., Finch, J.A., Laplante, A.R., 1986b. Apparent hindered settling in a gas–liquid– solid countercurrent column. International Journal of Mineral Processing 18,155– 165

Yianatos, J.B., Finch, J.A., Laplante, A.R., 1988. Selectivity in column flotation froths. Int.J. Miner. Process. 23 (3–4), 279–292.

Yianatos,J.B., Contreras. F., 2010. Particle entrainment model for industrial flotation cells, p*owder Technology* **197**: 260–267.

Yianatos, J.B., Moys, M.H., Contreras, F., Villanueva, A., 20, A., 2008. Froth Recovery of industrial flotation cells. Miner. Eng., 21:817-827

Yoon, R.H.,Luttrell, G.H., 1989. The effect of bubble size on fine particle flotation. Min. Proc. and Extra. Met. Rev., Vol 5,pp.101-122.

Young, P., 1982. Flotation machines. Mineralogical Magazine 145 (1), 35–39.

Zanin, M., Gredelj, S., Grano, S.R., 2008. Factors affecting froth stability in mineral flotation and implications on minerals recovery: a case study. In: Kuyvenhoven, R., Gomez, C., Casali, A. (Eds.), Proceedings of Procemin 2008, Santiago (Chile), pp. 197–206.

Zanin, M., Wightman, E., Grano, S., Franzidis, J.-P., 2009. Quantifying contributions to froth stability in porphyry copper plants. International Journal of Mineral Processing 91, 19–27.

Zheng, X., Franzidis, J.P., Manlapig, E., 2004. Modelling of transport in industrial flotation cells Part 1. Development of froth transportation models for attached particles. Minerals Engineering., 17, 981–988

Zheng, X., Johnson, N.W., Franzidis, J.P., 2006. Modelling of entrainment in industrial flotation cells: water recovery and degree of entrainment. Minerals Engineering., 19 (11),1191–1203

Zheng, X.,Franzidis,J.P.,Johnson,N.W.,Manlapig,E.V.,2005.Modelling of entrainment in industrial flotation cells: the effect of solids suspension. Minerals Engineering 18, 51-58.

Zheng,X., Franzidis,J.P., Manlapig, E.V., 2004. Modelling of froth transportation in industrial flotation cells Part I. Development of froth. Minerals Engineering 17 (2004) 981–988

Zhou, Y., Zhang, Q., Liu, H., Lei, H., 2012.Measurements and characterization of bubble dynamics in capillary two-phase flows by a micro double-tip conductivity probe. Flow Measurement and Instrumentation 24 (2012) 36–42

Zuniga H.G., 1935. Flotation recovery is an exponential function of its rate, Boln. Soc. Nac. Min. Santiago, 47, 83-6.

Zwietering, T. N., 1958. Suspending of solid particles in liquid by agitators. Chemical Engineering Science **8** (3-4): 244-253.